GASEOUS DIFFUSION IN POROUS SOLIDS AND ITS ROLE IN GAS/SOLID REACTIONS

A thesis presented for the
Degree of Doctor of Philosophy
of the University of London

by

FRANCIS RAPHAEL CAMPBELL

MARCH 1971

John Percy Research Group in
Process Metallurgy,
Royal School of Mines,
Imperial College of Science
and Technology,
Prince Consort Road,
LONDON, S.W.7.

ABSTRACT

Effective gaseous diffusion coefficients have been determined in three porous product layers: lime reduced by the thermal decomposition of calcium carbonate; iron reduced from ferrous chloride in hydrogen and nickel reduced from nickel oxide also in hydrogen. The experimental measurements, which were made using a hollow-sphere technique, have been interpreted by the use of the 'dusty-gas' model. Diffusion in the lime spheres has been shown to be almost entirely Knudsen in character while that in the iron spheres has been shown to be almost entirely in the molecular region. Diffusion in the product nickel spheres exhibited a mixed character.

The results of the diffusion coefficient determinations on the nickel spheres have been applied to reduction rate measurements on single nickel oxide spheres.

The reduction experiments were carried out under controlled conditions and the weight and temperature of reducing samples continuously measured. From a knowledge of the external gas flow conditions and the effective diffusion coefficients in the reduced layer, the chemical rate constant for the reaction has been calculated as a function of reduction temperature. The results show that the hydrogen reduction of the nickel oxide under study is a mixed control reaction at temperatures between 250 - 700^{o}C and indicate that it is almost entirely diffusion controlled at higher temperatures.

TABLE OF CONTENTS

Chapter I		INTRODUCTION	11
Chapter II		PREVIOUS WORK	15
	II-1	Diffusion in Porous Solids	16
		Measurement Techniques	16
		Interpretation	17
		Dusty - gas model background	20
		binary gas	24
		single gas.	25
	II-2	Role of Diffusion in Chemical Reactions Involving Porous Solids.	27
		Topochemical reaction behaviour	29
		Influence of gas phase mass transfer.	31
		Chemical control mechanisms	32
		Diffusion control	33
		Role of heat transfer	35
		Mixed control	36
		Elucidation of controlling step	38
		Reduction of nickel oxide by hydrogen	39
		Reduction of ferrous chloride by hydrogen	41
Chapter III		THEORETICAL WORK	42
		Transport Control Model	43
		Mixed Control Model	49
		Mixed Diffusion	54
Chapter IV		EXPERIMENTAL PROCEDURES	57
	IV-1	Diffusion Coefficient Measurement	58
		Introduction	58
	IV-1-A	Experimental Conditions and ancillary apparatus.	59

IV-1-A-1	Gas Train	59
IV-1-A-2	Furnace	60
IV-1-A-3	Gas Analysis	61
IV-1-A-4	Micro-Manometer	63
IV-1-A-5	Manostat	63
IV-1-A-6	Flow Metering	64
IV-1-A-7	Measurement of Sample volume	66
IV-1-A-8	Sample Preparation	69
IV-1-A-8a	Powders used for the preparation of samples.	69
IV-1-A-8b	Compaction	70
IV-1-A-8c	Hollow sphere formation	72
IV-1-A-8d	Treatment of Samples prior to reaction.	73
IV-1-A-8e	Reaction	75
IV-1-B	Diffusion Coefficient Measurement	77
	Introduction	77
IV-1-B-1	Initial Technique	78
IV-1-B-1a	Apparatus	78
IV-1-B-1b	Diffusion run	78
IV-1-B-2	Modified Technique	80
IV-1-B-2a	Initial apparatus	80
IV-1-B-2b	Final apparatus	89
IV-1-B-2c	Pressure equilization	92
IV-1-B-2d	Diffusion Run	93

IV-1-C	Mass Transfer Measurements	95
IV-1-C-1	External Mass Transfer measurements.	95
IV-1-C-2	Internal Mass Transfer measurements	96
IV-1-D	Permeability Measurements	100
IV-2	Reduction of Nickel Oxide	102
	Introduction	102
IV-2-A	Furnace	10
IV-2-B	Load cell	10
IV-2-C	Sample Suspension	106
IV-2-D	Gas Train	108
IV-2-E	Sample Preparation	110
IV-2-F	Data Recording	110
IV-2-G	Reduction Experiments	111
IV-2-H	Time Lag Experiment	112
IV-2-I	Determination of Temperature Gradient in Solid	113
Chapter V	EXPERIMENTAL RESULTS	114
V-1	Diffusion Results	115
V-1-A	Mass Transfer Results	115
V-1-A-1	External Mass Transfer	115
V-1-A-1a	Analysis of experimental measurements	115
V-1-A-1b	Results	116
V-1-A-2	Internal Mass Transfer Results	116

V-1-A-2a	Analysis of Experimental Measurements	116
	i) First determination	116
	ii) Second determination	118
V-1-A-2b	Results	119
	i) First determination	119
	ii) Second determination	119
V-1-B	Permeability Measurements	122
V-1-B-1	Analysis of Experimental Measurements	122
V-1-B-2	Results	122
V-1-C	Diffusion Measurements	126
V-1-C-1	First Technique	126
V-1-C-1a	Analysis of experimental measurements	126
V-1-C-1b	Results	127
V-1-C-2	Modified Technique	133
V-1-C-2a	Analysis of experimental results	133
	i) Flux equations	133
	ii) Evaluation of variables	137
	iii) Computation	140
	iv) Reversal of diffusion direction	140
V-1-C-2b	Results for porous iron	141
V-1-C-2c	Results for porous nickel	141
V-2	REDUCTION EXPERIMENTS	157
V-2-A	Gas Switching Time Lag Experiment	157
V-2-B	Temperature Gradient across Porous Layer	157
V-2-C	Rate of Reduction Experiments	157
V-2-Ca	Analysis of experimental measurements	157
V-2-Cb	Results	162

Chapter VI		DISCUSSION	185
	VI-A-1	Experimental Strategy	186
	VI-A-2	Determination of Effective Gas Diffusivities	187
	VI-B	Mass Transfer Results	188
	VI-B-1	External Mass Transfer	188
	VI-B-2	Internal Mass Transfer	189
	VI-C	Permeability Results	191
	VI-D	Lime Diffusion Results	191
	VI-E	Porous Iron Results	192
	VI-F	Porous Nickel Diffusion Results	194
	VI-G	Results of Gas Switching Time Lag Experiment	199
	VI-H	Results of Measurement of Temperature Gradient across Reducing Layer	199
	VI-I	Observation of Partially Reduced Spheres	200
	VI-J	Nickel Oxide Reduction Results	202
Chapter VII		CONCLUSIONS	207
		APPENDIX A	210
		ACKNOWLEDGEMENTS	212
		LIST OF SYMBOLS	213
		REFERENCES	216

LIST OF FIGURES

Figure No.	Title	Page No.
IV-1	Flowtrain for diffusion experiments.	60
IV-2	Mini-orifice meter.	65
IV-3	Calibration for mini-orifice meter No.7 for H_2 gas.	67
IV-4	Mercury displacement apparatus for volume measurement.	68
IV-5	Three part 'Vinamould' mould.	71
IV-6	Detail of diffusion cell. Initial technique.	79
IV-7	Detail of sphere fittings for modified diffusion apparatus.	82
IV-8	Diagram of 'Araldite' model for measuring local impact pressures.	85
IV-9a	Pressure difference vs. Reynolds Number for various positions around hollow sphere.	87
IV-9b	Internal pressure distribution.	88
IV-10	Detail of delivery end of final diffusion shaft.	91
IV-11	Two part lead mould for casting naphthalene spheres.	97
IV-12	Sphere-shaft connection for internal mass transfer measurements.	99
IV-13a	Reduction furnace assembly.	104
IV-13b	Detail of load cell and sample suspension system.	015
IV-14	Calibration curve for load cell.	107
IV-15	Gas supply for reduction experiments.	109

V-1-1	Log Sh-20/$Sc^{\frac{1}{3}}$ vs. Log Re . External mass transfer.	117
V-1-2	Results of first determination of internal mass transfer coefficient.	120
V-1-3	Log Sh-3.0/$Sc^{\frac{1}{3}}$ vs. Log Re Second determination.	121
V-1-4	Permeability vs. total pressure for lime spheres.	123
V-1-5	Permeability vs. total pressure for iron spheres.	124
V-1-6	Permeability vs. total pressure for nickel spheres.	125
V-1-7	Plot of total resistance vs. flow rate.	128
V-1-8a,b,c	Total resistance versus internal flow rate for lime spheres.	129 - 130
V-1-9	Significance of variables.	134
V-2-1	Gas-switching-time-lag results.	158
V-2-2	Temperature gradient in nickel spheres during reduction at 650°C.	159
V-2-3a,b,c,d, e,f, g.	Dimensionless mass versus time for NiO reduction.	170-176
V-2-4a,b,c,d, e,f,g.	Cube root of dimensionless mass versus time for NiO reduction.	177-183
VI-1a	Effect of sample porosity on diffusivity ratio (ϵ/q) for spheres with green porosity of 40%.	196
VI-1b	Change in tortuosity (q) with porosity (ϵ) for spheres with green porosity of 40%.	196
VI-2a	Effect of reduction temperature on diffusivity ratio (ϵ/q) for spheres with green porosity of 40%	197

VI-2b	Relationship between sample porosity and (D_{H2O})eff for spheres with green porosity of 40%.	197
VI-3	Relationship between chemical rate constant and reduction temperature.	203
VI-4	Relationship between overall rate constant and reduction temperature.	206

CHAPTER I

INTRODUCTION

The reactions between gases and solids are of significance in a large number of industrial processes. The chemical industry, in particular, makes wide use of catalysts in solid form to control the rates of processes involving the gaseous state and much of the academic interest in gas/solid reactions has been generated by chemical engineers. Metallurgists, however, are perhaps evenmore frequently concerned with gas/solid reactions. They encounter them in many processes, i.e. in packed bed processes, such as the blast furnace and sintering, in fluidised bed processes and in roasting. Many of these processes were developed empirically and it is only recently that they have been studied in a scientific manner. This study has included a range of laboratory investigations into the kineties of gas/solid reactions that occur in metallurgical processes.

These investigations have been conducted using small laboratory reactors or in special furnaces in which the reaction of a single particle has been studied in isolation. The behaviour of small laboratory reactors is difficult to interpret in terms of reaction kinetics, however, since it is determined not only by the reaction kinetics but also by the characteristics of the reactor. Thus the more fruitful approach is the one in which the reaction of isolated particles is studied, and it is this approach that has been adopted in this work.

In most of the gas/solid reactions of interest to the metallurgist, a new solid forms on the outside of the original particle. For the reactions to continue, then, the reactant and product gases must cross this solid product layer either by gaseous or by solid state diffusion.

In view of the extremely low rate of solid state diffusion, it is not surprising that most industrial processes involve the diffusion of gaseous species within a porous product layer.

The role this gaseous diffusion step plays in determining the overall reaction rate is perhaps the most important question to be answered in studies of gas/solid reactions. In one extreme, this gaseous diffusion can be slow enough for chemical equilibrium to be maintained in the reaction zone. Conversely, the chemical rate may be slow enough for there to be no appreciable gas concentration gradient between the particle surface and the reaction zone. Although these two conditions describe the possible limiting cases, many important reactions involve behaviour which is intermediate between the two.

The present work was undertaken to determine the importance of the diffusion step in certain reactions of metallurgical significance. An experimental technique was developed to measure gaseous diffusion coefficients in various porous product solids, the measurements being interpreted using the 'dusty gas' model[19,20]. These results were then used in the prediction of the rate of reaction of spherical particles according to an experimental strategy outlined by Mills[62].

The systems investigated were chosen because they were of some metallurgical importance and because they were not thought to be too complex for the initial stages of this experimental programme. Moreover, there existed in the literature some arguement as to the nature of the rate controlling step(s), for each of the reactions. They would thus provide a test of the validity of the experimental strategy.

Effective diffusion coefficients were measured in three porous product solids: lime produced by the thermal decomposition of calcium carbonate; iron reduced from ferrous chloride using hydrogen; and nickel reduced from nickel oxide also using hydrogen.

The experiments carried out on the calcium carbonate-lime system formed a continuation of a project which investigated the rate controlling factors in the thermal decomposition of calcium carbonate. This system provided an excellent starting point as it is a relatively simple reaction which has been extensively studied by other workers.

The reduction of ferrous chloride by hydrogen provided a more complex reaction involving non-equimolar fluxes. This reaction is attracting some attention as a direct route from low grade iron ores to high purity, non-pyrophoric iron powders, so that its investigation is of some direct technical importance.

The nickel oxide reduction reaction is of interest as a possible route to high purity nickel powder which can then be alloyed or directly formed by powder metallurgical techniques. In addition, the investigation of this reaction can be expected to provide information about many other gas/solid reduction reactions in which a metal is formed, the most important of which is the reduction of hematite to iron.

CHAPTER II

PREVIOUS WORK

PART 1 - DIFFUSION IN POROUS SOLIDS

More and more work has been carried out in recent years on gaseous diffusion in and through porous media. The increasing interest in this phenomenon is mainly due to its importance in determining the rates of chemical reactions, and this aspect will be discussed in a subsequent section. This section is solely concerned with work done on the diffusion of gases in porous media.

MEASUREMENT TECHNIQUES

Effective diffusion coefficients in porous media have been measured in a wide variety of ways, which are, in essence, variations of one of three basic methods.

The first method is analogous to that normally used in determining binary gas diffusion coefficients and has been used by Dye and Dallavalle[1] to determine the effect of porosity and sample thickness on the effective diffusivity of porous solids. In this method, two closed cells containing gas mixtures of known compositions are connected instantaneously through a disc of the porous solid to be investigated, and the diffusion coefficient determined from the subsequent transient behaviour.

Scott and Cox[2] and Scott and Dullien[3], on the other hand, have measured the electrical resistance of porous pellets which had been previously saturated with electrolyte, and determined effective gaseous diffusion coefficients from these measurements by analogy.

The third and by far most common method involves the monitoring of the composition of continuously flowing gases which bathe the ends of the porous solid under investigation. In some of these experiments

the chemical potential of one of the diffusing species is maintained by a chemical reaction, and thus the flux ratio of the diffusing species is externally fixed. Hoogschagen[4,5] and McKewan and Ollson[6] have used this technique. More frequently, the experiment is carried out under conditions which do not enforce any limits on the diffusive flux. This latter technique has been used by Scott and Dullien[3], Wakao and Smith[7], Currie[8] and Evans et al[9], among others.

Wakao and Smith[7], have also attempted to predict diffusivities on the basis of pore sizes and pore distribution. The predicted values were then compared with directly measured results. Szekely[10] has also used this technique in estimating the diffusion coefficient of reduced nickel oxide pellets.

INTERPRETATION

The analysis of these measurements, in some cases, requires the use of elaborate numerical analysis. Apart from this, the measurements are subject to a variety of theoretical interpretations.

Much of the original work on diffusion in porous media has been derived from the consideration of equations describing flow phenomena in single capillaries. Knudsen[11] derived an expression for the diffusion coefficient when the mean free path of the diffusing molecules was larger than the capillary diameter and thus molecule wall collisions became more important than molecule-molecule collisions. His equation is

$$D_{iK} = \frac{4}{3} r \left(\frac{2 RT}{\pi M_i}\right)^{\frac{1}{2}} \left(\frac{2 - f}{f}\right)$$

where f is the proportion of molecules which are reflected randomly and is normally taken as 1.

The numerical constant has been the subject of some discussion. Pollard and Present[12], for instance, have used $\pi/2$ instead of $4/3$. The equation for D yields the widely known result.

$$-\frac{\dot{n}_i}{\dot{n}_j} = \sqrt{\frac{M_j}{M_i}} = \frac{D_{i_K}}{D_{j_K}} \qquad \ldots\ldots \text{(II-1-1)}$$

Expressions describing flow in capillaries when the capillary diameter was much larger than the mean free path of the diffusing molecules (normal diffusion) were derived directly from Fick's Law.

Weber[13] was among the first to attempt the explanation of diffusive behaviour in the transition zone between Knudsen and normal diffusion by treating the overall flow as made up of three separate components; a Poiseuille term, a conductive flow term, and a pressure diffusion term. A similar solution has been given by Barrer[14].

Bosanquet[15] derived an important relationship between the Knudsen and normal diffusion coefficients which has been shown to apply to both capillary flow and flow through porous media. The relationship is known as Bosanquet's interpolation formula.

$$\frac{1}{D_i} = \frac{1}{D_{iK}} + \frac{1}{D_{ij}} \qquad \ldots\ldots\ldots \text{(II-1-2)}$$

Wicke and Kallenbach[16] first introduced the concept of effective diffusivities in porous media, using two proportionality constants.

$$D_{ieff} = D_i \frac{\epsilon}{q} \qquad \ldots\ldots\ldots \text{(II-1-3)}$$

The ratio of the fluxes of counter-diffusing species was for some time the subject of much discussion. It was well known that the diffusion ratio for flow in the Knudsen regime was that given by equation II-1-1.

It was assumed, however, that in the case of molecular diffusion, this ratio would be unity. This value was derived as an extension of results of binary gaseous diffusion coefficient measurements in which two closed vessels were allowed to diffuse into one another and thus the flux ratio was artificially constrained to be unity.

Hoogschagen[17] showed however, that for all diffusion regimes this ratio should be the same as that given for the Knudsen regime (equation II-1-1) in those experiments in which the pressures at both ends of the porous solid were equalized. Hoogschagen explained this phenomenon in terms of momentum transfer to the pore walls and showed it to be true experimentally in the normal diffusion region. This result was confirmed experimentally by Weisz[18] soon afterwards. Mason et al[19,20] and Scott and Dullien[3] use somewhat different arguments to arrive at the same conclusion. However, as the ratio of pore or capillary diameter to the mean free path increases to large values, Mason et al predict the diffusion ratio to be given by

$$\frac{n_i}{n_j} = -\frac{M_j}{M_i}$$

and Scott and Dullien give

$$-\frac{n_i}{n_j} = 1$$

The derivation of equations describing diffusive behaviour in both the Knudsen and molecular diffusion regimes as well as the transition zone had been attempted, as shown by Webber, for capillaries. However, the formulation of such equations for porous media is much more complex and normally requires some structure to be assumed for the porous media.

Scott and Dullien[3] have considered porous media as a collection of fine capillaries with randomly distributed radii. They equate the

pressure drop across the porous system to the sum of the resistances of the gas-wall and gas-gas collisions. Their final equation is

$$\dot{n}''_i = -\frac{p}{RTz}\left(\frac{D_{ij}}{1-B_i}\right)_{eff} \quad \ln\left\{\frac{(1-(1-B_i)\,\overline{C^*_i}_1 + D_{ij}/D_{jK}}{(1-(1-B_i)\,\overline{C^*_i}_2 + D_{ij}/D_{jK}}\right\}$$

Spiegler[21] assumed the media to be made up of randomly distributed particles in space and considered a driving force opposed by two forces; one arising from collisions with counter-currently moving molecules and another from wall collisions. His results are essentially the same as those of Scott and Dullien.

Mason and his co-workers[19,20,22], on the other hand, use an approach that does not require a structural model to be assumed. They treat the porous solid as an assembly of large 'molecules' of 'dust' which constitutes an additional component in the diffusing gas mixture. They have applied the kinetic theory of gases to analyse the motion of gas molecules passing through these 'dust molecules', the latter being constrained to remain stationary. Although their results are basically similar to those of other workers, they provide a concise and consistent viewpoint from which to derive the applicable equations. Mason et al have also extended their initial results to apply under even the most complex diffusion conditions. Their model will be discussed in more detail subsequently.

DUSTY-GAS MODEL BACKGROUND

A unified approach has been used by Mason et al[19,20,22] to describe the problem of gas transport in porous media from a consistent theoretical basis, up to a particular degree of kinetic theory approximation. It is noted that some of their equations were first formulated by Derjaguin and Bakanov[23] as is mentioned by Barrer[14]. Their generalized

treatment is based on the 'dusty-gas model', in which the porous medium is considered to be an assembly of uniformly distributed, giant 'molecules' of 'dust' constrained to remain stationary in space. They have used this model to predict the flow of gases in porous media involving various combinations of pressure, composition and temperature gradients. Their results have successfully interpreted experiments not only in the molecular and Knudsen diffusion regimes but also in the transition region, all from a single generalized equation.

These workers make no attempt to predict the structural parameters of porous media, their model being phenomenalogical rather than mechanistic. They assume that the important structural parameters are measured by a few straighforward experiments. Instead, they provide a consistent standpoint from which the results of such experiments can be interpreted and extended to other conditions.

The model will be discussed only in the lowest Chapman-Enskog approximation, in which only first order deviations from the equilibrium Maxwellian velocity distribution are considered. To this approximation, the flow problem can be separated into three parts, a diffusion part, a viscous-flow part, and a porous-medium geometry part. The first two parts are independent in this approximation and there are no cross terms. As mentioned before, the third part is treated from the standpoint of a few directly measured constants, which appear in the flow equations mainly as boundary conditions.

The starting point for the mathematical derivations of Mason and his co-workers was the equations derived by Zadanov, Kagan and Sazykin[24] which were obtained using Grad's 13-moment approximation.

For multicomponent diffusion in one dimension (z), Zhdanov et al derived the equation

$$\sum_{j=1}^{\nu} \frac{(1-\Delta_{ij})}{[D_{ij}]_1} R\theta(p_j * \dot{n}_i'' - p_i * \dot{n}_j'') = -\left(\frac{\partial p_i}{\partial z} - \frac{\rho_i}{\rho}\frac{\partial p}{\partial z}\right)$$

Composition and pressure diffusion term.

$$\frac{+1}{k\theta}\left(p_i F_i - \frac{\rho_i}{\rho}\sum_{j=1}^{\nu} p_j F_j\right) - p \sum_{j=1}^{\nu} p_i * p_j * \alpha_{ij} \frac{\partial \ln\theta}{\partial z}$$

Forced diffusion term.

Thermal diffusion term.

$$+ 2(\eta_i + \omega_i - \frac{\rho_i}{\rho}[\eta]_1)\left(\frac{\partial \epsilon_{zx}}{\partial x} + \frac{\partial \epsilon_{zy}}{\partial y} + \frac{\partial \epsilon_{zz}}{\partial z}\right)$$

Term involving the gradient of the rate of distortion tensor.

where

Δ_{ij} = Correction to the diffusioncoefficient in the second approximation.

$\left[D_{ij}\right]_i$ = Chapman-Enskog first approximation to the binary diffusion coefficient of species i and j.

k = Boltzman's constant

F_i = External force per molecule of species i

α_{ij} = Thermal diffusion factor which describes the relative separation of species i and j in a temperature gradient.

η_i = A sort of partial viscosity of mixture such that

$\sum \eta_i = [\eta]_1$ which is the Chapman-Enskog first approximation of the mixture viscosity.

ω_i = Correction to above viscosity term

ϵ_{xz} = Rate of distortion tensor $= \frac{\partial v_x}{\partial z}$

ν = Number of components in diffusing mixture.

Equation II-1-4 yields a set of $\nu-1$ independent equations, the νth equation being the sum of the others and thus not independent.

Zhadanov et al also demonstrated that the contribution of the ith species to the pressure tensor is

$$(p_i)_{\alpha\beta} = -2\eta_i \epsilon_{\alpha\beta}$$

which, summed over all species, yields

$$p_{\alpha\beta} = -2[\eta]_1 \epsilon_{\alpha\beta} .$$

Now, substituting this relation into the equation of motion for a gas mixture we get

$$2[\eta]_1 \left(\frac{\partial \epsilon_{zx}}{\partial x} + \frac{\partial \epsilon_{zy}}{\partial y} + \frac{\partial \epsilon_{zz}}{\partial z} \right) = \frac{\partial p}{\partial z} - \sum_{j=1}^{\nu} \frac{p_j}{k\theta} F_j \quad \ldots\ldots \text{(II-1-5)}$$

For isothermal conditions, substitution of equation II-1-5 into equation II-1-4 yields after some manipulation

$$\sum_{j=1}^{\nu} \frac{(1-\Delta_{ij}) R\theta}{[D_{ij}]_1} \left(p_j^* n_i'' - p_i^* n_j'' \right) = \left(\frac{\partial p_i}{\partial z} - \frac{\eta_i + \omega_i}{[\eta]_1} \frac{\partial p}{\partial z} \right) + \frac{1}{k\theta} \left(p_i F_i - \frac{\eta_i + \omega_i}{[\eta]_1} \sum_{j=1}^{\nu} p_j F_j \right) . \quad \ldots\ldots \text{(II-1-6)}$$

But only the 'dust' particles are acted upon by the external force and this force is given by

$$n_d F_d = \frac{dp}{dz}$$

where there are n_d particles per unit volume. Therefore we can define an effective partial pressure $p_d = n_d k\theta$

so that

$$\frac{p_d}{k\theta} F_d = \frac{dp}{dz} \qquad \ldots\ldots\ldots \text{(II-1-7)}$$

Substitution of equation II-1-7 into equation II-1-6 yields

$$\sum_{j=1}^{\nu} \frac{(1-\Delta'_{ij}) R\theta}{[D_{ij}]_1} \left(p_j^* n_i'' - p_i^* n_j'' \right) = - \frac{\partial p_i}{\partial t} , \quad \ldots\ldots \text{(II-1-8)}$$

where the prime refers to quantities calculated with the dust particles counted as molecules.

BINARY GAS

For binary gas diffusion (ternary mixture of two gases and dust particles) under isobaric conditions, equation II-1-8 reduces, for i = 1 ,to

$$\dot{n}''_1 = -\frac{[(D_1)_{eff}]_2}{R\Theta} p \frac{dp_1^*}{dz} + p_1^* [\delta_1]_2 \dot{n}'' \quad . \quad \ldots\ldots \text{(II-1-9)}$$

The subscript 2 refers to the second approximation of these coefficients in which both $[(D_1)_{eff}]_2$ and $[\delta_1]_2$ contain Δ'_{ij} terms, a very complex function of mixture properties. Only the first approximation will be used in this work, and equation II-1-9 reduces to

$$\dot{n}''_1 = -\frac{(D_1)_{eff}}{R\Theta} p \frac{dp_1^*}{dz} + p_1^* \delta_1 \dot{n}'' \quad . \quad \ldots\ldots \text{(II-1-10)}$$

where, by analogy to the Bosanquet's interpolation formula.

$$(D_1)_{eff} = \left[\frac{1}{D_{1k}} + \frac{1}{(D_{12})_{eff}} \right]^{-1} \quad \ldots\ldots \text{(II-1-11)}$$

and

$$\delta_1 = \frac{(D_1)_{eff}}{(D_{12})_{eff}} = \left[1 + \frac{(D_{12})_{eff}}{D_{1k}} \right]^{-1} \quad . \quad \ldots\ldots \text{(II-1-12)}$$

When bulk pressure gradients exist, only the diffusive flux is given by equation II-1-10. In order to obtain the viscous flux Mason et al considered a Stoke's Law equation for flow around a particle. Thus

$$F = - R_o \eta v \quad .$$

The viscous flux is thus

$$\dot{n}'' = \frac{p}{R\Theta} v = - \frac{p F}{R\Theta R_o \eta} \quad . \quad \ldots\ldots \text{(II-1-13)}$$

But, as shown previously, only the dust particles are acted upon by external forces. Thus substituting equation II-1-7 into equation II-1-13, the following relation is obtained.

$$\dot{n}''(\text{viscous}) = -\frac{p}{\eta R_o n_d R\Theta}\frac{dp}{dz} \qquad \ldots\ldots \text{(II-1-14)}$$

where $n_d = p_d/k\Theta$.

Thus, from equations II-1-10 and II-1-14, the combined diffusive and viscous flux in a pressure gradient is given as

$$\dot{n}''_1 = \frac{-(D_1)_{eff}}{R\Theta} P \frac{dp_1^*}{dz} + p_1^* \delta_1 \dot{n}'' - p_1^* (1-\delta_1)\frac{B_o}{\eta R\Theta} P \frac{dP}{dz} \quad \ldots \text{(II-1-15)}$$

where $Bo = \frac{1}{R_o n_d}$.

SINGLE GAS

For a single gas flowing through a porous layer (binary mixture of gas and 'dust') the diffusive flux from equation II-1-10 is given by

$$p_d \dot{n}''(diff) = -P\frac{(D_{1d})_{eff}}{R\Theta}\frac{dp}{dz} \quad . \qquad \ldots\ldots \text{(II-1-16)}$$

But, $(D_{1d})_{eff} = \frac{D_{1K}\, p_d}{p}$

and thus, making this substitution in equation II-1-16, equation II-1-17 is obtained.

$$\dot{n}''(diff) = -\frac{D_1 K}{R\Theta}\frac{dp}{dz} \qquad \ldots\ldots\ldots \text{(II-1-17)}$$

The viscous flux through the porous layer (Poiseuille flow) is given from equation II-1-14 by

$$\dot{n}''(viscous) = -\frac{pB_o}{\eta R\Theta}\frac{dp}{dz} \quad . \qquad \ldots\ldots\ldots \text{(II-1-18)}$$

Combining equation II-1-17 and II-1-18 the total flux is given by

$$\dot{n}''(total) = -\frac{D_{1K}}{R\Theta}\frac{dp}{dz} - \frac{pB_o}{\eta R\Theta}\frac{dp}{dz} \quad \ldots\ldots \text{(II-1-19)}$$

But the permeability of a porous solid is defined as

$$K = \frac{-\dot{n}''\, R\Theta}{\frac{dp}{dz}} \quad . \qquad \ldots\ldots\ldots \text{(II-1-20)}$$

Eliminating $\dot{n}''$ between equations II-1-19 and II-1-20, the permeability may be given as

$$K = D_{iK} + \frac{B_o p}{\eta} \quad \text{.....} \quad \text{(II-1-21)}$$

Mason et al have made little attempt at predicting structural parameters in order to evaluate the various diffusion coefficients. They suggest that these are best found by a few relatively straightforward experiments. Measurement of permeabilities as a function of total pressure yields the Knudsen diffusion coefficient D_{iK}, as the intercept and B_o/η as the slope, according to equation II-1-21. Using the value of the Knudsen diffusion coefficient, the effective diffusion coefficient, $(D_i)_{eff}$, can be evaluated from isobaric diffusion measurements according to an integrated form of equation II-1-10. Equation II-1-11 then gives a value for the effective molecular diffusion coefficient, $(D_{ij})_{eff}$, and hence the other structural parameter, ϵ/τ, from equation II-1-3. II-1-1 and II-1-3 can be used to extend these results to other gases and other gas mixtures. The temperature dependence of the effective diffusion coefficient must be determined by combining, by equation II-1-11, the molecular and Knudsen diffusion coefficients calculated at that temperature, where

$$(D_{ij})_{eff} \propto \theta^{3/2}*$$

and

$$D_{iK} \propto \theta^{1/2}$$

FOOTNOTE:

* For certain gas pairs, however, the molecular diffusivity varies more rapidly with temperature than indicated above, since the transport integral, Ω, which represents the deviation from rigidity of the diffusing molecules, can vary with temperature. This effect was not taken into account in this work since the values of the transport integral were not available for some of the gas pairs used. The resulting error was not considered to be large.

PART 2 - ROLE OF DIFFUSION IN CHEMICAL REACTIONS INVOLVING POROUS SOLIDS.

The investigation of the role of diffusion in those chemical reactions involving gases and solids and the formulation of equations describing these reactions have been active fields of study for a considerable period. These studies have been carried out on reactions of interest to both chemical engineers and metallurgists.

The bulk of the earlier work has been done in an attempt to explain the behaviour of catalysts. The concepts introduced were then extended to non-catalytic reactions. As, in this work, we are interested only in non-catalytic gas-solid reactions, only the basic concepts derived from consideration of catalytic reactions will be reviewed.

Thiele[25] was the first to quantitatively describe the reduction of catalyst activity due to diffusion effects. He derived a modulus for simple reaction types which contained both a chemical rate constant and an effective diffusivity and be determined the 'effectiveness' of the catalyst i.e. the ratio of the observed activity to the activity if only chemical reaction were controlling, as a function of this modulus. He shows the values of the modulus, for various basic reaction types, which give an effectiveness factor of unity. The work of Thiele was extended to more complex systems by Wheeler[26] who also gave a much more comprehensive theoretical treatment of the topic. Weisz and Prater[27] further extended the applicability of this concept and defined an 'effectiveness factor', η, such that

$$\eta = \left(1 + \frac{k L}{D} \right)^{-1}$$

where k = chemical rate constant

L = characteristic length

D = effective diffusion coefficient.

Weisz and Prater then demonstrated the criteria for which this factor would be effectively unity (no diffusion influence) for different reaction conditions. They also show how the k term in the equation can be replaced so that, in the case of first order reactions, only observable quantities are concerned. Walker, Rusinko and Austin[28] used this method of analysis to describe the reactions between carbon and various gases.

The effectiveness factor concept has been generalized and extended to non-catalytic gas/solid reactions by many wokrers. In particular Aris[29], Bischoff[30] and Petersen[31] have contributed greatly to the subject.

Although its use in the chemical literature is widespread, the use of the effectiveness factor in the study of reactions similar to those of interest in this work, is not common. Examples of its use in the reaction types of interest here can be seen in the work of Ishida and Wen[32] and **Calvelo** and Cunningham[33]. Even though the concept is not widely applied, the basic principles leading to its formulation were instrumental in the analysis of these latter reaction types.

The role of diffusion in non-catalytic gas/solid reactions has been the subject of intense discussion in recent years. The reactions of interest here have been investigated by measuring the rate of weight change of reaction samples as a function of various reacting variables. In many cases, partially reacted samples have been sectioned in order to follow the course of the reactions. Investigations of interest have generally made use of either spherical samples or samples which can be approximated to spheres, such as cubes or cylinders with a length to diameter ratio of unity.

The effect of such variables as temperature, partial pressure of reactant and product gases, total pressure, sample size and shape and gas flow rate on the rate of weight change, and the appearance of partially reduced samples, have led workers to interpret their results although similar, in a variety of ways. It is this variety of interpretations of similar results which makes the topic of gas-solid reactions in metallurgical processes so confusing.

TOPOCHEMICAL REACTION BEHAVIOUR

Many of these reactions exhibit a sharp, well-defined product/reactant interface and this interface has been repeatedly observed to move inward at an approximately constant rate during the reaction. This 'topochemical' behaviour has been observed in a wide range of porous solids. Even when no direct evidence has been obtained for a well defined interface, many workers have shown that the cube root of the fractional unreacted mass of the pellet varies almost linearly with time. This is, in fact, equivalent, in a topochemical reaction, to a constant rate of advance of the reaction interface.

Experimental results confirming these characteristics have been quoted by Spencer and Topley[34], who studied the rate of decomposition of silver carbonate, and Furnas[35], Zawadzki and Bretsnajder[36], Joseph, Beatty and Bitsianes[37], Ingraham and Marier[38] and Hills[39] among others on the decomposition of calcium carbonate. Themelis and Gauvin[40], Warner[41], McKewan[42], Kawasaki, Sanscrainte and Walsh[43] have reported this 'shrinking core' behaviour in hematite and magnetite reduction in both hydrogen and carbon monoxide. Similar observations have been made regarding the oxidation of cupric sulphate[44] and cupric sulphide[45] and the reduction of molybedenum oxides[46].

Yamaguchi and Moriyama[47] report this behaviour for the reduction of nickel oxide at low temperatures, as do Bandrowski et al[48] for the declining rate period of this reaction. Rigg[49] and Themelis and Yannopoulos[50] have observed this characteristic in ferrous chloride reduction.

However, Seth and Ross[51] report that some workers have observed deviations from the constant rate of advance, particularly in the later stages of reaction. Themelis and Gauvin[40] show the results of workers which do not strictly follow the linear trend. In addition, Hills[52] and Warner[53] have suggested that a constant rate of advance of the interface is not strictly adhered to in a large number of reactions. Lu and Bitsianes[54] have reported a variable rate of interfacial advance in their one dimensional reduction experiments on hematite.

Furthermore, some workers have reported on similar reactions in which either no interface was present, or that, although present, it was diffuse and of finite width. Bowen[55] states that his experiments on the reduction of ferrous chloride spheres in hydrogen occurred without the formation of a reaction interface. Kawasaki et al[43], reporting on their work on hematite reduction, did not observe a permanent interface until over 40% of the sample was reduced. Hartoutsios[56] and others have found retained wustite in the iron layer of partially reduced hematite pellets and thus there is evidence that this reaction interface may be diffuse. Hence, the presence of a sharp reaction interface which recedes toward the sample centre at a uniform rate, although frequently reported in these reactions, is not universally observed.

INFLUENCE OF GAS-PHASE MASS TRANSFER

The influence of mass transfer across the boundary layer surrounding the reacting sample is often imperfectly appreciated, and this lack of appreciation can lead to erroneous results. Most workers assume that once a critical gas flow has been reached, the diffusion of product and reactant gas across the boundary layer is unimportant. This has been reported even in some quite recent papers. Seth and Ross[51] have considered this to be true, as have McKewan[42,57,58,59] in his earlier work, and Themelis and Gauvin[40]. This assumption is also inherent in the analysis of Lu[60] and Oates and Todd[61] among others.

However, Warner[41] and Hills[62] have shown that the establishment of a critical gas flow rate does not preclude the existence of partial pressure gradients across the boundary layer. It merely indicates that the product gas partial pressure is not of sufficient magnitude to influence the reaction. Warner shows that at the low Reynolds numbers normally encountered in single sphere work, the mass transfer coefficient, calculated from known correlations, is not large enough to supply the large fluxes required in these reactions without an appreciable composition gradient between the bulk gas and the solid surface. He has demonstrated this effect by showing the asymmetrical reduction of a partially reacted hematite sphere which had been suspended in a reaction tube with one side of the sphere close to the wall.

CHEMICAL CONTROL MECHANISMS

Most early workers were content to observe the rate of reaction and the influence of reaction variables on this rate. They made little attempt to explain this behaviour by postulating a controlling mechanism. McKewan[42], however, observing that the linear rate of advance of the interface indicated that the overall reaction rate was proportional to the interfacial area, concluded that the hydrogen reduction of hematite was chemically controlled. He postulated that the reaction was controlled by the chemisorption of hydrogen molecules at the metal-oxide interface. He measured the influence of hydrogen partial pressure on the reaction rate in H_2-N_2-H_2O mixtures and found a curve which was linear at pressures below one atmosphere but which assumed a constant value at high pressures. He took this as further evidence of an absorption step, the constant value arising because of the complete coverage of available sites by hydrogen at high pressures. He further showed that the low entropy and enthalpy associated with the reaction were consistent with a physical (van der Waals) adsorption step. He formulated a rate equation

$$r_o d_o \left[1 - (1-R)^{\frac{1}{3}}\right] = kt$$

where r_o = initial radius of pellet

d_o = density of original pellet

k = rate constant mg/cm^2/min.

t = time in minutes

R = fraction of oxygen removed

Similar equations had been derived previously by Spencer and Topley[34] for the decomposition of silver carbonate and Stalhane and Malmberg[63] for hematite reduction.

Themelis and Gauvin[40] use this equation to correlate a large amount of experimental data obtained by themselves and other workers on hematite reduction. Oates and Todd[61] also assume the reduction of oxides to be chemically controlled, at least during the early stages of the reaction. They list all possible interfacial mechanisms and by subtle arguments eliminate all but the surface removal of oxygen as a rate controlling step. Quets et al[64] assume the hematite reaction to be controlled at the FeO/Fe interface by solid state diffusion and chemical reaction. Hyatt, Cutler and Wadsworth[65] have concluded from their work that the decomposition of calcium carbonate is controlled by a chemical step at the lime-carbonate interface involving active lime, lime, carbonate and absorbed CO_2. Yannopoulous and Themelis[50] have used an equation similar to McKewan's in their analysis of the reduction of ferrous chloride in hydrogen. Yamaguchi and Moriyama[47] have concluded that nickel oxide reduction can be satisfactorily described by this equation.

DIFFUSION CONTROL

Many workers have postulated that these reactions are controlled by gaseous diffusion through the boundary layer and through the reduced layer. Udy and Lorig[66] have concluded that the diffusion of water vapour through the reduced iron layer in hematite reduction is the controlling step. A similar conclusion was reached by Bogdandy and Janke[67]. Woods[68], in his analyses of the experimental data on this reaction obtained by Joseph[69] and Lewis[70], has assumed that the reduction rate is controlled by gaseous diffusion across the boundary layer and the reduced layer. Kawasaki[43] and his co-workers also considered diffusion across both layers in formulating their rate equation for hematite reduction.

On the other hand, Edstrom and Bitsianes[71] have concluded that hematite reduction is controlled by the solid state diffusion of iron in the wustite layer.

Ingraham and Marier[38] have suggested that the decomposition of $CaCO_3$ is controlled by diffusion of CO_2 through a thin layer of of active lime at the interface. Jorgensen, Cutler and Wadsworth[72] postulated that the oxidation of silicon carbide was controlled by gaseous diffusion through the product silica layer. Rigg[40] has concluded from his measurements of ferrous chloride reduction rates that the reaction is controlled by the diffusion of $FeCl_2$ vapour to sites of growing iron crystals.

Hills[62], in a recent paper, has shown that the evidence which had previously been taken to indicate either chemical control or mixed control (see subsection after next) could also be predicted and explained in terms of a mass transport control model. This model took account of both mass transfer resistance across the external boundary layer and diffusive resistance across the reduced layer. Such a model predicts approximately interfacial advance rates throughout the range of realistic values of mass transfer coefficients and diffusivities. Hills showed that the variation of reaction rate with hydrogen partial pressure as observed by McKewan and Warner on hematite reduction could be predicted by the interaction of molecular and Knudsen diffusion. At low pressures, Knudsen diffusion is dominant and the reaction rate increases rapidly as the partial pressure is increased, the diffusivity being independent of pressure. However, as the pressure is increased and molecular diffusion becomes more and more important, the rate of increase in reaction rate falls off as the increase in partial pressure is balanced by the inverse

relationship between the pressure and the molecular diffusion coefficient. Eventually, the reaction rate reaches a maximum where Knudsen diffusion is unimportant. Using the diffusion data of McKewan and Warner, Hills has shown how the experimental results of these workers lie on the curve predicted by this interaction of diffusion modes.

ROLE OF HEAT TRANSFER

The effect of heat transfer and its importance in determining the temperature of reacting samples is frequently neglected in studies of this kind. Changes of sample temperature can be very important as the rate constant, equilibrium constant and gaseous diffusion coefficients are all temperature dependent.

Azbe[23] seems to have been the first to consider the role of heat transfer in these reactions to be an important one. He put thermocouples in the centre of decomposing calcium carbonate samples. Because of the difference between the sample temperature and the surroundings, the results were interpreted in terms of a heat transfer mechanism. Normally, when heat transfer effects are considered they are found not to be in themselves rate controlling, but nevertheless important in determining the reaction rate. Even so, these effects have been considered by very few workers. Satterfield and Feakes[74] and Hills[52] have demonstrated the importance of this effect in the decomposition of calcium carbonate. Themelis and Yannopoulos[50,76] have shown the effects of heat transfer in the reduction of both cupric oxide and ferrous chloride in hydrogen.

Hills[52], in fact, has shown how a transport control model, involving both heat and mass transfer from the bulk gas to the reaction interface, can predict approximately constant rates of advance for the interface in a large number of reactions. The work of Hills and Campbell[59], Hills and Paulin[75] shows conclusively that such a dual mechanism is in fact operating in controlling the rate of decomposition of $CaCO_3$.

MIXED CONTROL

Warner[53] in a classic paper, showed conclusively that the experimental results which led McKewan to the postulation of a chemical control mechanism for the reduction of hematite, could also be interpreted in terms of a mixed control model; that is, a model which included both diffusion and chemical reaction as controlling steps. He pointed out that the linear rate of advance of the reaction interface could be predicted throughout all but the final stages of reaction by this mixed control model. Warner demonstrated that the temperature, pellet size and pressure dependency were also consistent with this model. He derived a general rate equation which included terms describing gaseous diffusion across the external gas and reduced iron layers as well as the chemical step at the interface.

Warner also pointed out that the van der Waals absorption mechanism which McKewan postulated for the chemical step would not be operative at the temperatures at which hematite was reduced. He further showed that the linear dependency of reaction rate on hydrogen partial pressure,

which McKewan found, was due to the complex behaviour of the ternary gas mixture used by McKewan in these determinations. Using varying total pressures of hydrogen-water vapour mixtures, Warner showed this relationship to be non-linear.

Rate equations based on a mixed control model have been formulated by many workers. These workers normally solve the equations describing the fluxes of product and reactant gases and the formation of solid product simultaneously with the reaction stoichiometry. By suitable combination of these equations, an overall driving force is obtained which is associated with a resistance term, the sum of the resistances associated with mass transfer, diffusion and chemical reaction.

Yagi and Ono[77] have formulated an equation similar to Warner's for hematite reduction. They consider three series resistances, associated with the gas-phase, the reduced layer and the chemical reaction. By suitable separation of variables they have been able to plot a function which yields the effective diffusion coefficient as the intercept and the chemical rate constant as the slope. The resultant values have been shown to compare favourably with those of other workers. Seth and Ross[51] have expressed their rate equation for hematite reduction in a similar manner. They investigated the effects of particle size on the reduction rate. The slope of a particle radius versus log time curve was found to be between the limiting values for chemical and diffusion control and thus the mixed control mechanism was assumed.

A number of workers have given general rate equations which have been derived without reference to a particular reaction. Lu[60] has given such an equation for an equi-molar reaction involving a first

order chemical step. However, Lu neglects the influence of gas-phase mass transfer in his derivation. St. Clair[78] has given an equation which can be applied to reduction reactions in general. He includes the three series resistance steps and gives an extensive treatment of the external mass transfer coefficients for his experimental conditions. His treatment is also limited to an equi-molar reaction with a first-order chemical step. Shen and Smith[79] have extended a similar three term equation to allow for a changing particle radius and changing temperature during reaction. Hawtin and Murdoch[80] have forumulated a general equation for a non equi-molar reaction involving an nth-order chemical step for a porous solid in which Knudsen diffusion is unimportant. They have treated the gas flux as arising from three sources, diffusion due to a composition gradient, bulk flow due to a pressure gradient and bulk flow due to the volume change on reaction.

ELUCIDATION OF CONTROLLING STEP

From the foregoing review, it can be seen that similar experimental results have led different workers to the intepretation of these results according to widely varied controlling mechanisms. Indeed Hills[62] has shown that the chemical control model, the mixed control model and the transport control model all predict behaviour which is qualitatively the same. Consequently, the results of reaction rate experiments are not in themselves sufficient to elucidate the controlling step or steps involved in a particular reaction. Nor are the ways in which this reaction behaves to changes in such variables as temperature, partial pressure, gas-flow rate, and sample size

sufficient evidence to state conclusively which steps are controlling.

Considering these facts, Hills has put forward an improved experimental strategy. He has suggested that the reduction experiments should be designed so that the external mass transfer coefficient can be either accurately known or easily measured. In addition to recording the weight loss of the sample, the temperature of the sample should be recorded by a thermocouple embedded in it. Reacted samples should be examined microscopically and the pore size and specific surface of the sample determined. Also, and perhaps most important, independent measurements of the effective conductivity and diffusivity in the reduced layer must be made. The information gathered from such an investigation would allow the worker to predict a reaction rate based on transport control. Only if the reaction were substantially slower than that predicted by this model, would an interfacial chemical step be considered as important in the rate equation.

REDUCTION OF NICKEL OXIDE BY HYDROGEN

The reaction between hydrogen and nickel oxide has been under study for quite some time, originally because of the use of the nickel product as a catalyst particularly in water vapour synthesis, and more recently because of the interest in the reaction as a route to high purity powdered nickel metal. However, almost all the published work has been carried out at relatively low temperatures.

The early work done on the reaction by Benton and Emmett[81] Taylor and Starkweather[82] Sabatier and Espil[83] and Berger[84] was mainly concerned with the reduction of the oxide at low temperatures (150°C to 350°C), as the catalytic activity of the product nickel was inversely dependent on the temperature of reduction. These workers produced their own nickel oxide by decomposition of carbonates, nitrates and basic oxides and carried out reductions with the nickel oxide in a finely divided state. Most results were qualitative but temperature dependence of the reaction rate was quantitatively determined. Also investigated were influence of starting material, pre-treatment, reducing gas flow rate and composition and impurity content. Benton and Emmett[81] also comment that a metal-oxide interface was noticeable in partially reduced particles and that the start of reaction had an auto-catalytic nature.

Yamaguchi and Moriyama[47] have more recently studied the kinetic aspects of this reaction. Using a thermo-balance technique, they have measured the reduction rates of powdered samples in the temperature range 210 - 290°C. They consider the reaction as occurring in three stages, an incubation period, a principal reduction period and a final reduction period. They have derived rate expressions and determined rate constants for each of these periods.

Paravano[85] has studied the effect of hydrogen gas concentration and solid impurity concentration on the reaction rate in the temperature range 150 - 350°C. Cech[86] measured the influence of water-hydrogen ratios on the final solid structure of single crystals of nickel oxide reduced at 650°C.

Bandrowski et al[48] have measured the reduction rates of beds of nickel oxide spheres by a dew-point technique. They describe three separate reaction periods, an incubation period in which reaction is negligible, an induction period where the rate increases progressively up to a maximum, and a falling rate period where the rate decreases from this maximum until reduction is complete. They postulate two simultaneous reactions to describe their model, first a reaction between NiO and H_2 absorbed on NiO, and second a reaction at the metal-oxide interface between NiO and hydrogen absorbed on nickel. They have noticed a falling off in the predicted rate at temperatures above 300°C, which they assume to be due to diffusional resistances.

REDUCTION OF FERROUS CHLORIDE BY HYDROGEN

Interest in the reduction of ferrous chloride had begun only very recently, with the work of Rigg and his co-workers. Rigg et al carried out both single sphere and packed bed studies of ferrous chloride during reduction by hydrogen. Their results led them to conclude that the reaction was controlled by the rate of vaporization of ferrous chloride which then reacted in the gaseous phase with hydrogen.

Yannopoulos and Themelis[50] on the other hand, concluded that the reaction was chemically controlled. Bowen[55] concluded that the reduction of all but very small pellets of ferrous chloride was controlled both by diffusion and chemical reaction.

CHAPTER III

THEORETICAL WORK

In this chapter, rate expressions will be formulated for a general reduction type reaction on the basis of assumed controlling mechanisms. Consider a gas/solid reaction of this type

$$\gamma_I S_I + b_I G_I \rightleftharpoons b_{II} G_{II} + S_{II} \quad \ldots\ldots \text{(III-1)}$$

It is assumed, in the derivations that follow, that the rate is being predicted for a spherical sample suspended in a flowing gas stream and that the sphere behaves topochemically during the reaction. It is also assumed that the only important diffusion mode is molecular diffusion. In addition, a simplifying assumption is made regarding the equilibrium coefficient, K_{EQ}, in that it is assumed to be a linear function of temperature over the narrow ranges involved. This last assumption is made only to simplify the resultant equations. The full expression could be substituted, but the resultant equations would be much more cumbersome.

It is further assumed that the diffusion coefficient and the thermal conductivity are constant in the product layer and that they are independent of temperature over the narrow ranges encountered in most non-isothermal reactions.

TRANSPORT CONTROL MODEL

The rate expression for a non-equimolar, non-isothermal reaction of the type given in equation III-1 will be derived assuming that the rate of the reaction is controlled solely by the transport of heat and mass to and from the reaction interface. Thus, it is assumed that equilibrium exists at the interface.

Describing all flows, both heat and mass, away fron the interface as positive, we have

$$\dot{n}_{II} = -\frac{b_{II}}{b_I} \quad \dot{n}_I = -\frac{\dot{n}_I}{\beta_{II}} \qquad \text{..... (III-2)}$$

The flux of GAS II across the porous product layer can be described by a form of Fick's Law, describing non-equimolar diffusion across a spherical layer. Thus

$$\dot{n}_{II} = -\frac{D_{I,II}\, p_T}{R\,\Theta_G}\,\frac{d\,p^*_{II}}{dr}\,4\pi r^2 + \dot{n}_{II}\,(1-\beta_{II})\,p^*_{II} \quad \text{.... (III-3)}$$

Rearranging equation III-3, we obtain

$$\dot{n}_{II}\,\frac{d\,r}{r^2} = -\frac{4\pi\, D_{I,II} p_T}{R\,\Theta_G}\,\frac{d\,p^*_{II}}{1-(1-\beta_{II})\,p^*_{II}} \qquad \text{..... (III-4)}$$

Integrating equation III-4 across the porous product layer yields

$$\dot{n}_{II} = \frac{S\,p_T\,D_{I,II}}{R\,\Theta_G(1-\beta_{II})}\,Ln\left\{\frac{1-(1-\beta_{II})\,\lceil p^*_{II}\rfloor_s}{1-(1-\beta_{II})\,\lceil p^*_{II}\rfloor_R}\right\} \qquad \text{..... (III-5)}$$

where S is the shape factor for a spherical layer = $\dfrac{4\pi r_i\, r_o}{r_o - r_i}$

The flux of GAS II across the external boundary layer can be described by a similar equation. Thus

$$\dot{n}_{II} = \frac{\alpha_o\, p_T}{R\Theta_G}\,\frac{d\,p^*_{II}}{dr}\,4\pi r^2 + \dot{n}_{II}\,(1-\beta_{II})\,p^*_{II}$$

which, when integrated, yields

$$\dot{n}_{II} = \frac{\alpha_o\, p_T\, 4\pi r_o^2}{R\,\Theta_G\,(1-\beta_{II})}\,Ln\left\{\frac{1-(1-\beta_{II})\,\lceil p^*_{II}\rfloor_G}{1-(1-\beta_{II})\,\lceil p^*_{II}\rfloor_s}\right\} \quad \text{... (III-6)}$$

Eliminating $(1-(1-\beta_{II})\,\lceil p^*_{II}\rfloor_s)$, the surface concentration term, between equations III-5 and III-6 yields

$$Ln\,(1-(1-\beta_{II})\lceil p^*_{II}\rfloor_G) - \frac{\dot{n}_{II} R\,\Theta_G(1-\beta_{II})}{\alpha_o\, p_T\, 4\pi r_o^2}$$

$$= Ln\,(1-(1-\beta_{II})\,\lceil p^*_{II}\rfloor_R) + \frac{\dot{n}_{II} R\,\Theta_G(1-\beta_{II})}{S\,p_T\,D_{I,II}}$$

which, rearranging gives

$$\dot{n}_{II} = \frac{\text{Ln}\left\{\frac{1 - (1-\beta_{II})\,[p^*_{II}]_G}{1 - (1-\beta_{II})\,[p^*_{II}]_R}\right\}}{\frac{R\,\theta_G}{p_T}\,(1-\beta_{II})\left\{\frac{1}{SD_{I,II}} + \frac{1}{\alpha_o A_o}\right\}} \qquad \text{.....(III-7)}$$

Now, defining a log-mean pressure term as

$$\zeta_{II} = [p^*_{II}]_{ln,m} = \frac{\text{Ln}\left\{\frac{1 - (1-\beta_{II})\,[p^*_{II}]_G}{1 - (1-\beta_{II})\,[p^*_{II}]_R}\right\}}{(1-\beta_{II})([p^*_{II}]_R - [p^*_{II}]_G)} \qquad \text{.... (III-8)}$$

and an effective resistance term as

$$\Omega_M = \frac{1}{S\,D_{I,II}} + \frac{1}{\alpha_o A_o} \qquad \text{..... (III-9)}$$

Substitution of equations III-8 and III-9 into equation III-7 yields

$$\dot{n}_{II} = \frac{\zeta_{II}([p_{II}]_R - [p_{II}]_G)}{R\,\theta_G\,\Omega_M} \qquad \text{..... (III-10)}$$

A similar treatment can be applied to the flux of GAS I across the boundary layer and porous product layer. Thus

$$\dot{n}_I = \frac{\text{Ln}\left\{\frac{1 - (1-\beta_I)\,[p^*_I]_G}{1 - (1-\beta_I)\,[p^*_I]_R}\right\}}{\frac{R\,\theta_G}{p_T}\,(1-\beta_I)\left\{\frac{1}{SD_{I,II}} + \frac{1}{\alpha_o A_o}\right\}} \qquad \text{.....(III-11)}$$

where $\beta_I = \frac{b_{II}}{b_I} = -\frac{\dot{n}_{II}}{\dot{n}_I}$

where again a log-mean pressure term can be defined as

$$\zeta_I = [p^*_I]_{ln,m} = \frac{\text{In}\left\{\frac{1 - (1-\beta_I)\,[p^*_I]_G}{1 - (1-\beta_I)\,[p^*_I]_R}\right\}}{(1-\beta_I)([p^*_I]_R - [p^*_I]_G)} \qquad \text{..... (III-12)}$$

and by analogy with equation III-10 for

$$\dot{n}_I = \frac{\zeta_I([p_I]_R - [p_I]_G)}{R\,\theta_G\,\Omega_M} \qquad \text{..... (III-13)}$$

Equations III-10 and III-13 can be combined via the reaction stoichiometry. Defining a modified reaction rate, $\dot{n}$, from equation III-10, such that

$$\dot{n} = \frac{\dot{n}_{II}{}^{R}\,\Theta_G}{\zeta_{II}} = \frac{\langle p_{II}\rangle_R - \langle p_{II}\rangle_G}{\Omega_M} \qquad \ldots\ldots \text{(III-14)}$$

and from III-13, dividing both sides by ζ_{II}

$$\frac{n_I{}^{R}\,\Theta_G}{\zeta_{II}} = \frac{\zeta_I}{\zeta_{II}}\,\frac{\langle p_I\rangle_R - \langle p_I\rangle_G}{\Omega_M} = \frac{-\dot{n}_{II}\beta_{II}{}^{R}\,\Theta_G}{\zeta_{II}}$$

or

$$\dot{n} = \frac{\zeta_I}{\beta_{II}\zeta_{II}}\,\frac{\langle p_I\rangle_G - \langle p_I\rangle_R}{\Omega_M} \qquad \ldots\ldots \text{(III-15)}$$

Solving equations III-14 and III-15 for the interfacial concentrations yields

$$\langle p_{II}\rangle_R = \dot{n}\Omega_M + \langle p_{II}\rangle_G \qquad \ldots\ldots \text{(III-16)}$$

and

$$\langle p_I\rangle_G = \langle p_I\rangle_G - \frac{\dot{n}\Omega_M\beta_{II}\zeta_{II}}{\zeta_I} = \langle p_I\rangle_G - b\,\dot{n}\Omega_M \qquad \ldots\ldots \text{(III-17)}$$

where $b = \dfrac{\beta_{II}\zeta_{II}}{\zeta_I}$

These interfacial concentrations are also linked by the equilibrium conditions which exist at the interface. Thus

$$K_{EQ} = \frac{\langle p_{II}\rangle_R^{\,b_{II}}}{\langle p_I\rangle_R^{\,b_I}} \qquad \ldots\ldots\ldots \text{(III-18)}$$

But, in the non-isothermal reaction under consideration

$$K_{EQ} = K_G + a'\,(\Theta_R - \Theta_G) \qquad \ldots\ldots\ldots \text{(III-19)}$$

and from the thermodynamics of the reaction, we have

$$-H\,\dot{n}_{II} = \frac{\Theta_G - \Theta_R}{\Omega_H}$$

or $$\Theta_R - \Theta_G = H\,\dot{n}_{II}\Omega_H \qquad \ldots\ldots\ldots\ldots \text{(III-20)}$$

where $\Omega_H = \dfrac{1}{Sk_p} + \dfrac{1}{A_o h_o}$

Substitution of equation III-20 into equation III-19 yields

$$K_{EQ} = K_G + a' H \dot{n}_{II} \Omega_H \qquad \text{..... (III-21)}$$

Multiplying and dividing the second term in equation III-21 by $\frac{R \Theta_G}{\zeta_{II}}$ we obtain

$$K_{EQ} = K_G + \frac{a' H \zeta_I}{R \Theta_G} \frac{\dot{n}_{II} R \Theta_G \Omega_H}{\zeta_{II}}$$

and thus defining a as

$$a = \frac{a' H \zeta_{II}}{R \Theta_G}$$

equation III-22 is obtained

$$K_{EQ} = K_G + a \dot{n} \Omega_H = \frac{\left[p_{II} \right]_R^{b_{II}}}{\left[p_I \right]_R^{b_I}} \qquad \text{..... (III-22)}$$

Substitution of equations III-16 and III-17 into equation III-22 yields

$$K_G + a \dot{n} \Omega_H = \frac{(\dot{n} \Omega_M + \left[p_{II} \right]_G)^{b_{II}}}{(\left[p_I \right]_G - b \dot{n} \Omega_M)^{b_I}} \qquad \text{..... (III-23)}$$

Equation III-23 describes fully any reaction of the type shown in equation III-1 which is transport controlled provided that the other assumptions are valid. The terms are all calculable from their defining equations in terms of measured values, standard thermodynamic data and the position of the reaction front. However, the order of the equation can become quite large when b_{II} and b_I are large, and the solution of this equation may require iterative techniques. Nevertheless, for most of the reactions of metallurgical interest, b_{II} and b_I are small, either 1 or 2, and equation III-23 can be solved analytically for these cases.

Consider a reaction of the type shown in equation III-1, in which

$$b_{II} = 2 \text{ and } b_I = 1$$

Such a reaction is

$$FeCl_2 + H_2 \rightleftharpoons Fe + 2HCl$$

For this reaction, equation III-23 becomes

$$K_G + a\dot{n}\Omega_H = \frac{(\dot{n}\Omega_M + [p_{II}]_G)^2}{[p_I]_G - b\dot{n}\Omega_M}$$

Performing the indicated operations and simplyfying, gives

$$(\dot{n}\Omega_M)^2 \frac{1 + ab\Omega_H}{\Omega_M} + \dot{n}\Omega_M \left(2[p_{II}]_G + aK_G - \frac{a\Omega_H}{\Omega_M}[p_I]_G\right) - (K_G[p_I]_G - [p_{II}]_G) = 0 \quad \ldots\ldots \text{(III-24)}$$

Equation III-24 can be solved analytically as a quadratic equation where the positive root is desired, as

$$\dot{n} = 0 \text{ when } K_G[p_I]_G = [p_{II}]_G$$

A further equation is available from a mass balance on the product solid. Thus

$$\dot{n}_{s_{II}} = -4\pi r_i^2 \rho_i \frac{dr_i}{dt} = -4\pi r_i^2 \rho_i r_o \frac{dr^*}{dt} \quad \ldots\ldots \text{(III-25)}$$

where, in general, $\dot{n}_{s_{II}} = \frac{\dot{n}_{II}}{b_{II}}$

and equation III-25 becomes

$$\dot{n} = \frac{R\,\theta_G b_{II}\, 4\pi r_i^2 \rho_i r_o \frac{dr^*_o}{dt}}{\zeta_{II}}$$

$$\dot{n} = f\, 4\pi r_i^2 \frac{dr^*}{dt} \quad \ldots\ldots \text{(III-26)}$$

where $f = \frac{R\,\theta_G\, b_{II} \rho_i\, r_o}{\zeta_{II}}$

Equation III-26 may be substituted into the solution of equation III-23 to obtain the rate of advance of the reaction interface, and thus the mass of the reducing sphere as a function of time.

MIXED CONTROL MODEL

A general rate expression will be derived for the reaction type shown in equation III-1, in which the reaction rate at the reactant/product solid interface is controlled not only by the transport of heat and mass to the reaction front, but also by the chemical step at this interface. Consequently, equilibrium does not exist at the interface. It is assumed that the reaction order is synonomous with the stoichiometry coefficients.

From consideration of chemical kinetics, the forward reaction rate is given by

$$\dot{n}''_f = k_f C_I^{b_I} \qquad \text{..... (III-28)}$$

and the backward reaction rate at the interface is given by

$$\dot{n}''_b = k_b C_{II}^{b_{II}} \qquad \text{..... (III-29)}$$

but, at equilibrium

$$\dot{n}''_f = \dot{n}''_b$$

and thus

$$\frac{k_f}{k_b} = \frac{C_{II}^{b_{II}}}{C_I^{b_I}} = K_{EQ} \qquad \text{..... (III-30)}$$

Therefore, as $C_{II} = \frac{p_{II}}{R\theta}$ and $C_I = \frac{p_I}{R\theta}$ ..... (III-30a)

$$K'_{EQ} = \frac{(\sqrt{p_{II}}/\sqrt{T}_{eq}/R\,\theta_R)^{b_{II}}}{(\sqrt{p_I}/\sqrt{T}_{eq}/R\,\theta_R)^{b_I}} \qquad \text{..... (III-31)}$$

But the equilibrium coefficient, K_{EQ}, is defined as

$$K_{EQ} = \frac{(\sqrt{p_{II}}/\sqrt{T}_{eq})^{b_{II}}}{(\sqrt{p_I}/\sqrt{T}_{eq})^{b_I}} \qquad \text{..... (III-32)}$$

and from equation III-31 and III-32

$$K'_{EQ} = K_{EQ}\left(\frac{1}{R\,\theta_R}\right)^{b_{II}-b_I}$$

Therefore, the overall chemical reaction rate, $\dot{n}_c$, from equations III-28, III-29 and III-30 is

$$\dot{n}_c = k_c A_i\left(C_I^{\,b_I} - \frac{C_{II}^{\,b_{II}}}{K_{EQ}}\right)$$

which, substituting equations III-30a and III-31, yields

$$\dot{n}_c = \frac{k_c A_i}{(R\,\theta_R)^{b_I}}\left\{\overline{p_I}^{\,b_I} - \frac{\overline{p_{II}}^{\,b_{II}}}{K_{EQ}}\right\}$$

where $k_c = k_f$

or, since $\overline{p_I} + \overline{p_{II}} = p_T$

$$\dot{n}_c = \frac{k_c A_i}{(R\,\theta_R)^{b_I}}\left\{(p_T - \overline{p_{II}})^{b_I} - \frac{\overline{p_{II}}^{\,b_{II}}}{K_{EQ}}\right\} \quad \text{..... (III-33)}$$

if $\dot{n}_c$ is the rate at which solid II is formed, then

$$\dot{n}_c = \frac{\dot{n}_{II}}{b_{II}}$$

and equation III-33 becomes

$$\dot{n}_{II} = \frac{b_{II}k_c A_i}{(R\,\theta_R)^{b_I}}\left\{(p_T - \overline{p_{II}})^{b_I} - \frac{\overline{p_{II}}^{\,b_{II}}}{K_{EQ}}\right\}$$

or substituting from equation III-14

$$\dot{n} = \frac{b_{II}k_c A_i}{\zeta_{II}(R\,\theta_R)^{b_1-1}}\left\{(p_T - \overline{p_{II}})^{b_I} - \frac{\overline{p_{II}}^{\,b_{II}}}{K_{EQ}}\right\} \text{..... (III-34)}$$

assuming that all compositions can be evaluated at the interface temperature without large errors being introduced.

Defining an effective chemical resistance, Ω_c, as

$$\Omega_c = \frac{\zeta_{II}(R\theta_R)^{b_1-1}}{b_{II}k_c A_i} \quad \text{..... (III-34a)}$$

then equation III-34 reduces to

$$\dot{n} = \frac{1}{\Omega_c}\left\{(p_T - \overline{p_{II}}_R)^{b_I} - \frac{\overline{p_{II}}_R^{b_{II}}}{K_{EQ}}\right\} \quad \text{..... (III-35)}$$

But the flux of GAS II across the porous product layer and across the external boundary layer can be described by equations exactly analogous to those developed for the transport model. However, it must be noted that the interfacial concentrations no longer refer to equilibrium compositions. Thus, from equation III-14

$$\dot{n} = \frac{\overline{p_{II}}_R - \overline{p_{II}}_G}{\Omega_M} \quad .$$

Eliminating $\overline{p_{II}}_R$, the interfacial concentration, between equations III-14 and III-35 yields

$$\dot{n} = \frac{1}{\Omega_c}\left\{(p_T - \Omega_M\dot{n} - \overline{p_{II}}_G)^{b_I} - \frac{(\Omega_M\dot{n} + \overline{p_{II}}_G)^{b_{II}}}{K_{EQ}}\right\}$$

or

$$\dot{n} = \frac{1}{\Omega_c}\left\{(\overline{p_I}_G - \Omega_M\dot{n})^{b_I} - \frac{(\Omega_M\dot{n} + \overline{p_{II}}_G)^{b_{II}}}{K_{EQ}}\right\} \quad \text{.... (III-36)}$$

For a non-isothermal reaction, assuming K_{EQ} is again a linear function of temperature, equation III-21 states

$$K_{EQ} = K_G + a\,\dot{n}\Omega_H$$

and substituting equation III-21 into equation III-36 gives

$$\dot{n} = \frac{1}{\Omega_c}\left\{(\overline{p_I}_G - \Omega_M\dot{n})^{b_I} - \frac{(\Omega_M\dot{n} + \overline{p_{II}}_G)^{b_{II}}}{K_G + a\,\dot{n}\Omega_H}\right\} \quad \text{.... (III-37)}$$

Another equation can be obtained by substituting equation III-15 into equation III-36 but the resultant equation is not independent. The form of equationIII-37 is misleading in that it appears that only observable bulk concentrations are required in its solution. It should be noted, however, that the evaluation of $\dot{n}$, a andΩ_c require the determination of the log-mean pressure term, ζ_{II}, which does contain interfacial concentrations.

Consequently, in its general form, equation III-37 requires a solution involving iterative procedures.

However, equation III-37 can be greatly simplified if the values of b_{II} and b_I are known. Consider the reaction

$$NiO + H_2 \rightleftharpoons Ni + H_2O$$

where $b_I = b_{II} = 1$

Therefore, equation III-36 becomes

$$\dot{n} = \frac{1}{\Omega_c}\left\{\Delta p_I \gamma_G - \Omega_M \dot{n} - \left(\Omega_M \dot{n} + \frac{\Delta p_{II} \gamma_G}{K_{EQ}}\right)\right\}$$

which, rearranging yields

$$\dot{n} = \frac{1}{\Omega_c}\left\{\Delta p_I \gamma_G - \frac{\Delta p_{II} \gamma_G}{K_{EQ}} - \Omega_M \dot{n}\left(\frac{K_{EQ}+1}{K_{EQ}}\right)\right\} \quad \ldots\ldots \text{(III-38)}$$

But it can be shown the K_{EQ} for the reduction of nickel oxide by hydrogen is a large value ($>10^2$)(Appendix A). Therefore, very little error is introduced into the equations if equation III-38 is reduced to

$$\dot{n} = \frac{1}{\Omega_c}\left\{\Delta p_I \gamma_G - \Omega_M \dot{n}\right\}$$

which becomes, by rearrangement

$$\dot{n} = \frac{\Delta p_I \gamma_G}{\Omega_M + \Omega_c} \quad \ldots\ldots\ldots \text{(III-39)}$$

By substiution from equations III-34a, III-9 and III-14, equation III-39 becomes

$$\frac{\dot{n}_{II}^R \Theta_R}{\zeta_{II}} = \frac{\Delta p_I \gamma_G}{\frac{1}{SD_{I,II}} + \frac{1}{\alpha_o A_o} + \frac{\zeta_{II}(R\Theta_R)^{b_I - 1}}{b_{II} k_c A_i}} \quad \ldots\ldots \text{(III-40)}$$

But, for an equi-molar reaction, ζ_{II} (equation III-8) is indeterminate.

However, its limit as β approaches zero can be shown to be 1.0. Consequently, equation III-40 becomes

$$\dot{n}_{II} = \frac{[p_I]_G}{R\theta_R \left\{ \frac{1}{SD_{I,II}} + \frac{1}{\alpha_o A_o} + \frac{1}{k_c A_i} \right\}} \qquad \ldots\ldots \text{(III-41)}$$

which describes the rate of production of product gas in a reaction of the type illustrated by nickel oxide reduction. Assuming a topochemical reaction, the rate of advance of the interface can be linked with the reaction rate via a mass balance. For the nickel oxide reaction, this equation may be expressed as

$$\dot{n}_{II} = -4\pi r_i^2 \rho_i \frac{d r_i}{dt} \qquad \ldots\ldots\ldots \text{(III-42)}$$

Eliminating the flux, $\dot{n}_{II}$, from the equations III-41 and III-42 and substituting factors r_o and r_i, yields

$$-4\pi r_i^2 \rho_i r_o \frac{dr^*}{dt} = \frac{4\pi r_o^2 D_{I,II} [p_I]_G}{R\theta_R \left\{ \frac{D_{I,II}}{\alpha_o} + r_o \left(\frac{1}{r^*} - 1 \right) + \frac{D_{I,II}}{r^{*2} k_c} \right\}}$$

where $r^* = \frac{r_i}{r_o}$

Separating the variables r* and t gives

$$r^{*2} \left\{ \frac{D_{I,II}}{\alpha_o} + r_o \left(\frac{1}{r^*} - 1 \right) + \frac{D_{I,II}}{r^{*2} k_c} \right\} dr^* = \frac{D_{I,II} [p_I]_G}{R\theta_R \rho_i r_o} dt$$

and integrating yields

$$\frac{D_{I,II}}{\alpha_o} \frac{r^{*3}}{3} + \frac{r_o r^{*2}}{2} - \frac{r_o r^{*3}}{3} + \frac{D_{I,II} r^*}{k_c} = \frac{-D_{I,II} [p_I]_G}{R\theta_R \rho_i r_o} t + C$$

$\ldots\ldots$ (III-43)

but, it can be shown that

$$r^* = m^{*\frac{1}{3}}$$

Making this substitution into equation III-43, and multiplying through by 6, yields

$$\frac{2\,D_{I,II}m^*}{\alpha_o} + 3\,r_o m^{*\frac{2}{3}} - 2\,r_o m^* + \frac{6\,D_{I,II}m^{*\frac{1}{3}}}{k_c} = -\frac{6\,D_{I,II}\left[\overline{p}_I - \overline{p}_G\right]}{R\Theta_R \rho_i r_o}\,t + C \qquad \text{.... (III-44)}$$

For normal single sphere experiments, the following boundary condition can be substituted into the above equation;

when $t = 0$ $m^* = 1$

and equation III-44 becomes

$$C = \frac{2\,D_{I,II}}{\alpha_o} + 3\,r_o - 2\,r_o + 6\,\frac{D_{I,II}}{k_c}$$

and thus

$$2\left(\frac{D_{I,II}}{\alpha_o} - r_o\right)(1 - m^*) + 3\,r_o(1 - m^{*\frac{2}{3}}) + \frac{6\,D_{I,II}}{k_c}(1 - m^{*\frac{1}{3}}) = \frac{6\,D_{I,II}\left[\overline{p}_I - \overline{p}_G\right]}{R\Theta_R \rho_i r_o}\,t \qquad \text{..... (III-45)}$$

MIXED DIFFUSION

The diffusion term in equation III-45 represents the effective binary diffusion coefficient of the product gas-reactant gas mixture in the product solid layer, as pure molecular diffusion was assumed in its derivation. However, under usual reaction conditions, gaseous diffusion in the porous product layer occurs by both molecular and Knudsen mechanisms. This mixed diffusion mechanism requires that the effective diffusion coefficient of the product and reactant gases be unequal because of the different Knudsen diffusion coefficients due to the difference in molecular weights of the two species (Equations II-1-1 and II-1-2).

However, in the reaction of interest here (the reduction of nickel oxide in hydrogen), the flux of the product and reactant gases is constrained

to be equal by the reaction stoichiometry. Therefore, since, when mixed diffusion is taking place, the effective diffusivity of hydrogen in the reduced layer is greater than that of water vapour, a pressure gradient will be present in the reduced layer to retard the flux of hydrogen and enhance the flux of water vapour until the fluxes are balanced. Equation III-45 should be modified to correct for this complication.

The flux of gases under combined composition and bulk pressure gradients is described by equations of the form of equation II-1-15. This equation must be first integrated across the porous layer, which would result in an equation implicitly containing both the total pressure and composition gradients as well as a changing mixture viscosity. This equation would then be analogous to equation III-5. Obviously, the resultant equations are exceedingly complex, and would require lengthy mathematical techniques for their solution.

However, the experimental work done in this study indicates that the diffusion in the product layer in the case of nickel oxide reduction is very largely molecular in nature, particularly at lower reduction temperatures. Consequently, it has been assumed that the increase in pressure at the reaction interface is small and can be ignored without serious error. Nevertheless, it is still more accurate to use the individual effective diffusion coefficients rather than the binary values as the former contain a correction for the Knudsen component. It can be shown that the Knudsen diffusion coefficient of hydrogen is three times that of water vapour. Also, because of its lower viscosity, the viscous slip of hydrogen in the pores of the product solid is greater than that of water vapour as well. For these reasons, the small increase of total pressure at the reaction interface will have less effect on the flux

of water vapour than of hydrogen. Consequently, it is most accurate to use the effective diffusivity of water vapour in equation III-45. This equation then becomes

$$2\left(\frac{(D_{II})_{eff}}{\alpha_o} - r_o\right)(1 - m^*) + 3\,r_o(1 - m^{*\frac{2}{3}}) + \frac{6(D_{II})_{eff}}{k_c}(1 - m^{*\frac{1}{3}}) = \frac{6(D_{II})_{eff}\,\Delta p_I}{RO_R \rho_i r_o}\,t \qquad \ldots\ldots \text{(III-46)}$$

CHAPTER IV

EXPERIMENTAL PROCEDURES

PART I - DIFFUSION COEFFICIENT MEASUREMENT

INTRODUCTION

The independent determination of effective diffusivities involved two separate experiments. The permeability experiment measured the flux of a single gas flowing through the porous sample under a bulk pressure gradient. The diffusion experiment measured the fluxes of two gases counter-diffusing across the porous sample under partial-pressure gradients. By combining these data, the effective Knudsen and molecular diffusion coefficients through the porous sample were calculated.

Essentially, the experimental technique involved the preparation of a hollow sphere which was then sealed onto a shaft. The shaft contained separate passages, to allow gas to be passed into the central cavity of the sphere and then removed from it. The assembly was sealed inside a larger tube so that a second gas could be passed over the outside of the sphere.

IV-1-A EXPERIMENTAL CONDITIONS AND ANCILLARY APPARATUS

IV-1-A-1 GAS TRAIN

The gas train used in the preparation of samples and in the diffusion measurement is shown in Fig. IV-1. The gas flow system was designed so that a wide range of gases and gas mixtures could be delivered under closely controlled conditions at accurately known flow rates and compositions. The flow train was constructed of pyrex glass and plastic tubing. Flexible poly-vinyl chloride tubing was normally used, but this was unsatisfactory when corrosive gases were used so that rigid polythene tubing was used instead.

Gases were supplied from commercially available cylinders. The gases were dried over silica gel and over magnesium perchlorate. The flow rates and pressures of the gas streams were determined and if desired the components of gas mixtures were fed into the mixing chamber. A system of stopcocks and ground glass joints was used to deliver the gases either to the furnace or to the diffusion cell.

The gas exiting from the furnace was passed through a condensation cell and a stripper to remove any contained vapours, through a flow metering device and through a gas burner and it was then exhausted by an extractor fan.

The two exit gas flows from the diffusion cell each passed through two pressure control valves and through a sampling chamber sealed with a rubber diaphragm. The flows were then metered and exhausted through the extractor fan.

IV-1-A-2 FURNACE

The furnace used for the preparation of diffusion samples was a standard horizontal tube furnace. The tube was of thermal aluminous porcelain 600 mms. long and 35 mms. inside diameter, wound

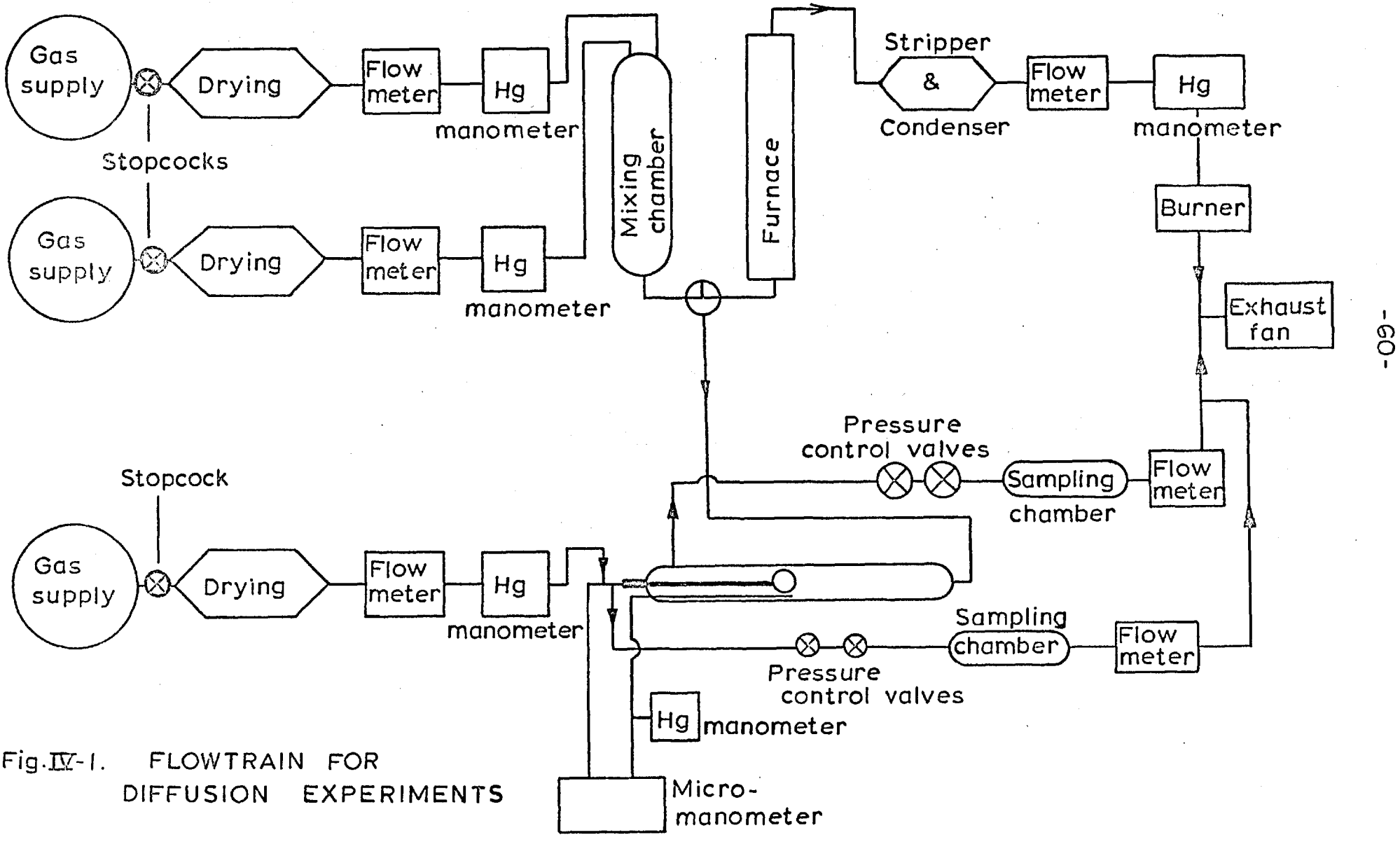


Fig.Ⅳ-1. FLOWTRAIN FOR DIFFUSION EXPERIMENTS

with 'Nichrome' wire with a total resistance of 28 ohms. This was placed in a 250 mm. diameter insulation chamber filled with diatomaceous earth. An 'Ether' fast cycling controller connected to a thermocouple placed in contact with the tube between two adjacent windings, was used to maintain the centre-line temperature of the furnace to $\pm$ 1°C of the set point. The hot zone was about 70 mm. in length.

Gases were passed through an 80 mm. bed of mullite chips immediately before the hot zone. An indicating thermocouple ran longitudinally through this bed and could be moved, by means of a sliding glass seal in the furnace end-cap, so that it could be placed adjacent to the sample in the furnace. The opposite furnace end-cap was also provided with a sliding glass seal so that the sample could be removed quickly from the hot zone for rapid cooling.

IV-1-A-3 GAS ANALYSIS

Two Fisher Gas Partitioners were used to analyse the gas mixtures exiting from the diffusion cell. Both these instruments were connected via a switch to a single pen Leeds and Northrup 'Speedomax H' recorder. This recorder was used with a chart speed of 1 cm. per min. and ranges of 0-1, 0-2.5, 0-5 and 0-10 mv. Helium was used as the carrier gas in the analysis of all gases except hydrogen, in which case argon was used as the carrier gas.

Samples were taken using one millilitre syringes. The diaphragm of the sampling chamber was pierced, the syringe flushed several times and then filled. After filling it was left in situ for several minutes to ensure that the pressure in the syringe was the same as that in the sampling chamber. The syringe was then removed, the sample volume adjusted and the sample introduced quickly into the partitioner. The height of the appropriate peaks shown on the

output recorder was taken as a measure of the relative amounts of gases present. The relationship between peak height and sample composition was determined by calibration.

The instruments were calibrated frequently, normally just before each set of samples was analysed. The calibration was performed using gas mixtures of known composition, the peak heights being found to be directly proportional to the gas composition, so that only one standard was required for each gas.

Known gas mixtures were prepared in two ways. The first method involved the continuous supply of a known mixture to the sampling chamber from which a sample was taken in the usual manner. The mixture's composition was fixed by determiningthe flow rate of each component. This method was not ideal because it involved interrupting the diffusion runs in order to use the flow meter and the sampling port.

In the second method a large (5 L.) bottle was fitted with a stopcock at the bottom and the top was sealed with a rubber stopper. The bottle was connected to a mercury manometer (and a vacuum pump) and evacuated. Each component of the gas mixture was then bled into this bottle until the pressure had risen to a predetermined level, the final level being slightly above atmospheric pressure. The volume fraction of each gas was then equal to the rise in pressure that had occurred due to that gas being bled in divided by the final pressure. Once this mixture had been prepared, syringe samples could be removed through the rubber stopper on top of the bottle .

IV-1-A-4 MICRO-MANOMETER

In certain of the diffusion experiments it was necessary to control the pressure difference across the porous layer very accurately. An electronic micro-manometer, manufactured by Furness Controls Ltd., was used to do this. The instrument was capable of measuring very small pressure differences. The full scale deflection at maximum sensitivity was 5 N/m^2 (0.5 mm water gauge) and the smallest pressure changes to which the instrument responded were about 0.5% of the full scale deflection. By decreasing the signal amplification, the sensitivity of the instrument could also be decreased so that the full scale deflection was 50N/m^2.

Because of the extremely low range of the instrument, it could be easily overloaded, causing the calibration to change. Recalibration was relatively simple. Two large aspirator bottles (5 l.) were partially evacuated and one connected to each side of the micro-manometer. Provision was made to equalize the pressures in both bottles. Then the volume of one of the bottles was changed by a very small amount through the movement of a syringe. This known decrease in volume produced a small but known increase in pressure. Using this technique, the micro-manometer was accurately calibrated over its working range.

IV-1-A-5 MANOSTAT

A 'precision' pressure and vacuum regulating valve' was purchased from Negretti and Zambra Ltd. in order to maintain a constant mean pressure within the apparatus (system pressure) during the permeability measurements. It had a working range of 18 KN/m^2 to 550 KN/m^2 and could be controlled to $\pm$ 3.5 N/m^2 in an open ended or dynamic system .

By proper adjustment of this instrument, system pressures could be maintained indefinitely at any desired level, even though a steady flow of gas was passing through the apparatus.

IV-1-A-6 FLOW METERING

Gas flow rates were measured using soap film flow meters, rotameters and 'mini-orifice meters'. Whereas the first two devices are widely known and used, the last, at least in the form used in these experiments, should be an innovation to most.

These flow meters were made from standard 'Quickfit' glassware and pyrex tubing. (Fig. IV-2). The orifices themselves were made by partially closing the ends of B10 cones in a flame.

Normally, small capillary flow meters are used in similar laboratory applications. However, although the basic construction is similar, the nature of the pressure drop through the two constrictions is different. In the case of the capillary flow meter the flow resistance is offered first by a sudden contraction, followed by the long narrow constriction and a sudden enlargement.

This can be described by an equation of the form

$$\Delta p_c = \underbrace{C_{II}\,\rho\,Q^2}_{\text{inertial flow term}} + \underbrace{C_I\,\mu\,Q}_{\text{viscous flow term}}$$

However, in the case of an orifice meter, the pressure drop arises only from a sudden contraction and sudden enlargement.

$\therefore \Delta p_o = C_{III}\rho\,Q^2$ (inertial term only)

Thus a plot of $\left(\frac{\Delta P_o}{\rho}\right)^{\frac{1}{2}}$ vs Q yields a straight line of slope C_{III} running through the origin.

In practice, however, the lines deviated from linearity at low flow rates (Fig. IV-3). This was because the orifices could not be

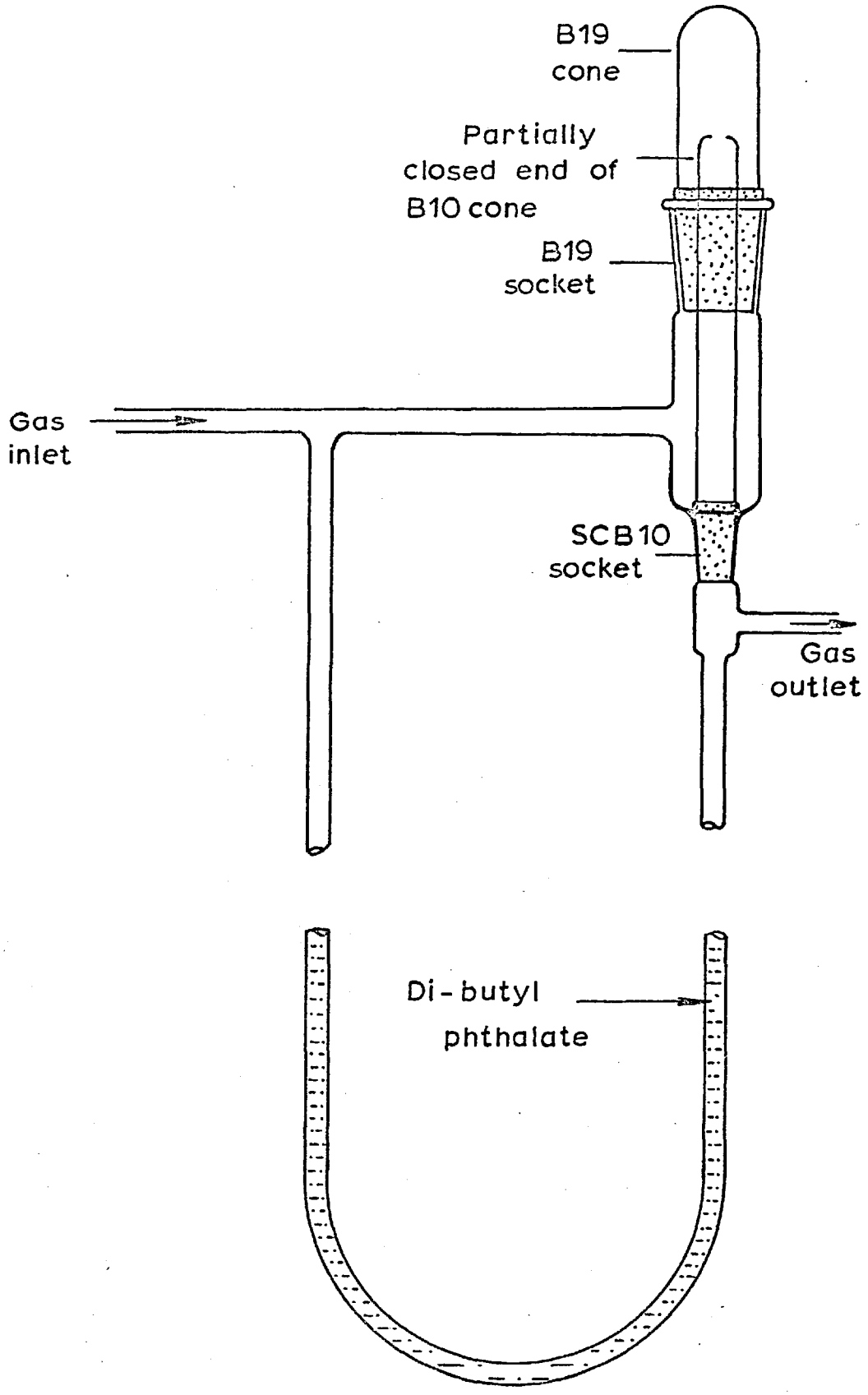


Fig. IV-2. MINI-ORIFICE METER

expected to be perfect sharp edged orifices when constructed by blowing glass.

These orifice flow meters were calibrated with appropriately sized soap-film flow meters using a precision 'three-second sweep' stopwatch. A typical calibration curve is shown in Fig. IV-3 and these calibrations were found to have a re-producibility of better than $\frac{1}{2}\%$ provided care was taken to keep the orifices clean.

The real advantage of such flow-meters is that one calibration may be used for a variety of gases of different densities without loss in accuracy. Thus one calibration can also be used for gases delivered at different pressures. However, when density changes of greater than two-fold are encountered errors do become appreciable.

IV-1-A-7 MEASUREMENT OF SAMPLE VOLUME

The apparent volumes of the porous solids investigated were measured using a mercury displacement technique. The apparatus is sketched in Fig. IV-4. In order to zero the instrument, an amount of mercury was trapped between upper and lower reference points (D and C respectively), the upper reference point being the zero end of a burette scale. Then this volume of mercury was allowed to flow back into the resevoir. The sample was placed in the sample chamber, which was constructed from two glass hemispheres fitted with glass flanges. The mercury was then forced out of the resevoir , either by applying a vacuum at A (see diagram) or a positive pressure at B, until the level coincided with the lower reference point C. The mercury level was then above the upper reference point because of the additional volume of the sample, and this volume could be

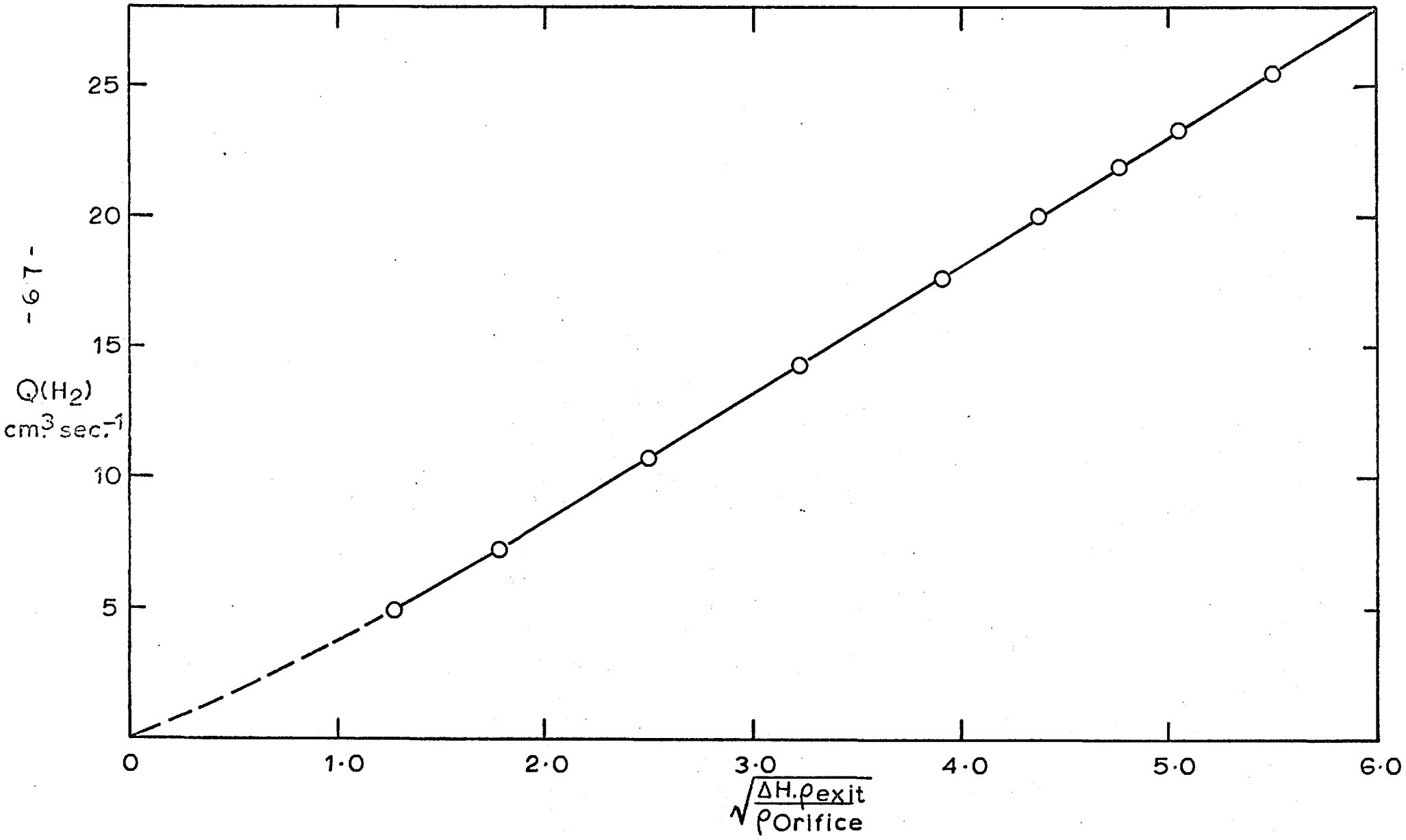


Fig. IV-3. CALIBRATION FOR MINI-ORIFICE METER #7 FOR H_2 GAS AT ROOM TEMPERATURE

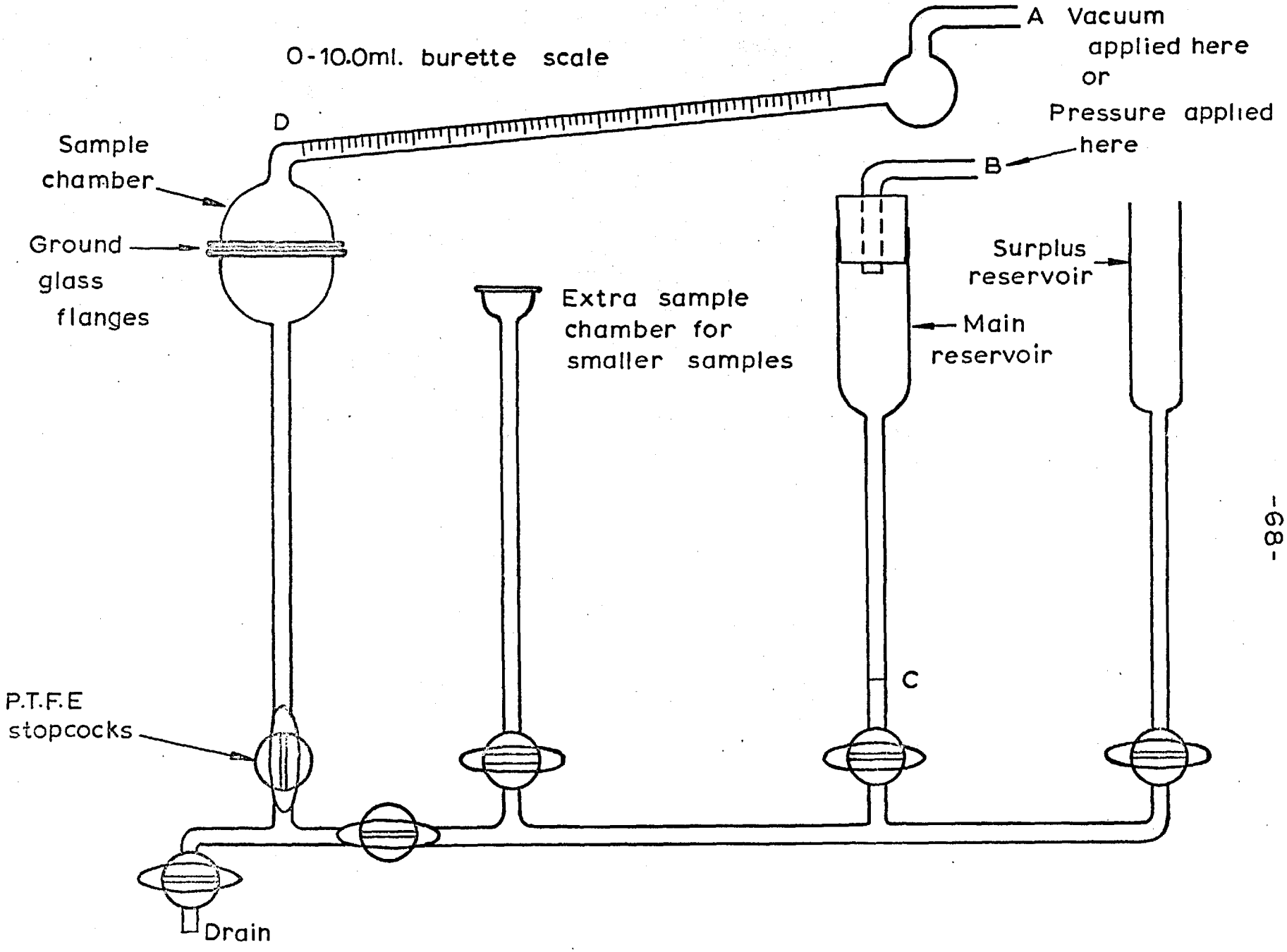


Fig. IV. 4. MERCURY DISPLACEMENT APPARATUS FOR VOLUME MEASUREMENT.

read directly from the burette scale. Apparent volumes were measured to 1.0 mm^3 using this technique.

IV-1-A-8 SAMPLE PREPARATION

Effective diffusion coefficients were measured in three product solids, CaO decomposed from $CaCO_3$, Fe reduced from $FeCl_2 \cdot x H_2O$, and Ni reduced from NiO. The variation of sample properties in these three systems required somewhat different techniques for the preparation of the samples.

IV-1-A-8(a) POWDERS USED FOR THE PREPARATION OF SAMPLES

(i) $CaCO_3$

'Analar' grade precipitated calcium carbonate obtained from Hopkin and Williams Ltd. was used in this investigation. Paulin used material from the same batch so that the results obtained here could be compared more closely with his. He measured the average particle size as 6.5 microns with a standard deviation of 0.9 microns.

The manufacturer gives the following maximum limits for impurity concentrations.

Soluble alkali	=	0.25 ml N/1.
Chloride	=	0.001 %
Sulphate	=	0.01 %
Nitrate	=	0.02%
Phosphate	=	0.002%
Silicate	=	0.01 %
Iron	=	0.001%
Heavy metals (Pb)	=	0.002%
Magnesium	=	0.02 %
Sodium Potassium	=	0.05 %
Ammonium	=	0.05 %

$FeCl_2 \cdot x H_2O$

Two sources of hydrated ferrous chloride were used. G.P.R.$FeCl_2.4H_2O$ was obtained from Hopkin and Williams and industrial grade $FeCl_2 .1.7H_2O$ was received from Woodall Duckhams Ltd. Both materials were subsequently analysed for iron by the hydroxy-quinolate method given by Vogel[88]. The tetrahydrate contained 98.0% available iron and the lower hydrate 97.1% available iron. The major impurity in both samples was oxygen.

(iii) NiO

Grade II (< 50 ppm impurity) nickel oxide (NiO) from a single batch was purchased from Johnson and Matthey Co. Ltd. An analysis of this material yielded an oxygen content of 21.26 weight per cent. Particle sizes ranged from 3 to 20 microns.

Before compacting this powder, it was necessary to add a binder. One weight percent of 'Bedacryl 144 TL', an organic resin supplied by Imperial Chemical Industries, was used. The binder was mixed with sufficient toluene to form a thick slurry when added to the NiO powder. The toluene was removed by evaporation and the resultant cake thoroughly crushed in a mortar and pestle to the original particle size.

IV-1-A-8(b) COMPACTION

All diffusion samples were pressed in three-part 'Vinamold' molds in a conventional die and ram on a Tangye hydraulic press. A sketch of the three part mold is shown in Fig IV-5. 'Vinamold' could be easily melted and cast in any desired shape and behaves as a liquid when under high pressure. The compaction of powders in 'Vinamold' is thus an isostatic pressing process so that spherical shapes could be produced directly.

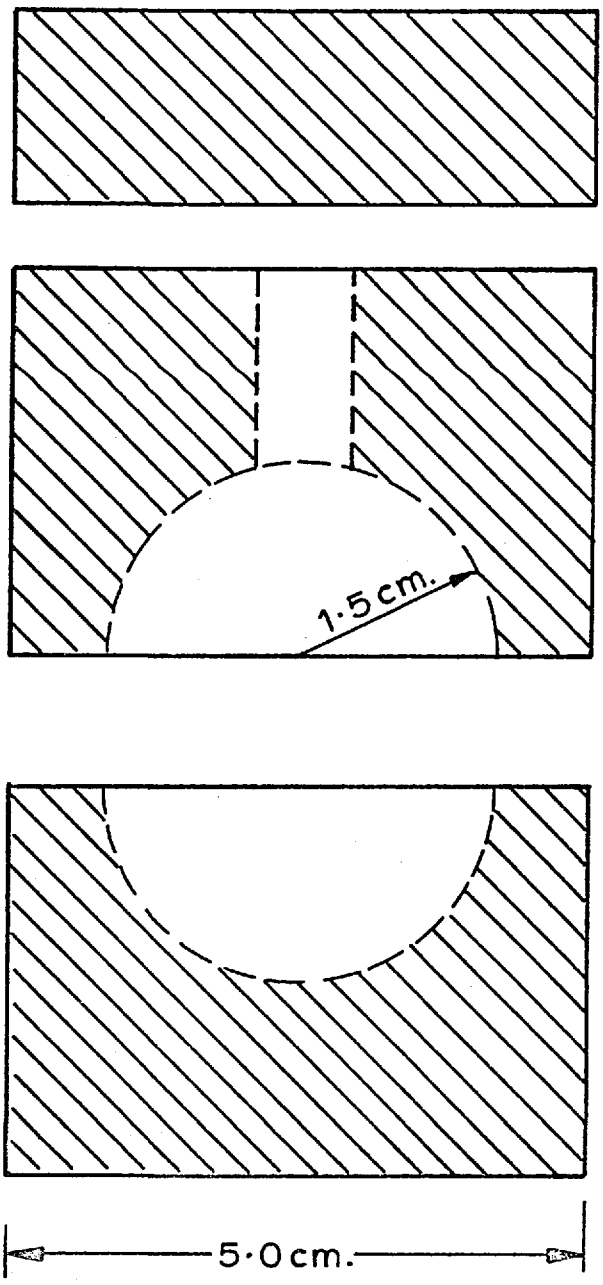


Fig. IV-5. THREE PART "VINAMOULD" MOULD

The compacting pressures used for the various reactant solids and the green porosities produced are shown in TABLE IV-1.

Reactant Solid	Compacting Pressure (Range)	Green Porosity (Range)
$CaCO_3$	200 - 500 KN/m^2	30 - 20 %
$FeCl_2 \cdot x\ H_2O$	25 - 200 KN/m^2	8 - 2 %
NiO	25 - 600 KN/m^2	50 - 25 %

IV-1-A-8(c) HOLLOW SPHERE FORMATION

The hollow spheres used in the diffusion measurements were formed by compacting a spherical shape in the centre of the porous sphere and removing it when pressing was complete. Wood's metal, a lead base quaternary eutectic alloy which melts at 72°C, was used to make spherical cores. These spheres were cast in two-part $\frac{1}{2}$ inch spherical molds.

In order to make a hollow sphere of reactant solid , the bottom part of the three part 'Vinamold' mold was first filled with the required powder, in position in the die and ram, and the Wood's metal core centered in this powder. The second part of the mold was placed over this and filled, the plug put in position, and the cap placed over the other two pieces. This assembly was then placed on the press, the pressure applied and maintained for three minutes. On removal from the press, the spheres were radially drilled until the Wood's metal core was exposed.

The Wood's metal core was removed from the $CaCO_3$ spheres by heating these spheres with a hot air blower until the metal fused

and ran out. However, the addition of this heat to the hydrated ferrous chloride caused dehydration and oxidation. Therefore, the metal core was removed by amalgamation. This proved so successful that it was also used in the case of nickel oxide. Both removal techniques left clean, even internal surfaces. Examples of spheres produced by the amalgamation technique are shown in Plate 1.

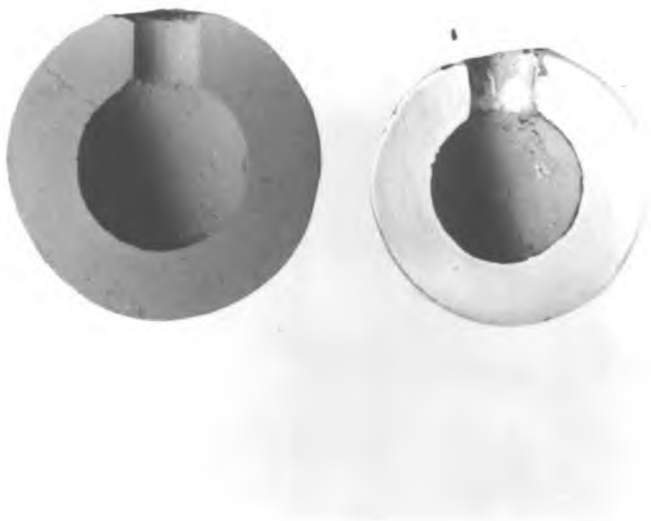
IV-1-A-8(d) TREATMENT OF SAMPLES PRIOR TO REACTION

(i) $CaCO_3$

The calcium carbonate hollow spheres were drilled and placed on the diffusion measurement shaft prior to being placed in the sintering furnace. The hole was drilled in the hollow sphere such that, after sintering and decomposition, a gas-tight seal was formed between the sphere and the shaft due to the shrinkage of the sphere during these processes. The spheres were sintered for 90 minutes in the tube furnace at 870°C under an atmosphere of pure CO_2.

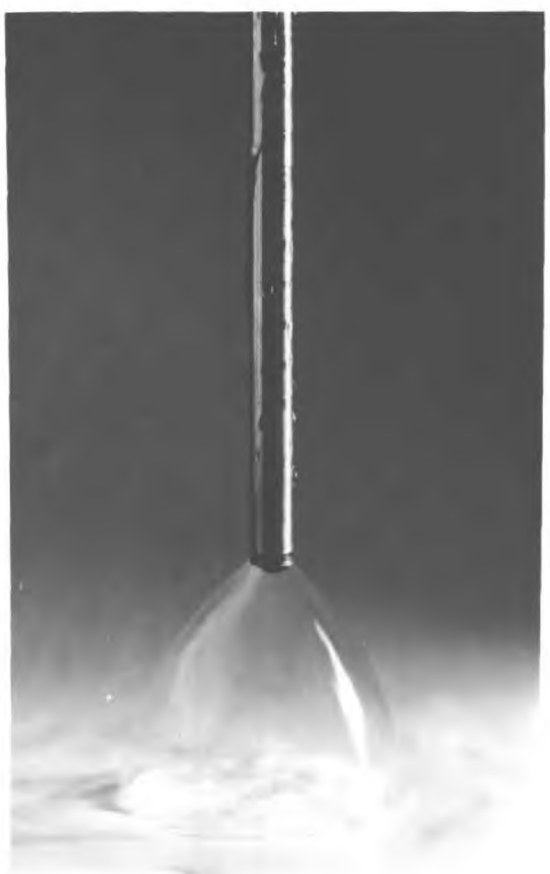
(ii) $FeCl_2 \cdot x\, H_2O$

The ferrous chloride spheres were not sintered but were dried in a hydrogen chloride atmosphere. The hydrated spheres were placed in the cold furnace and its temperature brought up to 200°C over a period of 4 - 6 hours, after which dehydration was complete. As will be described in Section IV-1-B-2(a), it was not attempted to shrink these spheres onto the diffusion measurement shaft because of their low mechanical strength.



(A)

X 1·5



(B)

X 1·0

PLATE 1, (A) SECTIONED HOLLOW SPHERES

Left – Nickel Oxide ; Right – Nickel

(B) CONICAL FLOW PATTERN PRODUCED BY FINAL DIFFUSION SHAFT (Water used for visual clarity) Q_{H_2O} = 2·0 litres/min.

(iii) NiO

Nickel oxide spheres were heated to 400°C for 3 hours in air to burn off all traces of the binder.* They were then heated in air to 750°C and held for 24 hours.** Again, it was not attempted to shrink the spheres onto the diffusion shaft, as, in this case, the shaft could not be heated to this temperature without damage.

IV-1-A-8(e) REACTION

(i) $CaCO_3$

After sintering, the calcium carbonate hollow spheres were rapidly heated to 950°C in CO_2. Once this temperature had been reached, the gas stream was changed to air and the spheres left at temperature for 90 minutes to ensure complete decomposition.

Porosities and physical dimensions were measured after the diffusion measurement was complete. Sintered and decomposed samples were approximately 1 cm. in radius with 0.5 cm. radius cavities. Porosities ranged from 45% to 55%.

(ii) $FeCl_2 \cdot x\ H_2O$

Because of the extremely porous nature ($\simeq$ 90%) of the product iron, the ferrous chloride spheres were supported in stainless steel mesh cradles during the drying and reduction cycles. Even with this precaution, only spheres produced from the lower hydrate ($FeCl_2\ 1.7H_2O$) had sufficient mechanical strength to maintain a

---

FOOTNOTES:

* I.C.I. informed the worker that the times and temperatures necessary to burn off the binder were as follows: 250°C - 3 hours, 300°C - 30 mins., 400°C - 8 mins., 450°C - 1 min.

** Some diffusion samples underwent somewhat different conditions as given in Section V-1-C-2c
All reduction rate samples were given the standard treatment.

reasonably spherical shape during reduction. Consequently, only spheres from this source were fully investigated.

Fully dried spheres were rapidly heated in HCl to reaction temperatures which ranged from 400°C to 650°C. When the desired temperature was attained, H_2 gas was substituted for the HCl and the reaction allowed to proceed to completion (up to 5 hours at low temperatures). The samples were then furnace cooled in hydrogen, removed and their physical dimensions and porosity measured.

(iii) NiO

Nickel oxide reductions were done at temperatures from 250°C to 800°C with the hollow spheres hung loosely on the end of the longitudinal thermocouple shaft. After preheating in nitrogen to reaction temperature, hydrogen replaced the nitrogen flow and the reaction was allowed to continue to completion .

The spheres were furnace cooled in hydrogen, removed and their physical dimensions and porosity determined. Dimensions were of the same order as those for lime spheres and iron spheres. The nickel spheres had porosities of 35 - 65 %.

IV-1-B DIFFUSION COEFFICIENT MEASUREMENT

INTRODUCTION

Differences in the physical properties of the porous solids investigated in this work necessitated different experimental techniques for the diffusion coefficient measurements. The initial technique, which was nonisobaric, could be used in systems in which Knudsen diffusion was the predominanat diffusion mode. When molecular diffusion was important however, an isobaric technique had to be used, the pressures on both sides of the porous layer being kept equal. Consequently the apparatus and technique used initially were modified so that this could be done.

IV-1-B-1 INITIAL TECHNIQUE

IV-1-B-1(a) APPARATUS

The initial diffusion measurements were carried out using the technique developed by Paulin. The measurements were made at reaction temperatures in the tube furnace previously described. The sample had been sealed by shrinkage to the diffusion shaft which was a twin-bored alumina thermocouple sheath, 4 mms. in diameter with 1 mm. bores. This shaft had been previously sealed into a glass collar which was 'blown' onto a B34 socket. (See Fig. IV-6). The end of the alumina furnace tube was ground to a standard B34 cone so that, when fitted, the furnace end cap formed a gas tight seal. The opposite end of the furnace was similarly sealed.

Both end caps were fitted with S13 ball and socket joints for gas connections. The twin-bored diffusion shaft was also fitted with gas connections so that a gas could be passed into the sphere down one bore and removed from it up the other.

IV-1-B-1(b) DIFFUSION RUN

After the sphere was sealed into the furnace, a constant flow rate $(Q_I)_o$, of gas (GAS I)* was passed down the furnace tube and over the sphere. A known flow rate $(Q_{II})_i$, of another gas (GAS II) was then passed into the centre of the sphere. After steady state conditions had been reached, the concentration of GAS I $\left[C_I^*\right]_{i,b}$ in the flow exiting from the central cavity was determined by

---

FOOTNOTE:

* In the experiments described in this section gas I refers to CO_2 and gas II to Argon.

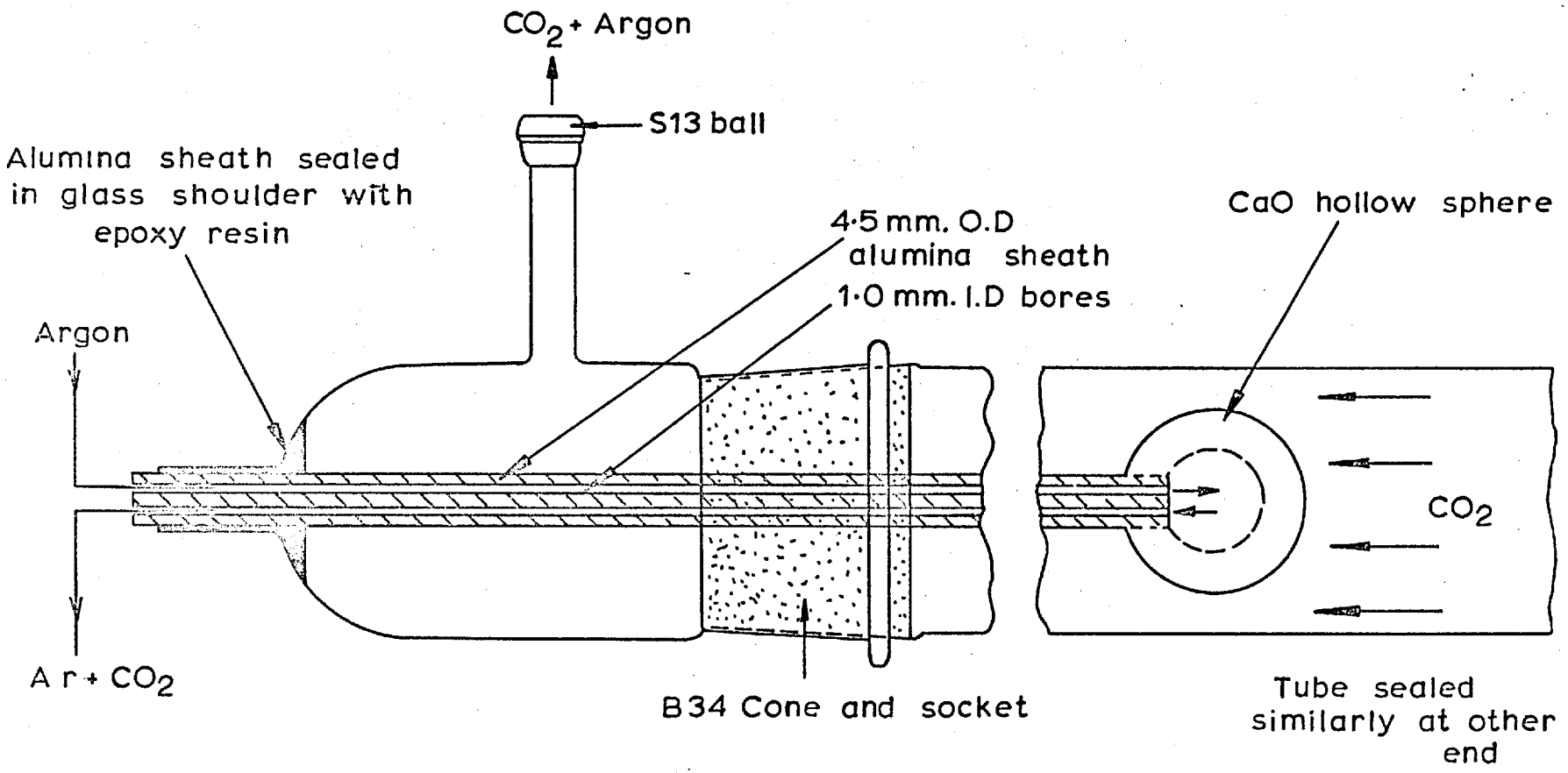


Fig. IV.6. DETAIL OF DIFFUSION CELL. INITIAL TECHNIQUE.

analysis in one of the gas partioners. The flow rate of this exiting mixture $(Q_{I,II})_i$ was measured using a soap-film flow meter. The bulk pressure inside the sphere relative to atmospheric pressure, (p_T) , was taken as the mean of the pressures at the ends of the input and exit bores of the shaft.

The flux of GAS I , $\dot{n}_I$, inward through the porous layer is then given by

$$\dot{n}_i = [c_I^*]_{i,b} \cdot (Q_{I,II})_i$$

The partial pressure gradient giving rise to this flux is

$$\Delta p_I = [c_I^*]_{o,b} (p_T)_o - [c_I^*]_{i,b} (p_T)_i \quad .$$

In these experiments, the fluxes were very low compared to the flow of GAS I and the external pressure was essentially atmospheric. Thus

$$\Delta p_I = 1.0 - [c_I^*]_{i,b} (p_T)_i \quad .$$

When these values had been determined, the flow rate of GAS II was increased and the procedure repeated until the ratio $\Delta p_I / \dot{n}_I$ reached and maintained a constant value. Flow rates of GAS II from 0.25 to 5.0 cm^3/sec were used.

IV-1-B-2 MODIFIED TECHNIQUE

IV-1-B-2(a) INITIAL APPARATUS

The porous materials produced when $FeCl_2 \cdot 1.7H_2O$ and nickel oxide were reduced, could not be expected to exhibit diffusion in the Knudsen regime. Thus isobaric diffusion measurements had to be carried out on these materials. The diffusion apparatus was modified to allow the pressures inside and outside the sphere to be measured and controlled.

Also, because of the fragility of the porous layer and the

difficulty of sealing it to the shaft, diffusion measurements were made at room temperatures. A glass tube of similar dimensions was substituted for the furnace tube, and the sphere sealed to the modified shaft using a cold-cure silastomer.

In addition to the modification of the apparatus, two important modifications were made to the experimental procedure. The compositions and fluxes of both diffusing species were measured so that an experimental flux ratio could be determined and compared with the theoretical value. Also, after a complete run of varying internal flow rates, the diffusion direction was reversed and the run repeated. This provided an excellent check on the experimental results.

The external pressure was measured by placing a small flexible tube (2 mm I.D.) parallel to the gas flow with its end just ahead of the sphere in the diffusion tube. (See FIG.IV-7). However, in order to measure the internal gas pressure, another passage into the sphere centre was required. Therefore, a new support and feed shaft (diffusion shaft) was constructed having three separate passages. This was done by placing two small flexible tubes (0.8 mm. I.D.) inside the bore of a larger tube (4.5 mm.I.D.) (See PLATE 2). One of the smaller tubes protruded from the end of the main shaft so that it could measure the pressure more or less at the centre of the cavity. The other small tube carried the gas at high velocity into the sphere, the exit gas returning up the bore of the large tube. Spheres were sealed to this diffusion shaft so that the end of the large tube coincided with the internal sphere wall. The shaft was sealed into the diffusion tube end cap in the same way as for the initial technique.

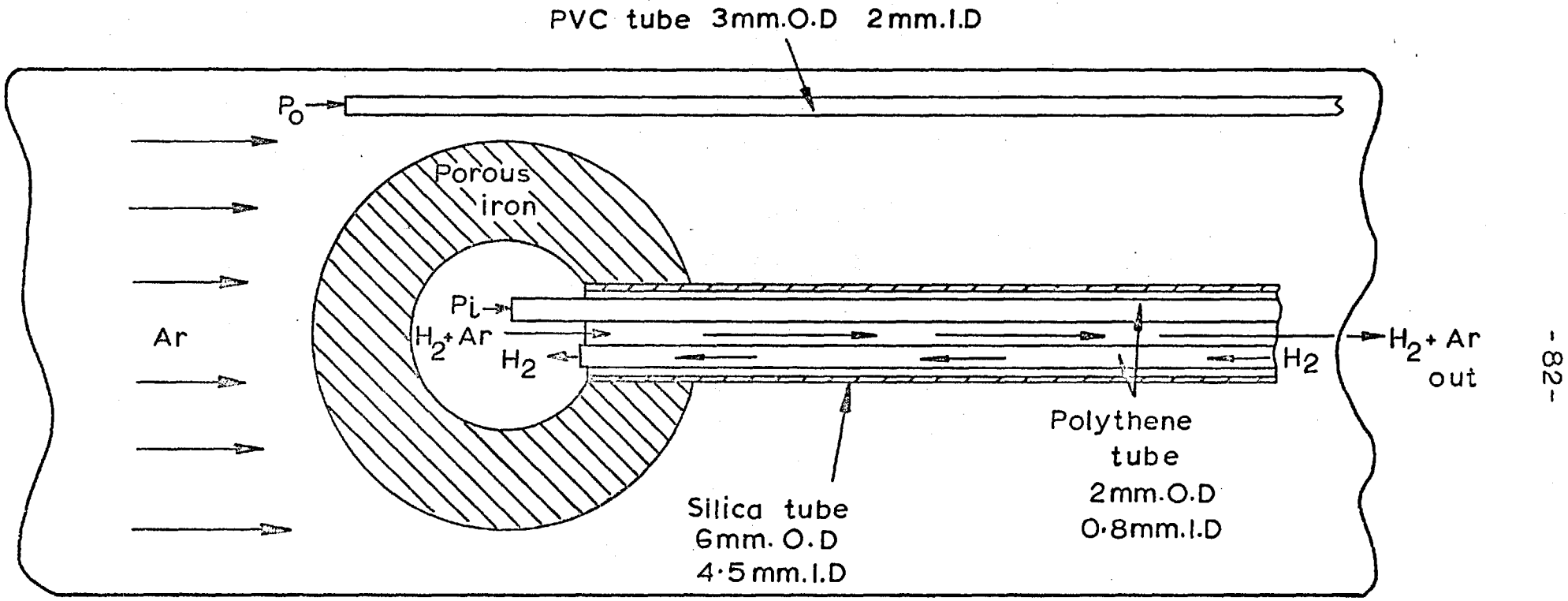


Fig. Ⅳ-7. DETAIL OF SPHERE FITTINGS FOR MODIFIED DIFFUSION APPARATUS

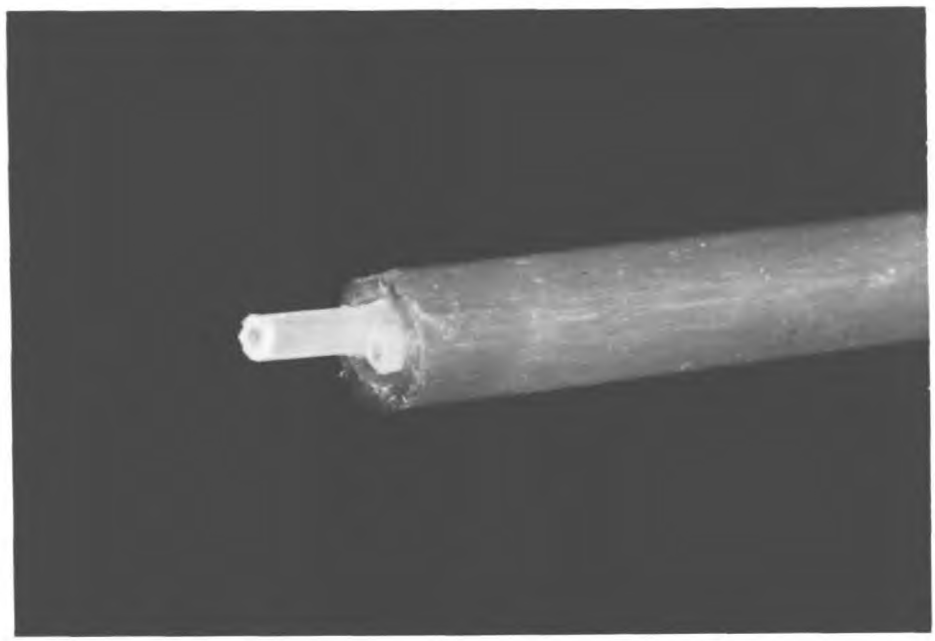
A complete diffusion run was carried out on this apparatus using a porous iron sphere following the procedure outlined in Section IV-1-B-2(d). The initial results obtained with this system showed that the resistances associated with mass transfer inside and outside the hollow sphere were of the same order of magnitude as the resistance due to diffusion across the porous spherical shell. It was therefore necessary to measure the mass transfer coefficients to the inner and outer surfaces of the hollow sphere in experiments that were independent of the diffusion experiments.

The measurements were made by studying the evaporation of naphthalene ($C_{10}H_8$) spheres under gas flow conditions hydrodynamically similar to those involved in the diffusion experiments. These measurements are described in detail in Section IV-1-C.

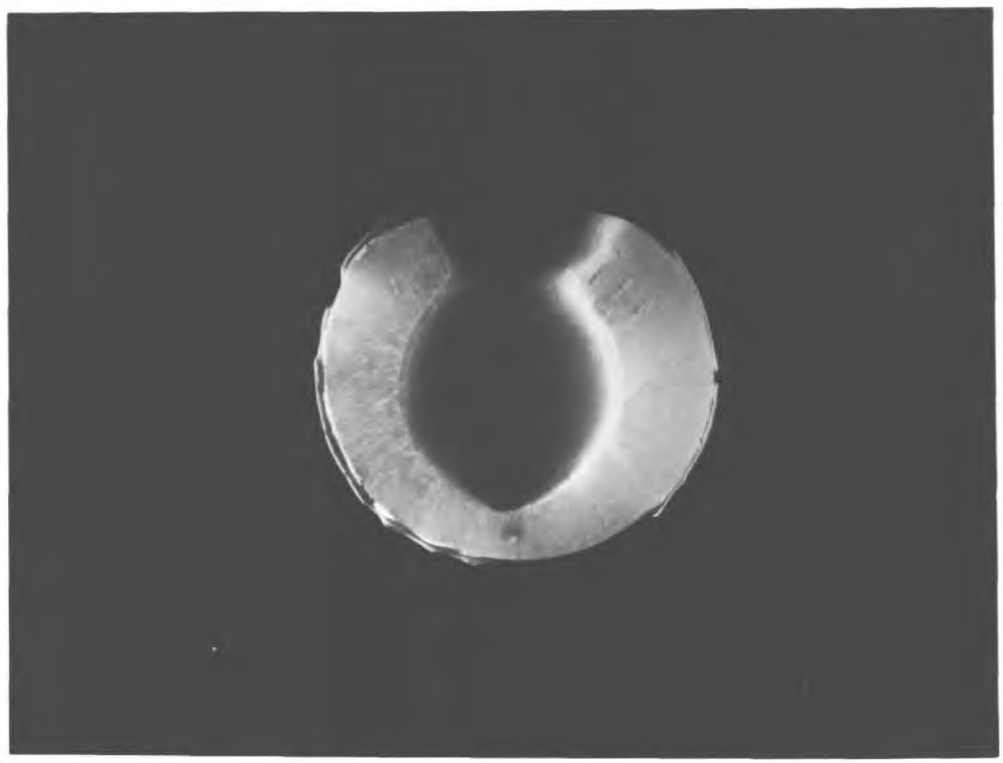
When the hollow naphthalene spheres were sectioned after these experiments, it was found that the internal mass transfer coefficient varied considerably with position. PLATE 2 shows that very high mass transfer rates occurred opposite the gas exit in the diffusion shaft, but that the rates were very much lower over the rest of the surface.

This observation not only indicated large variations in the mass transfer coefficient over the internal surface, but also suggested that the pressure was varying over this surface as well. Consequently it was decided to investigate the nature of this pressure distribution.

A model of the internal cavity of a hollow sphere was made from araldite (See FIG IV-8). Two 'pills' of araldite, each with a $\frac{1}{2}$" hemispherical depression on one end, were fixed together so that the hemispheres formed a continuous spherical suface. Radial holes



(A)
X 3·0



(B)
X 1·5

PLATE 2, (A) INITIAL MODIFIED DIFFUSION SHAFT (Detail)

(B) LOCAL EROSION PRODUCED DURING MASS TRANSFER MEASUREMENTS WITH ABOVE SHAFT

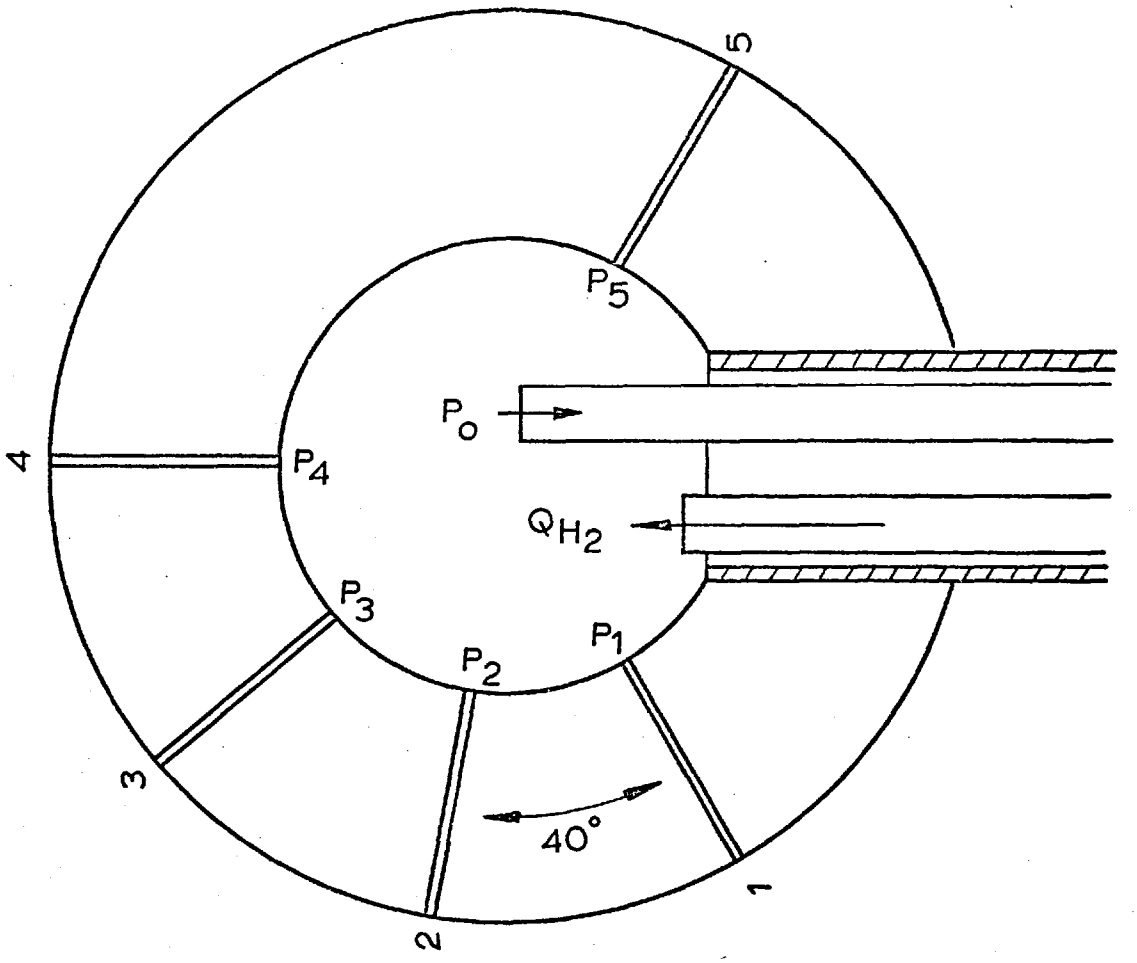


Fig. IV.8. DIAGRAM OF ARALDITE MODEL FOR MEASURING LOCAL IMPACT PRESSURES

(1mm. diameter) were then drilled around one circumference of the cavity and hypodermic needles fixed in each hole so that the end of the needle was flush with the internal surface. This assembly was sealed on the diffusion shaft with the shaft positioned as before.

Each of these radial pressure taps was connected, via a stop-cock, to a manifold which was in turn connected to one side of the micro-manometer. The other side of the micro-manometer was connected to the central pressure probe of the diffusion shaft.

Pressure readings at each radial position were taken relative to the central probe under flow conditions similar to those encountered in diffusion experiments.

These results (Fig.IV-9) show that the pressure was not uniform over the internal sphere surface during diffusion measurements using this diffusion shaft. Therefore, even though the overall bulk flow across the porous spherical layer may be zero during diffusion runs, (See Section IV-1-B-2(c)), localized bulk flows would occur. The flow of gas out of the sphere in those regions where a high pressure was indicated, and the flow of gas into the sphere in low pressure regions would set up a circulating flow which would seriously effect the diffusive behavior of the diffusing species. For this reason, and because of the uneven mass transfer coefficients, a new diffusion shaft was designed.

It was also realized that pressure variations in the gas flowing outside the sphere could also result in some localized flows. As this gas flows through the annulus between the sphere and the diffusion tube under typical experimental conditions, it is accelerated from about 4cm/sec to about 6cm/sec. The pressure change resulting from this velocity increase is of the order of 10^{-4} inches of water. Localized f flows could result from this pressure variation, but the permeability data show that they would be neglegible.

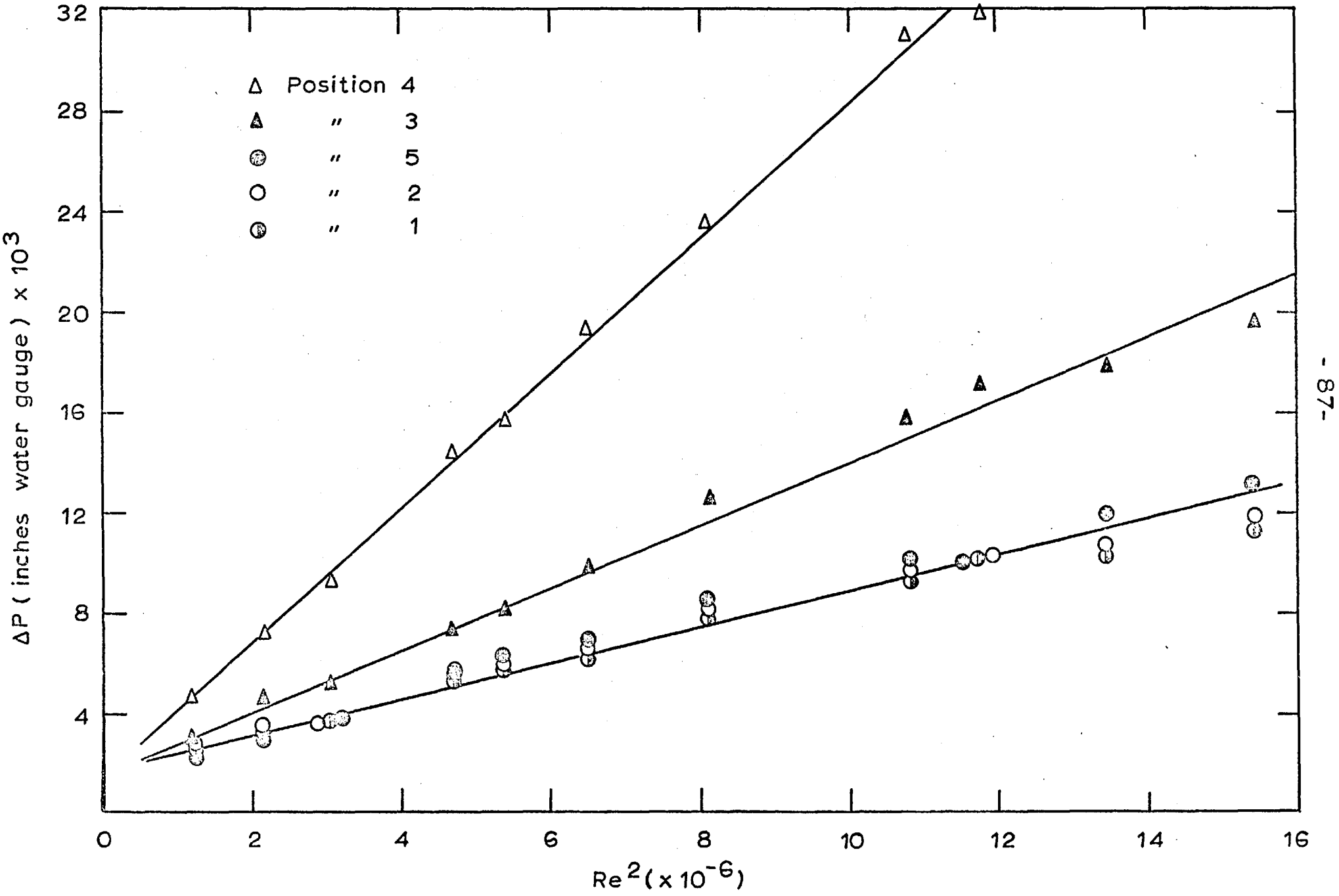


Fig.Ⅳ-9a.PRESSURE DIFFERENCE vs. REYNOLDS No. FOR VARIOUS POSITIONS AROUND HOLLOW SPHERE.

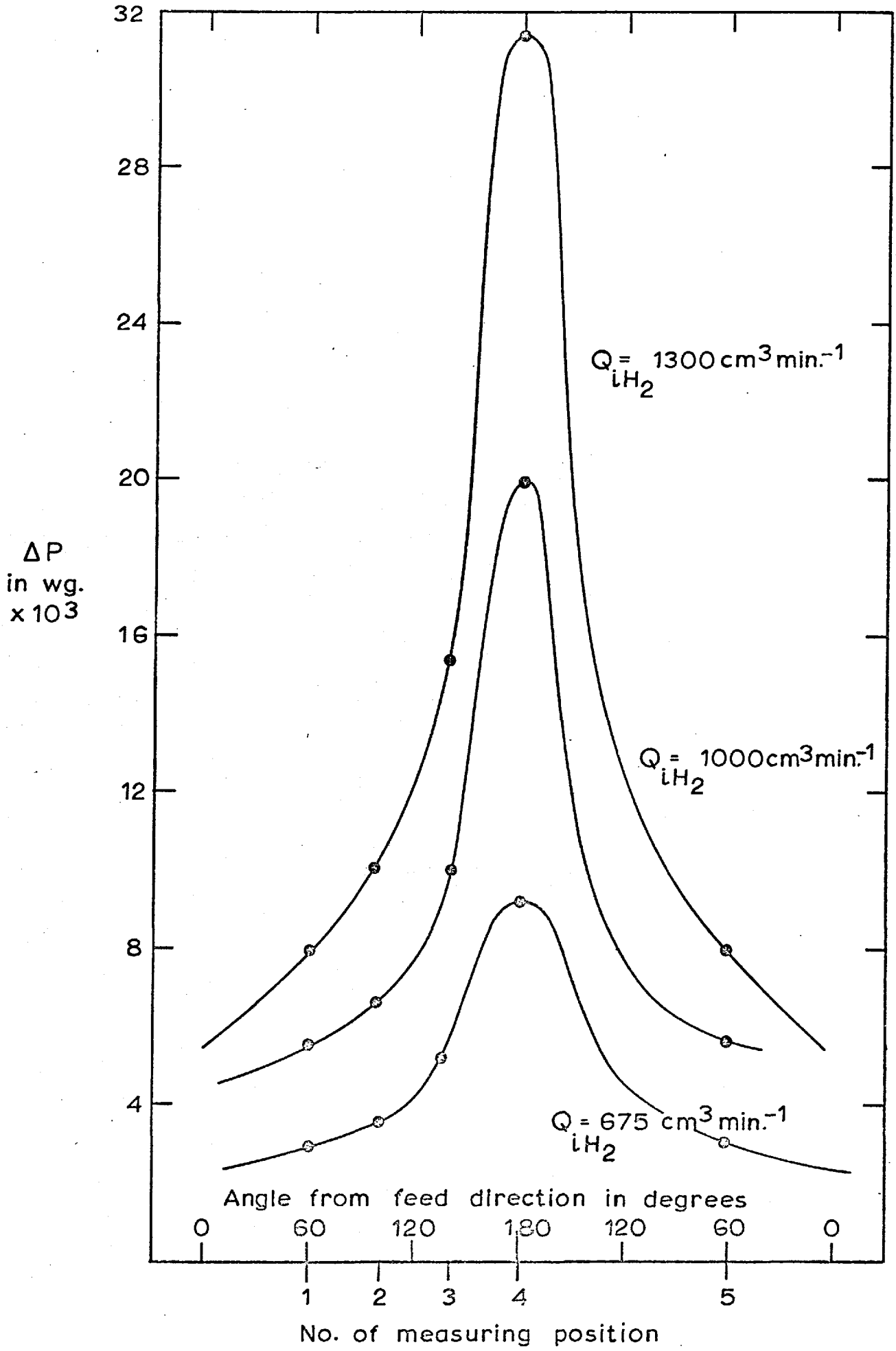


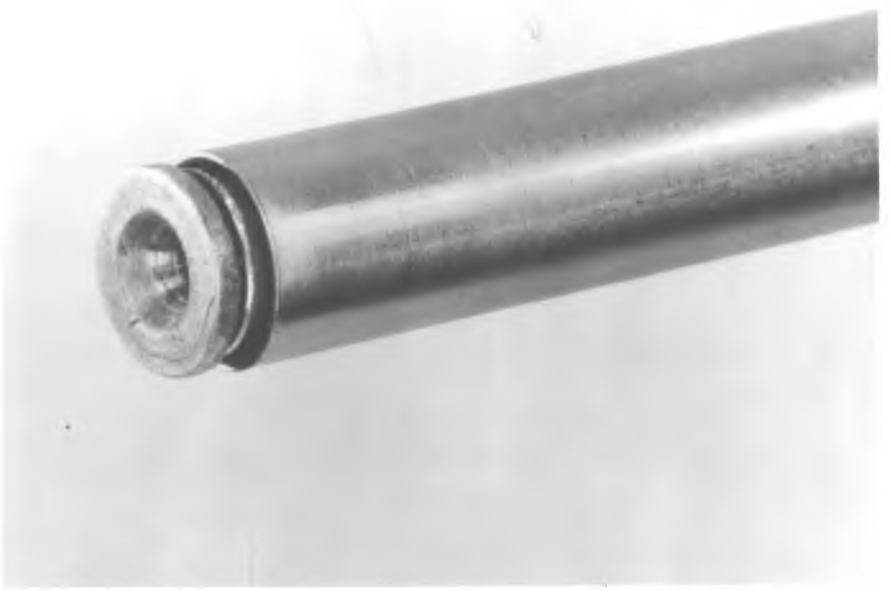
Fig.IV-9b. INTERNAL PRESSURE DISTRIBUTION

IV-1-B-2(b) FINAL APPARATUS

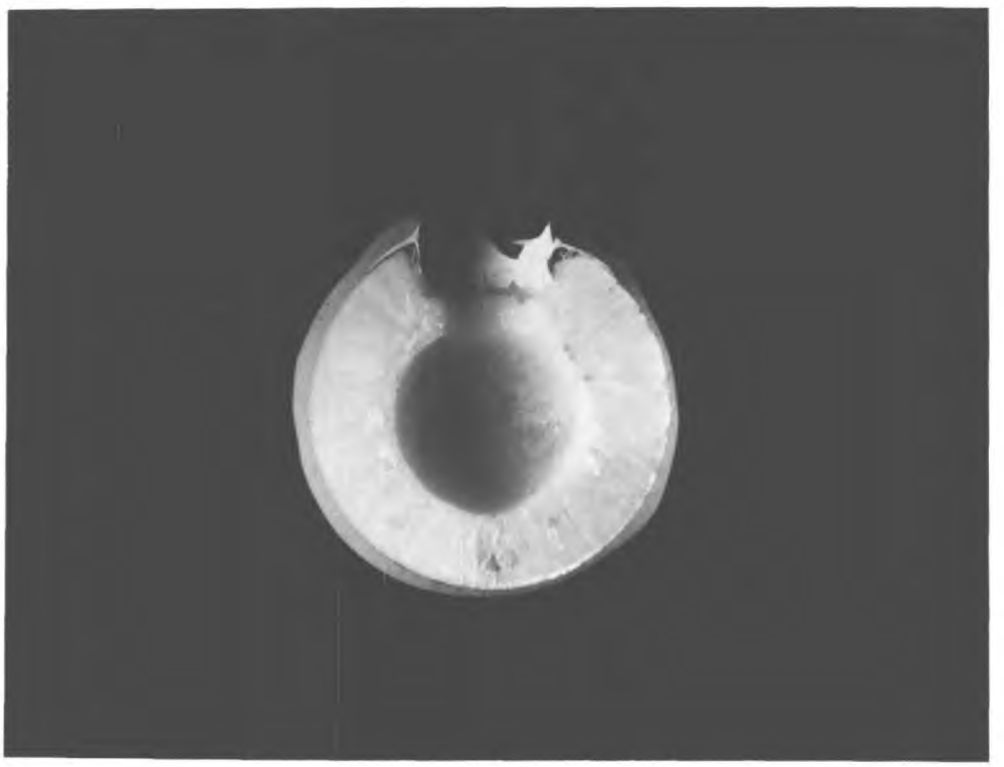
The work described in the previous section showed that regions of high pressure and high mass transfer coefficient existed opposite the diffusion shaft, and it appeared that they were produced by the direct impingement of the incoming gas stream. It was thus necessary to modify the diffusion shaft so as to avoid this direct impingement, whilst maintaining a high degree of mixing inside the hollow sphere.

A diffusion shaft which gave a very fine conical gas jet was constructed (PLATES 1 & 3 and FIG IV-10). It consisted of three concentric stainless steel tubes held concentrically by small spacers at intervals in the annuli. The outer annulus allowed the pressure inside the sphere to be measured. The inner annulus carried the gas into the sphere and the gas returned along the central tube. Additional metal was welded to the end of this central tube, and the end of the middle tube was slightly flanged, as shown in Fig. IV-10. The central and middle tubes were positioned and welded together so that the desired conical flow pattern was produced - (PLATE 1). The outer tube was positioned so that a narrow opening for pressure reading was formed at the delivery end of the shaft, and it was then welded to the other two tubes.

External pressures were measured using a 1 mm. bore stainless steel tube which was positioned at right angles to the flow direction and placed just behind the sphere. Spheres were sealed to the shaft as with the previous technique, care being taken that the internal sphere surface coincided with the end of the largest tube.



(A)
X 4·0



(B)
X 1·5

PLATE 3, (A) FINAL DIFFUSION SHAFT (Detail)

(B) EVEN EROSION PRODUCED DURING MASS TRANSFER MEASUREMENTS WITH ABOVE SHAFT

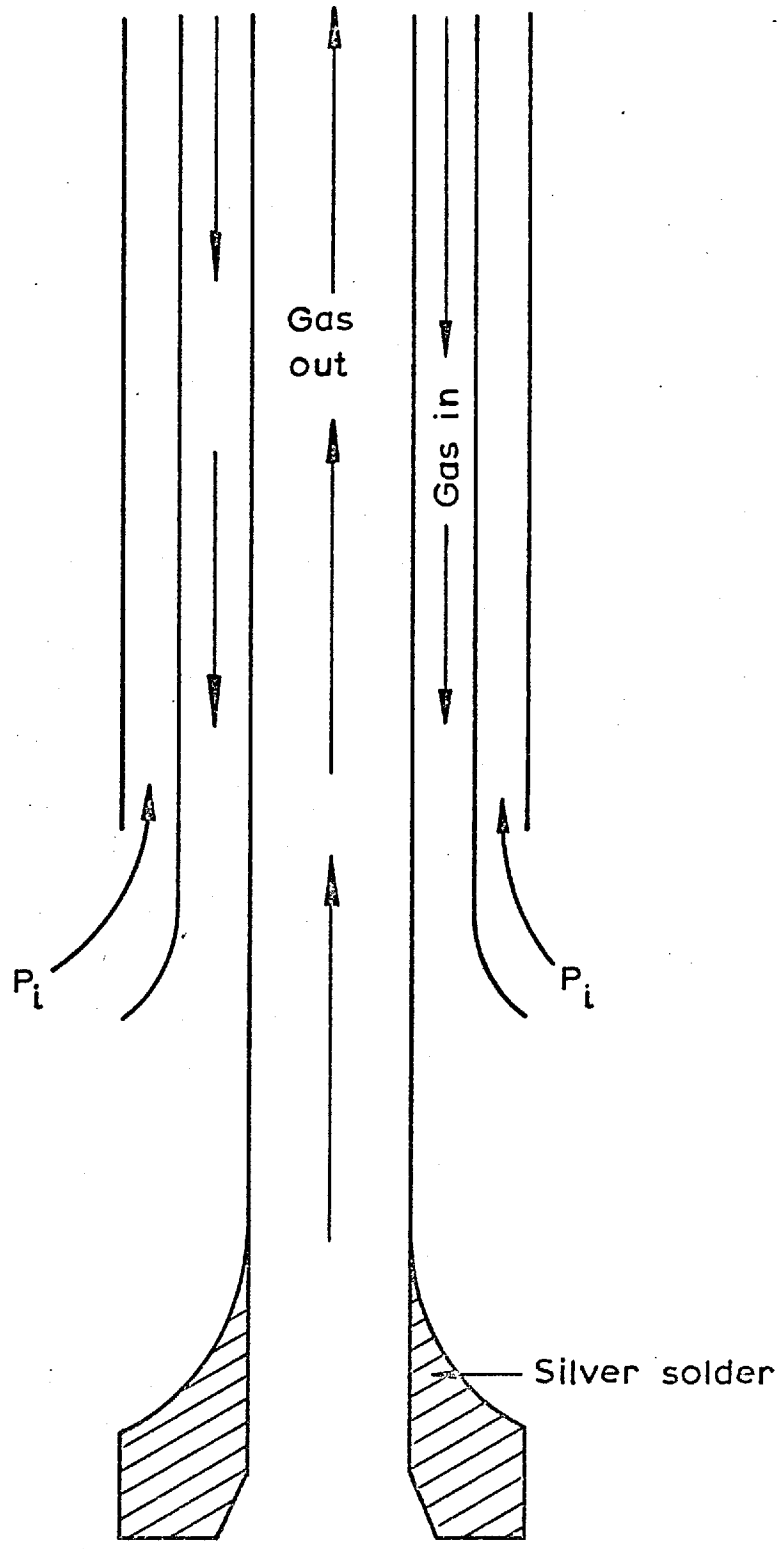


Fig.IV.10 DETAIL OF DELIVERY END OF FINAL DIFFUSION SHAFT (3 tubes displaced longitudinally for clarity)

When the naphthalene evaporation experiments were repeated using this diffusion shaft, no preferential erosion was observed as PLATE 3 shows. Furthermore, when the pressure distribution inside the 'araldite' hollow sphere was investigated, no measurable differences ($\pm$ 0.1 N/m^2) were found between the pressure at the sphere end of the outer annulus and the pressure at any position on the internal surface of the sphere. Thus, the conical flow pattern produced by this modified diffusion shaft eliminated any regions of direct impingement. The conical nozzle of the diffusion shaft had a very small cross-section (approximately 1.0 mm^2.) so that gas still emerged from the shaft at high velocity, thus retaining the mixing ability of the previous shaft.

IV-1-B-2(c) PRESSURE EQUALISATION

Different types of flow pattern existed in these dynamic systems around the pressure probes inside and outside the sphere. Thus gas could flow across the spherical shell even though the two probes were indicating the same pressure. A series of experiments was thus carried out to determine the actual pressure differences that corresponded to zero net gas flow across the spherical shell under different internal and external gas flow rates.

These experiments were carried out by passing the same gas on both sides of the sphere, each stream having a known flow rate. The pressures of each stream were then adjusted using two sensitive valves on the exit side of each gas train so that the input and exit flow rates of each stream were equal. When this condition was satisfied there was no bulk flow across the porous layer and the pressure

difference between the two probes was recorded. This procedure was followed for several spheres using each diffusing gas. Typical values determined for porous iron spheres are presented in the results section, and it can be seen that the pressure differences were small. (Table V-2)

Diffusion experiments were then carried out with these pressure differences maintained across the porous shell under corresponding flow conditions and it was found that the flux ratios of the diffusing species were very close to those predicted theoretically for isobaric diffusion:-

$$\beta_I = -\frac{\dot{n}_{II}}{\dot{n}_I} = \sqrt{\frac{M_I}{M_{II}}}$$

The establishment of this ratio was thus used to check that isobaric conditions were maintained during the subsequent diffusion experiments, since this resulted in a considerable saving of experimental effort.

IV-1-B-2(d) DIFFUSION RUN

As has been previously mentioned, the modified diffusion measurement involved the determination of the compositions and fluxes of both diffusing species and the reversal of the diffusion direction. That is, one complete run of varying internal flow rates was done with GAS I outside and GAS II inside, and one run with GAS II outside and GAS I inside.

In the latter case, after the apparatus was sealed as in the initial technique, a constant flow rate of GAS II was introduced into the diffusion tube, $(Q_{II})_o$, and a known flow rate of GAS I into the hollow sphere, $(Q_I)_i$. After the pressures had been properly

balanced for isobaric conditions, the compositions of GAS I in the external stream, $[C_I^*]_{o,b}$ and GAS II in the internal stream, $[C_{II}^*]_{i,b}$ were determined using the gas partioners. The flow rate of gas exiting from the sphere, $(Q_{I,II})_i$, was measured using a soap-film flow meter. The system pressure (p_T) was measured by means of the external pressure probe connected to a mercury manometer. The micro-manometer reading was also noted.

The results of these measurements and the determination of effective diffusivities from them are discussed in Section V-1-C-2.

All quoted results for porous iron and porous nickel were determined using this procedure. A hydrogen-argon couple was used in the measurements on porous iron, but both H_2 - A_R and H_2 - CO_2 were used in the measurements on porous nickel. The hydrogen-carbon dioxide couple was used instead of the H_2 - A_R couple in the nickel system when the analysed argon compositions were low. This was necessary as considerable amounts of the mixture were diffusing out of the sampling syringe between the removal of the sample from the flowtrain and its introduction into the gas analyser, due to the high diffusivity of the hydrogen-argon system. This was replaced, then, largely by nitrogen counter-diffusing into the syringe from the atmosphere. However, since the chromatographic columns did not separate nitrogen from argon, the argon peak was considerably reinforced by the presence of nitrogen. Consequently, calculated argon fluxes were too high, leading to erroneous flux ratios and diffusion coefficients. As the chromatograph did separate carbon dioxide from nitrogen, this diffusion couple was used instead.

IV-1-C MASS TRANSFER MEASUREMENTS

Although the resistance due to mass transfer inside and outside the hollow lime spheres was very much smaller than the resistance due to diffusion across it, this was not true for the more porous nickel and iron spheres. It was thus necessary to measure the mass transfer coefficients inside and outside the sphere directly before the diffusion experiments could be interpreted correctly.

These spheres were made using naphthalene, ($C_{10}H_8$), spheres of the same size as those used in the diffusion experiments. The use of naphthalene is common for such applications as its vapour pressure at room temperature (approximately .05 mmHG) is accurately known as a function of temperature and since it can be easily melted and cast. Care must be taken, however, in the method of casting. The grain size of the solidified naphthalene is important. If the grain size is too small, evaporation from grain boundaries becomes important and if too large, preferential evaporation due to crystal orientation may be appreciable. The naphthalene spheres used in this work were chill cast in cold molds from a melt with very little superheat, a method that produced the optimum grain size.

IV-1-C-1 EXTERNAL MASS TRANSFER MEASUREMENTS

Although mass transfer to spheres is normally determined by the Frossling equation

$$Sh = 2.0 + 0.60\ Re^{\frac{1}{2}}\ Sc^{\frac{1}{3}} ,$$

the relationship between these dimensionless groups could be quite different in the diffusion measurement experiments because of the proximity of the diffusion tube.

To investigate this relationship, solid spheres of naphthalene of similar size to the porous sphereswere cast in two part lead molds (Fig. IV-11). These spheres were subsequently radially drilled and placed on the support shaft and sealed into the diffusion tube. Known flow rates of air were passed over the sphere while the gas temperature adjacent to the sphere was continuously measured. The sphere was allowed to evaporate into the flowing air stream for times from 3 to 10 hours and the weight loss due to evaporation determined. Several different spheres were used at air flow rates of 50 to 1000 cm^3/min. Each sphere was allowed a total weight loss of only a few hundred milligrams before it was discarded, so that the initial geometry was not appreciably effected. The results obtained are presented in Section V-1-A-1.

IV-1-C-2 INTERNAL MASS TRANSFER MEASUREMENTS

The internal mass transfer coefficient was also assumed to depend on the three dimensionless groups and to be of the form

$$Sh = A + BRe^{n} Sc^{\frac{1}{3}}$$

In order to determine the exact form of this relationship, hollow spheres of naphthalene were made. These were chill cast in the same two part lead mold as the solid naphthalene spheres. In this case, however, a sphere of tin chloride ($SnCl_2$) was suspended by means of a copper rod in the centre of the mold cavity, the tin chloride spheres having been cast in the two part mold used previously to make the Wood's metal spheres. The naphthalene was poured into the mold around the tin chloride sphere, allowed to solidify and then removed from the mold together with the copper rod. This could easily be removed from the sphere by gently heating the end so that

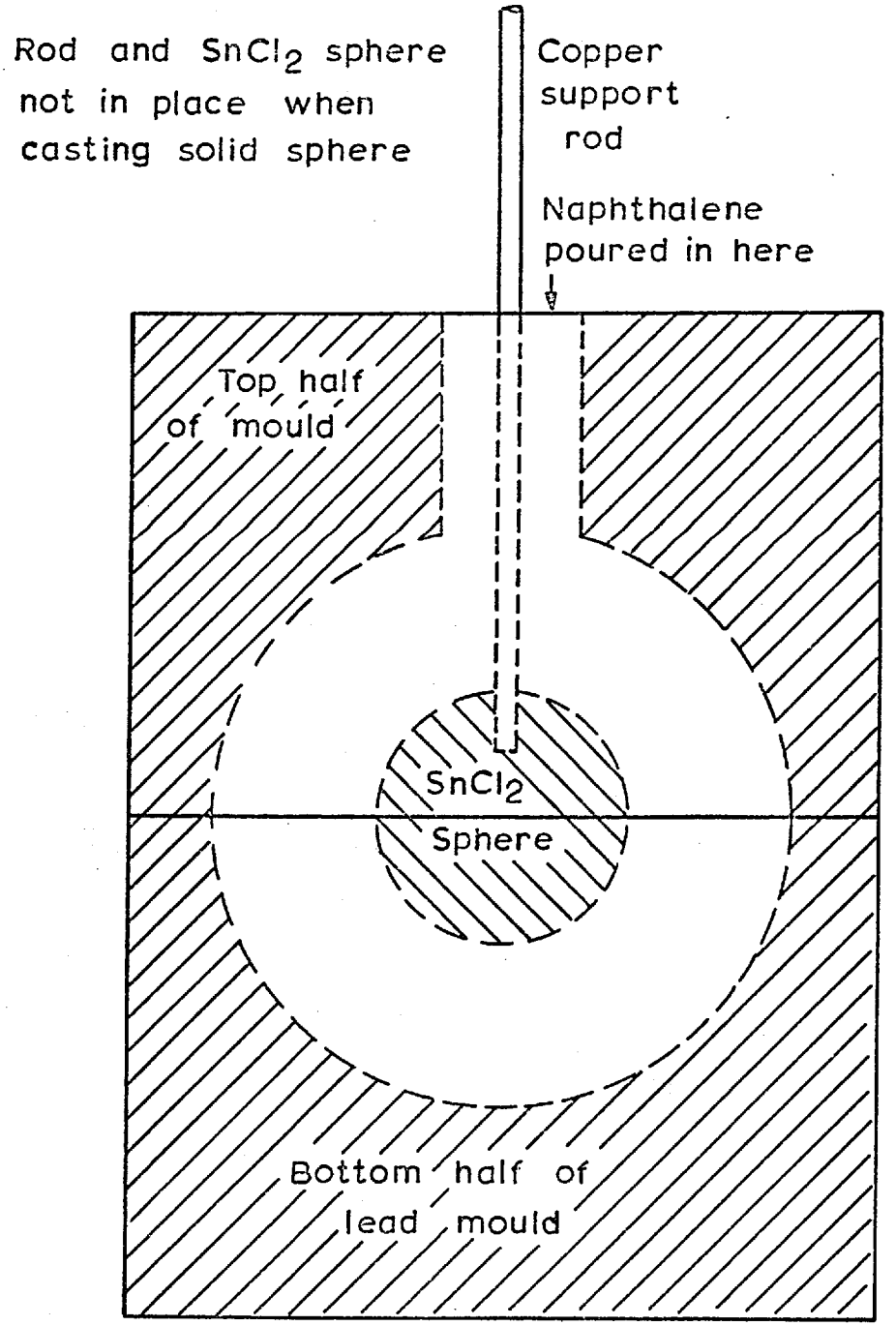


Fig.IV-11. TWO PART LEAD MOULD FOR CASTING NAPHTHALENE SPHERES

the naphthalene immediately surrounding the rod melted. The tin chloride sphere was then removed by dissolving it in water in which naphthalene is insoluble. The surface of the inner spherical cavity was then cleaned with a small artists' paint brush to remove any foreign material.

This hollow naphthalene sphere was drilled to accept an aluminium collar which was sealed in position with cold cure silastomer. This assembly was then placed on the shaft used in the diffusion experiments so that the inner end of the large tube was flush with the internal naphthalene surface. The sphere assembly was then sealed to the shaft by means of an 'O-ring' seal. See Fig. IV-12. A very fine (0.55 mm.) thermocouple was forced down the bore of the central tube so that its point was approximately in the centre of the spherical cavity. The outside of the sphere was sealed with 'araldite' to prevent any evaporation from this surface.

Weight losses were measured over the range of internal gas flow rates that were used in the diffusion coefficient experiments.*

When partially evaporated spheres were sectioned after mass transfer experiments in which the original modified probe had been used, it was noted that mass transfer rates had been very much higher at the point opposite the probe than elsewhere. Erosion at this point was very marked (See PLATE 2).

The previous procedure was thus repeated for the new diffusion shaft. A change in the relative spacing of the concentric tubes made two determinations of the internal mass transfer equation necessary.

FOOTNOTE:

* In some measurements, gases different from those encountered in in diffusion experiments were used, in which case dynamic similarity was maintained.

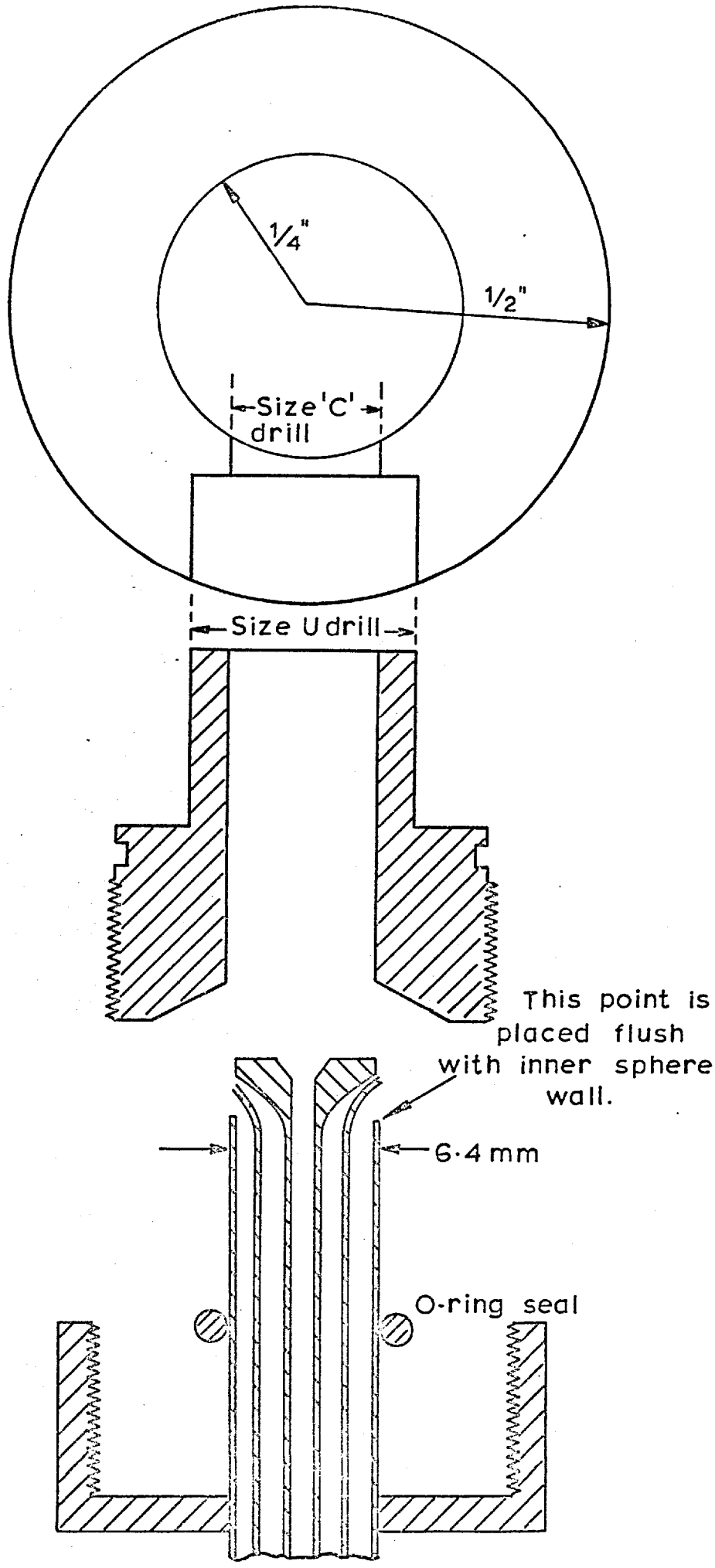


Fig. IV. 12. SPHERE—SHAFT CONNECTION FOR INTERNAL MASS TRANSFER MEASUREMENTS

The first of these determinations was done using air flow rates from 50 to 600 cm^3/sec. The results of these measurements were applied to the porous iron diffusion experiments.

The spacing change was made between the end of the iron experiments and the beginning of those on nickel. The second determination was done using both CO_2 and hydrogen at flow rates similar to those encountered in the diffusion experiments, hydrogen flows of 500 to 2500 cm^3/min and CO_2 flows of 400 - 1600 cm^3/min.

A picture of a sectioned $C_{10}H_8$ sphere used in the second determination is shown in PLATE 3 and may be compared with one used with the shaft of the first modification, PLATE 2.

IV-1-D PERMEABILITY MEASUREMENTS

The permeabilities of the product solids were measured at varying total pressures so that the Knudsen diffusion coefficients through them could be determined by extrapolation. These measurements were done at room temperature using the final diffusion apparatus.

The external gas exit and internal gas inlet were sealed so that all gas entering the diffusion tube had to flow through the porous solid layer and out via the internal gas exit. The pressure difference across the sphere accompanying this flux was measured by the internal and external pressure probes. These were connected to a mercury manometer in the case of dense spheres and to the micro-manometer in the case of highly porous spheres. Fluxes were measured using soap-film flow meters.

A 'manostat' was connected in series with the internal gas exit and was used to control the system pressure. Gas flow rates

were adjusted to measureable values using the regulator on the gas supply cylinder. Positive pressures were supplied by suitable adjustment of the cylinder delivery pressure. For pressures below atmospheric, a vacuum pump connected to the outlet side of the manostat served to lower the pressure and remove the flowing gas.

PART II - REDUCTION OF NICKEL OXIDE

INTRODUCTION

In order to investigate the rate of reduction of nickel oxide, spherical compacts were prepared from the nickel oxide powder previously described. Reduction rates were determined by continuously measuring the weight of these spheres during reaction with H_2.

The spheres were suspended from a load cell in a vertical furnace and the load cell output signal fed to recording devices. The temperatures of samples undergoing reduction were also continuously measured. The furnace and load cell system were designed and built mainly by Mr. A. MATYAS for the study of hematite reduction. The gas supply system was designed and built by the author in conjunction with Mr. Matyas. Similarly, improvements to the apparatus were carried out by both workers.

IV-2-A FURNACE

Reduction rate measurements were made in a vertical tube furnace which could be raised and lowered around a sample suspended from a load cell. The apparatus is illustrated in Fig.IV-13. The alumina furnace tube was 5 cm. in diameter and had a heated length of 450 cm. The furnace was wound with Kanthal A1 wire with a total resistance of 21 ohms, and insulated with a 5" thick vermiculite layer. An Ether fast-cycling controller connected to a Pt/Pt-13%/Rh thermocouple, placed adjacent to the furnace windings, was used to control the furnace temperature to $\pm$ 0.5°C. A bed of alumina chips was placed just before the sample zone to bring gases passed into the furnace up to temperature. These gases were introduced at the bottom end of the furnace from the gas train described in Section IV-2- D.

The furnace was mounted on hydraulically operated pistons, which were used to raise and lower the furnace around the sample. The furnace was sealed when in its raised position by an 'O-ring' set in a water-cooled jacket, which was held against the gas exit chamber by the hydraulic pressure (See Fig. IV-13A).

The whole of this assembly, i.e. furnace, gas-exit chamber and sample suspension chamber, was supported on an angle iron frame which was mounted on a heavy slab of slate which acted as a base. This base was insulated against vibrations in the laboratory floor by cork pads.

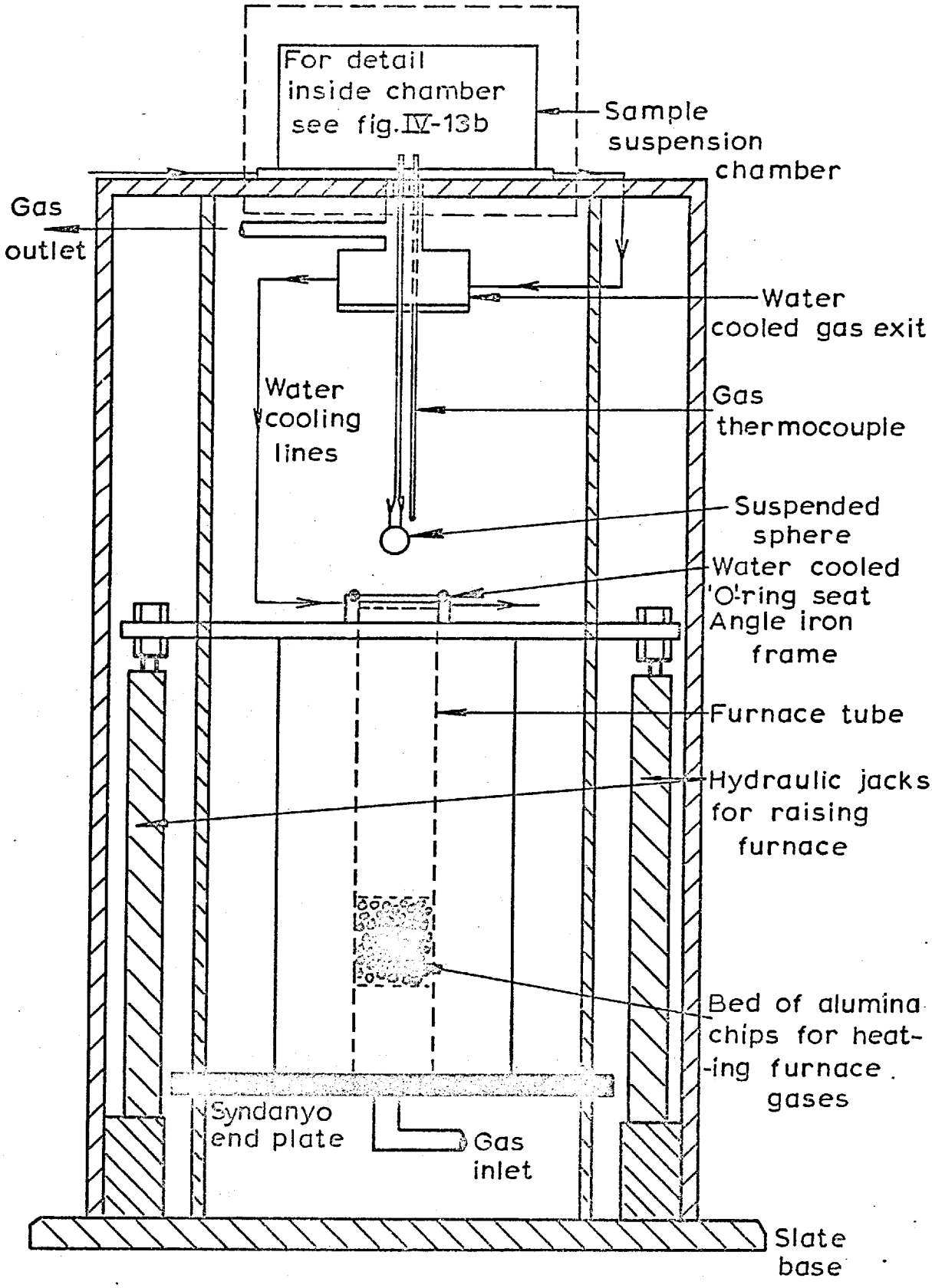


Fig.IV-13a. REDUCTION FURNACE ASSEMBLY

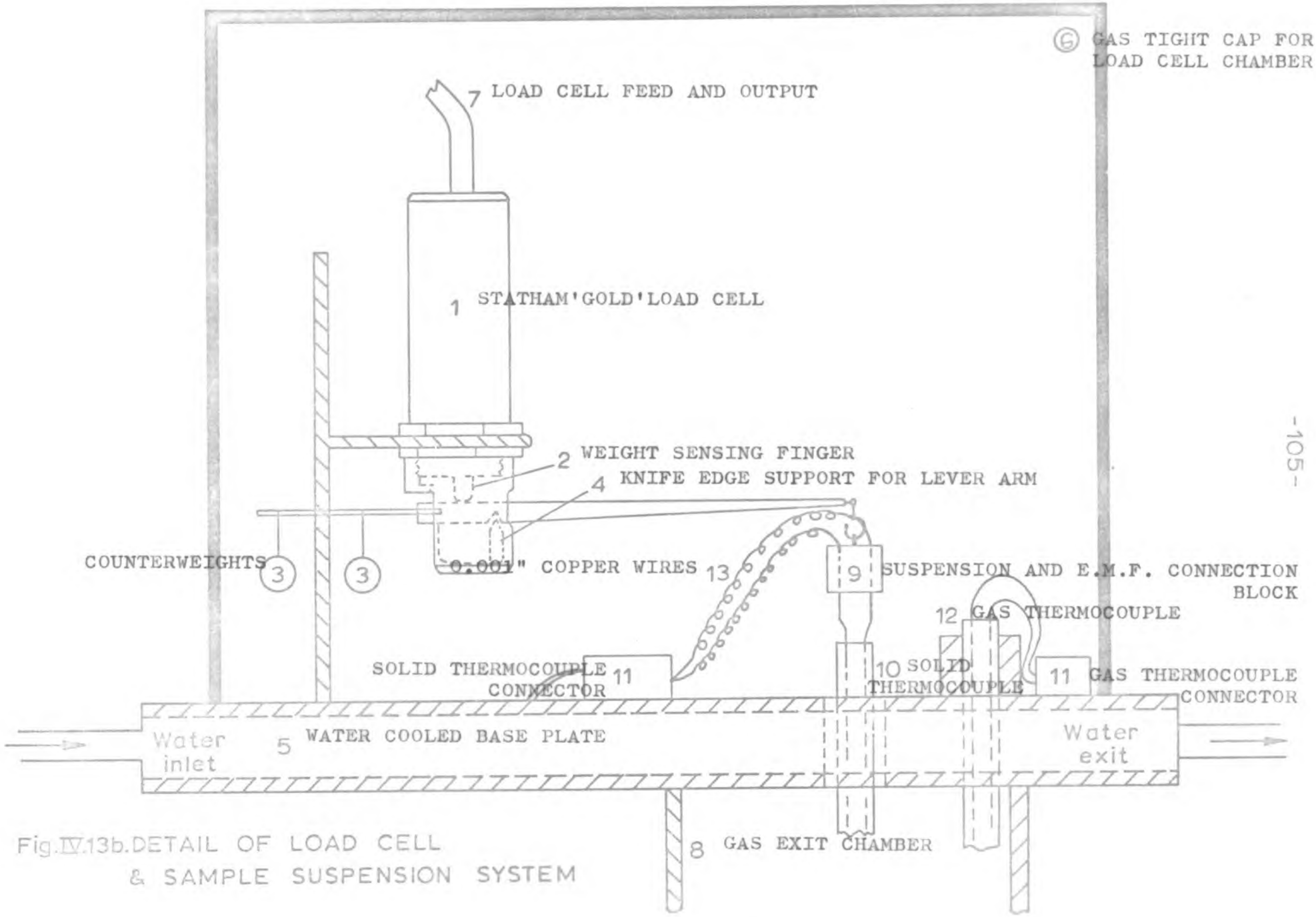


Fig.IV.13b.DETAIL OF LOAD CELL & SAMPLE SUSPENSION SYSTEM

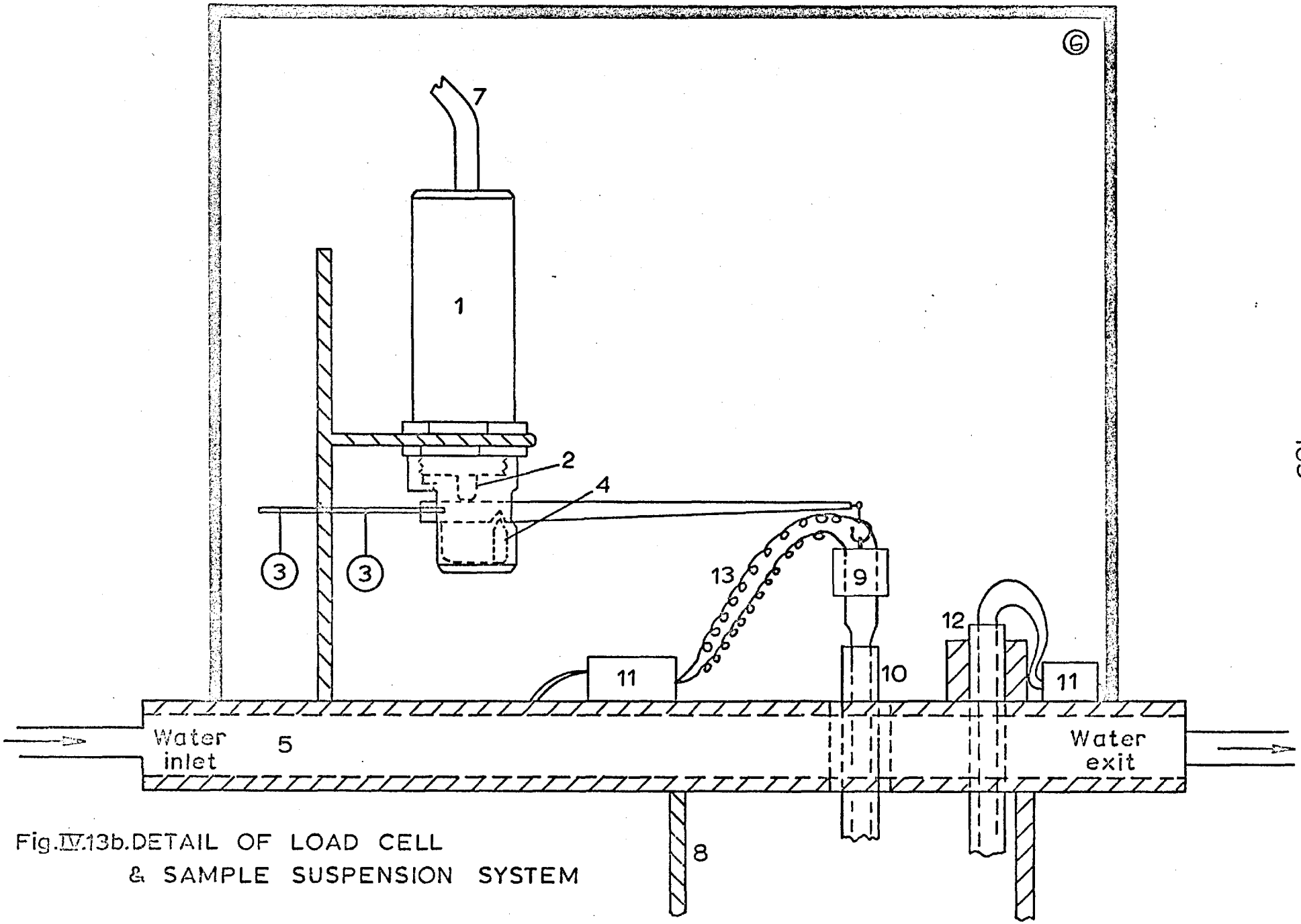


Fig.IV.13b.DETAIL OF LOAD CELL & SAMPLE SUSPENSION SYSTEM

IV-2-B LOAD CELL

A load cell, supplied by Statham Instruments Ltd., was used to measure the weight of the samples during the reduction experiments. The load cell was capable of measuring a total compressive load of 60 gms. but was equipped with a lever arm which, properly adjusted, could increase its sensitivity by factors of 2, 5 or 10 and which changed the actuating load from compressive to tensile. Provision was also made for counterbalancing part of the load suspended from the lever arm so that higher sensitivities could be used. The load cell was calibrated by determining its output when a series of known weights were suspended from it. The resultant calibration curve was linear and is shown in Fig. IV-14.

IV-2-C SAMPLE SUSPENSION

The sample suspension system and the load cell installation are shown in Fig. IV-13B. The thermocouple wires protruding from the prepared spherical sample were looped over corresponding thermocouple wires which hung vertically down from the load cell chamber, passing through the gas-exit chamber. The upper ends of these thermocouple wires were joined to a small connector which was suspended from the load cell lever arm. From this connector, copper wires, 0.001" in diameter, carried the thermocouple E.M.F. to another connector fixed to the load cell chamber base plate.

The suspension thermocouple was of such a length that with the furnace in the raised position, the sample was centred in

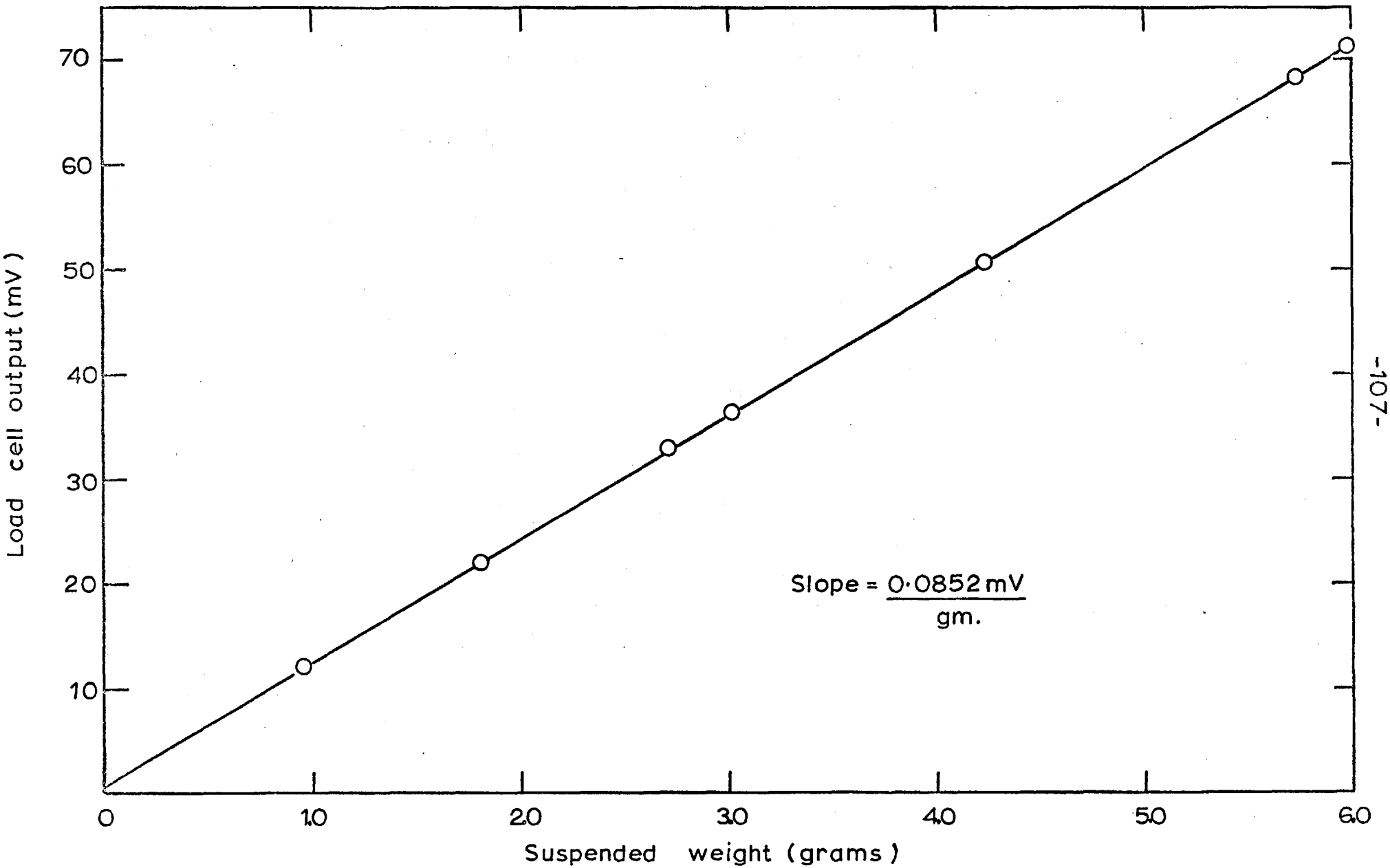


Fig. IV-14. CALIBRATION CURVE FOR LOAD CELL.

the furnace hot zone. The thermocouple sheath, which shielded most of the length of the suspension thermocouple, passed through holes in the load cell chamber base plate and gas exit chamber so that it hung freely. A gas thermocouple also passed through similar holes so that it was just above and to one side of the reacting sample. See Fig. IV-13A.

A gas tight cap was placed over the load cell system to form the load cell chamber and all the electrical connections were made through gas tight seals in the load cell chamber base plate. The base plate also contained a water jacket which was used to control the temperature in the load cell chamber above the dew point of the furnace exit gases.

IV-2-D GAS TRAIN

The gas train, which is illustrated in Fig. IV-15, was designed to provide two separate gas streams, either of which could be fed to the furnace. It was also designed to allow a rapid change to be made from one gas stream to the other. One of the two gas streams was inert, or slightly oxidizing, and was used to preheat the sample prior to reduction and to quench it afterwards; the other stream was the reducing gas mixture. Both streams were dried over silica gel and magnesium perchlorate, but the inert stream was metered by rotameters, whereas the reducing gas stream was metered by orifice flow meters. Immediately before the furnace gas inlet, both streams passed through a series of two-way stopcocks by means of which each stream could be delivered either to the furnace or to a

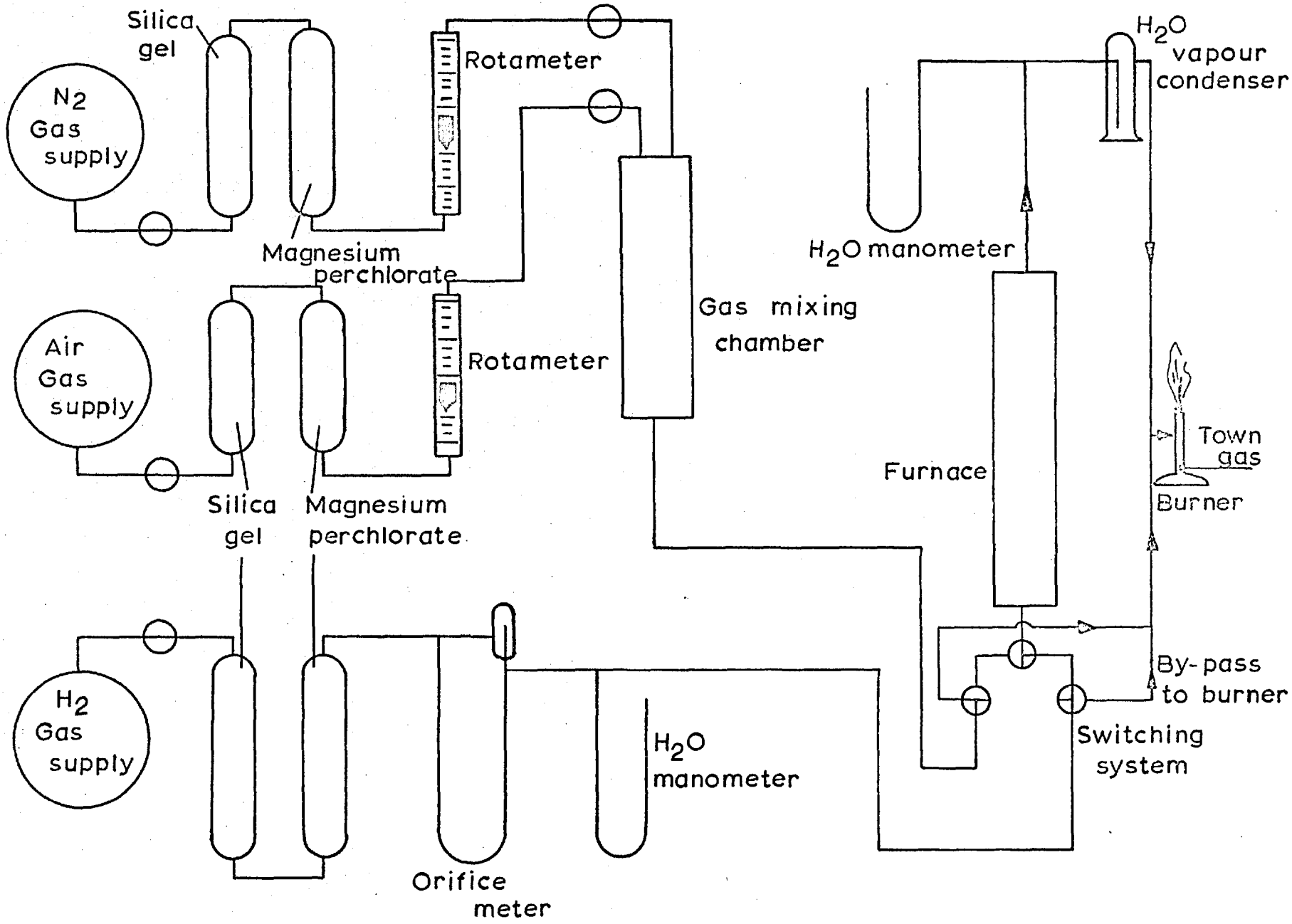


Fig.Ⅳ-15. GAS SUPPLY FOR REDUCTION EXPERIMENTS.

bypass. After exiting from the furnace, the gas passed through a water condensation cell and through a gas burner. All bypass flows also passed through the burner.

IV-2-E SAMPLE PREPARATION

Solid spheres of nickel oxide for the reduction rate experiments were made by the method used for the preparation of the diffusion samples. In this case, however, a Pt-Pt/13%Rh thermocouple was compacted into the centre of the sphere, not a Wood's metal core. These thermocouples were only 2 cms. long and each wire (0.2 mm diameter) protruded about 1 cm. from the surface of the sphere. Approximately 12 gms. of NiO powder (with 1% binder) were compacted under pressure, 100 kN/m^2 being the pressure used for most of the experiments.

These spheres were then treated similarly to the diffusion samples prior to reduction. See Section IV-1-A-8. After this treatment, the samples were accurately weighed and the radius and porosity determined. This procedure produced nickel oxide spheres of approximately 9 mm. in diameter , with a porosity of about 40%.

IV-2-F DATA RECORDING

The output from the sample thermocouple was measured by a single-pen Leeds and Northrup 'Speedomax H' recorder with a range of 0 - 1mv. The signal was biased so that the e.m.f. corresponding to the steady initial reduction temperature was near the middle of the scale.

The gas temperature was continuously measured during the first several reduction runs but was found to be constantly 4 - 6^{o}C above the solid temperature and consequently this temperature was subsequently

checked only intermittently.

The load cell ouput was fed both to a 'Servoscribe' recorder via a 'Vibron' electrometer for visual output and to a data logger for a permanent record on paper tape of the changing weight. The data logger was used with a reading rate of 1 channel per second and a range of 0 - 100 mv. A filtering mechanism built into the data logger was used to electrically damp the input signal. This was necessary because of oscillations in the signal, probably due to vibrations in the sample suspension system.

IV-2-G REDUCTION EXPERIMENTS

When the sphere had been properly suspended from the thermocouple leads, the load cell lever arm was counterbalanced so that the load cell output was below 72 mv. (corresponding to maximum load of approximately 6 gms.). The load cell chamber cap was then put in place and the load cell chamber sealed. A check was made to ensure that the suspension system was swinging freely and the furnace was then raised. The furnace was turned on and the water passed into the water jackets in the load cell base plate and surrounding the 'O-ring' seal. A N_2-AIR mixture was passed through the furnace.

When the solid temperature reached the desired value, the air was switched off and the furnace swept with nitrogen. During this time, the flow of reducing gas (H_2) was adjusted to the desired value while the gas bypassed the furnace and was fed to the burner. The data logger was then started as were the temperature and weight loss recorders. Immediately, the N_2 flow into the furnace was replaced by H_2. (See Section IV-2-H). The reaction was then allowed

to proceed until the sample weight reached a steady value or until a predetermined weight loss had occurred. At this time the recording instruments were stopped and the hydrogen flow was replaced by a high flow rate of oxygen-free nitrogen. The samples were allowed to furnace cool. Even with samples held in the furnace, cooling was quite rapid; for instance the temperature could be reduced from 850°C to 600°C in 15 minutes.

IV-2-H TIME LAG EXPERIMENT

The time delay between switching the reducing gas into the furnace and the complete replacement of the preheat gas around the sample, was investigated. The furnace tube was sealed at the top with a rubber bung and a glass tube was set in this bung so that its end was in the sample zone. This glass tube was then connected to a conductivity cell so that gases passing through it were fed over two branches of a four branch thermistor circuit.

A steady flow rate of nitrogen was passed into the furnace and through the glasstube to the thermistors. The other side of the thermistor circuit acted as a reference, argon being used as a carrier gas. The cell currents were then balanced so that a steady base line was maintained on the output recorder.

When steady state had been reached, a preset flow rate of hydrogen was switched into the furnace and the nitrogen flow bypassed. The difference in flow rate and thermal conductivity of the hydrogen stream caused a miss-match in the balanced thermistor circuit, leading to a deflection on the ouput recorder. The time required for a new steady value to be shown on the recorder, corresponding to

complete replacement, was noted. This experiment was repeated for various hydrogen flow rates.

The results of these experiments are shown in Section V-2-A.

IV-2-1

DETERMINATION OF TEMPERATURE GRADIENT IN SOLID

The difference between the temperature at the sphere centre and sphere surface during reduction was investigated. An NiO sphere was prepared with a mineralally insulated thermocouple compacted in the centre of the sphere and another compacted just under the sphere surface. After burning off the binder and soaking at 750°C in the usual manner, the sphere was suspended in the reduction furnace and heated to approximately 650°C. The e.m.f. of both thermocouples was fed to a two-pen recorder, the initial signal having been checked with a potentiometer. The sphere was reduced in hydrogen and the two solid temperatures recorded.

The result of this experiment is shown in Section V-2-B.

CHAPTER V

EXPERIMENTAL RESULTS.

V-1 DIFFUSION RESULTS

V-1-A MASS TRANSFER RESULTS

V-1-A-1 EXTERNAL MASS TRANSFER

V-1-A-1a ANALYSIS OF EXPERIMENTAL MEASUREMENTS

Mass transfer coefficients were determined from napthalene evaporation measurements according to the equation

$$\alpha_o = \frac{\dot{n}\, RT}{A\, \Delta p}$$

where $\dot{n}$ is the rate of weight loss of naphthalene in molar units and A is the surface area of the sphere minus the cross-sectional area of the shaft. Δp is the effective driving force for evaporation given as the equilibrium vapour pressure of naphthalene, $p_{v.p.}$, at the temperature, T, minus the average bulk partial pressure of naphthalene. Thus

$$\Delta p = p_{v.p.} - \frac{\dot{n}}{2Q} p_o$$

where Q is also measured in molar units.

As the total elapsed time for each run was at least four hours, temperatures were read from the record of the gas thermocouple output as averages for each half hour interval. Equilibrium vapour pressures of naphthalene were calculated for each of these temperatures from the equation[89].

$$\log_{10} \text{Vapour Pressure (mmHg)} = 11.55 - \frac{3765}{^oK} \quad .... \text{(V-1)}$$

The vapour pressures thus determined and the temperature readings were then averaged to determine mean values to be used in the calculation of the mass transfer coefficients. The diffusivity of naphthalene into the flowing air stream was assumed to be constant over the narrow temperature range encountered ($\pm$ 3°C) and was taken as 0.0611 cm^2/sec[89]. The property values used in the calculation of the Reynolds and Schmidt numbers were calculated assuming the bulk gas composition to be that of the feed gas.

V-1-A-1b RESULTS

The results of the external mass transfer coefficient experiments are shown in Fig. V-1-1, where LOG ($\frac{Sh - 2.0}{Sc^{\frac{1}{3}}}$) is shown as a function of LOG (Re). The line drawn through the experimental points is that given by the computer for a least squares linear correlation. The slope and intercept calculated from this correlation lead to the following equation for the external mass transfer coefficient in the experiments:

$$Sh = 2.0 + 2.33\ Re^{0.3385} Sc^{\frac{1}{3}} \qquad \ldots\ldots\ldots \text{(V-2)}$$

V-1-A-2 INTERNAL MASS TRANSFER RESULTS

V-1-A-2a Analysis of Experimental Measurements

The internal mass transfer coefficients were calculated from the experimentally measured naphthalene evaporation rates in substantially the same way as the external coefficients. However, the definition of the driving force for mass transfer was slightly altered.

i) First Determination

The measurement of the internal mass transfer coefficient for the first exit spacing of the diffusion shaft was carried out using air as the flowing gas stream. In the results shown here, the driving force for mass transfer was defined as the vapour pressure of naphthalene as given by equation V-1 .. These results were later recalculated using a driving force defined as the equilibrium vapour pressure of naphthalene at temperature T minus the exit bulk partial pressure of naphthalene and therefore

$$\Delta p = \text{pv.p.} - \frac{\dot{n}}{Q} p_o$$

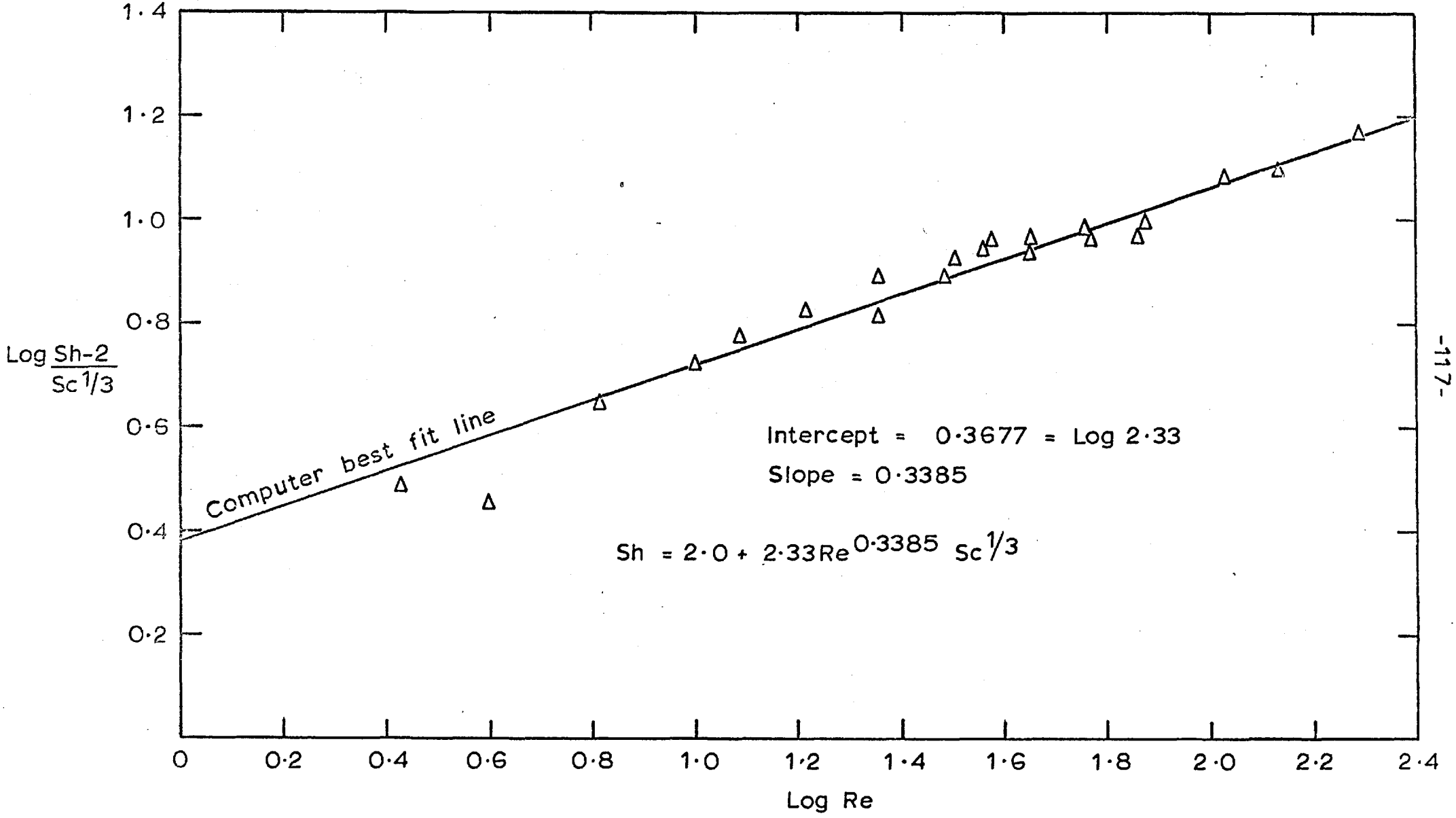


Fig. V-1-1. LOG $Sh-2/Sc^{1/3}$ vs. LOG Re. EXTERNAL MASS TRANSFER.

The exit composition is used because the internal cavity is assumed to be perfectly mixed.

Unfortunately, the correlation of these recalculated values was very poor. This was attributed to evaporation of napthalene vapour through the external surface coating. Consequently, the results of these experiments were applied only in a modified form to the porous iron diffusion measurements.

ii) Second Determination

The naphthalene evaporation experiment was repeated for the final exit spacing of the diffusion shaft using hydrogen and carbon dioxide as the flowing gas streams. The driving force used in the calculations was defined similarly to that previously described. Thus

$$\triangle p = pv.p. - \frac{\dot{n}}{Q} p_o$$

where again perfect internal mixing is assumed. The flow rates of hydrogen and carbon dioxide were similar to those encountered in the diffusion experiments. Diffusion coefficients for the $C_{10}H_8 - H_2$ and $C_{10}H_8 - CO_2$ systems were determined by an interpolative technique applied to the values of the binary diffusion coefficients shown in Perry[90].

These were also assumed to remain constant over the small temperature changes encountered.

Values used were:

$$C_{10}H_8 - H_2 = 0.25 \frac{cm^2}{sec}$$

$$C_{10}H_8 - CO_2 = 0.041 \frac{cm^2}{sec}$$

The results of this second determination of the internal mass transfer coefficients are applied directly to the nickel diffusion measurements.

V-1-A-2b RESULTS

i) First determination

The results of the first series of internal mass transfer measurements are shown in Figure V-1-2, where the mass transfer coefficient, α_i, is shown as a function of the internal air flow rate. It must again be pointed out that the equation shown on the figure is not the same as that used in the porous iron diffusion measurements. Unfortunately, this latter value could be arrived at only by a more or less educated guess. In any event, the final form of the equation used in the diffusion calculations was

$$Sh = 9.00 + 0.05\ Re\ Sc^{\frac{1}{3}} \qquad \ldots\ldots\ldots \text{(V-3-a)}$$

ii) Second determination

The results of the second series of internal napthalene evaporation experiments are shown in Figure V-1-3, where LOG $\frac{Sh-3.0}{Sc^{\frac{1}{3}}}$ is shown as a function of the log of the internal Reynolds number. The characteristic dimension used in the Reynold's number calculation was the internal sphere diameter, and the velocity used was the diffusion shaft exit velocity. The constant, 3.0, in the ordinate was determined as the intercept of the mass transfer vs. Reynold's number curve. From the slope and intercept of Figure V-1-3, the expression for the internal mass transfer coefficient is of the form

$$Sh = 3.0 + 0.0138\ Re\ Sc^{\frac{1}{3}} \qquad \ldots\ldots\ldots \text{(V-3-b)}$$

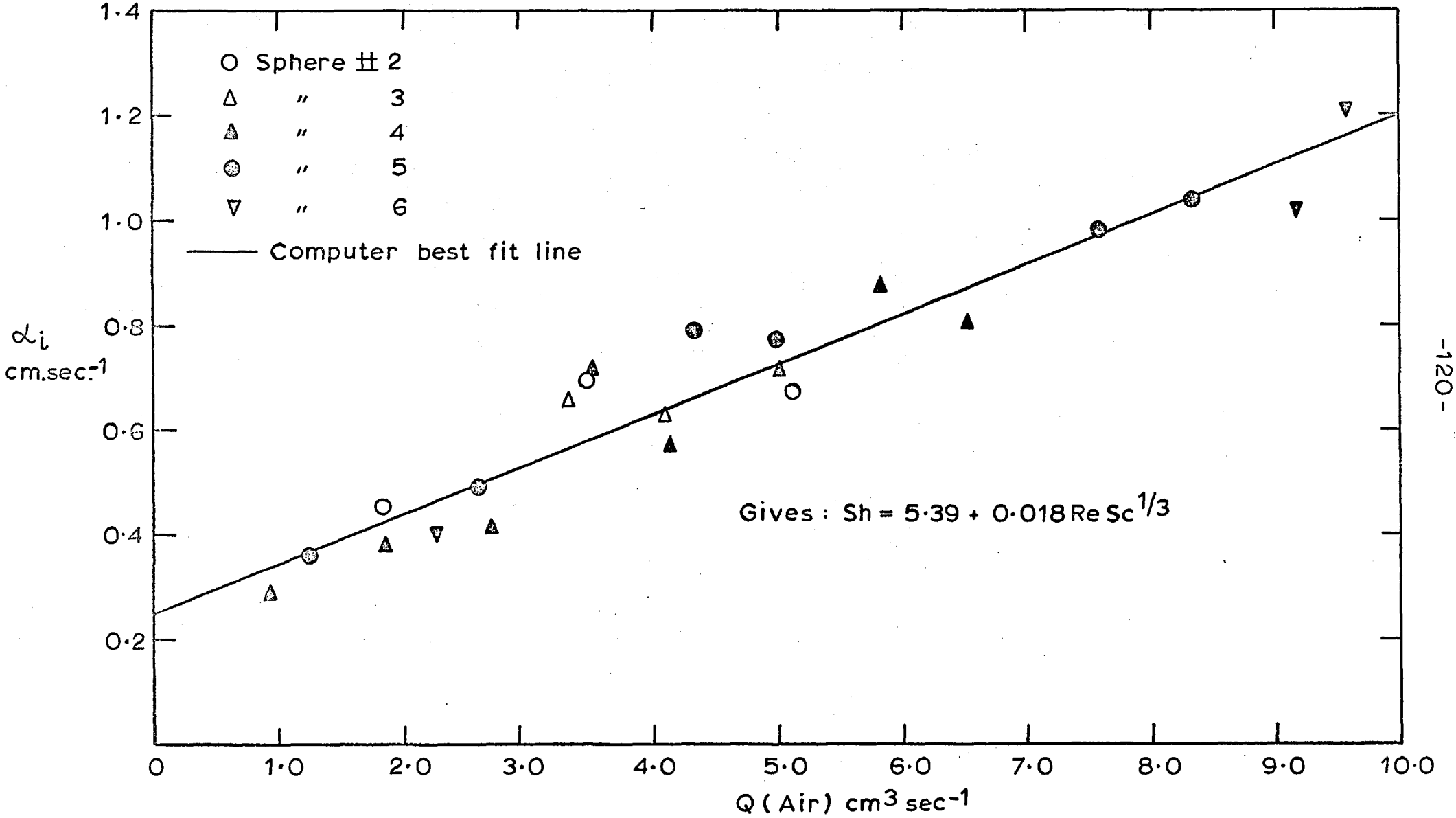


Fig.V-1-2. RESULTS OF FIRST DETERMINATION OF INTERNAL MASS TRANSFER COEFFICIENT

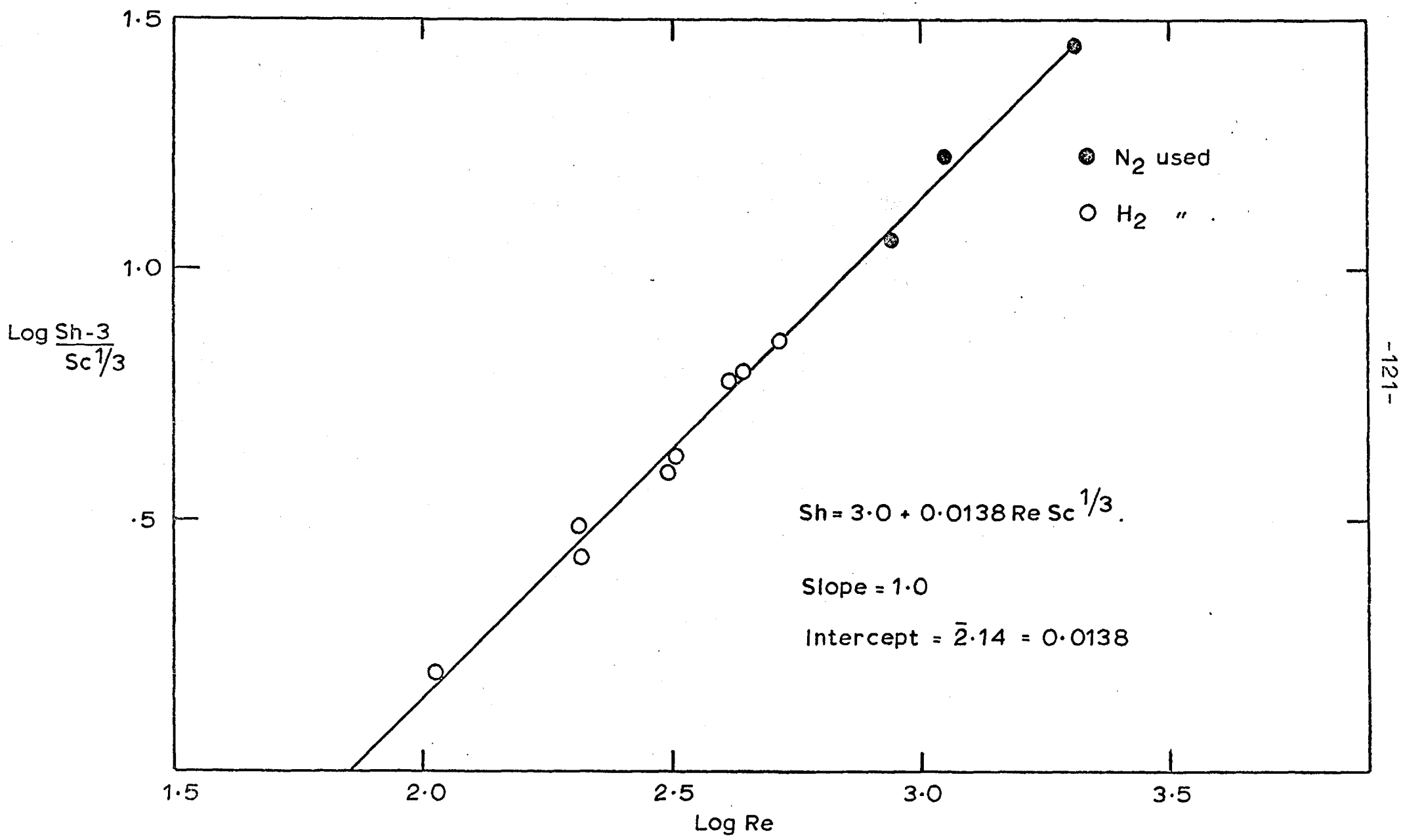


Fig.V-1-3. LOG $\frac{Sh-3}{Sc^{1/3}}$ vs. LOG Re SECOND DETERMINATION

V-1-B PERMEABILITY MEASUREMENTS

V-1-B-1 Analysis of Experimental Measurements

The hydrogen permeability of the various product solids was calculated from

$$K_{H2} = \frac{\dot{n}_{H2}\, RT}{S\ \Delta p_{H2}}$$

where S = shape factor for hollow sphere including shaft area

$$= \frac{3.80\ \pi\ r_i r_o}{r_o - r_i}$$

and Δp_{H2} is the absolute pressure difference across the porous shell (atm).

Values of K were determined for several different values of p_s (system pressure) for each sphere where, for the gas flowing inwards,

$$p_s = \frac{p_i + (p_i + \Delta p)}{2} \quad .$$

The Knudsen diffusion coefficient, D_{H2K}, was taken as the value of K when the system pressure was zero. Thus the intercept of a K vs. p_s curve was equal to D_{H2K}. Knudsen diffusion coefficients for other gases through any particular layer were calculated according to equation II-1.-1.

V-1-B-2 RESULTS

Typical relationships between system pressure and permeability for the various product solids are shown graphically in Figures V-1-4, V-1-5, V-1-6. The results of permeability measurements are tabulated along with the diffusion results for the three different product solids in Tables V-1, V-4 and V-7.

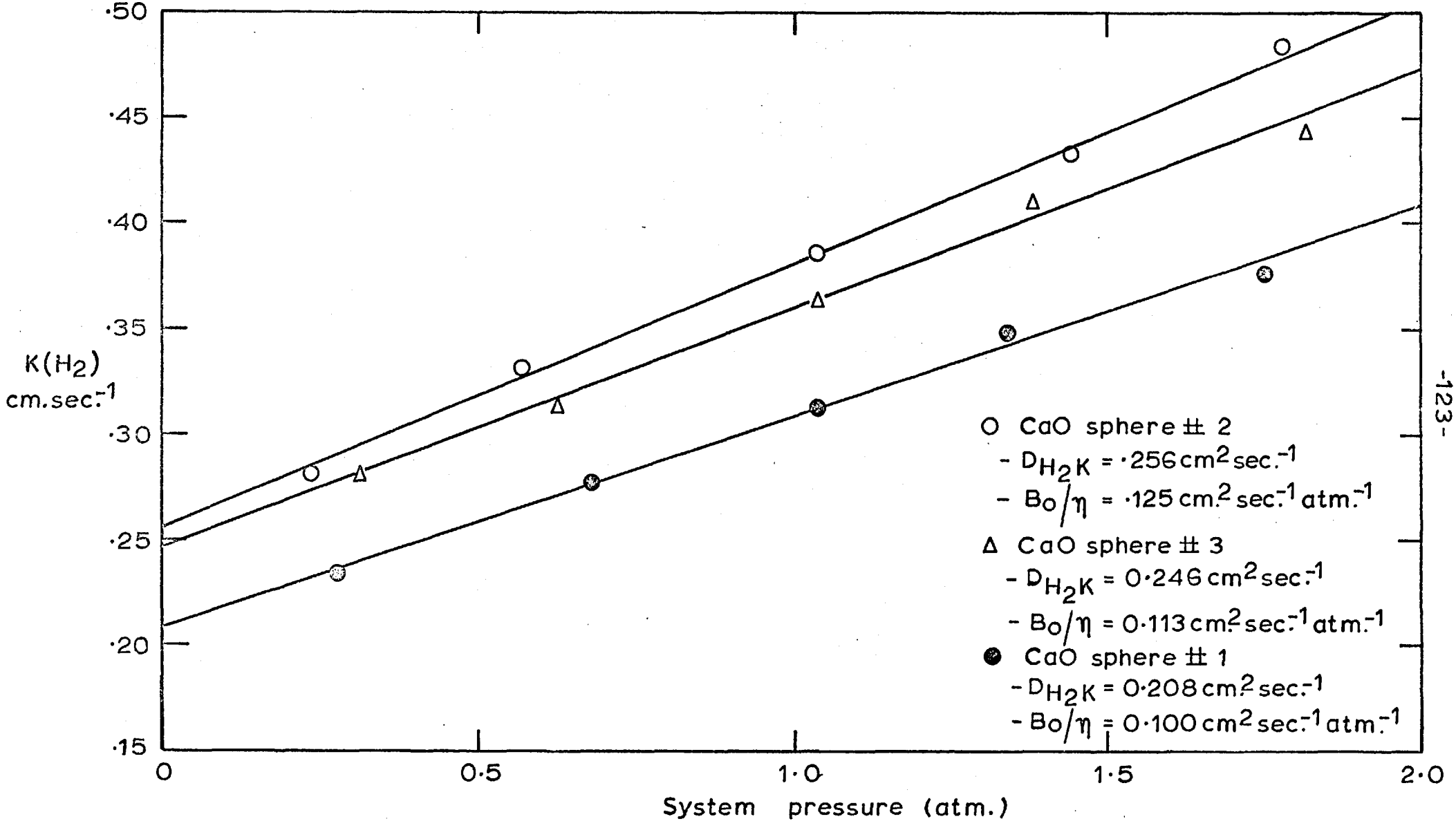


Fig.V-1-4. PERMEABILITY vs. TOTAL PRESSURE FOR LIME SPHERES

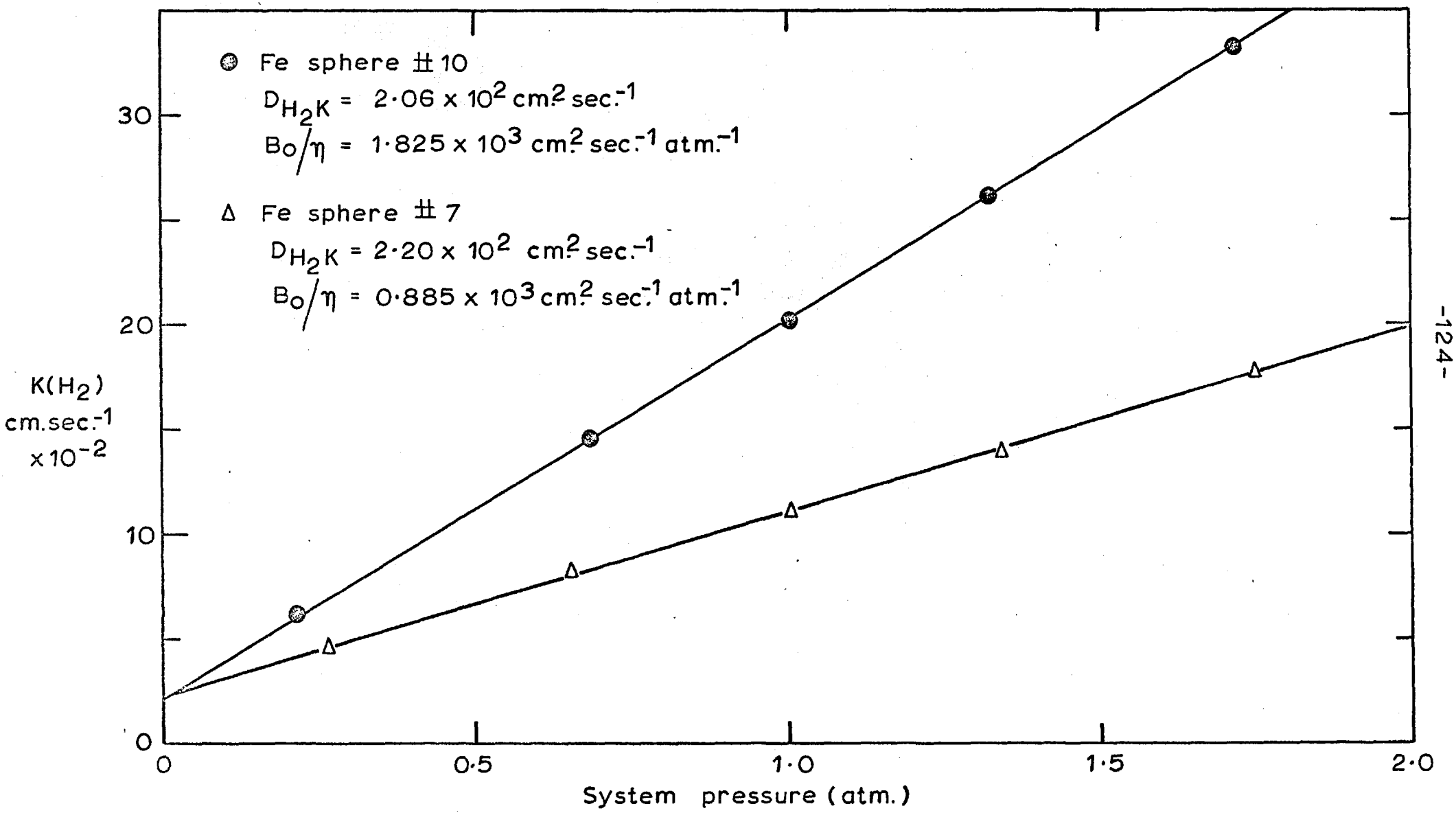


Fig. V-1-5. PERMEABILITY vs. TOTAL PRESSURE FOR IRON SPHERES.

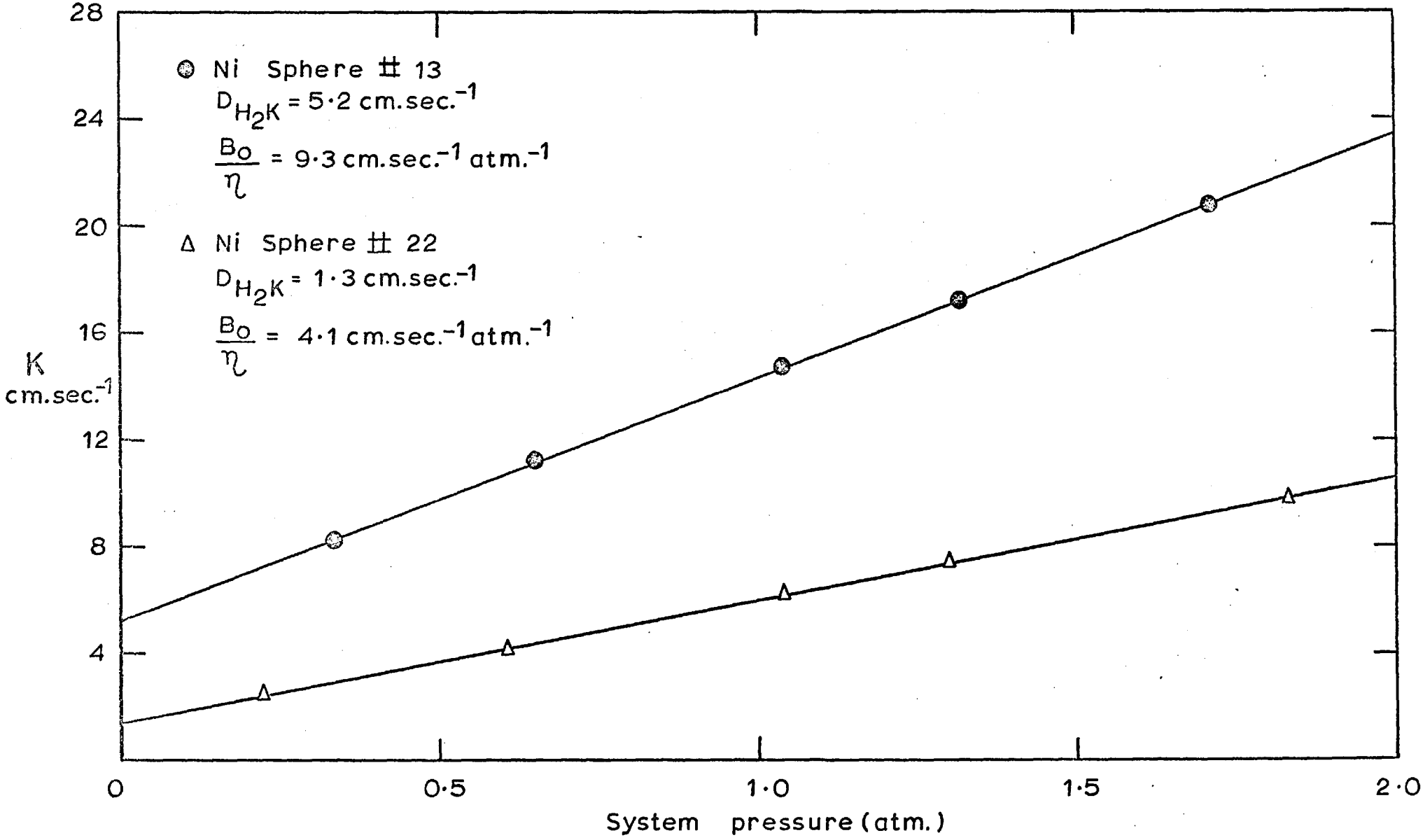


Fig. V-1-6. PERMEABILITY vs. TOTAL PRESSURE FOR NICKEL SPHERES

V-1-C DIFFUSION MEASUREMENTS

V-1-C-1 FIRST TECHNIQUE

V-1-C-1a Analysis of Experimental Measurements

Assuming equi-molar counter-diffusion, the flux of GAS I from the outside bulk gas to the inside bulk gas is given by three separate equations

i) External Mass Transfer

$$\dot{n}_I = \frac{A_o \alpha_o \left([p_I]_{o,b} - [p_I]_{o,s} \right)}{RT}$$

$$= \frac{[p_I]_{o,b} - [p_I]_{o,s}}{R_1}$$

ii) Diffusion Across Porous Layer

$$\dot{n}_I = \frac{SD \left([p_I]_{o,s} - [p_I]_{i,s} \right)}{RT}$$

$$= \frac{[p_I]_{o,s} - [p_I]_{i,s}}{R_2}$$

iii) Internal Mass Transfer

$$\dot{n}_I = \frac{A_i \alpha_i \left([p_I]_{i,s} - [p_I]_{i,b} \right)}{RT}$$

$$= \frac{[p_I]_{i,s} - [p_I]_{i,b}}{R_3}$$

These equations may be combined in order to eliminate intermediate partial pressures.

Thus

$$\dot{n}_I = \frac{\Delta p_I}{RT \left\{ \frac{1}{A_o \alpha_o} + \frac{1}{SD} + \frac{1}{A_i \alpha_i} \right\}}$$

where $\Delta p_I = [p_I]_{o,b} - [p_I]_{i,b}$

and $\dot{n}_I$ and Δp_I were determined as shown in Section IV-1-B-1b.

Thus the ratio $\frac{\Delta P_I}{\mathring{n}_I}$ was a measure of the total resistance to the flux of GAS I, and was made up of three series resistances R_1, the external mass transfer resistance, R_2, the diffusive resistance and R_3, the internal mass transfer resistance. When this ratio was calculated from the experimental results, and plotted as a function of internal gas flow rate, $(Q_{II})i$, a curve of the form shown in Figure V-1-7 was obtained. It was assumed that the level portion of the curve, at high values of $(Q_{II})i$, corresponded to sufficiently high values of the internal mass transfer coefficient that its contribution to the overall resistance could be neglected. The contribution of the external mass transfer to the total resistance was approximately constant. Since it was such a small portion of the total resistance, it could be calculated with sufficient accuracy for these experiments using the Frossling equation.

Consequently, only that portion of the total resistance associated with diffusion remained. Thus, the effective diffusivity of GAS I in the porous layer was given by

$$D_{ieff} = \frac{RT}{R_2 S}$$

where S again includes a correction for the presence of the shaft.

V-1-C-1b RESULTS

Experimental curves of $\sum R$ vs. $(Q_{II})i$ are given in Figure V-1-8. The determined values of the effective diffusion coefficient of CO_2 in porous lime at reaction temperatures are shown in Table V-1.

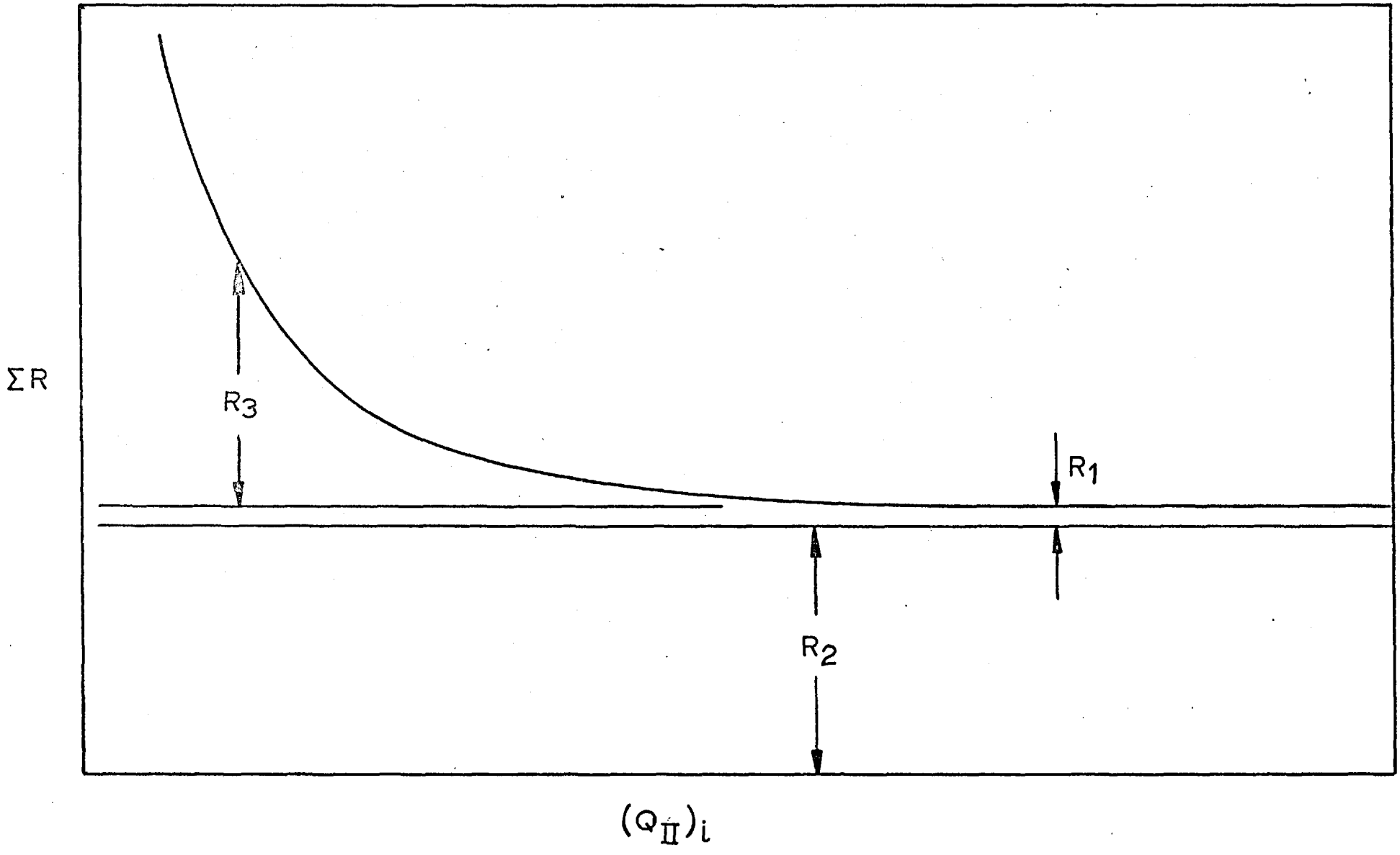


Fig. V-1-7. PLOT OF TOTAL RESISTANCE vs. INTERNAL FLOW RATE

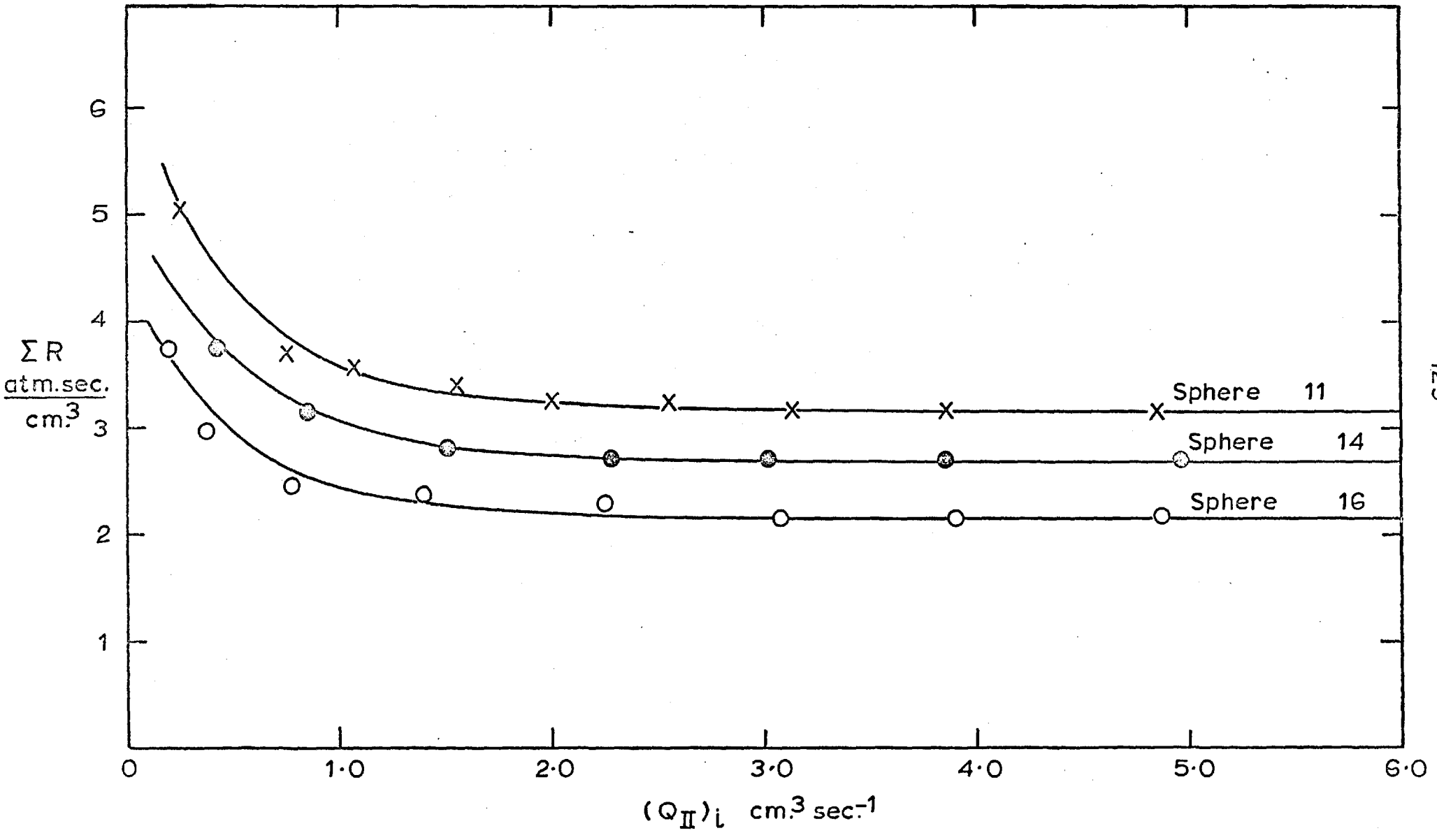


Fig. V.1.8a. TOTAL RESISTANCE vs. INTERNAL FLOW RATE FOR LIME SPHERES

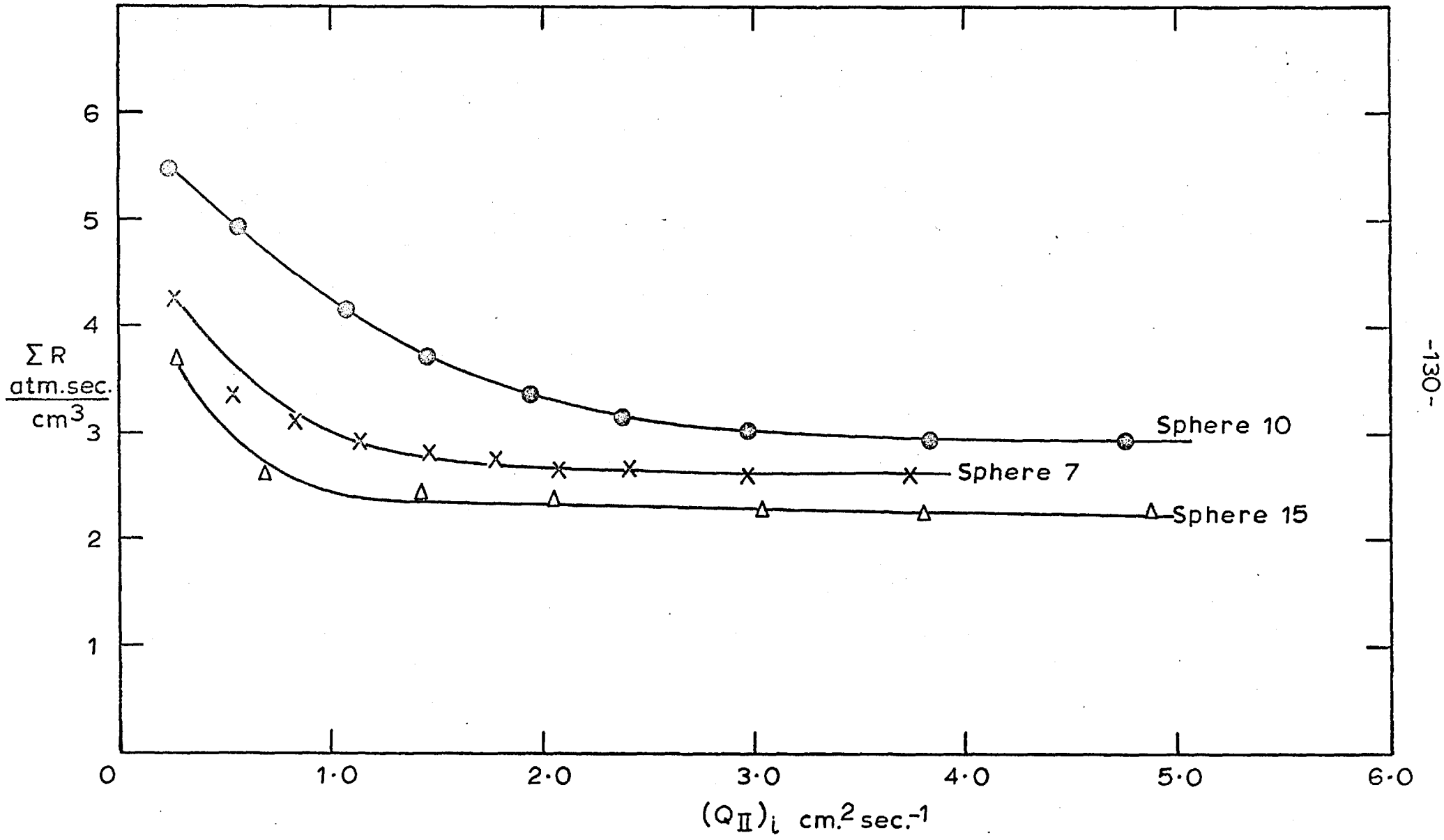


Fig. V-1-8b TOTAL RESISTANCE vs. INTERNAL FLOW RATE FOR LIME SPHERES

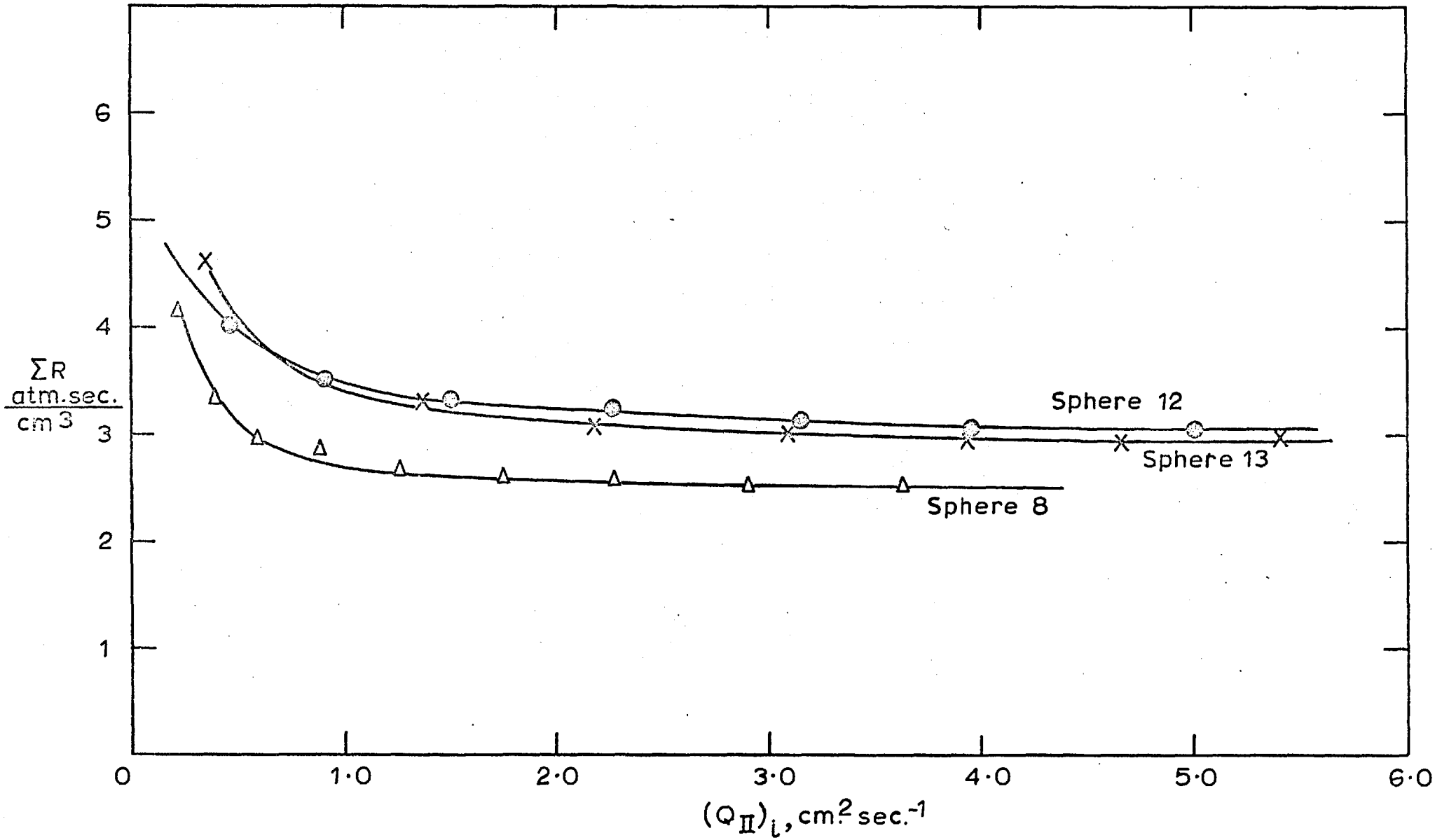


Fig.Ⅴ-1-8c. TOTAL RESISTANCE vs. INTERNAL FLOW RATE FOR LIME SPHERES

TABLE V-1 RESULTS OF DIFFUSION AND PERMEABILITY MEASUREMENTS ON LIME SPHERES.

Sphere	Compacting Pressure	ϵ_{CaCO_3}	ϵ_{CaO}	Internal CaO Radius mm.	External CaO Radius mm.	D_{AR-CO_2} at 950°C X10	D_{CO_2} at 950°C	Bo $\frac{cm.gm.}{sec.atm.}$
1	450kN/m^2	21.1%	48.1%	5.96	10.8	-	0.0925 $\frac{cm^2}{sec}$	8.7×10^{-6}
2	250kN/m^2	27.0%	53.2%	5.81	10.4	-	0.114 $\frac{cm^2}{sec}$	10.9×10^{-6}
3	350kN/m^2	23.9%	51.0%	5.88	10.3	-	0.109 $\frac{cm^2}{sec}$	9.8×10^{-6}
6	500kN/m^2	19.8%	44.2%	5.49	9.23	0.803 $cm.sec^{-1}$	-	-
7	450kN/m^2	20.8%	49.6%	5.87	10.13	0.958 $cm.sec^{-1}$	-	-
8	400kN/m^2	22.8%	51.0%	5.72	10.06	1.05 $cm.sec^{-1}$	-	-
10	450kN/m^2	21.6%	45.9%	5.61	9.77	0.906 $cm.sec^{-1}$	-	-
11	450kN/m^2	21.7%	47.3%	5.68	9.93	0.860 $cm.sec^{-1}$	-	-
12	400kN/m^2	23.2%	49.1%	5.58	9.83	0.911 cm^2sec^{-1}	-	-
13	350kN/m^2	24.2%	51.0%	5.63	9.96	0.955 cm^2sec^{-1}	-	-
14	300kN/m^2	25.7%	52.8%	5.59	9.96	1.05 cm^2sec^{-1}	-	-
15	250kN/m^2	27.3%	53.6%	5.70	10.27	1.23 cm^2sec^{-1}	-	-
16	200kN/m^2	29.3%	54.5%	5.63	10.10	1.28 cm^2sec^{-1}	-	-

V-1-C-2 MODIFIED TECHNIQUE

V-1-C-2a Analysis of Experimental Results

i) Flux Equations

The equations describing the fluxes of GAS I and GAS II across the porous iron and nickel spheres involved when using the modified technique were not so easily formulated as the corresponding equations for the initial technique. The conditions were made more complex by the smaller diffusion resistance and because the counter-current diffusion was no longer assumed to be equi-molar. Also, both Knudsen and molecular diffusion may have been operative in the porous layers concerned.

Considering GAS I diffusing outwards against a counter-flux GAS II, the flux of GAS I is described by each of three independent equations i.e. one equation describing mass transfer across the external boundary layer, another describing mass transfer across the internal boundary layer, and a third describing the diffusive flux across the porous layer. In order to solve the third equation, the concentration of GAS I at the internal and external surfaces must be obtained from the solution of the corresponding mass transfer equations.

The significance of the symbols used in these equations may be more easily understood with reference to Figure V-1-9.

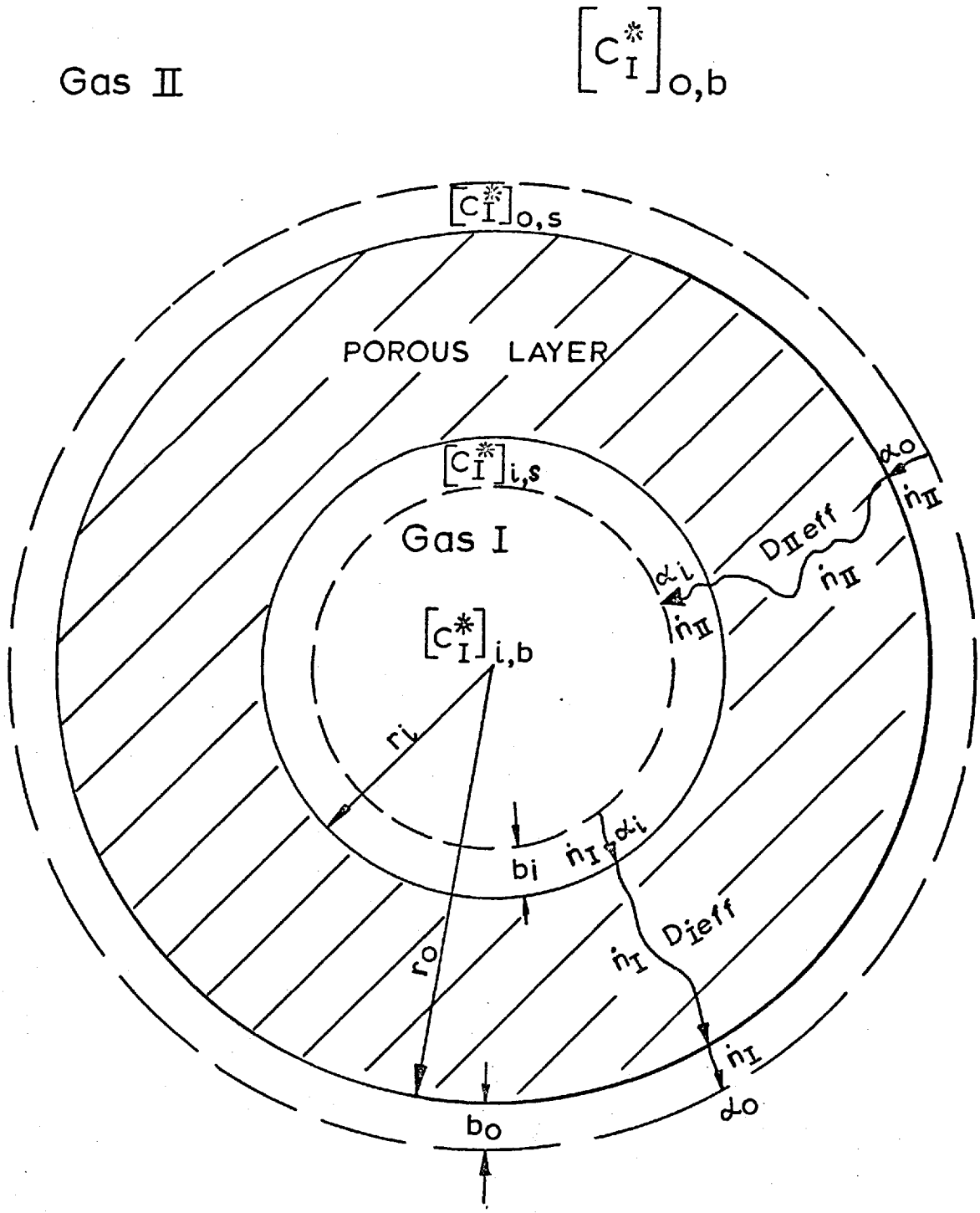


Fig.V-1-9. SIGNIFICANCE OF VARIABLES

MASS TRANSFER ACROSS EXTERNAL BOUNDARY LAYER

This is an example of non-limiting mass transfer in a binary mixture of constant molar density i.e. constant pressure.

FOR GAS I DIFFUSING OUTWARDS AGAINST A FLUX OF GAS II

Define β_I such that

$$-\beta_I = \frac{[\dot{n}''_{II}]}{[\dot{n}''_{I}]} = \frac{[\dot{n}_{II}]}{[\dot{n}_{I}]}$$

Therefore from Fick's first law we have, for a plane surface

$$\dot{n}''_I = -C_T D_{I,II} \frac{d C^*_I}{dx} + \dot{n}''_I (1-\beta_I) C^*_I \quad \ldots\ldots (V\text{-}5)$$

(diffusive term) (bulk flow term)

For spherical geometry the flux per unit area, $\dot{n}''$, is not constant, but, $\dot{n}$, the total flux is. Therefore, including the diffusion area in equation (2) and integrating across the boundary layer, we have

$$\dot{n}_I = \frac{C_T\, 4\pi r_o^2\, D_{I,II}}{b_o\,(1-\beta_I)} \ln \left\{ \frac{1 - (1-\beta_I)[C^*_I]_{o,b}}{1 - (1-\beta_I)[C^*_I]_{o,s}} \right\}$$

but $\alpha_o = \frac{D_{I,II}}{b_o}$

Thus

$$\dot{n} = \frac{C_T\, 4\pi r_o^2\, \alpha_o}{(1-\beta_I)} \ln \left\{ \frac{1 - (1-\beta_I)[C^*_I]_{o,b}}{1 - (1-\beta_I)[C^*_I]_{o,s}} \right\} \quad \ldots\ldots (V\text{-}6)$$

and rearranging

$$[C^*_I]_{o,s} = \frac{1 - (1 - (1-\beta_I)[C^*_I]_{o,b}) \exp\left\{ - \frac{\dot{n}_I (1-\beta_I)}{C_T \alpha_o (4\pi r_o^2 - A_s)} \right\}}{1 - \beta_I} \quad \ldots\ldots (V\text{-}7)$$

where As (= 0.316 cm^2) is the cross-sectional area of the shaft.

MASS TRANSFER ACROSS INTERNAL BOUNDARY LAYER

An analogous treatment leads to an equation expressing the concentration of GAS I at the internal sphere surface from consideration of the flux across the internal boundary layer, Thus

$$\overline{C^*_I}_{i,s} = \frac{1 - \left(1 - (1-\beta_I)\,\overline{C^*_I}_{i,b}\right) \exp\left[\frac{\dot{n}_I\,(1-\beta_I)}{G\alpha_i(4\pi r_i^2 - A_s)}\right]}{1-\beta_I} \quad \ldots \text{(V-8)}$$

where again the cross-sectional area of the diffusion shaft has been subtracted from the internal surface area.

DIFFUSION ACROSS THE POROUS LAYER

The 'dusty gas' model for diffusion in porous media, as discussed in Chapter II, gave a differential equation describing the flux of a gas diffusing in a ternary mixture of two gases and 'dust' particles for isobaric conditions (Equation II-1-10). This equation is directly analogous to Fick's first law and can be written in terms of the symbols used in this section as

$$\dot{n}''_i = - C_T D_{i,eff} \frac{dC^*_i}{dx} + \dot{n}''_i \delta_i (1-\beta_i)\, C^*_i$$

For flux of GAS I across a spherical layer, this equation becomes

$$\dot{n}_I = - C_T D_{I,eff} 4\pi r^2 \frac{dC^*_I}{dr} + \dot{n}_I \delta_I (1-\beta_I)\, C^*_I \quad \ldots \text{(V-9)}$$

Rearranging equation (V-9) and integrating across the porous layer, we obtain

$$\dot{n}_I = \frac{C_T D_{I,eff} 4\pi r_i r_o}{\delta_I(1-\beta_I)(r_o - r_i)} \ln\left\{\frac{1 - \delta_I(1-\beta_I)\overline{C^*_I}_{o,s}}{1 - \delta_I(1-\beta_I)\overline{C^*_I}_{i,s}}\right\} \quad \ldots\ldots \text{(V-10)}$$

But $$\delta_I = \left[1 + \frac{D_{I,II,eff}}{D_{I,K}} \right]^{-1} \quad \ldots\ldots \text{(V-11)}$$

and $$D_{I,eff} = \left[D_{I,II,eff}^{-1} + D_{I,K}^{-1} \right]^{-1} \quad \ldots\ldots \text{(V-12)}$$

Substitution of equations V-11 and V-12 into equation V-10 and some rearrangement yields

$$D_{I,IIeff} = \frac{\frac{\mathring{n}_I (1-\beta_I) r_o - r_i}{C_T (4\pi r_o r_i - As.)}}{Ln\left\{ \frac{1 - \delta_I(1-\beta_I)[C^*_{I-o,s}]}{1 - \delta_I(1-\beta_I)[C^*_{I-i,s}]} \right\}} \quad \ldots\ldots \text{(V-13)}$$

which describes the effective binary diffusion coefficient of GASES I and II in the porous layer in terms of the observed fluxes, calculated compositions, sphere geometry, and a Knudsen-molecular diffusion parameter.

The equations describing the flux of GAS II inward are exactly analogous to these provided the subscripts are interchanged.

ii) EVALUATION OF VARIABLES FOR EQUATIONS V-7, V-8 and V-13

Compositions

The calculation of values for the variables which occur in the foregoing equations required some assumptions as to the nature of the internal and external flows. It was assumed, in this treatment, that the average composition around the outside of the sphere was the arithmetic mean of the external inlet and exit compositions. It was also assumed, because of the high velocity of the internal gas flow, that the internal gas was perfectly mixed so that the average concentration was that of the exit stream.

Thus $\left[C^*_I\right]_{o,b} = \left[C^*_I\right]_{o,b\ meas} / 2.0$

and $\left[C^*_I\right]_{i,b} = \left[C^*_I\right]_{i,b\ meas}$.

MASS TRANSFER COEFFICIENTS

As outlined in Section I-A of this chapter, independent evaluation of the mass transfer coefficients yielded correlations of the form

$$Sh = A + B\ Re^n\ Sc^{\frac{1}{3}}$$

or

$$\alpha = \frac{D_{I,II}}{2r}\left\{A + B\left[\frac{u_f \rho_f d}{\mu_f}\right]^n\left[\frac{\mu_f}{\rho_f D}\right]^{\frac{1}{3}}\right\}$$

However, the Reynolds number should express the ratio of the inertial to the viscous forces. Under these experimental conditions, the changing compositions make the above expression invalid, as the inertial forces are supplied by the feed stream and the viscous forces by the bulk stream. The inertial forces should be evaluated for feed stream conditions and the viscous forces for the average bulk gas composition. Thus the expression for the modified Reynolds number becomes

$$Re_m = \frac{\sqrt{\rho_f \rho_b}\ u_f\ d}{\mu_b}$$

where ρ_f is the feed gas density

ρ_b is the density of gas mixture at the bulk composition

u_f is the approach velocity of the feed stream

d is the sphere diameter

μ_b is the viscosity of the gas mixture at the bulk composition.

The Schmidt number was evaluated at the bulk gas composition. Therefore, considering hydrogen diffusing outwards against a counter-flux of argon, the expression for the internal mass transfer coefficient becomes (from equation V-3)

$$\alpha_i = \frac{D_{H2\text{-}Ar}}{2r_i}\left[3.00 + 0.0138\left[\frac{\sqrt{\rho_{H_2}\,\rho_{i,b}}\;u_J\;2r_i}{\mu_{i,b}}\right]\left[\frac{\mu_{i,b}}{\rho_{i,b} D_{H2\text{-}A_R}}\right]^{\frac{1}{3}}\right]$$

FLUXES

The flux of GAS I, $\dot{n}_I$, is given by its concentration in the external stream times the external exit flow rate. This flow rate is given by the entrance flow rate plus the flux of GAS I minus the flux of GAS II. Thus

$$\dot{n}_I = \left[C^*_I\right]_{o,b}\left\{(Q_{II})_o + (Q_I)_i - \left[C^*_I\right]_{i,b}(Q_{I,II})_i - (Q_{I,II})_i\left[C^*_{II}\right]_{i,b}\right\}$$

where $\left[C^*_I\right]_{i,b} = 1.0 - \left[C^*_{II}\right]_{i,b}$

The flux of GAS II, $\dot{n}_{II}$, is given by the concentration of GAS II in the internal stream times the exit flow rate of the internal stream. Thus

$$\dot{n}_{II} = \left[C^*_{II}\right]_{i,b}(Q_{I,II})_i$$

iii) COMPUTATION

A computer programme was written to evaluate mass transfer coefficients and fluxes according to the previous expressions. Using these values, the programme calculated surface concentrations from equations V-7 and V-8 for use in equation V-13. Equations V-11 and V-13 were then solved simultaneously for $D_{I,IIeff}$, by an iterative procedure until the difference between the effective diffusion coefficients values, $D_{I,II,eff}$, from these two equations was sufficiently small ($\pm$ 0.0001). The programme calculated the effective binary diffusivity on the basis on the flux of GAS I and also on the basis of the flux of GAS II.

iv) REVERSAL OF DIFFUSION DIRECTION

When the diffusion direction was reversed, i.e. the gas previously fed into the hollow sphere was fed over the outside of the sphere and vice versa, the equations describing the fluxes of the diffusing species were the same as those given above. However, the property values of GAS I and GAS II had to be redefined, the internal gas always being defined as GAS I and the external gas as GAS II.

V-1-C-2b RESULTS FOR POROUS IRON

All experimental data for the diffusion measurements on porous iron are given in Table V-2.* A sample set of computed results for sphere number 1 and the resultant effective binary diffusion coefficient calculated from measured data are shown in Table V-3.* The results of all porous iron diffusion measurements are summarized in Table V-4 where the effective diffusivities were calculated by averaging the values calculated for this parameter at the various flow rates.

V-1-C-2c RESULTS FOR POROUS NICKEL

All experimental data determined during diffusion measurements on porous nickel are shown in Table V-5*. A complete set of computed results for sphere number 17 is shown in Table V-6.* The results for all the nickel spheres are summarized in Table V-7 where the effective diffusivities are quoted as average values of all determinations.

---

* FOOTNOTE:
The meanings of the column headings used in Tables V-2,V-3,V-5,V-6 are as follows.

COMOB - Measured exit dimensionless concentration of external bulk stream (GAS I).
COMIB - Measured exit dimensionless concentration of internal bulk stream (GAS I).
FLO1S - Flow rate, in cm^3/sec of GAS I into hollow sphere.
FLO2T - Flow rate, in cm^3/sec of GAS II into external tube.
FLO12S Flow rate, in cm^3/sec of exit gas mixture from hollow sphere.
PRESS - Bulk pressure on either side of porous layer. (mm. Hg)
DELTAP- Pressure difference between external gas stream and internal gas stream (po-pi). (IN w.g.x 1000)
DEFF12- Effective binary diffusion coefficient of GAS I and II in porous layer.
CONIB - Calculated average internal bulk concentration of GAS I.
CONIS - Calculated internal surface concentration of GAS I.
CONOS - Calculated external surface concentration of GAS I.
CONOB - Calculated external bulk concentration of GAS I.
DELTA - Parameter indicating relative importance of Knudsen diffusion in porous layer (Equation II-1-12).
FLUX1 - Flux in moles per sec. of gas I outwards across the porous layer.
FLUX2 - Flux in moles per sec. of gas II inwards across the porous layer.
BETA - Flux ratio of diffusing species, $-\mathring{n}_{II}/\mathring{n}_{I}$.
ALPHAI- Internal mass transfer coefficient.
ALPHAO- External mass transfer coefficient.

TABLE V-2 EXPERIMENTAL DATA OBTAINED IN IRON DIFFUSION EXPERIMENTS

IRON SPHERE NUMBER 1

INTERNAL GAS IS HYDROGEN EXTERNAL GAS IS ARGON

COMOB	COMIB	FLO1S	FLO2T	FLO12S	PRESS	DELTAP
0.1660	0.7480	10.130	33.700	5.300	769.0	2.0
0.1700	0.8060	12.730	33.500	7.360	772.0	4.0
0.1980	0.8400	16.350	33.100	10.530	778.0	1.0
0.2100	0.8670	20.000	33.330	13.530	785.0	5.0
0.2240	0.8860	24.000	33.730	16.850	795.0	2.0

INTERNAL GAS IS ARGON EXTERNAL GAS IS HYDROGEN

COMOB	COMIB	FLO1S	FLO2T	FLO12S	PRESS	DELTAP
0.0204	0.1950	1.500	48.800	4.970	767.0	-3.0
0.0233	0.2430	2.150	49.700	6.400	771.0	-3.0
0.0260	0.2750	3.200	51.100	7.700	767.0	-5.0
0.0330	0.3440	4.900	50.000	10.480	770.0	-4.0
0.0351	0.3940	6.160	50.700	12.300	773.0	-5.0

****

IRON SPHERE NUMBER 6

INTERNAL GAS IS HYDROGEN EXTERNAL GAS IS ARGON

COMOB	COMIB	FLO1S	FLO2T	FLO12S	PRESS	DELTAP
0.2050	0.8361	15.640	33.150	9.640	777.0	2.0
0.2000	0.8534	18.000	33.670	12.370	784.0	13.0
0.2118	0.8708	20.500	33.330	14.400	788.0	8.0
0.2200	0.8990	25.100	32.670	18.550	774.0	9.0
0.2250	0.9135	29.950	32.670	22.950	778.0	10.0

INTERNAL GAS IS ARGON EXTERNAL GAS IS HYDROGEN

COMOB	COMIB	FLO1S	FLO2T	FLO12S	PRESS	DELTAP
0.0361	0.3320	5.000	51.150	13.210	774.0	-2.0
0.0454	0.3810	7.110	49.870	14.400	776.0	-3.0
0.0520	0.4380	10.410	50.330	18.230	786.0	-7.0
0.0579	0.4950	13.000	50.170	22.000	796.0	-9.0

****

IRON SPHERE NUMBER 7

INTERNAL GAS IS HYDROGEN EXTERNAL GAS IS ARGON

COMOB	COMIB	FLO1S	FLO2T	FLO12S	PRESS	DELTAP
0.1570	0.7200	10.000	33.330	6.180	771.0	3.0
0.1770	0.7790	13.090	34.150	8.330	776.0	0.0
0.1990	0.8299	16.830	33.900	11.810	783.0	-2.0
0.2120	0.8637	20.750	34.100	14.540	791.0	-5.0
0.2270	0.8887	24.350	32.650	17.570	774.0	-8.0
0.2330	0.9032	29.500	33.650	21.950	777.0	-10.0

INTERNAL GAS IS ARGON EXTERNAL GAS IS HYDROGEN

COMOB	COMIB	FLO1S	FLO2T	FLO12S	PRESS	DELTAP
0.0330	0.3120	5.450	53.330	12.570	774.0	-7.0
0.0451	0.3760	8.970	47.150	13.540	775.0	-22.0
0.0471	0.4080	8.750	50.850	16.190	781.0	-20.0
0.0521	0.4350	10.170	49.650	17.830	785.0	-20.0
0.0550	0.4750	12.300	49.330	21.200	794.0	-13.0
0.0575	0.4960	13.700	51.330	22.350	799.0	-24.0

****

TABLE V-2 Cont.....

IRON SPHERE NUMBER 8

INTERNAL GAS IS HYDROGEN EXTERNAL GAS IS ARGON

COMOB	COMIB	FLO1S	FLO2T	FLC12S	PRESS	DELTAP
0.1680	0.7060	10.000	32.750	5.450	770.0	-6.0
0.1864	0.7280	12.920	33.330	7.440	774.0	-10.0
0.2090	0.8175	16.900	33.650	10.600	781.0	-8.0
0.2213	0.8563	20.650	33.750	14.110	790.0	-10.0
0.2340	0.8793	24.660	33.330	17.410	775.0	-10.0
0.2400	0.8942	28.600	33.650	20.750	777.0	-7.0
0.2450	0.9070	32.900	33.650	24.750	761.0	-5.0

IRON SPHERE NUMBER 9

INTERNAL GAS IS HYDROGEN EXTERNAL GAS IS ARGON

COMOB	COMIB	FLO1S	FLO2T	FLC12S	PRESS	DELTAP
0.2030	0.8204	13.600	32.600	7.780	773.0	0.0
0.1972	0.8523	18.330	32.330	13.030	787.0	8.0
0.2170	0.8840	21.950	33.330	15.300	791.0	5.0
0.2260	0.9042	28.750	33.100	21.700	777.0	6.5
0.2415	0.9177	33.700	32.750	25.850	781.0	6.0

INTERNAL GAS IS ARGON EXTERNAL GAS IS HYDROGEN

COMOB	COMIB	FLO1S	FLO2T	FLC12S	PRESS	DELTAP
0.0390	0.3450	6.670	51.700	12.800	774.0	-4.0
0.0498	0.4050	9.410	51.800	16.000	781.0	-5.0
0.0585	0.4800	12.870	50.000	20.330	793.0	-6.0
0.0595	0.5200	16.270	51.850	24.500	784.0	-5.0

IRON SPHERE NUMBER 10

INTERNAL GAS IS HYDROGEN EXTERNAL GAS IS ARGON

COMOB	COMIB	FLO1S	FLO2T	FLC12S	PRESS	DELTAP
0.2020	0.7820	13.730	32.750	7.890	775.0	4.0
0.2215	0.8397	18.250	32.000	11.330	763.0	5.0
0.2270	0.8676	22.250	32.750	15.030	792.0	5.0
0.2400	0.8870	27.850	33.600	19.600	775.0	4.0
0.2500	0.9055	33.400	32.650	24.170	780.0	5.0

INTERNAL GAS IS ARGON EXTERNAL GAS IS HYDROGEN

COMOB	COMIB	FLO1S	FLO2T	FLC12S	PRESS	DELTAP
0.0421	0.3700	7.050	52.150	13.970	777.0	-5.0
0.0471	0.4100	9.140	50.350	17.000	783.0	-6.0
0.0511	0.4520	11.530	52.150	20.000	791.0	-6.0
0.0600	0.5020	13.720	48.650	22.550	799.0	-6.0

TABLE V-3 COMPUTED DATA AND RESULTS FOR IRON SPHERE NO.1 WITH H_2 - AR DIFFUSION COUPLE.

A) HYDROGEN AS INTERNAL GAS (GAS I)

N	DEFF12	FLOIS	CONIB	CONIS	CONOS	CONOB	DELTA H_2	FLUX1 x 10^5	FLUX2 x 10^5	BETA	ALPHAI	ALPHAO
1	0.4180	10.130	0.7480	0.6916	0.2116	0.0830	0.9917	26.17	5.56	0.213	8.912	2.566
2	0.3989	12.730	0.8060	0.7557	0.2307	0.0890	0.9921	28.53	5.96	0.209	9.823	2.564
3	0.4136	16.330	0.8400	0.7933	0.2532	0.0990	0.9918	31.64	7.02	0.222	11.097	2.560
4	0.4178	20.000	0.8670	0.8251	0.2699	0.1050	0.9917	34.64	7.50	0.216	12.432	2.566
5	0.4313	24.000	0.8860	0.8481	0.2877	0.1120	0.9915	38.02	7.99	0.210	13.906	2.576

B) ARGON AS INTERNAL GAS (GASI)

N	DEFF12	FLOIS	CONIB	CONIS	CONOS	CONOB	DELTA Ar	FLUX1 x 10^5	FLUX2 x 10^5	BETA	ALPHAI	ALPHAO
1	0.5128	1.500	0.1950	0.1591	0.0326	0.0102	0.9564	3.85	16.67	4.326	7.772	2.708
2	0.4821	2.150	0.2430	0.2018	0.0375	0.0116	0.9589	4.41	20.19	4.575	8.723	2.713
3	0.5147	3.200	0.2750	0.2317	0.0439	0.0133	0.9562	5.16	23.26	4.504	10.276	2.724
4	0.5152	4.900	0.3440	0.2967	0.0539	0.0165	0.9562	6.11	28.65	4.690	12.801	2.693
5	0.4876	6.160	0.3940	0.3460	0.0577	0.0175	0.9584	6.52	31.06	4.766	14.696	2.697

TABLE V-4 RESULTS OF DIFFUSION AND PERMEABILITY MEASUREMENTS ON IRON SPHERES.

Sphere Number	Compacting Pressure (kN/m^2)	Iron Porosity %	Internal Radius (cm.)	External Radius (cm.)	Reduction Temperature	(D_{H_2-Ar}) eff. H_2 Inside ($cm^2/sec.$)	(D_{H_2-Ar}) eff. Ar Inside (cm^2/sec)	ϵ/a_b	$(D_{H_2})K$ (cm^2/sec)	$\frac{B_o}{cm^2}/\eta$ secatm $x10^{-3}$
1	200	88.0	0.66	1.14	500°C	.4183	.5025	.54	160.0	1.05
6	100	89.5	0.62	1.04	500°C	.4312	.5744	.56	150.0	1.15
7	50	87.8	0.68	1.10	450°C	.4393	.5512	.57	140.0	0.98
8	50	88.0	0.69	1.11	550°C	.3986	-	.52	110.0	0.81
9	100	90.0	0.66	1.07	400°C	.3983	.5454	.52	250.0	2.08
10	100	89.0	0.67	1.07	450°C	.4471	.5685	.58	200.0	1.83

TABLE V-5A EXPERIMENTAL DATA OBTAINED IN NICKEL DIFFUSION MEASUREMENTS WITH H_2-AR DIFFUSION COUPLE

NICKEL SPHERE NUMBER 1

INTERNAL GAS IS HYDROGEN EXTERNAL GAS IS ARGON

COMOB	COMIB	FLO1S	FLO2T	FLO12S	PRESS	DELTAP
0.1365	0.8614	11.580	32.850	7.700	770.0	15.0
0.1465	0.9074	17.670	33.850	13.280	781.0	15.0
0.1572	0.9260	22.000	33.600	17.430	790.0	15.0
0.1702	0.9391	27.850	33.600	22.830	775.0	15.0
0.1732	0.9508	33.500	33.500	27.950	779.0	15.0

NICKEL SPHERE NUMBER 2

INTERNAL GAS IS HYDROGEN EXTERNAL GAS IS ARGON

COMOB	COMIB	FLO1S	FLO2T	FLO12S	PRESS	DELTAP
0.1151	0.8529	8.650	32.400	5.500	767.0	0.0
0.1252	0.9013	12.460	32.150	9.090	771.0	20.0
0.1286	0.9231	15.730	32.330	12.120	777.0	50.0
0.1310	0.9399	20.700	33.830	17.040	786.0	75.0
0.1380	0.9519	25.000	32.830	21.000	773.0	100.0
0.1435	0.9583	29.850	32.750	25.670	777.0	150.0
0.1468	0.9614	33.250	32.500	28.930	780.0	150.0

INTERNAL GAS IS ARGON EXTERNAL GAS IS HYDROGEN

COMOB	COMIB	FLO1S	FLO2T	FLO12S	PRESS	DELTAP
0.0198	0.5430	5.780	49.700	9.150	770.0	-200.0
0.0216	0.5860	7.630	49.850	11.280	775.0	-200.0
0.0227	0.6080	9.750	50.500	13.630	780.0	-250.0
0.0235	0.6695	11.860	50.800	15.830	786.0	-250.0
0.0244	0.7080	13.970	51.200	18.060	793.0	-300.0

NICKEL SPHERE NUMBER 3

INTERNAL GAS IS HYDROGEN EXTERNAL GAS IS ARGON

COMOB	COMIB	FLO1S	FLO2T	FLO12S	PRESS	DELTAP
0.1200	0.8863	11.720	32.170	7.980	771.0	400.0
0.1240	0.9138	14.920	33.500	11.120	777.0	500.0
0.1283	0.9298	18.630	32.830	14.930	784.0	470.0
0.1320	0.9415	22.580	33.000	18.670	792.0	3750.0
0.1417	0.9530	28.670	31.000	24.330	777.0	750.0
0.1425	0.9592	33.160	32.420	28.300	780.0	750.0

INTERNAL GAS IS ARGON EXTERNAL GAS IS HYDROGEN

COMOB	COMIB	FLO1S	FLO2T	FLO12S	PRESS	DELTAP
0.0235	0.5240	5.920	49.330	9.270	771.0	-200.0
0.0251	0.5940	8.350	47.750	12.080	777.0	-50.0
0.0247	0.6560	11.670	51.850	15.000	784.0	-200.0
0.0249	0.7100	14.170	53.500	18.100	795.0	-75.0

TABLE V-5A Cont.....

NICKEL SPHERE NUMBER 4

INTERNAL GAS IS HYDROGEN EXTERNAL GAS IS ARGON

COMOB	COMIB	FLO1S	FLO2T	FLO12S	PRESS	DELTAP
0.1053	0.8965	10.500	32.670	7.390	770.0	350.0
0.1142	0.9224	13.970	32.600	10.630	775.0	700.0
0.1120	0.9437	18.670	33.830	15.170	783.0	750.0
0.1187	0.9511	23.000	33.500	19.550	791.0	1000.0
0.1219	0.9592	28.330	32.830	24.160	777.0	1000.0
0.1270	0.9630	33.670	33.000	29.250	781.0	1000.0

INTERNAL GAS IS ARGON EXTERNAL GAS IS HYDROGEN

COMOB	COMIB	FLO1S	FLO2T	FLO12S	PRESS	DELTAP
0.0217	0.5040	5.750	47.000	8.550	770.0	-250.0
0.0224	0.6440	8.440	48.330	11.500	776.0	0.0
0.0227	0.6970	10.960	49.670	14.170	784.0	300.0
0.0236	0.7460	14.170	49.000	17.690	795.0	750.0

****

NICKEL SPHERE NUMBER 6

INTERNAL GAS IS HYDROGEN EXTERNAL GAS IS ARGON

COMOB	COMIB	FLO1S	FLO2T	FLO12S	PRESS	DELTAP
0.1157	0.8859	11.750	32.500	8.520	772.0	700.0
0.1210	0.9261	17.080	32.670	13.520	779.0	650.0
0.1261	0.9407	21.580	33.330	19.430	790.0	300.0
0.1330	0.9531	28.670	32.250	24.220	776.0	300.0
0.1415	0.9579	35.920	32.170	29.020	780.0	300.0

****

NICKEL SPHERE NUMBER 7

INTERNAL GAS IS HYDROGEN EXTERNAL GAS IS ARGON

COMOB	COMIB	FLO1S	FLO2T	FLO12S	PRESS	DELTAP
0.1085	0.8850	11.000	33.670	7.720	771.0	750.0
0.1143	0.9244	16.000	33.000	12.470	779.0	750.0
0.1235	0.9448	22.250	32.580	18.670	791.0	750.0
0.1202	0.9520	26.420	33.330	22.300	775.0	700.0
0.1335	0.9577	31.670	32.820	27.030	779.0	650.0
0.1370	0.9632	37.500	33.170	32.330	783.0	500.0

INTERNAL GAS IS ARGON EXTERNAL GAS IS HYDROGEN

COMOB	COMIB	FLO1S	FLO2T	FLO12S	PRESS	DELTAP
0.0236	0.5500	6.830	51.330	10.550	774.0	425.0
0.0249	0.6640	10.080	51.080	14.280	783.0	800.0
0.0270	0.7110	13.550	48.830	18.050	795.0	1100.0
0.0279	0.7490	17.000	49.500	21.670	781.0	1100.0
0.0285	0.7790	20.830	49.500	25.670	787.0	1250.0

****

TABLE V-5A Cont.....

NICKEL SPHERE NUMBER 8

INTERNAL GAS IS HYDROGEN EXTERNAL GAS IS ARGON

COMOB	COMIB	FLO1S	FLO2T	FLO12S	PRESS	DELTAP
0.1147	0.8860	11.600	32.580	8.270	772.0	750.0
0.1165	0.9232	16.450	33.670	12.880	780.0	750.0
0.1240	0.9432	22.420	33.560	18.620	791.0	500.0
0.1305	0.9536	28.670	32.830	24.280	776.0	500.0
0.1400	0.9585	33.750	33.000	28.750	780.0	400.0

INTERNAL GAS IS ARGON EXTERNAL GAS IS HYDROGEN

COMOB	COMIB	FLO1S	FLO2T	FLO12S	PRESS	DELTAP
0.0251	0.0290	8.250	50.500	12.750	780.0	1000.0
0.0268	0.7140	13.970	50.330	18.500	797.0	1000.0
0.0282	0.7630	19.250	51.160	24.170	785.0	1250.0
0.0274	0.7980	23.920	53.170	29.000	791.5	1300.0

****

NICKEL SPHERE NUMBER 9

INTERNAL GAS IS HYDROGEN EXTERNAL GAS IS ARGON

COMOB	COMIB	FLO1S	FLO2T	FLO12S	PRESS	DELTAP
0.1110	0.8955	12.000	33.830	8.670	772.0	750.0
0.1180	0.9295	17.500	33.580	13.880	780.0	600.0
0.1215	0.9435	21.830	33.500	18.080	789.0	500.0
0.1311	0.9536	28.420	33.000	24.170	776.0	400.0
0.1360	0.9580	33.670	33.000	28.580	780.0	300.0

****

NICKEL SPHERE NUMBER 10

INTERNAL GAS IS HYDROGEN EXTERNAL GAS IS ARGON

COMOB	COMIB	FLO1S	FLO2T	FLO12S	PRESS	DELTAP
0.1210	0.9122	14.330	32.670	10.720	776.0	650.0
0.1230	0.9431	22.550	34.000	18.620	790.0	600.0
0.1385	0.9582	32.830	32.350	27.920	779.0	300.0

****

NICKEL SPHERE NUMBER 12

INTERNAL GAS IS HYDROGEN EXTERNAL GAS IS ARGON

COMOB	COMIB	FLO1S	FLO2T	FLO12S	PRESS	DELTAP
0.1375	0.8505	11.420	32.670	7.600	771.0	700.0
0.1487	0.9039	16.750	33.000	12.380	780.0	500.0
0.1570	0.9287	22.330	32.330	17.850	793.0	650.0
0.1715	0.9390	29.920	32.330	22.670	776.0	350.0
0.1779	0.9474	34.500	33.830	28.420	781.0	400.0

****

TABLE V-5A Cont.....

NICKEL SPHERE NUMBER 13

INTERNAL GAS IS HYDROGEN EXTERNAL GAS IS ARGON

COMOB	COMIB	FLO1S	FLO2T	FLO12S	PRESS	DELTAP
0.1250	0.8393	12.850	33.000	9.220	775.0	650.0
0.1300	0.9246	16.920	32.830	13.230	780.0	800.0
0.1320	0.9417	22.920	34.170	18.850	792.0	850.0
0.1443	0.9516	28.670	33.250	23.830	776.0	650.0
0.1525	0.9575	35.500	33.080	30.330	782.0	800.0

INTERNAL GAS IS ARGON EXTERNAL GAS IS HYDROGEN

COMOB	COMIB	FLO1S	FLO2T	FLO12S	PRESS	DELTAP
0.0219	0.5450	6.750	49.330	10.680	774.0	350.0
0.0263	0.6270	10.200	50.170	14.480	783.0	100.0
0.0286	0.6850	14.170	51.170	19.100	797.0	250.0
0.0307	0.7360	18.670	49.330	25.330	782.0	250.0
0.0313	0.7740	23.670	51.500	28.750	790.0	300.0

****

NICKEL SPHERE NUMBER 14

INTERNAL GAS IS HYDROGEN EXTERNAL GAS IS ARGON

COMOB	COMIB	FLO1S	FLO2T	FLO12S	PRESS	DELTAP
0.1170	0.8774	10.500	33.170	7.230	770.0	800.0
0.1252	0.9266	17.020	33.000	13.300	780.0	700.0
0.1317	0.9444	22.580	32.920	18.580	791.0	600.0
0.1391	0.9529	28.500	33.420	23.970	775.0	450.0
0.1450	0.9592	34.500	32.670	29.330	780.0	350.0

INTERNAL GAS IS ARGON EXTERNAL GAS IS HYDROGEN

COMOB	COMIB	FLO1S	FLO2T	FLO12S	PRESS	DELTAP
0.0265	0.6060	8.450	50.500	12.580	778.0	300.0
0.0284	0.6940	13.750	50.000	18.330	795.0	650.0
0.0281	0.7470	18.750	51.500	23.330	783.0	950.0

****

NICKEL SPHERE NUMBER 15

INTERNAL GAS IS HYDROGEN EXTERNAL GAS IS ARGON

COMOB	COMIB	FLO1S	FLO2T	FLO12S	PRESS	DELTAP
0.0963	0.9081	10.250	33.330	7.500	770.0	700.0
0.1035	0.9415	16.830	32.670	13.670	780.0	1000.0
0.1070	0.9539	22.250	32.920	18.880	791.0	1000.0
0.1131	0.9625	28.330	32.500	24.280	775.0	800.0
0.1190	0.9680	34.750	32.500	30.330	781.0	550.0

INTERNAL GAS IS ARGON EXTERNAL GAS IS HYDROGEN

COMOB	COMIB	FLO1S	FLO2T	FLO12S	PRESS	DELTAP
0.0219	0.6330	7.450	50.330	10.330	775.0	450.0
0.0215	0.7315	13.420	54.170	16.850	793.0	1000.0
0.0239	0.7830	18.250	50.670	21.370	782.0	1000.0
0.0240	0.8270	24.080	50.830	27.770	790.0	1000.0

****

TABLE V-5A Cont.....

NICKEL SPHERE NUMBER 16

INTERNAL GAS IS HYDROGEN EXTERNAL GAS IS ARGON

COMOB	COMIB	FLO1S	FLO2T	FLC12S	PRESS	DELTAP
0.1370	0.8520	10.730	32.830	6.930	770.0	625.0
0.1470	0.9055	16.330	32.920	12.080	780.0	650.0
0.1580	0.9301	22.380	32.330	17.660	792.0	600.0
0.1633	0.9417	27.830	32.920	22.520	775.0	550.0
0.1760	0.9497	34.630	32.500	28.900	782.0	600.0

INTERNAL GAS IS ARGON EXTERNAL GAS IS HYDROGEN

COMOB	COMIB	FLO1S	FLO2T	FLC12S	PRESS	DELTAP
0.0293	0.5290	8.100	50.000	13.220	779.0	600.0
0.0314	0.6320	14.100	52.830	19.380	797.0	500.0
0.0351	0.7050	19.630	51.170	25.000	784.0	350.0
0.0375	0.7500	25.920	51.500	31.750	794.0	300.0

****

NICKEL SPHERE NUMBER 17

INTERNAL GAS IS HYDROGEN EXTERNAL GAS IS ARGON

COMOB	COMIB	FLO1S	FLO2T	FLC12S	PRESS	DELTAP
0.1207	0.8971	12.170	33.330	9.050	773.0	550.0
0.1261	0.9266	16.420	32.830	13.380	781.0	750.0
0.1281	0.9446	22.330	33.250	19.500	793.0	850.0
0.1390	0.9546	29.000	32.920	25.830	778.0	750.0
0.1430	0.9607	35.830	33.330	32.500	783.0	750.0

INTERNAL GAS IS ARGON EXTERNAL GAS IS HYDROGEN

COMOB	COMIB	FLO1S	FLO2T	FLC12S	PRESS	DELTAP
0.0255	0.6090	8.370	50.830	12.680	780.0	3000.0
0.0273	0.6975	14.000	50.330	18.800	798.0	1000.0
0.0288	0.7465	19.000	50.500	23.950	785.0	1000.0
0.0290	0.7980	20.170	52.670	31.080	796.0	900.0

****

NICKEL OXIDE SPHERE NUMBER 20

INTERNAL GAS IS HYDROGEN EXTERNAL GAS IS ARGON

COMOB	COMIB	FLO1S	FLO2T	FLC12S	PRESS	DELTAP
0.0959	0.9073	10.670	32.660	7.870	769.0	450.0
0.0979	0.9430	16.630	33.080	13.580	778.0	750.0
0.1006	0.9581	22.500	33.830	20.470	791.0	700.0
0.1111	0.9642	29.000	32.820	26.300	776.0	750.0
0.1185	0.9694	35.330	33.330	32.060	781.0	500.0

INTERNAL GAS IS ARGON EXTERNAL GAS IS HYDROGEN

COMOB	COMIB	FLO1S	FLO2T	FLC12S	PRESS	DELTAP
0.0211	0.6660	8.330	50.000	11.420	778.0	800.0
0.0216	0.7480	13.660	52.000	16.970	794.0	1000.0
0.0230	0.8030	19.160	50.330	22.360	783.0	1200.0
0.0232	0.8432	20.000	51.000	29.000	794.0	1400.0

****

TABLE V-5B EXPERIMENTAL DATA OBTAINED IN DIFFUSION MEASUREMENTS ON NICKEL SPHERES WITH H_2-CO_2- DIFFUSION COUPLE

NICKEL SPHERE NUMBER 7

INTERNAL GAS IS HYDROGEN EXTERNAL GAS IS CARBON DIOXIDE

COMOB	COMIB	FLO1S	FLO2T	FLC12S	PRESS	DELTAP
0.1071	0.9114	11.250	31.000	8.480	769.0	0.0
0.1162	0.9554	21.170	31.420	18.270	787.0	0.0
0.1193	0.9674	30.330	31.500	27.170	775.0	150.0
0.1270	0.9752	39.830	30.750	36.500	781.0	150.0

INTERNAL GAS IS CARBON DIOXIDE EXTERNAL GAS IS HYDROGEN

COMOB	COMIB	FLO1S	FLO2T	FLC12S	PRESS	DELTAP
0.0162	0.6440	7.370	50.670	10.470	773.0	0.0
0.0184	0.7445	12.750	50.830	16.280	789.0	0.0
0.0195	0.8090	19.500	50.750	23.080	778.0	0.0

****

NICKEL SPHERE NUMBER 16

INTERNAL GAS IS HYDROGEN EXTERNAL GAS IS CARBON DIOXIDE

COMOB	COMIB	FLO1S	FLO2T	FLC12S	PRESS	DELTAP
0.1270	0.8850	11.200	30.580	7.700	770.0	50.0
0.1344	0.9229	16.330	30.830	12.380	778.0	5.0
0.1430	0.9439	21.830	31.080	17.250	787.0	5.0
0.1500	0.9533	28.670	30.830	24.030	774.0	250.0
0.1590	0.9632	36.830	30.670	31.500	780.0	250.0

INTERNAL GAS IS CARBON DIOXIDE EXTERNAL GAS IS HYDROGEN

COMOB	COMIB	FLO1S	FLO2T	FLC12S	PRESS	DELTAP
0.0219	0.5730	6.780	49.830	10.680	772.0	0.0
0.0250	0.6900	13.000	50.330	16.970	790.0	0.0
0.0270	0.7620	20.000	50.330	24.750	791.0	0.0
0.0297	0.8072	26.670	50.000	31.250	796.0	100.0

****

NICKEL SPHERE NUMBER 17

INTERNAL GAS IS HYDROGEN EXTERNAL GAS IS CARBON DIOXIDE

COMOB	COMIB	FLO1S	FLO2T	FLC12S	PRESS	DELTAP
0.1082	0.9040	11.000	30.710	8.120	768.0	-100.0
0.1160	0.9410	16.670	31.250	13.900	778.0	-100.0
0.1210	0.9541	22.500	30.920	19.550	790.0	200.0
0.1285	0.9664	31.000	30.920	27.670	777.0	50.0
0.1342	0.9712	37.750	30.830	34.330	782.0	100.0

INTERNAL GAS IS CARBON DIOXIDE EXTERNAL GAS IS HYDROGEN

COMOB	COMIB	FLO1S	FLO2T	FLC12S	PRESS	DELTAP
0.0181	0.6495	7.830	50.170	11.350	774.0	0.0
0.0202	0.7290	13.100	49.500	16.830	790.0	0.0
0.0222	0.7930	18.580	49.500	22.670	777.0	-500.0
0.0224	0.8290	24.750	50.170	29.230	789.0	-200.0

****

TABLE V-5B Cont.....

NICKEL SPHERE NUMBER 21

INTERNAL GAS IS HYDROGEN EXTERNAL GAS IS CARBON DIOXIDE

COMOB	COMIB	FLO1S	FLO2T	FLC12S	PRESS	DELTAP
0.0417	0.9766	12.500	31.080	11.530	770.0	-150.0
0.0429	0.9867	21.670	31.580	20.830	784.0	0.0
0.0435	0.9899	30.000	31.080	28.750	775.0	150.0
0.0436	0.9919	37.000	31.330	35.750	780.0	800.0

INTERNAL GAS IS CARBON DIOXIDE EXTERNAL GAS IS HYDROGEN

COMOB	COMIB	FLO1S	FLO2T	FLC12S	PRESS	DELTAP
0.0064	0.8420	7.420	51.170	8.430	770.0	-500.0
0.0062	0.9980	12.970	50.670	14.130	788.0	1000.0
0.0064	0.9935	20.920	49.330	22.330	780.0	-500.0
0.0064	0.9972	26.670	50.330	28.330	796.0	0.0

****

NICKEL SPHERE NUMBER 21

INTERNAL GAS IS HYDROGEN EXTERNAL GAS IS CARBON DIOXIDE

COMOB	COMIB	FLO1S	FLO2T	FLC12S	PRESS	DELTAP
0.0427	0.9716	10.970	30.600	10.000	768.0	500.0
0.0427	0.9824	16.830	30.830	16.030	776.0	100.0
0.0433	0.9864	22.770	31.100	21.970	787.0	200.0
0.0448	0.9895	28.900	30.830	27.800	774.0	-100.0
0.0450	0.9912	36.200	31.100	35.000	781.0	600.0

INTERNAL GAS IS CARBON DIOXIDE EXTERNAL GAS IS HYDROGEN

COMOB	COMIB	FLO1S	FLO2T	FLC12S	PRESS	DELTAP
0.0066	0.8360	7.090	46.160	8.290	770.0	0.0
0.0069	0.9000	13.110	45.330	14.430	786.0	100.0
0.0072	0.9268	18.590	44.670	20.030	775.0	-500.0
0.0068	0.9410	23.600	45.670	25.150	785.0	-500.0

****

NICKEL SPHERE NUMBER 22

INTERNAL GAS IS HYDROGEN EXTERNAL GAS IS CARBON DIOXIDE

COMOB	COMIB	FLO1S	FLO2T	FLC12S	PRESS	DELTAP
0.0655	0.9537	10.670	31.000	9.160	769.0	100.0
0.0684	0.9771	20.500	31.330	19.000	784.0	0.0
0.0706	0.9829	29.500	31.330	27.780	774.0	0.0
0.0717	0.9878	41.000	31.000	39.000	784.0	0.0

INTERNAL GAS IS CARBON DIOXIDE EXTERNAL GAS IS HYDROGEN

COMOB	COMIB	FLO1S	FLO2T	FLC12S	PRESS	DELTAP
0.0098	0.7550	6.920	49.830	9.020	770.0	0.0
0.0099	0.8378	12.370	51.000	14.170	785.0	0.0
0.0100	0.8833	18.830	50.830	20.830	777.0	0.0
0.0104	0.9094	25.000	51.170	27.080	790.0	0.0

****

TABLE V-5B Cont.....

NICKEL SPHERE NUMBER 23

INTERNAL GAS IS HYDROGEN EXTERNAL GAS IS CARBON DIOXIDE

COMOB	COMIB	FLO1S	FLO2T	FLC12S	PRESS	DELTAP
0.0762	0.9452	11.180	31.000	9.260	770.0	10.0
0.0802	0.9708	20.070	31.700	18.800	783.0	50.0
0.0849	0.9792	30.540	30.900	28.650	773.0	0.0
0.0863	0.9840	40.900	31.000	38.800	785.0	0.0

****

TABLE V-6 COMPUTED DATA FOR SPHERE NO.17 WITH CO_2 - H_2 DIFFUSION COUPLE

A) HYDROGEN AS INTERNAL GAS (GAS I)

N	DEFF12	FLOIS	CONIB	CONIS	CONOS	CONOB	DELTA H_2	FLUX1 x 10^5	FLUX2 x 10^5	BETA	ALPHA I	ALPHAO
1	0.2142	11.000	0.9040	0.8004	0.1497	0.0541	0.9620	15.14	3.25	0.214	2.528	2.120
2	0.1981	16.670	0.9410	0.8619	0.1593	0.0580	0.9647	16.44	3.42	0.208	3.071	2.131
3	0.1941	22.500	0.9541	0.8867	0.1642	0.0605	0.9654	17.08	3.74	0.219	3.632	2.126
4	0.2009	31.000	0.9664	0.9110	0.1765	0.0642	0.9640	18.34	3.87	0.211	4.458	2.127
5	0.2058	37.750	0.9712	0.9215	0.1832	0.0671	0.9634	19.15	4.12	0.215	5.113	2.126

B) CARBON DIOXIDE AS INTERNAL GAS

N	DEFF12	FLOIS	CONIB	CONIS	CONOS	CONOB	DELTA CO_2	FLUX1 x 10^5	FLUX2 x 10^5	BETA	ALPHA I	ALPHAO
1	0.2111	7.380	0.6495	0.5395	0.0327	0.0090	0.8460	3.52	16.58	4.711	5.347	2.315
2	0.2087	13.100	0.7290	0.6389	0.0359	0.0101	0.8470	3.85	19.00	4.933	8.059	2.302
3	0.2096	18.580	0.7930	0.7180	0.0399	0.0111	0.8470	4.20	19.55	4.655	10.939	2.297
4	0.2067	24.750	0.8290	0.7659	0.0400	0.0112	0.8480	4.26	20.83	4.884	14.173	2.304

TABLE V-7A RESULTS OF DIFFUSION AND PERMEABILITY MEASUREMENTS ON NICKEL SPHERES USING A H_2-A_R DIFFUSION COUPLE

Sphere No.	Compacting Pressure kN/m^2	Porosity % NiO	Porosity % Ni	Internal Radius Ni cm.	External Radius Ni cm.	Sintering Conditions	Reduction Temp.. (initial)	Average D_{H_2} A_R eff H_2 inside	Average D_{H_2} A_R eff A_R inside	D_{H_2} K. $\frac{cm^2}{sec}$	$\frac{B_o}{\eta}$ $\frac{cm^2}{sec}$	$\frac{\epsilon}{\tau}$
1	200	33.9	59.5	0.639	1.187	4hrs.at 650°C	325°C	.3472	-	5.40	7.06	.451
2	100	41.0	61.6	0.616	1.142	24hrs.at 650°C	350°C	.2633	.3106	3.75	4.22	.342
3	150	37.1	60.5	0.620	1.140	24hrs.at 650°C	350°C	.2599	.2899	3.45	4.08	.338
4	300	30.9	55.5	0.615	1.100	None	358°C	.2312	.2637	1.98	1.45	.301
6	100	40.8	62.6	0.625	1.182	None	358°C	.2457	-	6.50	9.00	.319
7	100	40.2	61.5	0.619	1.150	48hrs.at 750°C	350°C	.2414	.2822	4.55	4.82	.314
8	100	40.2	61.5	0.621	1.150	48hrs.at 750°C	350°C	.2448	.2763	5.15	8.42	.318
9	100	40.1	61.3	0.620	1.152	24hrs.at 750°C	350°C	.2476	-	3.98	5.23	.321
10	100	40.1	61.4	0.616	1.130	24hrs.at 750°C	350°C	.2519	-	3.95	5.11	.327
12	100	40.8	63.7	0.648	1.172	24hrs.at 750°C	250°C	.3132	-	10.60	18.97	.410
13	100	40.8	60.9	0.614	1.152	24hrs.at 750°C	450°C	.2804	.3374	5.35	9.09	.364
14	100	40.75	59.5	0.613	1.132	24hrs.at 750°C	550°C	.2577	.3106	5.30	8.92	.335
15	100	40.70	53.85	0.588	1.107	24hrs.at 750°C	650°C	.2031	.2493	4.50	7.25	.264
16	100	40.65	64.0	0.650	1.202	24hrs.at 750°C	250°C	.3068	.3717	9.10	17.04	.398
17	100	40.8	60.3	0.620	1.150	24hrs.at 750°C	450°C	.2469	.2969	5.40	8.37	.321
20 (NiO)	100	40.8	-	0.640	1.198	24hrs.at 750°C	-	.1739	.2098	2.90	4.26	.226

TABLE V-7B RESULTS OF DIFFUSION AND PERMEABILITY MEASUREMENTS ON NICKEL SPHERES USING A H_2-CO_2 DIFFUSION COUPLE

Sphere No.	Compacting Pressure kN/m²	Porosity % NiO	Porosity % Ni	Internal Radius Ni cm	External Radius Ni cm	Sintering Conditions	Reduction Temp.	Average $D_{H_2CO_2}$ eff H_2inside	Average $D_{H_2CO_2}$ eff CO_2inside	D_{H_2} k cm²/sec	B_o/η cm²/sec.atm	ϵ/q
7	100	40.2	61.5	0.619	1.150	24hrs.at 750°C	350°C	.1880	.1910	4.45	4.82	0.306
16	100	40.65	64.0	0.650	1.202	24hrs.at 750°C	250°C	.2420	.2475	9.10	18.97	0.395
17	100	40.8	60.3	0.620	1.150	24hrs.at 750°C	450°C	.2026	.2086	5.40	8.37	0.332
21	600	24.5	38.8	0.581	1.024	24hrs.at 750°C	650°C	.0567	.0592	0.62	0.58	0.0936
21	R E P E A T							.0584	.0596	-	-	0.0952
22	100	40.6	40.8	0.543	1.030	24hrs.at 750°C	800°C	.1179	.1208	1.33	3.20	0.193
23	100	40.6	46.6	0.573	1.050	24hrs.at 750°C	750°C	.1380	-	3.04	4.10	0.222

V-2 REDUCTION EXPERIMENTS

V-2-A GAS SWITCHING TIME LAG EXPERIMENT

The times for the composition of the bulk gas at the sphere location to change, as indicated by the changing conductivity, from pure nitrogen to any specific concentration of hydrogen are shown in Figure V-2-1 as a function of the hydrogen flow rate. The lowest line represents the time elapsed before any change in gas conductivity was observed. The middle line represents the time elapsed when the conductivity change was 90% of the total change. The uppermost line shows the times when approximately 99% of the total conductivity change had occurred.

V-2-B TEMPERATURE GRADIENT ACROSS POROUS LAYER

The temperature traces of the two embedded thermocouples taken during a reduction experiment at 650°C are shown in Figure V-2-2.

V-2-C RATE OF REDUCTION EXPERIMENTS

V-2-C(i) Analysis of Experimental Measurements

As stated in Chapter IV, the voltage output of the load cell was fed to a data logger which transferred this information to paper tape. This paper tape, along with other pertinent experimental data, was then submitted to a CDC 6600 binary computer, along with the necessary programme, to analyse the information contained thereon. The programme instructed the computer to decode the data on the paper tape into millivolts and then by means of the load cell calibration and the initial weight of the sample, into absolute weights. The

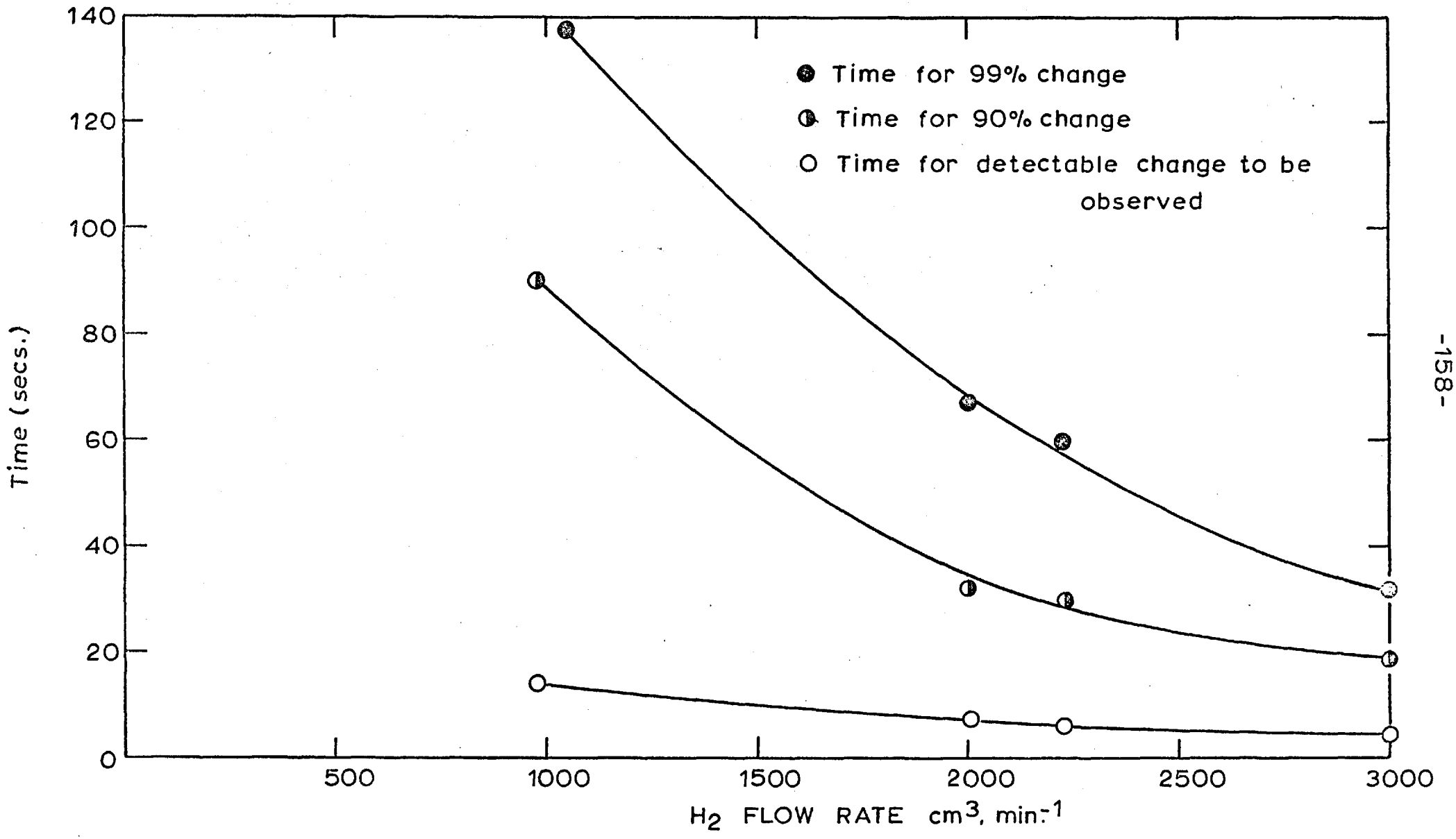


Fig.V-2-1. GAS SWITCHING TIME LAG RESULTS

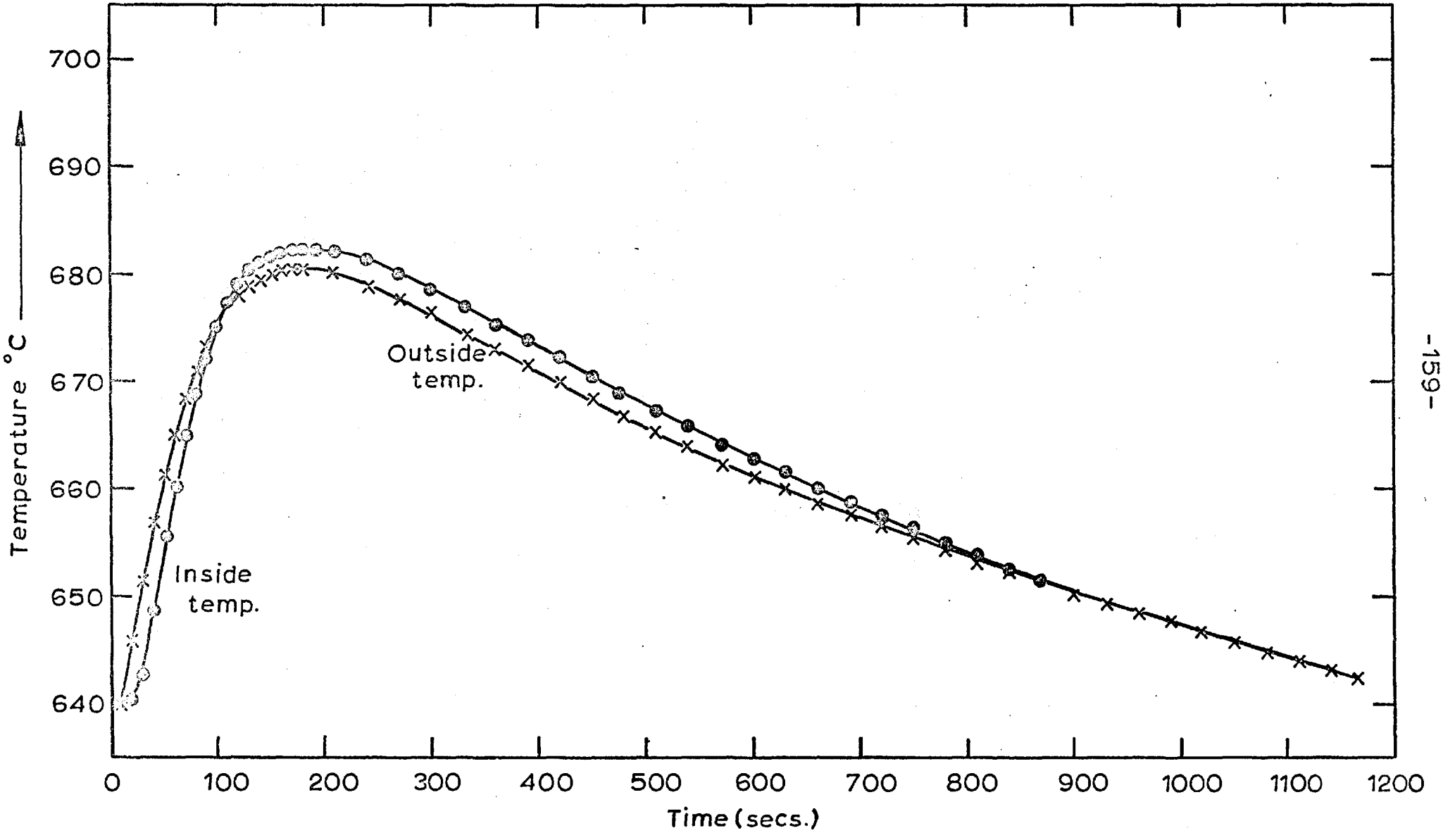


Fig.V-2-2. TEMPERATURE GRADIENT IN NICKEL SPHERE DURING REDUCTION AT 650°C

computer established the starting time for the reaction by checking the weight readings until two successive weight losses of at least 1.5 milligrams were recorded. The programme then set to zero the time of the reading immediately before the two successive drops, and it considered the reaction to start at that point.

In those experiments which proceeded to complete reduction, the dimensionless mass at any time was defined as the weight loss up to that time divided by the total weight loss. This was found to be a realistic simplification as the total weight loss during such runs was within one per cent of that predicted by the sample analysis. However, in experiments which did not proceed to complete reduction, such as experiments carried out at low reduction temperatures, i.e. 250°C, or experiments in which samples were only partially reduced, the final mass calculated from the sample analysis was used to calculate the total weight change. By defining the dimensionless mass of the reacting sphere in this way, the computer was able to set up an array of experimental values of time and dimensionless mass.

The programme also computed theoretical values of time as a function of the dimensionless mass from equation III-46. The values of gas flow rate, reaction temperature and sphere diameter were provided as data for this part of the programme. The Knudsen diffusion coefficient of hydrogen and the effective diffusivity, $((\epsilon/q)\, D_{12})$, measured in a hollow sphere of similar physical properties were also supplied as data. From this information, the external mass transfer

coefficient was calculated, at the reaction temperature, from the Frossling equation.

The effective diffusion coefficient of water vapour in the product layer was also calculated at the reaction temperature. An average reaction temperature was used in these calculations, calculated by integrating under the experimental time-temperature curve and dividing by the elapsed time. The driving force in all experiments was assumed to be 1.0 atmosphere partial pressure of hydrogen.

This data was then used to calculate a value of the chemical reaction rate constant. A starting value of 5.00 cm/sec was chosen and the programme then evaluated the theoretical times corresponding to each of the experimental dimensionless mass values. Then, by multiple regression analysis (CERN MINCON ROUTINE), the sum of the squares of the errors between the observed times and the calculated times was minimised by altering the value of k_c. The programme then printed out the final value of k_c, an error analysis on the fit of the experimental curve, and a summarized list of dimensionless mass, experimental time and predicted time. The programme also prepared a magnetic tape which could be fed to an automatic plotter. Graphs of dimensionless mass versus time could be visually compared by this method to demonstrate the validity of the predictions. Also, the programme computed and plotted the experimental values of the cube root of the dimensionless weight as a function of the reduction time.

Some experiments were also carried out in which the sample temperature was compiled by the computer and outputed as part of the results list.

V-2-Cb RESULTS

The data obtained in the reduction experiments is shown in Tables V-8A and V-8B where the time interval between successive readings has been chosen so that 50 readings are given for each run. Note that sample numbers start at 101 to avoid confusion with the diffusion samples.

Figures V-2-3A, B, C, D, E, F and G show the agreement obtained between predicted and experimental curves for different reduction temperatures. Figures V-2-4A, B, C, D, E, F and G show the dependence of the cube root of the dimensionless mass on time.

A summary of results obtained in the reduction experiments is given in Table V-9.

TABLE V-8A - WEIGHT LOSS AND TEMPERATURE DATA

RUN NUMBER 105			RUN NUMBER 107		
Time (Seconds)	Dimensionless Weight	Solid Temperature °C	Time (Seconds)	Dimensionless Weight	Solid Temperature °C
0	1.000	355	0	1.000	450
27	1.000	359	18	0.984	450
54	0.989	362	36	0.959	457
81	0.963	366	54	0.918	463
108	0.925	370	72	0.865	471
135	0.904	374	90	0.824	474
162	0.869	377	108	0.776	480
189	0.824	381	126	0.735	483
216	0.794	383	144	0.694	487
243	0.757	384	162	0.649	489
270	0.697	387	180	0.608	488
297	0.674	389	198	0.580	491
324	0.618	389	216	0.539	491
351	0.581	389	234	0.510	491
378	0.554	390	252	0.482	492
405	0.513	390	270	0.449	490
432	0.479	390	288	0.420	490
459	0.427	389	306	0.380	488
486	0.412	389	324	0.343	488
513	0.378	388	342	0.331	486
540	0.345	387	360	0.302	486
567	0.330	386	378	0.282	485
594	0.300	385	396	0.265	484
621	0.262	384	414	0.245	483
648	0.247	382	432	0.229	482
675	0.232	381	450	0.216	482
702	0.213	380	468	0.176	481
729	0.191	379	486	0.159	480
756	0.180	379	504	0.151	480
783	0.165	378	522	0.143	479
810	0.150	378	540	0.118	478
837	0.135	376	558	0.102	477
864	0.116	376	576	0.114	477
891	0.105	376	594	0.102	476
918	0.090	375	612	0.082	475
945	0.082	375	630	0.073	474
972	0.067	374	648	0.061	474
999	0.060	373	666	0.053	474
1026	0.049	372	684	0.045	473
1053	0.041	371	702	0.033	473
1080	0.034	371	720	0.029	472
1107	0.030	371	738	0.029	472
1134	0.022	370	756	0.024	471
1161	0.007	369	774	0.020	470
1188	0.004	369	792	0.008	469
1215	0.004	369	810	0.004	469
1242	0.002	368	828	0.002	468
1269	0.000	367	846	0.000	467
1296	0.000	366	864	0.000	467
1323	0.000	366	882	0.000	466

TABLE V-8A (Continued)

RUN NUMBER 108

Time (Seconds)	Dimensionless Weight	Solid Temperature °C
0	1.000	552
18	0.956	553
36	0.916	554
54	0.869	561
72	0.832	568
90	0.796	575
108	0.74[illegible]	580
126	0.704	583
144	0.672	585
162	0.635	587
180	0.599	588
198	0.562	588
216	0.536	588
234	0.511	589
252	0.474	589
270	0.445	589
288	0.420	588
306	0.398	588
324	0.365	587
342	0.347	586
360	0.328	585
378	0.310	581
396	0.281	583
414	0.263	582
432	0.237	581
450	0.219	581
468	0.208	580
486	0.190	580
504	0.175	579
522	0.157	579
540	0.142	578
558	0.128	578
576	0.120	575
594	0.106	576
612	0.095	575
630	0.084	574
648	0.073	574
666	0.058	573
684	0.051	573
702	0.040	572
720	0.033	571
738	0.026	571
756	0.018	571
774	0.011	571
792	0.007	569
810	0.007	569
828	0.004	568
846	0.000	566
864	0.000	566
882	0.000	565

TABLE V-8B EXPERIMENTAL DATA OBTAINED IN NICKEL OXIDE REDUCTION EXPERIMENTS

RUN NUMBER 116		RUN NUMBER 122		RUN NUMBER 123	
TIME (SECONDS)	DIMENSION -LESS WEIGHT	TIME (SECONDS)	DIMENSION -LESS WEIGHT	TIME (SECONDS)	DIMENSION -LESS WEIGHT
0.0	1.000	0.0	1.000	0.0	1.000
18.0	.953	23.0	.941	18.0	.936
37.0	.891	45.0	.870	37.0	.868
56.0	.834	67.0	.801	56.0	.804
75.0	.779	89.0	.737	75.0	.747
94.0	.726	111.0	.678	94.0	.693
113.0	.675	133.0	.625	113.0	.644
132.0	.627	155.0	.575	132.0	.598
151.0	.582	177.0	.530	151.0	.555
170.0	.540	199.0	.488	170.0	.515
189.0	.501	221.0	.450	189.0	.477
208.0	.464	243.0	.415	208.0	.441
227.0	.430	265.0	.382	227.0	.408
246.0	.397	287.0	.351	246.0	.377
265.0	.367	309.0	.323	265.0	.348
284.0	.339	331.0	.296	284.0	.321
303.0	.312	353.0	.271	303.0	.295
322.0	.287	375.0	.248	322.0	.271
341.0	.264	397.0	.226	341.0	.248
360.0	.242	419.0	.206	360.0	.226
379.0	.221	441.0	.187	379.0	.206
398.0	.202	463.0	.169	398.0	.187
417.0	.183	485.0	.153	417.0	.169
436.0	.166	507.0	.138	436.0	.153
455.0	.150	529.0	.123	455.0	.137
474.0	.135	551.0	.110	474.0	.123
493.0	.120	573.0	.097	493.0	.109
512.0	.107	595.0	.085	512.0	.096
531.0	.094	617.0	.075	531.0	.085
550.0	.083	639.0	.065	550.0	.074
569.0	.071	661.0	.056	569.0	.064
588.0	.060	683.0	.048	588.0	.055
607.0	.051	705.0	.040	607.0	.046
626.0	.043	727.0	.034	626.0	.038
645.0	.036	749.0	.028	645.0	.031
664.0	.029	771.0	.023	664.0	.025
683.0	.023	793.0	.018	683.0	.019
702.0	.017	815.0	.014	702.0	.015
721.0	.013	837.0	.012	721.0	.011
740.0	.009	859.0	.009	740.0	.008
759.0	.006	881.0	.008	759.0	.006
778.0	.004	903.0	.007	778.0	.004
797.0	.003	925.0	.006	797.0	.003
816.0	.003	947.0	.005	816.0	.003
835.0	.002	969.0	.004	835.0	.002
854.0	.002	991.0	.003	854.0	.001
873.0	.001	1013.0	.002	873.0	.001
892.0	.001	1035.0	.002	892.0	.001
911.0	.000	1057.0	.001	911.0	.001
930.0	.000	1079.0	.001	930.0	.000
950.0	.000	1140.0	*.000	960.0	*.000

TABLE V-8B EXPERIMENTAL DATA (cont.....)

RUN NUMBER 118		RUN NUMBER 119		RUN NUMBER 120	
TIME (SECONDS)	DIMENSION-LESS WEIGHT	TIME (SECONDS)	DIMENSION-LESS WEIGHT	TIME (SECONDS)	DIMENSION-LESS WEIGHT
0.0	1.000	0.0	1.000	0.0	1.000
18.0	.946	19.0	.921	18.0	.922
37.0	.884	39.0	.843	38.0	.837
56.0	.821	66.0	.747	57.0	.761
75.0	.763	96.0	.672	75.0	.696
94.0	.708	112.0	.610	93.0	.637
113.0	.656	132.0	.558	111.0	.582
132.0	.610	154.0	.506	129.0	.531
151.0	.566	174.0	.463	147.0	.483
170.0	.524	195.0	.421	165.0	.440
189.0	.485	217.0	.381	183.0	.401
208.0	.450	239.0	.344	201.0	.365
227.0	.417	259.0	.314	219.0	.332
246.0	.385	279.0	.285	237.0	.302
265.0	.356	301.0	.256	255.0	.273
284.0	.328	323.0	.230	273.0	.247
303.0	.303	345.0	.206	291.0	.223
322.0	.278	364.0	.186	309.0	.201
341.0	.256	383.0	.168	327.0	.180
360.0	.234	403.0	.150	345.0	.161
379.0	.214	424.0	.133	363.0	.144
398.0	.195	443.0	.118	381.0	.128
417.0	.177	462.0	.105	399.0	.113
436.0	.160	481.0	.093	417.0	.100
455.0	.145	500.0	.082	435.0	.088
474.0	.126	519.0	.071	453.0	.077
493.0	.114	538.0	.062	471.0	.067
512.0	.101	557.0	.053	489.0	.059
531.0	.090	576.0	.046	507.0	.051
550.0	.079	595.0	.038	525.0	.044
569.0	.069	614.0	.032	543.0	.038
588.0	.059	633.0	.027	561.0	.033
607.0	.051	653.0	.022	579.0	.029
626.0	.042	672.0	.019	597.0	.025
645.0	.035	691.0	.016	615.0	.022
664.0	.029	710.0	.013	633.0	.019
683.0	.025	729.0	.012	651.0	.017
702.0	.018	748.0	.010	669.0	.015
721.0	.013	767.0	.009	687.0	.013
740.0	.009	786.0	.007	705.0	.011
759.0	.006	805.0	.007	723.0	.009
778.0	.004	824.0	.006	741.0	.008
797.0	.003	843.0	.005	759.0	.007
815.0	.003	862.0	.004	777.0	.006
835.0	.002	881.0	.004	795.0	.005
854.0	.002	900.0	.003	813.0	.004
873.0	.001	919.0	.003	831.0	.003
892.0	.001	938.0	.002	849.0	.002
911.0	.001	957.0	.002	867.0	.001
930.0	.001	976.0	.001	885.0	.001
960.0	-.000	1030.0	-.000	900.0	-.000

TABLE V-8B Cont.....

RUN NUMBER 124		RUN NUMBER 125		RUN NUMBER 126	
TIME (SECONDS)	DIMENSION -LESS WEIGHT	TIME (SECONDS)	DIMENSION -LESS WEIGHT	TIME (SECONDS)	DIMENSION -LESS WEIGHT
0.0	1.000	1.0	1.000	0.0	1.000
22.0	.982	28.0	.970	19.0	.956
45.0	.960	56.0	.933	39.0	.893
68.0	.934	82.0	.897	59.0	.827
91.0	.913	108.0	.859	79.0	.763
114.0	.886	134.0	.820	99.0	.703
137.0	.859	160.0	.781	119.0	.649
160.0	.830	186.0	.741	139.0	.600
183.0	.801	212.0	.702	159.0	.554
206.0	.772	238.0	.663	179.0	.512
229.0	.742	264.0	.626	199.0	.474
252.0	.712	290.0	.589	219.0	.438
275.0	.682	316.0	.555	239.0	.404
298.0	.653	342.0	.523	259.0	.373
321.0	.624	368.0	.492	279.0	.344
344.0	.596	394.0	.462	299.0	.317
367.0	.569	420.0	.434	319.0	.292
390.0	.544	446.0	.407	339.0	.268
413.0	.519	472.0	.381	359.0	.246
436.0	.495	498.0	.356	379.0	.225
459.0	.473	524.0	.332	399.0	.206
482.0	.452	550.0	.310	419.0	.187
505.0	.432	576.0	.289	439.0	.170
528.0	.414	602.0	.268	459.0	.154
551.0	.397	628.0	.249	479.0	.139
574.0	.381	654.0	.230	499.0	.125
597.0	.366	680.0	.212	519.0	.111
620.0	.353	706.0	.196	539.0	.099
643.0	.340	732.0	.180	559.0	.088
666.0	.329	758.0	.165	579.0	.077
689.0	.319	784.0	.150	599.0	.067
712.0	.310	810.0	.136	619.0	.058
735.0	.301	836.0	.123	639.0	.050
758.0	.293	862.0	.111	659.0	.042
781.0	.286	888.0	.100	679.0	.035
804.0	.279	914.0	.089	699.0	.029
827.0	.273	940.0	.079	719.0	.024
850.0	.267	966.0	.069	739.0	.019
873.0	.262	992.0	.060	759.0	.015
896.0	.258	1018.0	.051	779.0	.012
919.0	.253	1044.0	.044	799.0	.010
942.0	.249	1070.0	.036	819.0	.008
965.0	.246	1096.0	.030	839.0	.007
988.0	.243	1122.0	.024	859.0	.005
1011.0	.240	1148.0	.019	879.0	.004
1034.0	.237	1174.0	.013	899.0	.004
1057.0	.234	1200.0	.009	919.0	.003
1080.0	.232	1226.0	.005	939.0	.002
1103.0	.230	1252.0	.003	959.0	.001
1126.0	.227	1279.0	.001	979.0	.001
1180.0	.223	1295.0	0.000	1030.0	0.000

TABLE V-8B Cont.....

RUN NUMBER 133		RUN NUMBER 127		RUN NUMBER 131	
TIME (SECONDS)	DIMENSION -LESS WEIGHT	TIME (SECONDS)	DIMENSION -LESS WEIGHT	TIME (SECONDS)	DIMENSION -LESS WEIGHT
0.0	1.000	1.0	1.000	0.0	1.000
21.0	.924	23.0	.925	12.0	.946
43.0	.842	46.0	.844	25.0	.883
65.0	.767	69.0	.770	38.0	.824
87.0	.698	92.0	.702	51.0	.768
109.0	.635	115.0	.639	65.0	.711
131.0	.578	138.0	.581	80.0	.655
153.0	.525	161.0	.528	95.0	.603
175.0	.477	184.0	.480	109.0	.558
197.0	.433	207.0	.435	122.0	.519
219.0	.393	230.0	.394	135.0	.482
241.0	.355	253.0	.356	148.0	.447
263.0	.321	275.0	.321	161.0	.415
285.0	.289	299.0	.288	174.0	.385
307.0	.260	322.0	.259	187.0	.356
329.0	.233	345.0	.231	200.0	.330
351.0	.208	368.0	.206	213.0	.304
373.0	.185	391.0	.182	227.0	.279
395.0	.164	414.0	.161	240.0	.257
417.0	.144	437.0	.141	253.0	.236
439.0	.126	460.0	.123	266.0	.216
461.0	.110	483.0	.106	279.0	.198
483.0	.094	506.0	.091	292.0	.181
505.0	.081	529.0	.077	305.0	.165
527.0	.068	552.0	.065	318.0	.149
549.0	.056	575.0	.054	331.0	.135
571.0	.046	598.0	.045	345.0	.121
593.0	.037	621.0	.036	358.0	.108
615.0	.029	644.0	.029	371.0	.097
637.0	.021	667.0	.023	384.0	.086
659.0	.016	690.0	.019	398.0	.076
681.0	.011	713.0	.016	411.0	.066
703.0	.007	736.0	.013	424.0	.058
725.0	.005	759.0	.012	437.0	.050
747.0	.004	782.0	.010	450.0	.043
769.0	.004	805.0	.008	463.0	.037
791.0	.003	828.0	.008	476.0	.031
813.0	.003	851.0	.007	489.0	.026
835.0	.003	874.0	.005	502.0	.022
857.0	.002	897.0	.005	515.0	.018
879.0	.002	920.0	.004	528.0	.014
901.0	.001	943.0	.004	541.0	.012
923.0	.001	966.0	.003	554.0	.010
945.0	.001	989.0	.003	567.0	.008
967.0	.001	1012.0	.002	580.0	.007
989.0	.001	1035.0	.001	593.0	.005
1011.0	.000	1058.0	.001	606.0	.004
1033.0	.000	1081.0	.001	619.0	.004
1055.0	.000	1104.0	.001	632.0	.003
1077.0	.000	1127.0	.000	645.0	.002
1120.0	.000	1151.0	.000	698.0	.000

TABLE V-8B Cont.....

RUN NUMBER 132

TIME (SECONDS)	DIMENSION -LESS WEIGHT
0.0	1.000
21.0	.946
43.0	.870
65.0	.796
87.0	.728
109.0	.667
131.0	.611
153.0	.561
175.0	.515
197.0	.472
219.0	.432
241.0	.396
263.0	.361
285.0	.329
307.0	.299
329.0	.271
351.0	.245
373.0	.221
395.0	.199
417.0	.178
439.0	.159
461.0	.141
483.0	.124
505.0	.109
527.0	.095
549.0	.082
571.0	.070
593.0	.059
615.0	.049
637.0	.040
659.0	.032
681.0	.025
703.0	.018
725.0	.014
747.0	.010
769.0	.007
791.0	.005
813.0	.004
835.0	.004
857.0	.003
879.0	.003
901.0	.002
923.0	.002
945.0	.001
967.0	.001
989.0	.001
1011.0	.001
1033.0	.001
1055.0	.000
1077.0	.000
1090.0	0.000

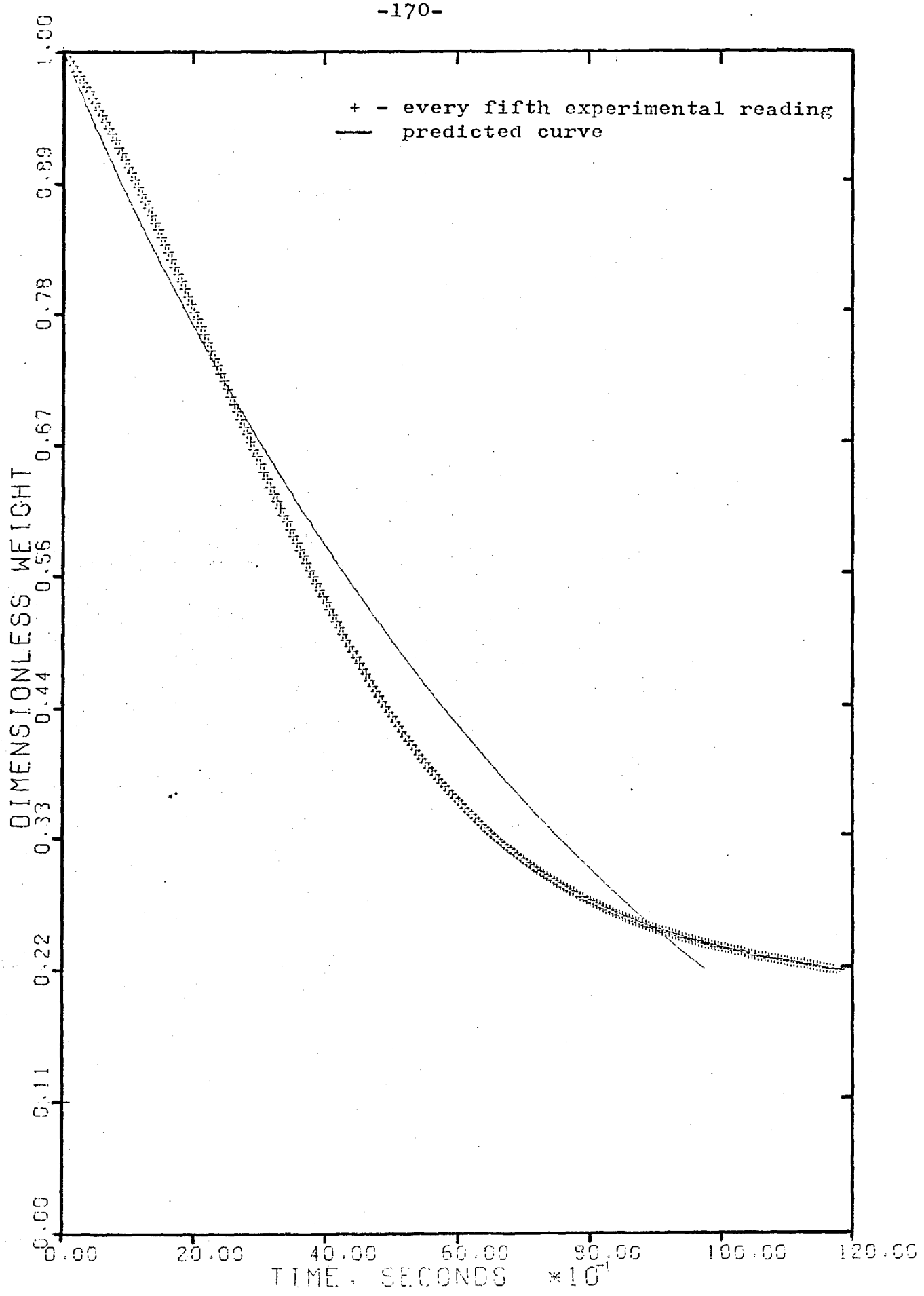


FIGURE V-2-3a UNREACTED MASS AS A FUNCTION OF TIME FOR SPHERE NUMBER 124 (RED. AT 257 °C)

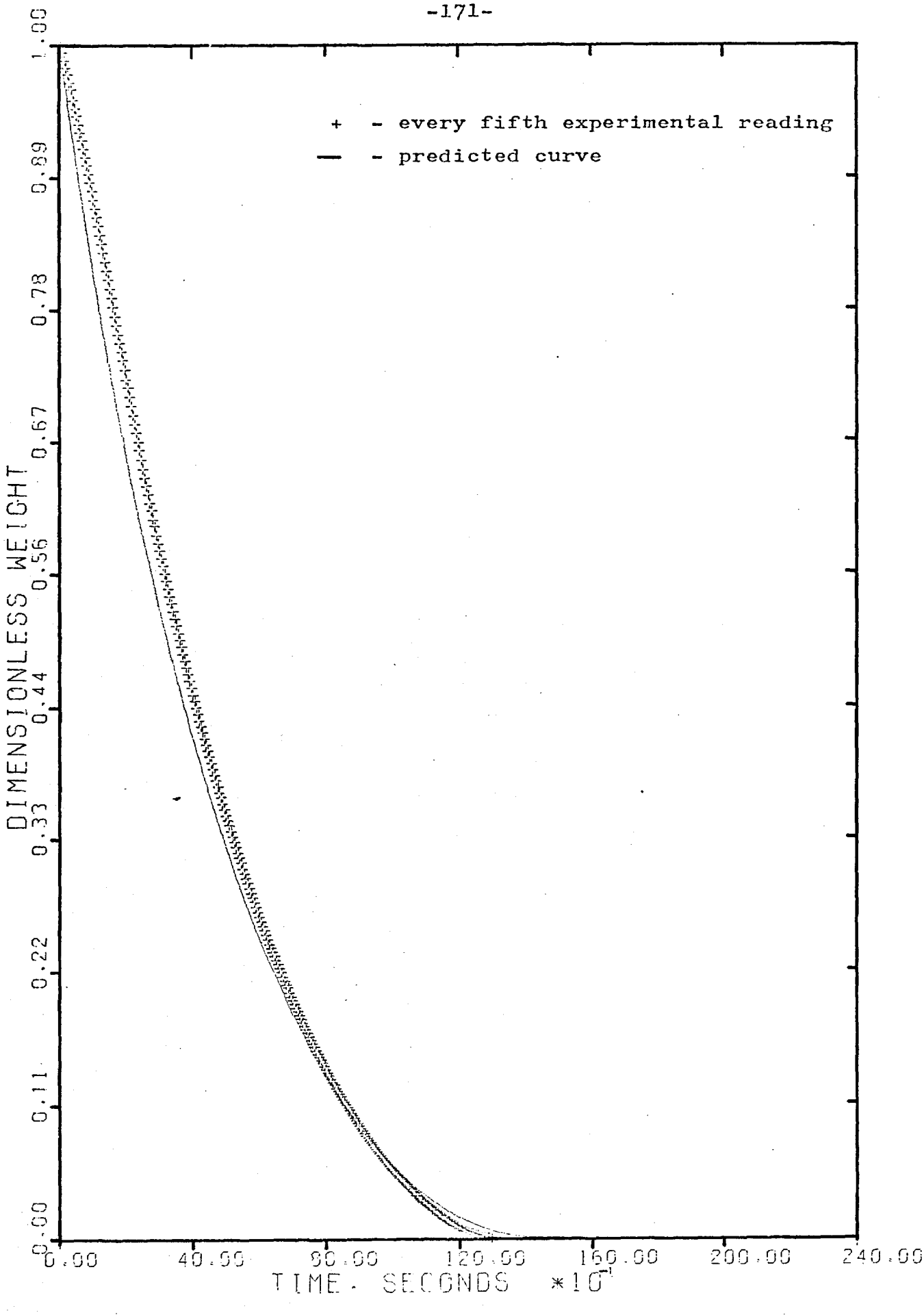


FIGURE V-2-3b UNREACTED MASS AS A FUNCTION OF TIME FOR SPHERE NUMBER 125 (RED. AT 362 °C)

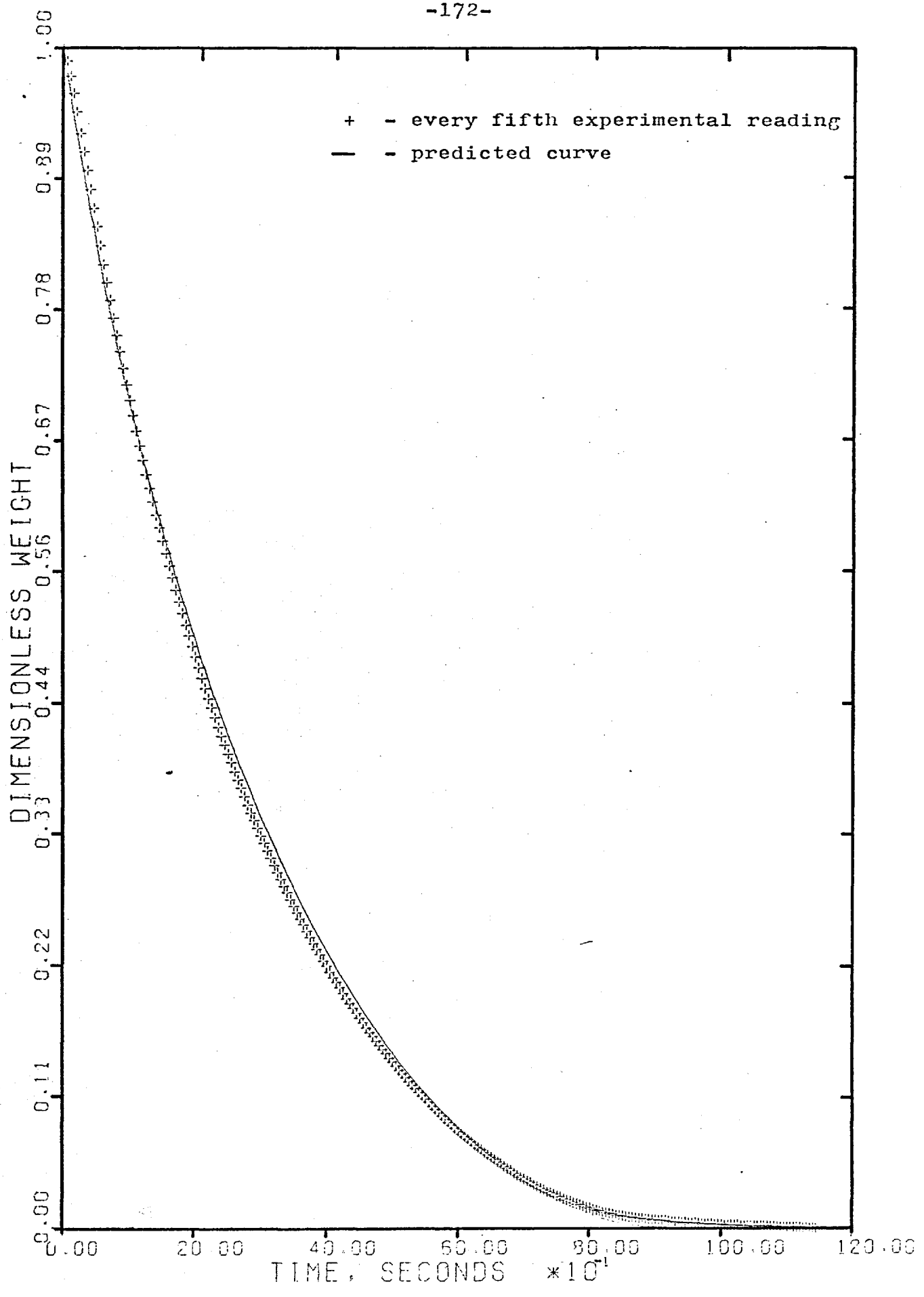


FIGURE V-2-3c UNREACTED MASS AS A FUNCTION OF TIME FOR SPHERE NUMBER 122 (RED. AT 468 °C)

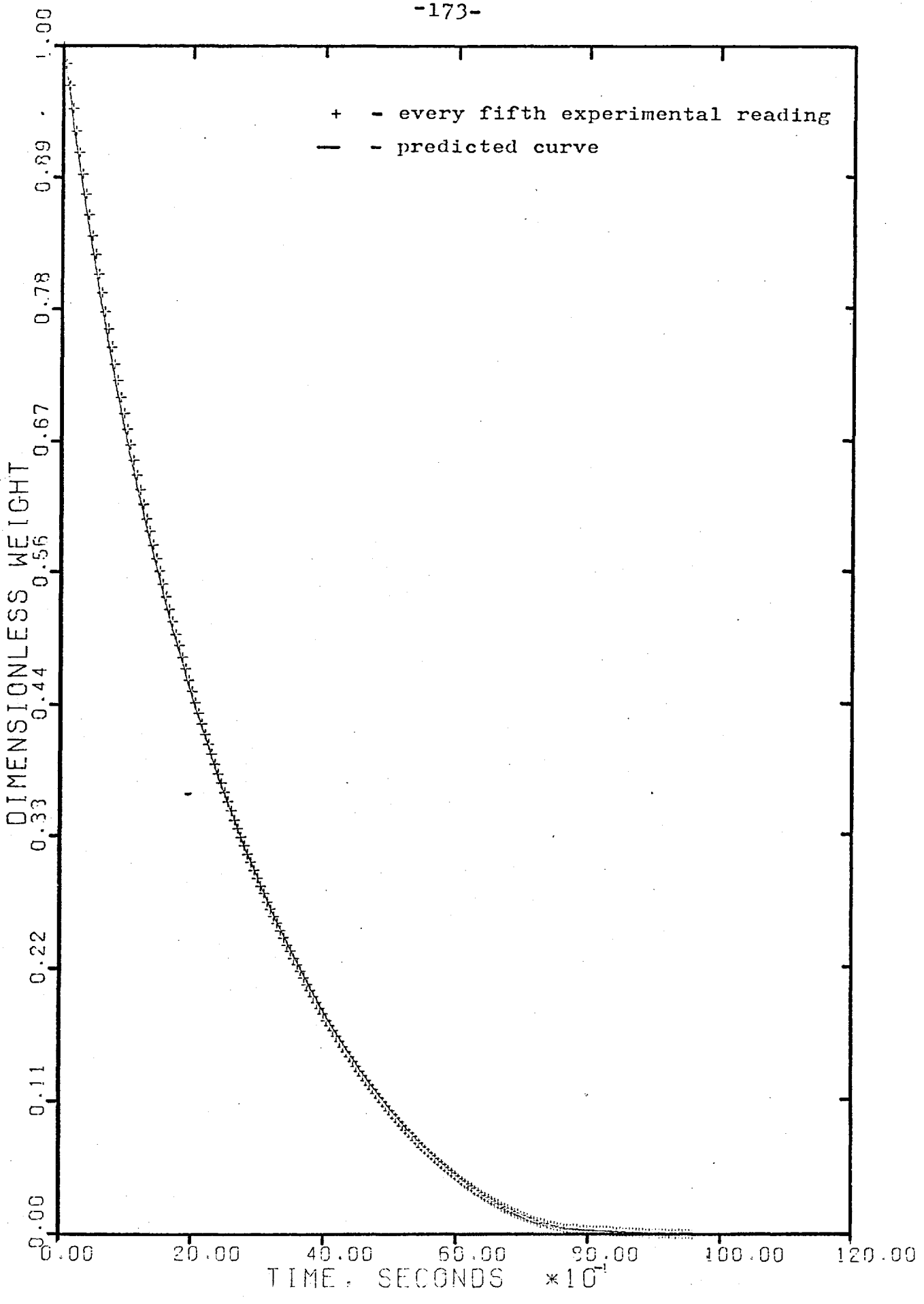


FIGURE V-2-3d UNREACTED MASS AS A FUNCTION OF TIME FOR SPHERE NUMBER 123 (RED. AT 571 °C)

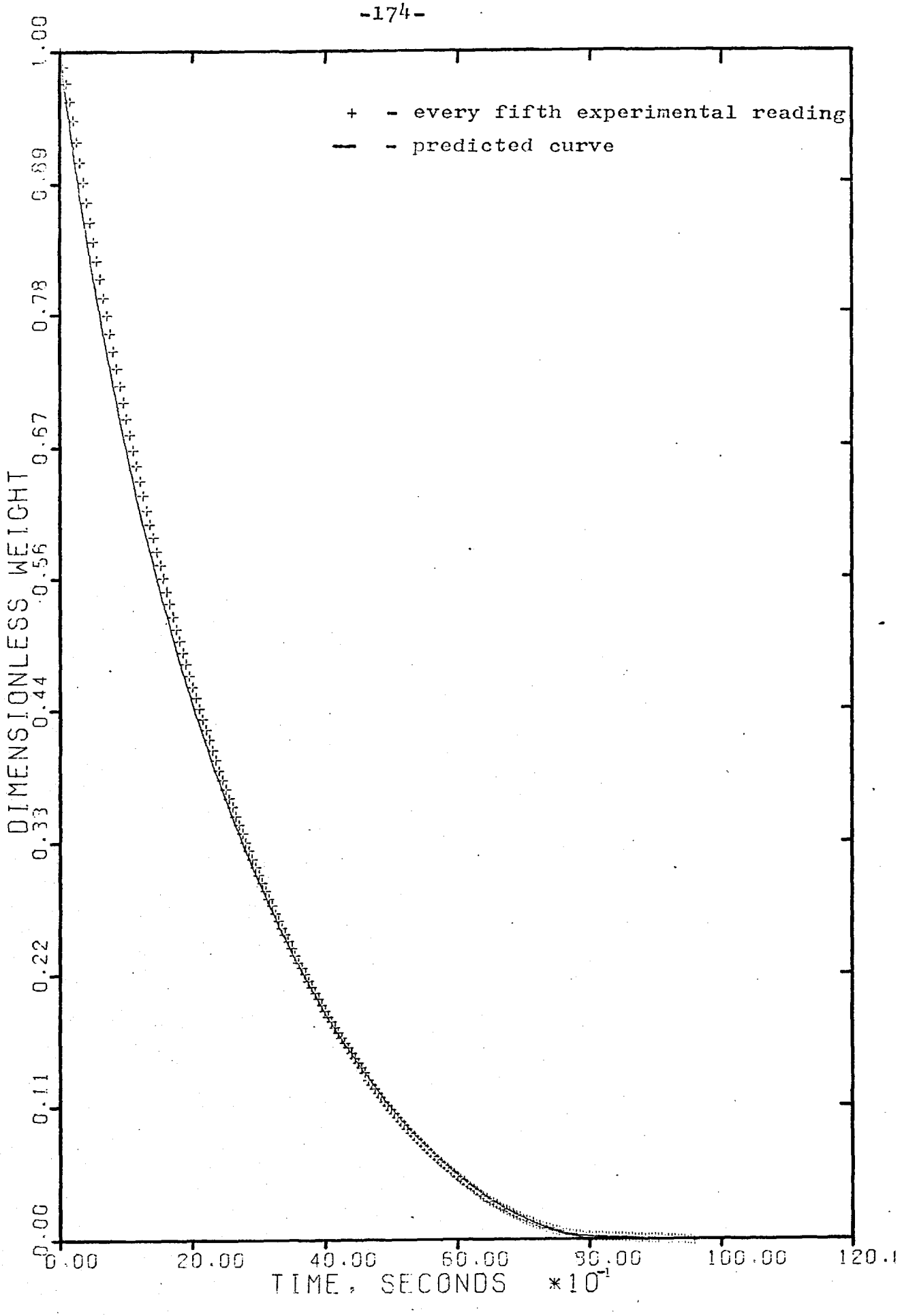


FIGURE V-2-3e UNREACTED MASS AS A FUNCTION OF TIME FOR SPHERE NUMBER 118 (RED. AT 674 °C)

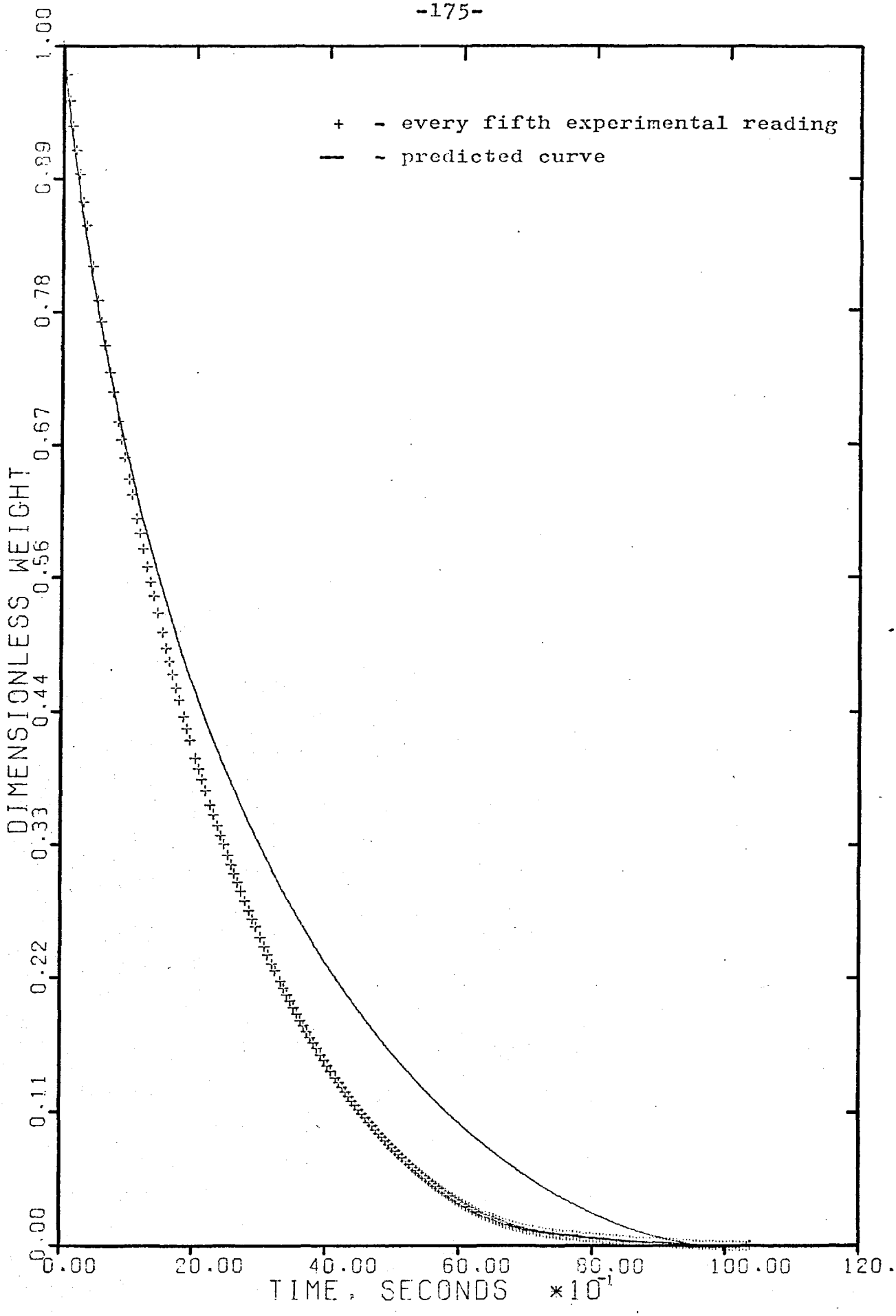


FIGURE V-2-3f UNREACTED MASS AS A FUNCTION OF TIME FOR SPHERE NUMBER 119 (RED. AT 777°C)

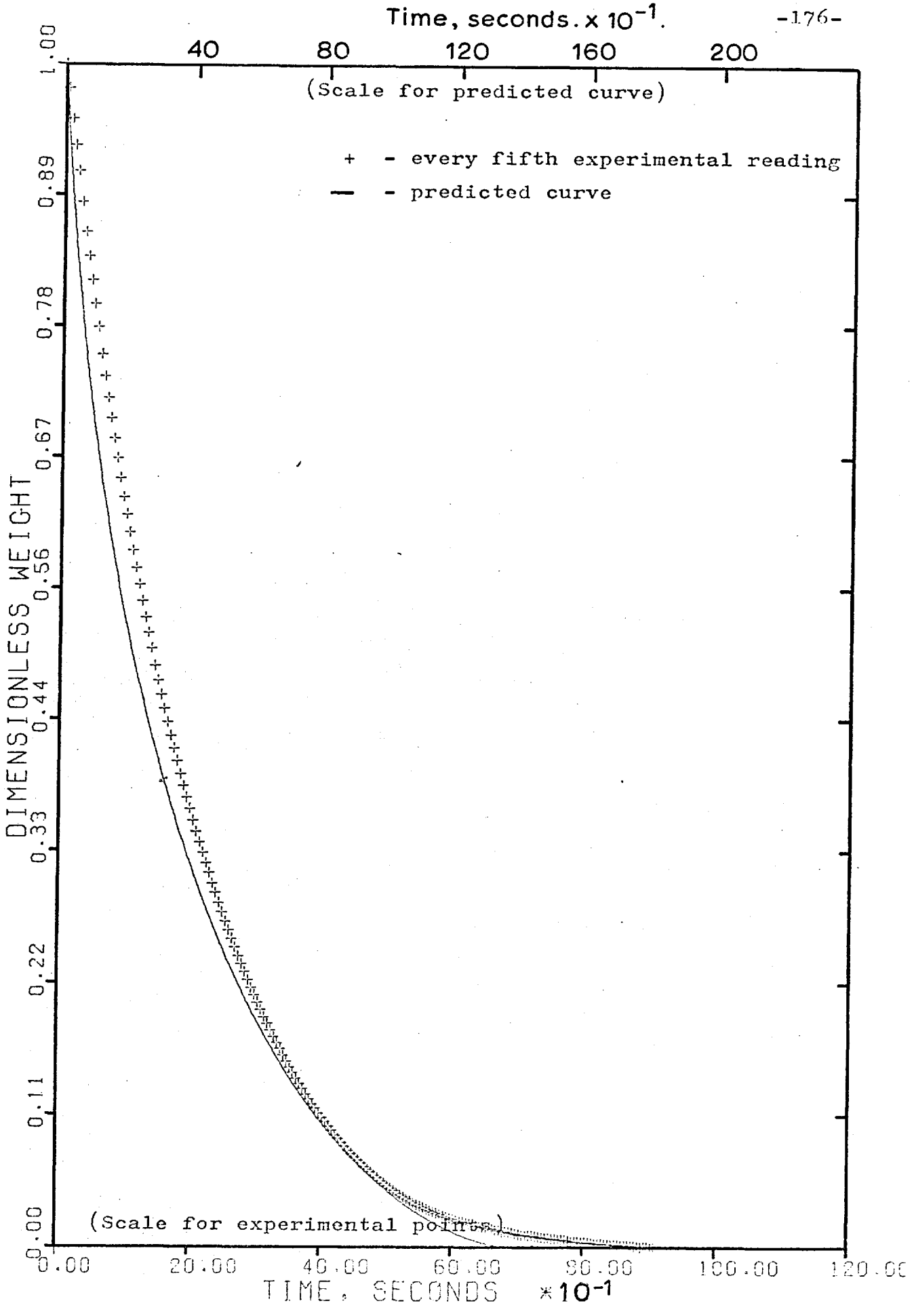


FIGURE V-2-3g UNREACTED MASS AS A FUNCTION OF TIME FOR SPHERE NUMBER 120 (RED.AT 866 °C)

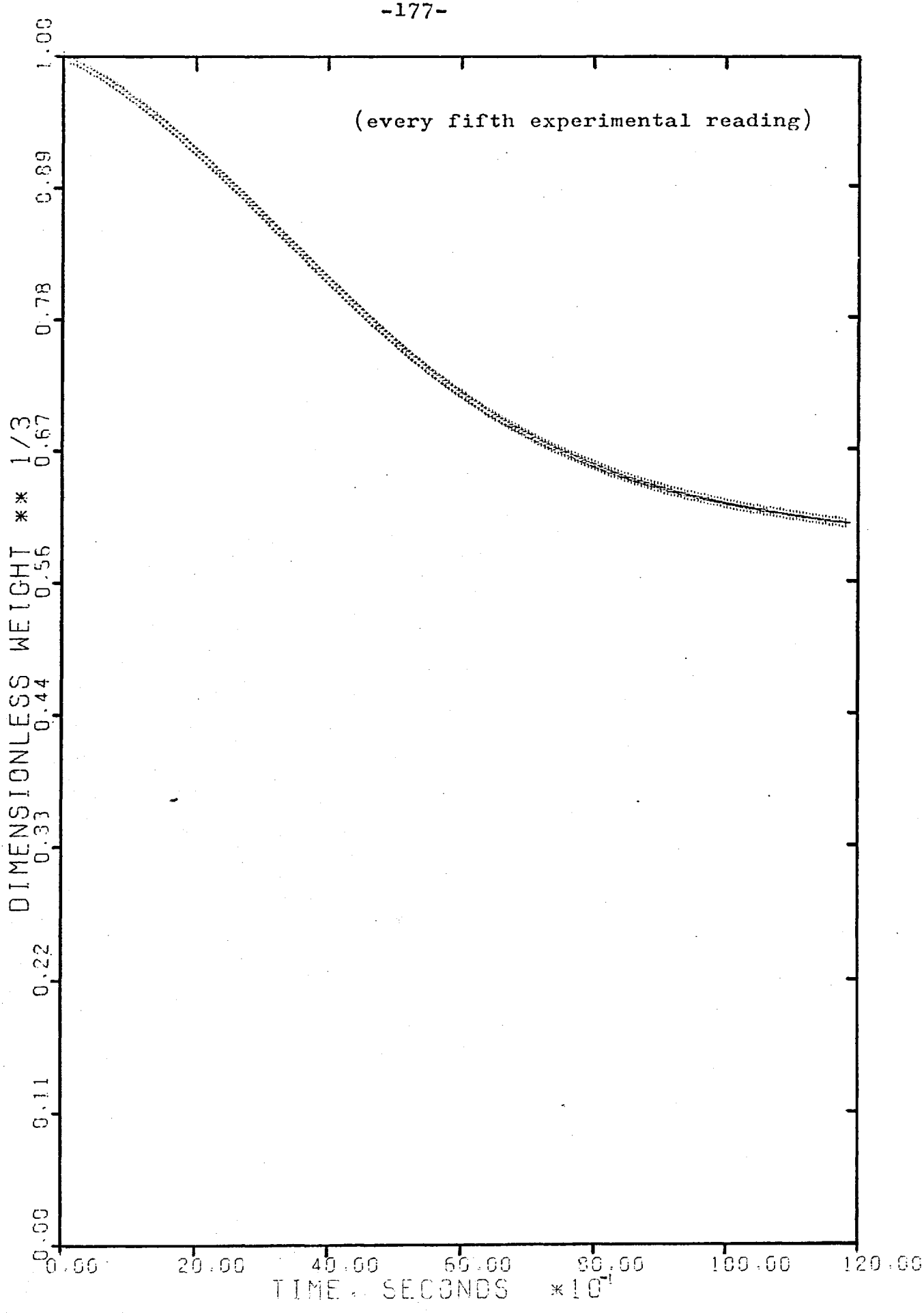


FIGURE V-2-4a CUBE ROOT OF THE UNREACTED MASS AS A FUNCTION OF TIME FOR SPHERE NUMBER 124 (RED. AT 257 °C)

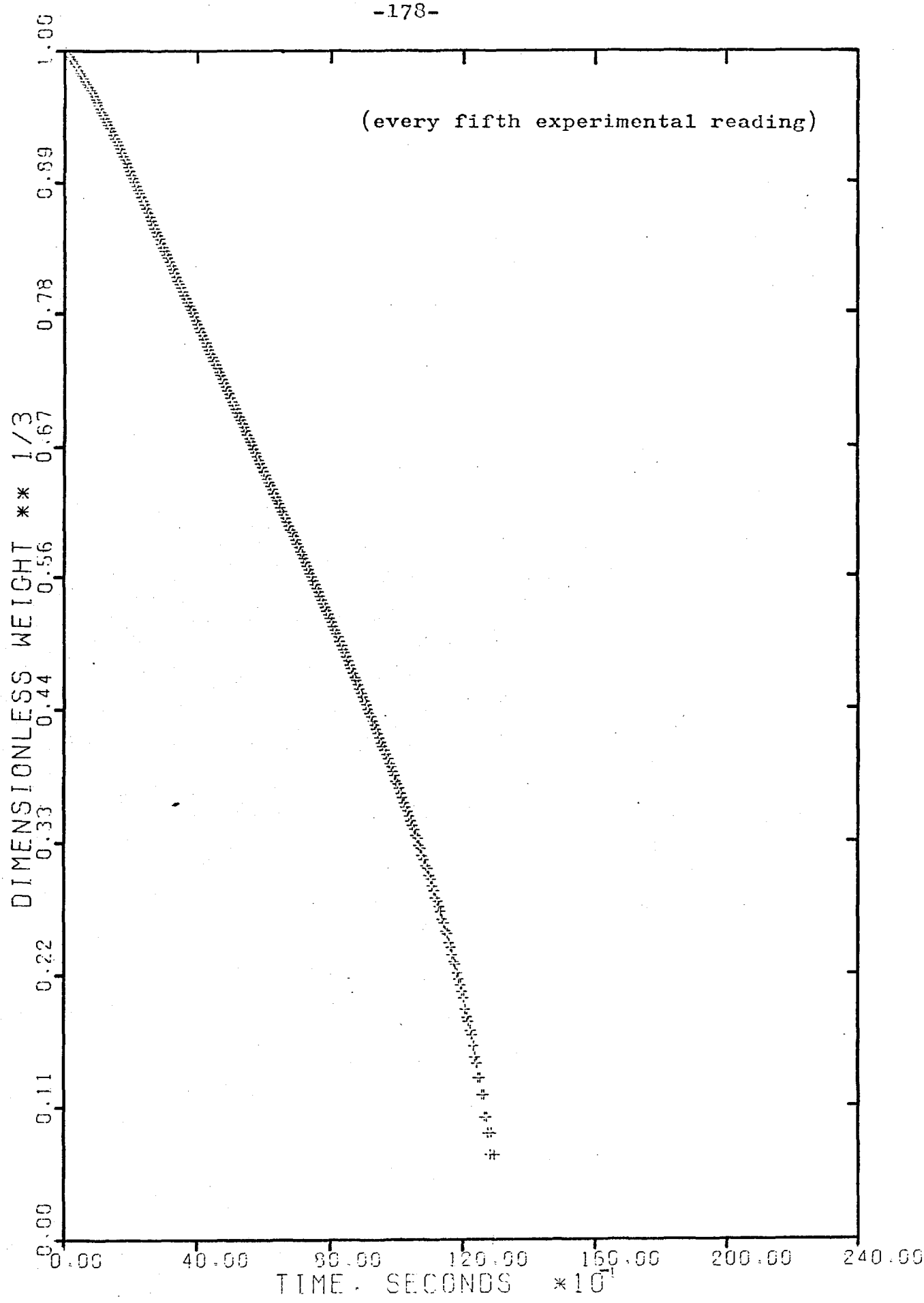


FIGURE V-2-4b CUBE ROOT OF THE UNREACTED MASS AS A FUNCTION OF TIME FOR SPHERE NUMBER 125 (RED. AT 362°C)

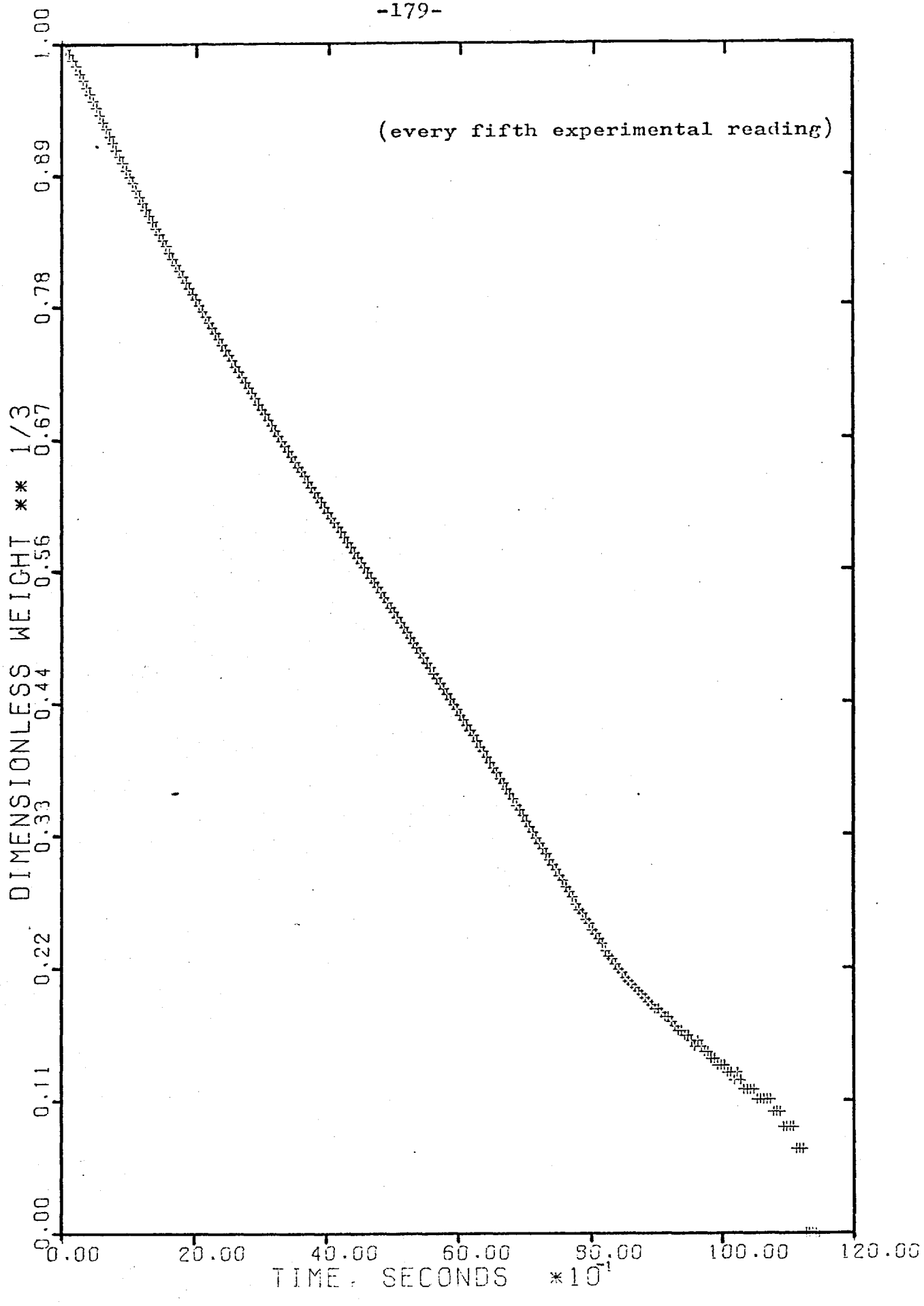


FIGURE V-2-4c CUBE ROOT OF THE UNREACTED MASS AS A FUNCTION OF TIME FOR SPHERE NUMBER 122 (RED. AT 468 °C)

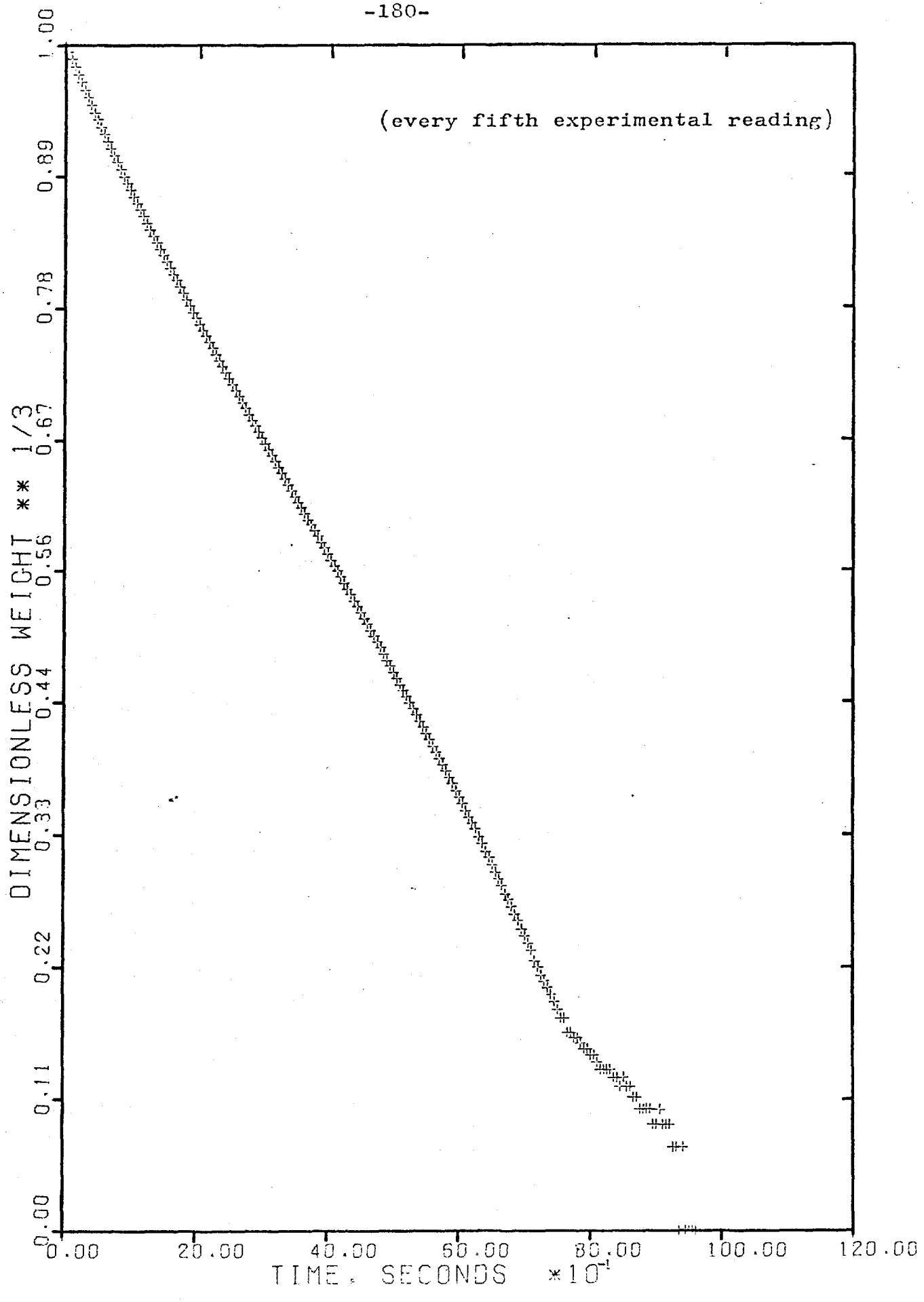


FIGURE V-2-4d CUBE ROOT OF THE UNREACTED MASS AS A FUNCTION OF TIME FOR SPHERE NUMBER 123 (RED. AT 571 °C)

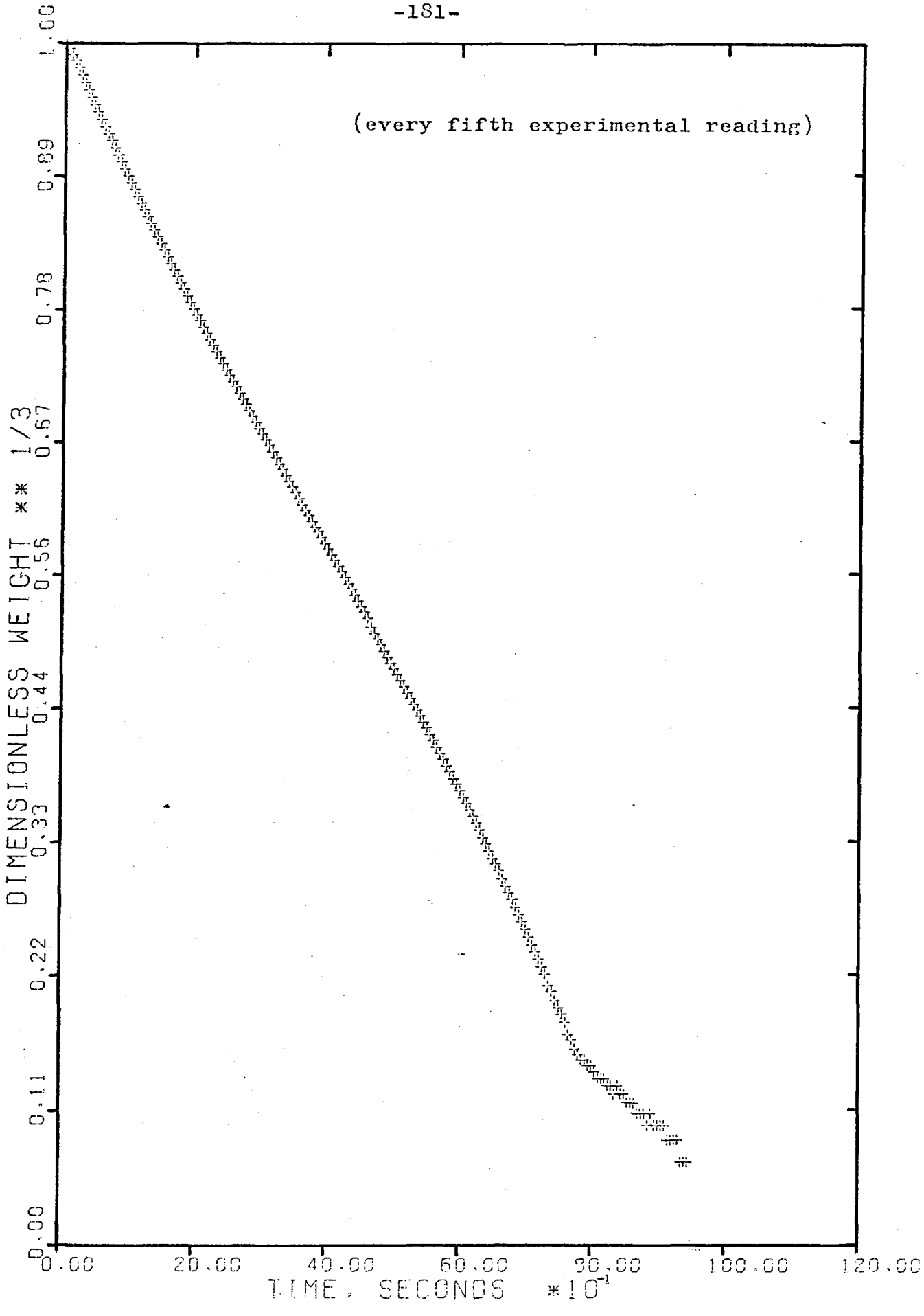


FIGURE V-2-4e CUBE ROOT OF THE UNREACTED MASS AS A FUNCTION OF TIME FOR SPHERE NUMBER 118 (RED. AT 674 °C)

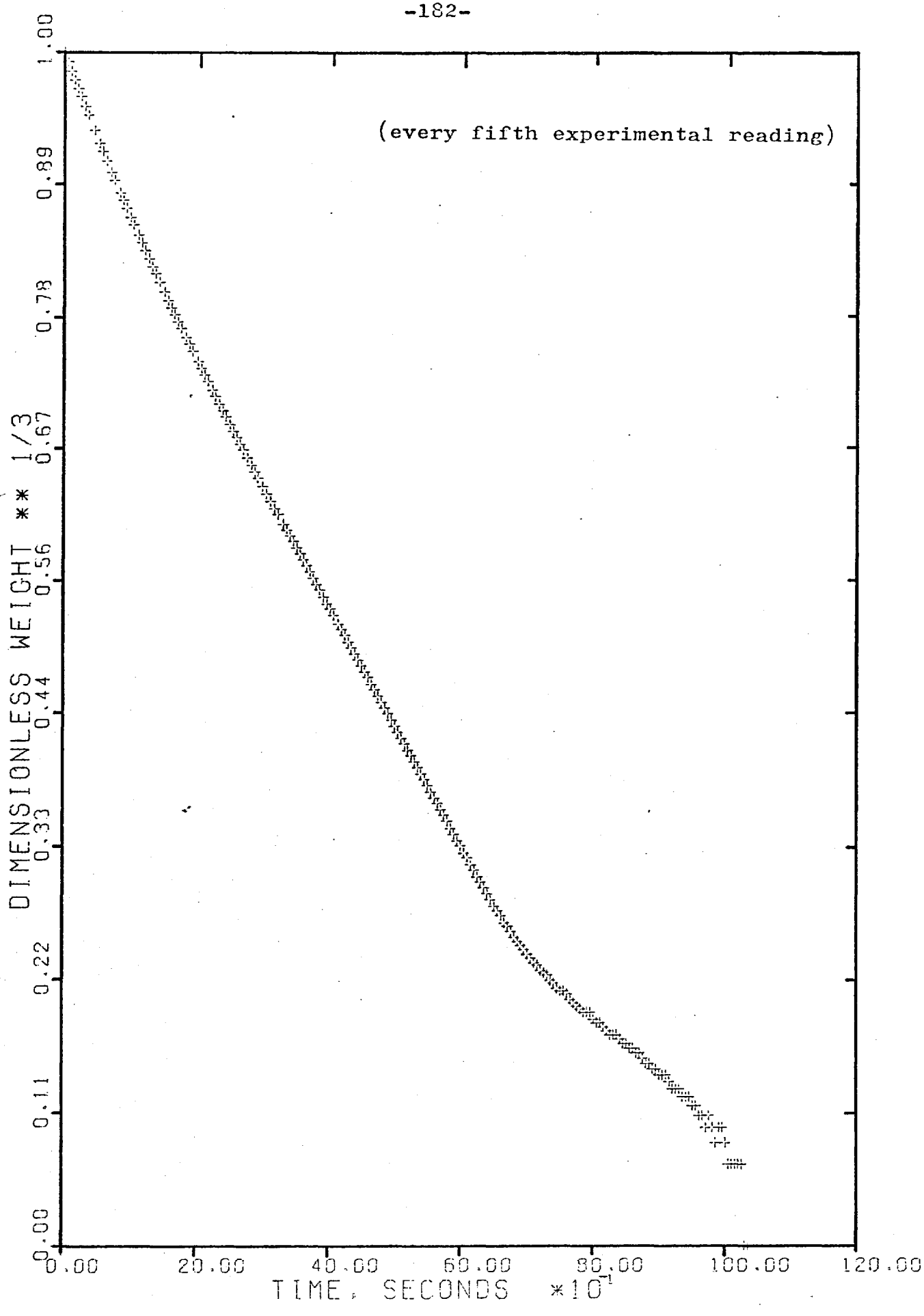


FIGURE V-2-4f CUBE ROOT OF THE UNREACTED MASS AS A FUNCTION OF TIME FOR SPHERE NUMBER 119 (RED.AT 777 °C)

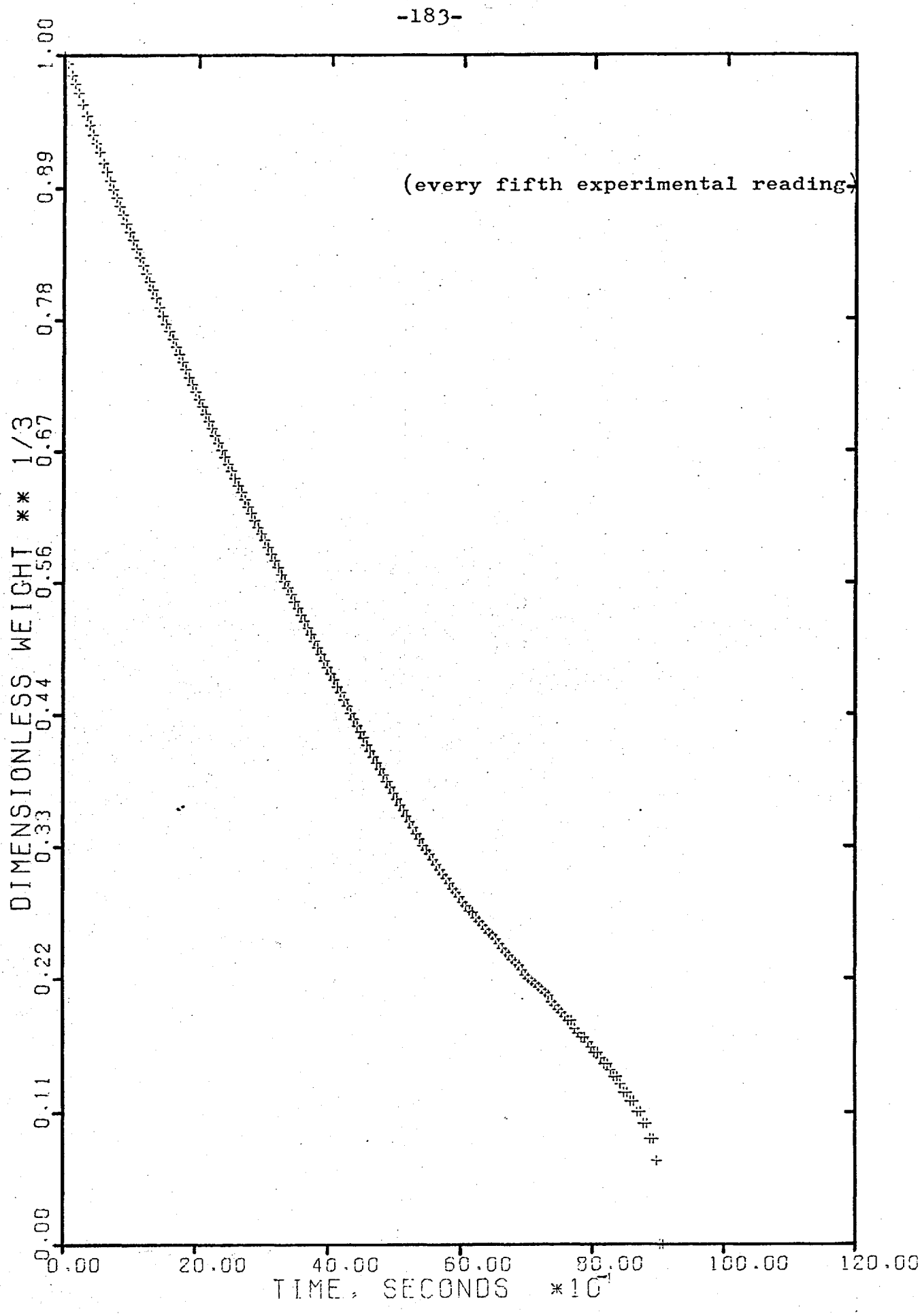


FIGURE V-2-4g CUBE ROOT OF THE UNREACTED MASS AS A FUNCTION OF TIME FOR SPHERE NUMBER 120 (RED.AT 866 °C)

TABLE V-9 NICKEL OXIDE REDUCTION RESULTS

Run No.	Wt. of NiO gms.	Rad.of NiO sphere cm.	Red.Temp. (AVG) °C	Red. %	Porosity Ni sphere %	ϵ/q_b	D_{H_2} k	D_{H_2O}, eff at Red. temp.	α_o	k_c
105	11.516	.885	364	100	63.0	0.380	5.50	.733	3.54	4.10
107	10.646	.864	470	100	62.1	0.360	5.00	.852	4.24	21.0
108	11.673	.890	572	100	61.2	0.350	4.80	.948	5.41	30.2
111	12.030	.900	476	44	-	-	-	-	-	-
112	11.679	.890	677	39	-	-	-	-	-	-
113	11.465	.886	574	42	-	-	-	-	-	-
114	11.759	.894	253	40	-	-	-	-	-	-
130	11.136	.875	826	76	-	-	-	-	-	-
116	12.351	.906	668	100	59.1	0.336	4.75	.996	6.46	47.6
118	12.384	.909	674	100	59.4	0.341	5.00	1.06	6.54	38.0
119	12.751	.920	777	100	49.6	0.250	3.00	.807	7.67	$>10^6$
120	11.928	.899	866	100	41.6	.200	1.50	.556	8.37	$>10^6$
122	11.991	.898	468	100	62.5	.355	5.50	.843	4.59	15.0
123	11.527	.885	571	100	61.4	.347	5.00	.940	5.39	36.0
124	11.757	.890	257	89.5	63.0	.380	9.50	.650	2.82	1.28
125	11.345	.879	362	100	62.8	.370	5.50	.719	3.59	3.16
126	11.278	.879	473	100	62.2	.350	5.00	.817	4.50	20.9
127	11.261	.885	770	100	50.7	.255	3.00	.811	7.26	$>10^6$
131	11.217	.878	876	100	42.0	.205	1.50	.561	8.32	$>10^6$
132	11.224	.879	570	100	61.0	.345	5.00	.935	5.33	27.0
133	11.355	.881	668	100	59.5	.336	4.75	1.02	6.25	70.0

CHAPTER VI

DISCUSSION

VI-A-1 EXPERIMENTAL STRATEGY

This study has attempted to follow, in general, the experimental strategy put forward by Hills[62] and reiterated by Bradshaw[91] for the elucidation of rate controlling factors in gas/solid reactions. Reduction experiments were carried out using spherical samples under gas flow conditions for which mass transfer coefficients may be calculated with sufficient accuracy from known correlations i.e. the Frossling Equation. The temperature of reacting samples was recorded by an imbedded thermocouple. Microscopic studies were carried out on partially reduced pellets to determine the nature of the reaction interface and the effect of reduction temperature on the structure of the reduced layer. Most important, independent measurements were made of the effective gas diffusivities of reactant and product gases in reduced layers. Experiments to determine the effective conductivity of reduced layers were unnecessary because of the small temperature gradient within the solid during reaction (Section VI-H) and the large equilibrium coefficient (Appendix A).

The outlined strategy enables quantitative calculations to be made of the rate of reaction based on the assumption of transport control (Chapter III), if the microscopic examination shows the assumption of topochemical behaviour to be valid. If the experimental rate is substantially slower than that given by the transport model, a chemical step at the interface may be concluded to be of importance. By suitable allowance for this additional step (Chapter III), the value of the chemical rate constant can be determined from the experimental data.

VI-A-2 DETERMINATION OF EFFECTIVE GAS DIFFUSIVITIES

The independent measurement of the effective gaseous diffusion coefficients required the development of a suitable technique. This technique was developed, to a large extent, by my predecessor, Paulin, who, in conjunction with Hills, selected the basic geometry and used the technique to determine the effective diffusion coefficient of carbon dioxide in both calcium carbonate and lime spheres. The hollow sphere technique was chosen because it provided a small self contained unit which could be easily held under isothermal conditions during experimental measurements. Also, the geometry took advantage of the shrinkage behaviour of most metallurgically important reactant solids in that samples could be so drilled that they would form a tight seal when they shrunk onto the diffusion shaft during reaction. For solids which do not exhibit this shrinkage behaviour, the hollow spheres could be sealed to the shaft with a sealing compound. As the area over which sealing must be effected is relatively small, this would be a simple matter. For high temperature measurements, a glass which fuses at an appropriate temperature or a refractory cement may be used whereas room temperature measurments can make use of rubber cements.

This basic technique was used in this work but was modified so that the measurements could be carried out iso-barically and so that permeability measurements could be made. The results could then be analysed by equations derived from the dusty-gas model (Chapter II), by straightforward mathematical techniques.

VI-B MASS TRANSFER RESULTS

VI-B-1 EXTERNAL MASS TRANSFER

The results of the measurement of the external mass transfer coefficients (Figure V-1-1) can be favourably compared with the correlations of other workers. For mass transfer to a sphere from a gas stream whose boundaries are remote from the sphere, Frossling proposed an empirical correlation between the relevant dimensionless groups, which has been almost universally accepted:-

$$Sh = 2.0 + 0.60\ Re^{\frac{1}{2}}\ Sc^{\frac{1}{3}}$$

The form of the experimental equation was assumed to be similar to that of Frossling. However, the constant, 0.60, and the exponent, $\frac{1}{2}$, were kept as variables to be determined from the experimental measurement. Rowe and Claxton[92] have studied mass transfer from spheres in arrays of varying porosity and determined the effect of porosity on the constant, 0.60, and the effect of Reynolds numbers on the value of the exponent. Because of the different geometry used the results cannot be compared quantitatively. However, they found that at low Reynolds numbers the exponent of the Reynolds number approached $\frac{1}{3}$. Also, as the porosity of the array of spheres decreased towards the closest packing density, the constant term approached 3.0. It can be seen that the experimental results obtained in this work follow this general trend.

VI-B-2 INTERNAL MASS TRANSFER

Although no correlations are available for comparison with the results of the internal mass transfer measurements obtained in this work, results which Paulin[87] derived from his work are of some interest. Using a gas delivery geometry similar to that shown in Figure IV-1-6, Paulin showed that the change in the internal mass transfer coefficient, calculated from curves of the form of Figure V-1-7, was proportional to the square of the Reynolds number. The relationship between Reynolds number and pressure difference in the araldite hollow sphere model, using a similar delivery geometry (Figure IV-1-7), lends support to this conclusion.

Paulin explained this square relationship by considering the impingement of the cylindrical feed stream on the concave spherical surface. The high velocity stream spreads out on impingement , slowing down as it spreads, forming a layer whose velocity is inversely proportional to its distance from the area of impingement. Eventually, a point on the concave surface is reached where the velocity is small enough so that the mass transfer occurring past this point may be neglected. As the stream velocity increases, this point is further removed from the area of impingement. Thus, as the internal flow rate is increased, mass transfer is increased because of the higher velocity and the greater effective area over which mass transfer is occurring. The high exponent of the Reynolds number reflects the dual source of increased mass transfer.

However, the results of the measurements of internal mass transfer coefficients in this work, using a gas delivery geometry which gave a conical feed pattern, showed the coefficients to be directly proportional

to the Reynolds number. This exponent of unity can be explained by considering the greatly improved distribution of the internal feed stream as indicated by the lack of preferential erosion of the hollow naphthalene spheres.* If the gas stream is well distributed over the internal sphere surface, then an increase in the internal flow rate does not provide an increased area for mass transfer, and the rate of mass transfer is increased solely because of the decrease in boundary layer thickness.

Although the form of the equation linking the Sherwood, Reynolds and Schmidt numbers was assumed to be the same as for the external determination, the linear dependence of the mass transfer coefficient on Reynolds number allowed the results to be extrapolated with some confidence to a Reynolds number of zero. The intercepts so obtained can be compared with the factor, 2.0, in the Frossling equation. Although the values obtained in this work may be larger than those predicted by purely theoretical considerations, this certainly does not invalidate them. In fact, Cornish[93] has suggested that such values cannot be derived from a theoretical approach as they are theoretically meaningless. He has suggested that the concept of mass transfer in a stagnant fluid and mass transfer to a flowing gas stream are mutally exclusive events and that this intercept, particularly for enclosed geometries, can be regarded as merely a curve fitting device.

The rather low value of the constant modifying the Reynolds number stems from the definition of the characteristic length used in the calculation of Reynolds number, and the small cross-sectional area used for velocity calculations, both of which tend to overestimate the true values of the Reynolds numbers at the sphere wall.

---

* FOOTNOTE:
It should be noted that, although, for reasons explained in Section V-1-A-2, the initial determination of internal mass transfer coefficients was poor, the source of error could not be expected to affect the exponent of the Reynolds number.

VI-C PERMEABILITY RESULTS

The results of any experiment which determined the effect of system pressure on the permeability of a porous layer were assumed to lie on a straight line. However, some porous solids exhibit anomalies in this relationship at very low system pressures[14], i.e. the Knudsen permeability minimum. Nevertheless, this assumption is consistent with the first order approximations used in the application of the dusty-gas model.

VI-D LIME DIFFUSION RESULTS

The results of the diffusion coefficient measurements in lime spheres, shown in Table V-1, are plotted along with those of Paulin and Hills on page 935 of reference number 75.* Paulin's measurements were made using the same technique as that used here, but the apparatus and sphere dimensions were somewhat different. Hills results were calculated from data on the decomposition of calcium carbonate spheres assuming a heat and mass transfer control model in which all gaseous diffusion was assumed to be Knudsen in character.

Even more important, the agreement between the results of the diffusion measurements and the permeability measurements tends to confirm the validity not only of both experimental techniques but also the decomposition model chosen by Hills.

---

* FOOTNOTE:

A copy of this reference is enclosed, inside the back cover.

The Knudsen character of the diffusion in these lime spheres justifies the assumptions made in the experimental technique and in the subsequent analysis of the experimental results. The non-isobaric technique used in the diffusion measurements on lime spheres was not a source of error when the overall partial pressure driving force was known, as Knudsen diffusion is independent of total pressure. Similarly, the analysis of the results, which did not consider bulk flow, was equally valid, as the flux of a gas diffusing by Knudsen diffusion is independent of the behaviour of other components in the system. Also, the assumption of negligible internal mass transfer resistance at high values of the internal flow rate seems to be confirmed by the excellent agreement between the two series of results (Table V-1).

VI-E POROUS IRON RESULTS

The results of the diffusion coefficient measurements on the porous iron spheres, shown in Table V-4, were, at best, disappointing. It was to be expected that errors in this system would be large and as such it provided an extreme test of the capabilities of the experimental technique. The source of most of the error was, of course, the very high porosity of the reduced samples, a consequence of the high weight-low density starting material and the low weight-high density product.

Because of this extreme porosity, samples tended to deform on reduction and only a few samples were sufficiently intact to attempt a diffusion measurement. Because of the very low mechanical strength of these reduced spheres, the accurate measurement of their physical

dimensions was vitually impossible and loss of some of the solid material due to abrasion was inevitable. The low mechnical strength also made the complete sealing of the samples to the diffusion shaft a difficult task. The high porosity indicated that non-homogeneity in the reduced sample might lead to inordinately large void spaces in localized areas.

Not only did the high porosity prove detrimental to the physical condition of the pellets, but the large fluxes of the diffusing species due to the high porosity created additional difficulties. These large fluxes would have seriously affected the boundary layers both inside and outside the hollow sphere and would thus have lead to errors in extraplating the naphthalene results to the diffusion measurements. This, coupled with the already poor correlation obtained for the first naphthalene determination, was probably a large source of error. Also, the large fluxes seriously reduced the driving forces for diffusion, as can be seen from the tabulated data of Table V-2, the exit concentrations of both streams being far from the inlet concentrations. This behaviour called into question the method used in calculating the effective bulk concentrations, described in Section V-1-C-2. In particular the assumption of perfect mixing inside the hollow sphere could lead to very large errors when the difference between the exit and inlet concentrations was large. This last source of error was the reason for the decision to reject the diffusion results determined with argon on the inside and hydrogen on the outside of the hollow iron sphere. The difficulties encountered with the argon-hydrogen mixture during the measurement of effective diffusivities in porous nickel (Section IV-1-B-2) also

lend support to this decision. Consequently, the values for the ϵ/q ratio in Table V-4 were determined from the diffusivities measured when the internal gas was hydrogen and the external gas was argon.

In spite of the numerous sources of error discussed above, the diffusivity values obtained with hydrogen as the internal gas and argon as the external gas are of the same order as those measured by Harwell in a study of the reduction of ferrous chloride by hydrogen[94]. In fact, they are consistent with the values of the diffusivity predicted by the heat and mass transfer control model discussed and derived in Chapter III, when applied to the ferrous chloride reduction rates measured at Harwell.

VI-F POROUS NICKEL DIFFUSION RESULTS

As can be seen from the tabulated results of the diffusion measurements in porous nickel (Table V-7), insufficient samples were treated to firmly establish the relationship between all the variables controlling the structure of the porous product and the effective diffusivity of various gases in this product. After some preliminary determinations, it was decided to confine this investigation almost entirely to nickel produced from oxide spheres of uniform porosity which were reduced at varying temperatures.

After the preliminary determinations mentioned above, it was decided to use a pre-treatment temperature of 750°C and to determine the effect of different soaking times on the final diffusivity.

(Spheres No. 6, 7, 8, 9, and 10) As the tabulated data shows, any noticeable effect was absent and afterwards all spheres were soaked at 750°C for 24 hours.

The determinations of effective diffusivities of these five spheres, which were identically prepared, served as an excellent check on the precision and reproducibility of the experimental technique. However, it may be noticed that the measured effective diffusivities of these five spheres are somewhat lower than the values determined for other spheres, ostensibly prepared under the same conditions. Although it was attempted to make all starting material identical, three mixtures of binder and nickel oxide powder were prepared. Although the prepared compositions were identical, the mixing, drying and subsequent grinding were not necessarily the same. This can possibly explain the discrepancy as only spheres 6 to 10 were taken from the second of these three mixtures. However, all subsequent diffusion samples and all reduction samples were taken from a single large mixture of binder and nickel oxide powder, which made up the third mixture.

Enough samples were pressed at 100 kN/m^2 and reduced at varying temperatures that the trends in the measured variables may be shown graphically. Figures VI-2, VI-3, VI-4 and VI-5 show the relationships between the important parameters. Unfortunately, relationships involving porosity show most of the experimental points clustered about one part of the curve. This can be explained by the fact that all samples reduced at temperatures below 550°C had similar porosities, large changes in porosity only occurring as the reduction temperature exceeded 550°C.

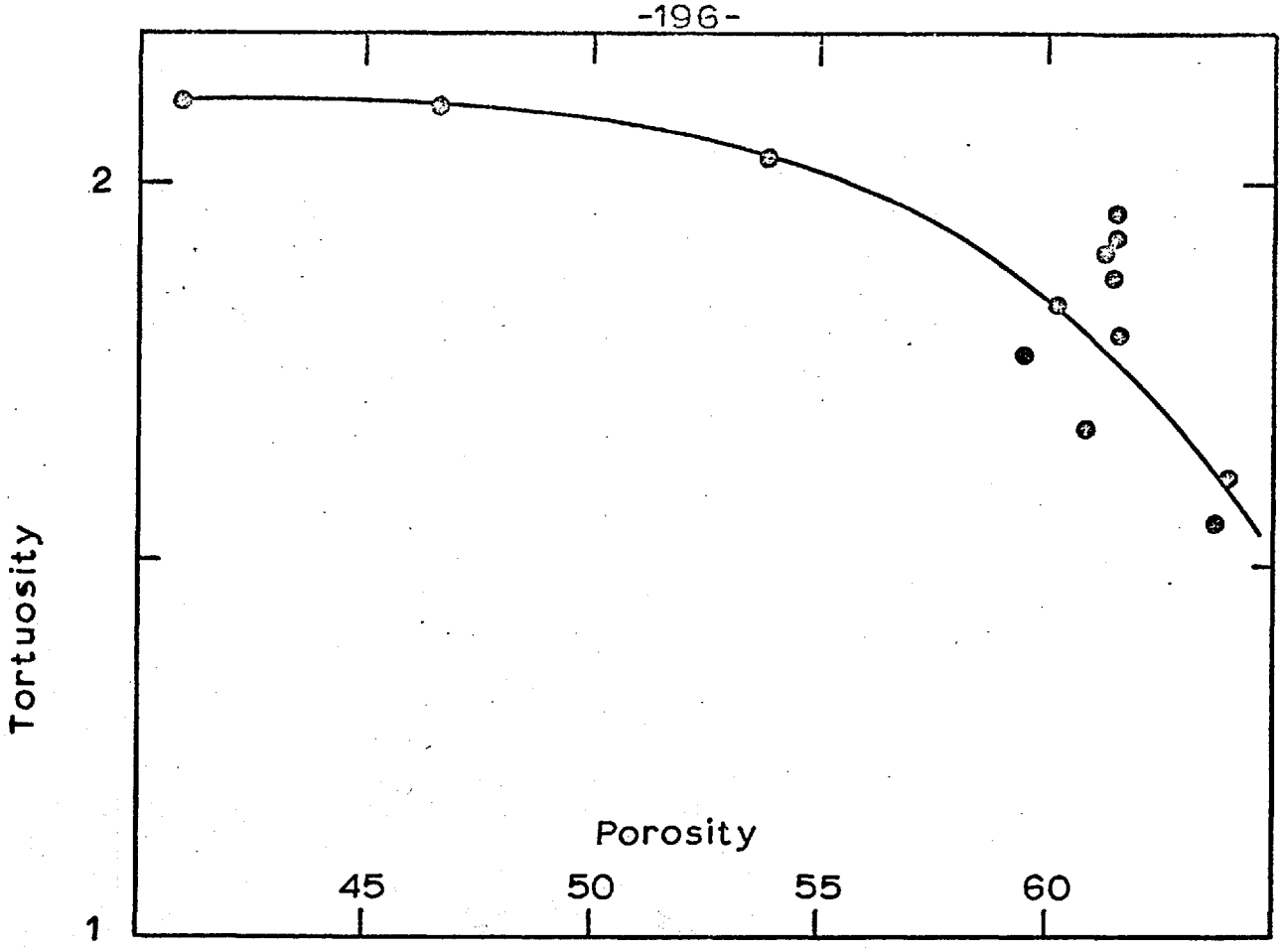


Fig. VI.1b. CHANGE IN TORTUOSITY(q) WITH POROSITY(ε) FOR SPHERES WITH GREEN POROSITY OF 40%

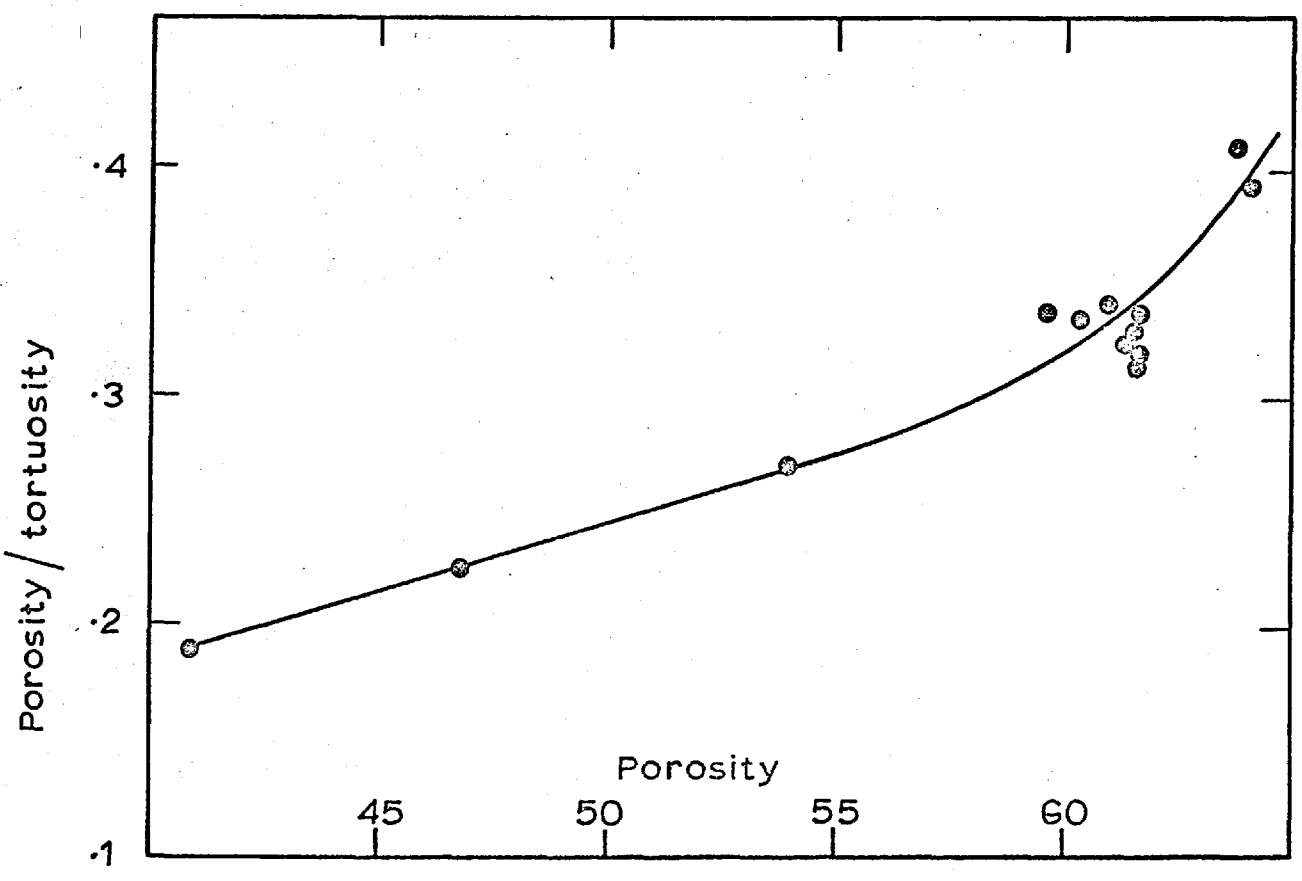


Fig. VI.1a EFFECT OF SAMPLE POROSITY ON DIFFUSIVITY RATIO (ε/q) FOR SPHERES WITH GREEN POROSITY OF 40%.

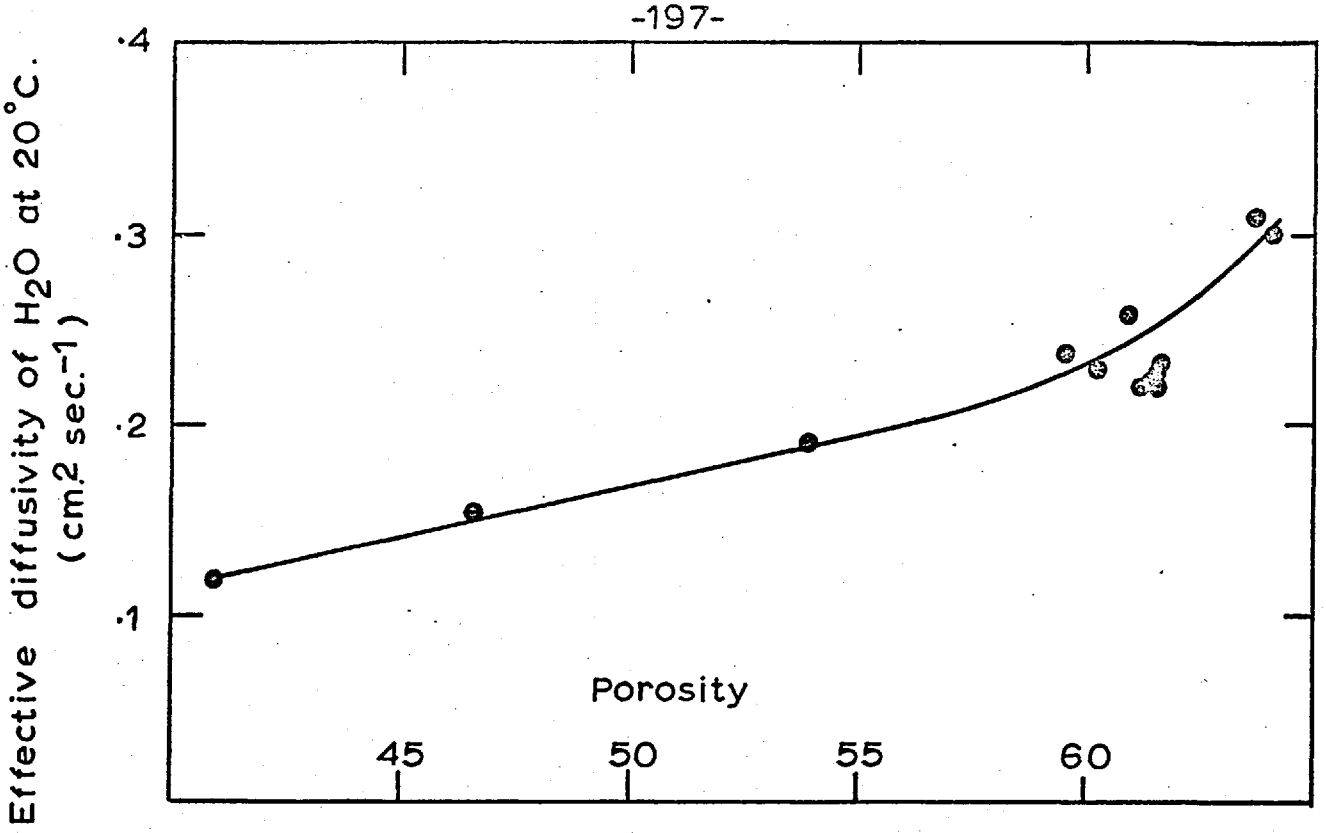


Fig. VI. 2b RELATIONSHIP BETWEEN SAMPLE POROSITY AND $(D_{H_2O})_{eff.}$ FOR SPHERES WITH GREEN POROSITY OF 40%.

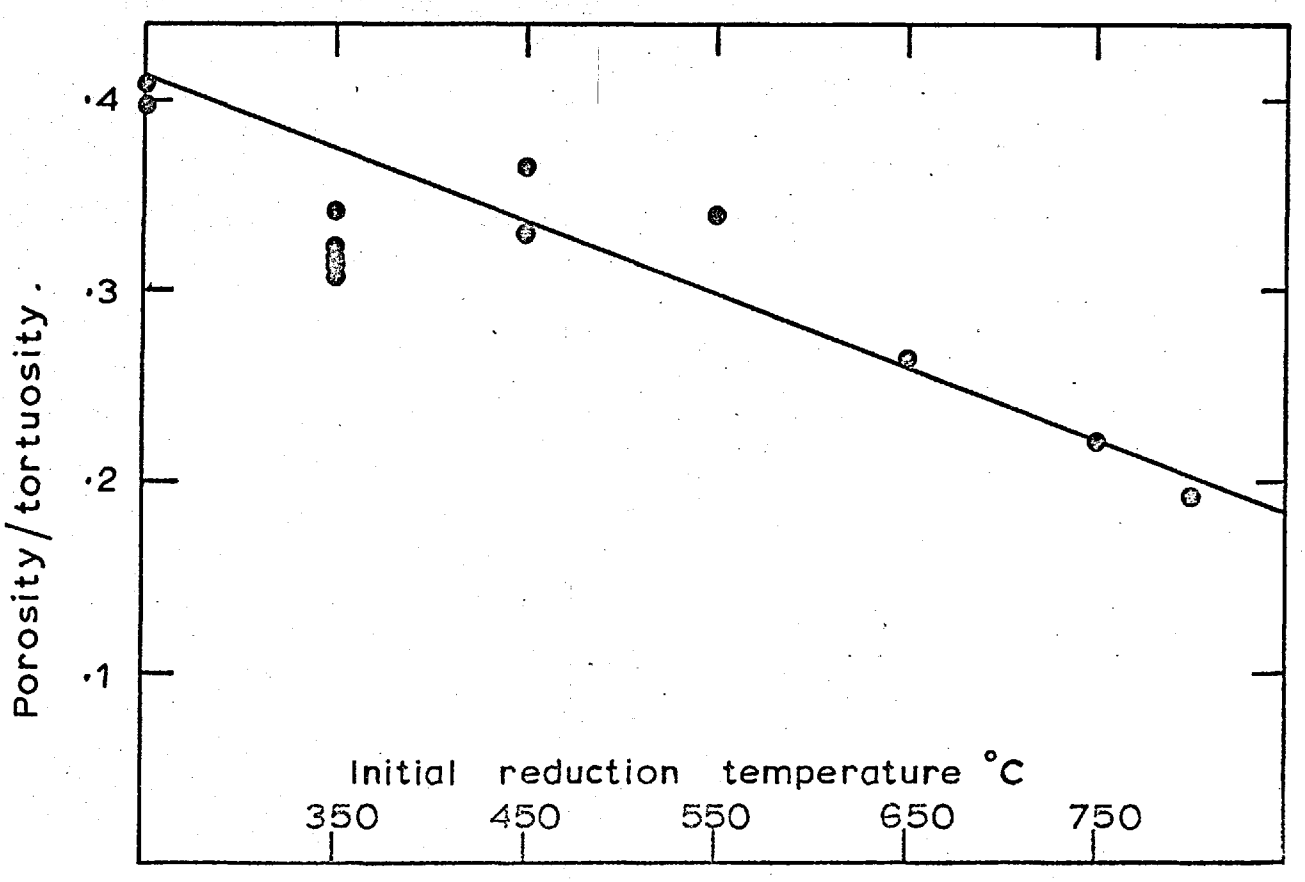


Fig. VI. 2a. EFFECT OF REDUCTION TEMPERATURE ON DIFFUSIVITY RATIO (ε/q) FOR SPHERES WITH GREEN POROSITY OF 40%.

Figure VI-1a shows the relationship between the directly measured sample porosity and the ratio of porosity and tortuosity calculated from the observed effective binary diffusion coefficient. in the porous layer, and equation II-1-2. Most workers observe a linear form for this relationship, usually determined for samples pressed to different porosities.
(See for instance, the curve for lime spheres in enclosed reprint). However, in this case the varying porosity is a result of varying the reduction temperature, and as can be seen from Figure VI-1b, this brings about a change in the tortuosity of the diffusion path, the tortuosity decreasing as the porosity increases. This is not normally observed in the aforementioned systems, the tortuosity appearing to remain constant. The increase in tortuosity and decrease in porosity as the reduction temperature increases should not necessarily be associated with a sintering process. It is a consequence of the c hanging chemical reaction step rather than an agglomeration of reduced particles by solid state diffusion, as all but the highest reduction temperatures are below the Tamann temperature. Even at temperatures below 300°C where any sintering would be out of the question, the changes in the specific surface area and porosity of reduced porous nickel spheres have been extensively studied (See Chapter II). The increase in activity of nickel reduced at such low temperature, due to these changes, is well known and is applied in its production for use as a catalyst.

Figure VI-2a shows the effect of reduction temperature on the ratio of porosity andtortuosity. The straight line does not represent a conclusion as to the form of the relationship but presents only an

average correlation of the experimental data.

Figure VI-2b shows the effective diffusivity of water through the reduced nickel layer at room temperature as a function of the sample porosity. The values for the diffusivity of water were calculated from the ϵ/q values shown in Figures VI-1a and VI-2a and the Knudsen diffusion coefficients determined from the permeability measurements on the corresponding sphere , combined via equation II-1-3.

VI-G RESULTS OF GAS SWITCHING TIME LAG EXPERIMENT

Figure V-2-1 shows the effect of increasing the flow rate of reducing gas on the time required for the composition around the sample to change to specific concentrationsof a reducing gas stream. The figure shows that a relatively high flow rate of reducing gas is required to reduce this time lag to a realistic value. In all reduction experiments a flow rate of 3.0 litres per minute (NTP) of hydrogen was used.

This experiment also shows the danger in attempting to extrapolate rate of weight loss curves to zero time in order to calculate specific reaction rate constants in the absence of diffusion effects. As the figure demonstrates, the error involved in such an extraplation could be considerable.

VI-H RESULTS OF MEASUREMENT OF TEMPERATURE GRADIENT ACROSS REDUCING LAYER

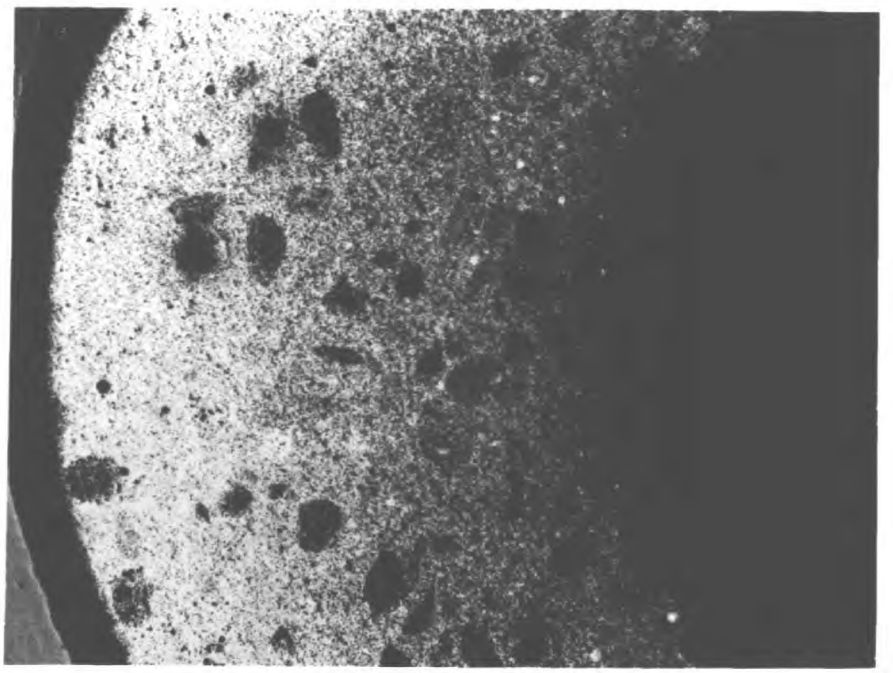
Figure V-2-2 shows that the temperature difference in the porous solid during reduction is very small. The initial increase in the temperature at the sample surface due to reaction at that point is quickly assumed by the centre of the sphere as the heat of reaction is conducted inwards. It can be concluded, in this case, therefore, that the bulk of resistance to heat transfer is in the gas layer surrounding the sample.

VI-I OBSERVATION OF PARTIALLY REDUCED SPHERES

Plates 5 and 6 show the changing character of the reaction zone as the reduction temperature is increased. Metallic nickel appears white on these plates and the unreduced oxide appears black. Reduction conditions for each sample can be found with reference to Table V-9 . Each photomacrograph has been placed so that the extreme left side shows the exterior surface of the sample and the right side a part of the sample sufficiently remote from the reaction interface to show the overall appearance of the unreduced layer. Note that the reaction zone is extremely diffuse at the lowest reduction temperature (250°C) and that at this temperature some islands exist in this zone which appear even less reduced than the surrounding sample. As the reaction temperature is increased, the chemical rate constant increases (see next section) and the reaction zone contracts until at temperatures above 550°C the reaction zone may be approximated by an interface.

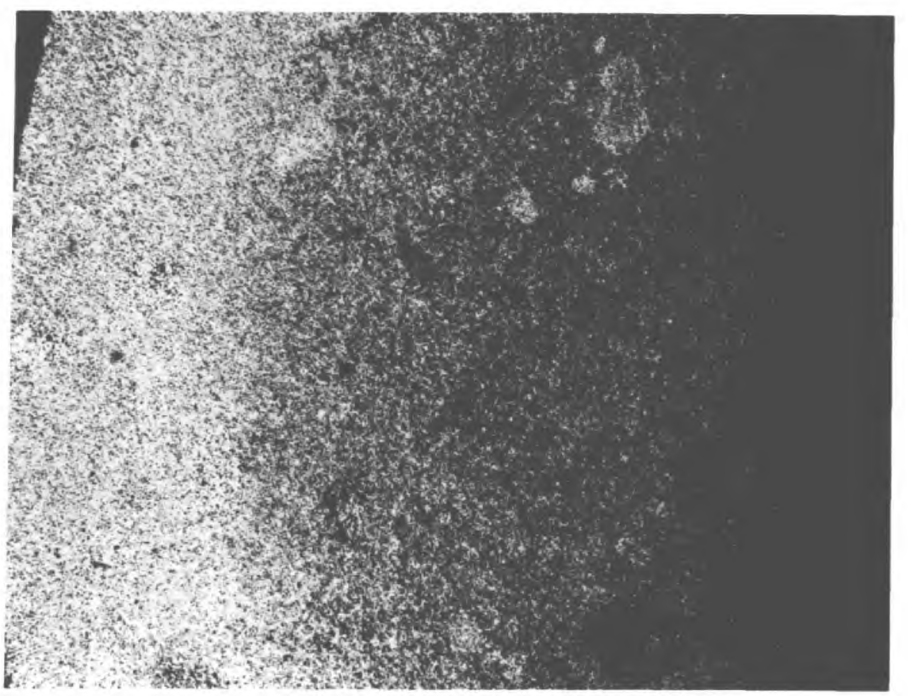
Plate 7(A) shows the appearance, at high magnification, of a fully reduced layer produced at 476°C. The spaces between reduced particles have been filled with 'Araldite' epoxy resin by mounting specimens under vacuum. Note the micro-porosity produced within each reduced particle and the apparent lack of sintering of these particles.

Plate 7(B) shows the appearance of reduced particles adjacent to unreduced particles. The sample shown was reduced at 677° C, but the characteristics observed have been found in all samples. The most important characteristic shown in this sample is the almost complete lack of semi-reduced particles. Each lump of oxide appears



(A)

X 13·5

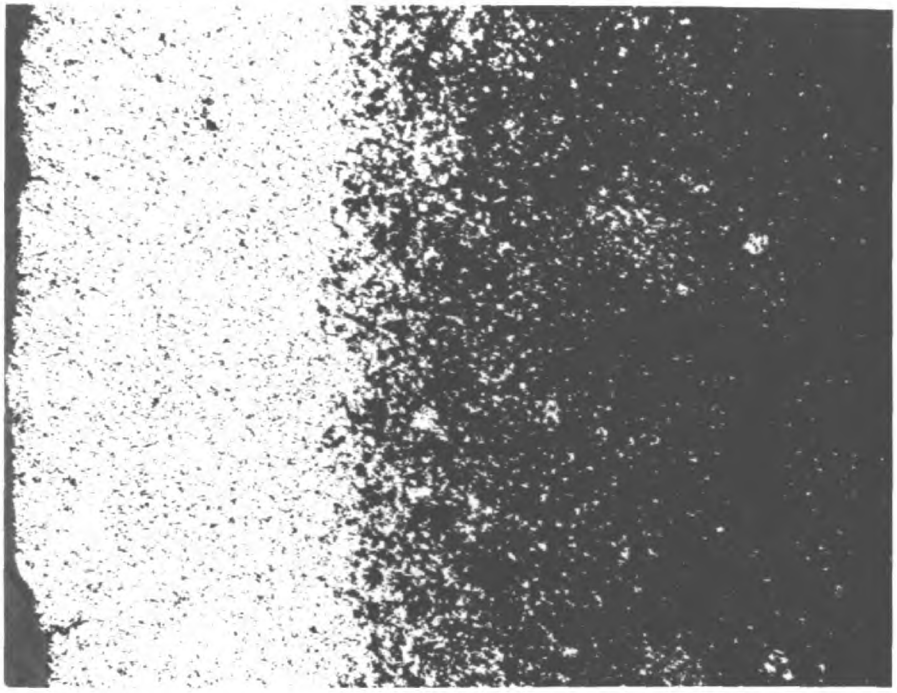


(B)

X 23·0

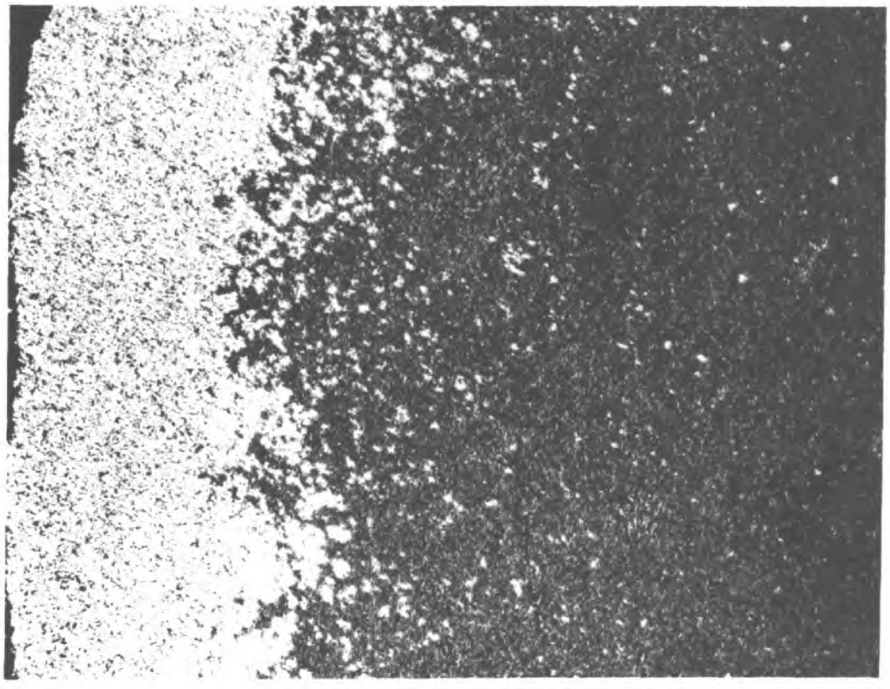
PLATE 4 (A) PHOTOMACROGRAPH OF SAMPLE NO. 114

(B) PHOTOMACROGRAPH OF SAMPLE NO. 111



(A)

X 29·5

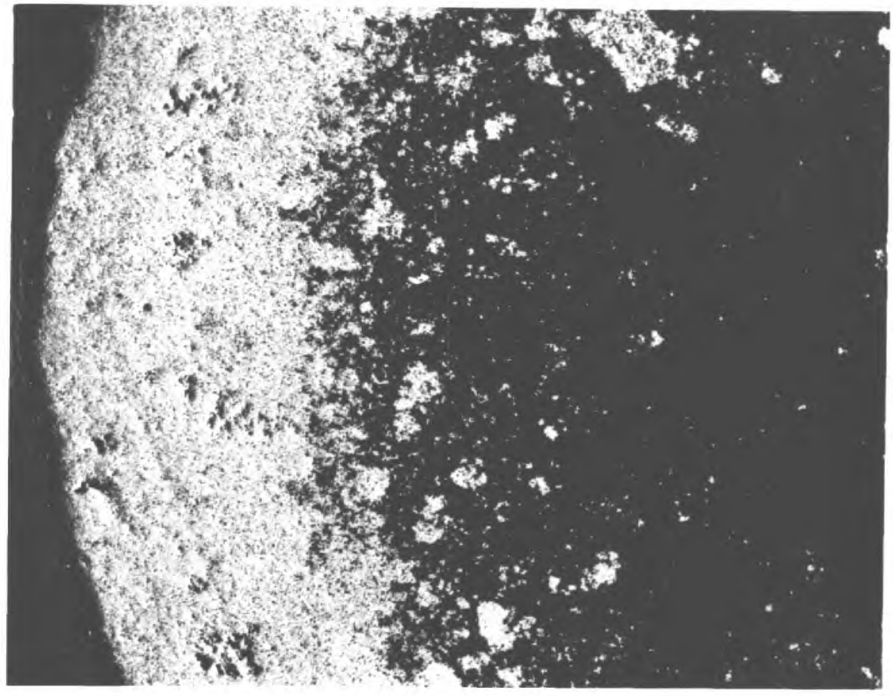


(B)

X 29·5

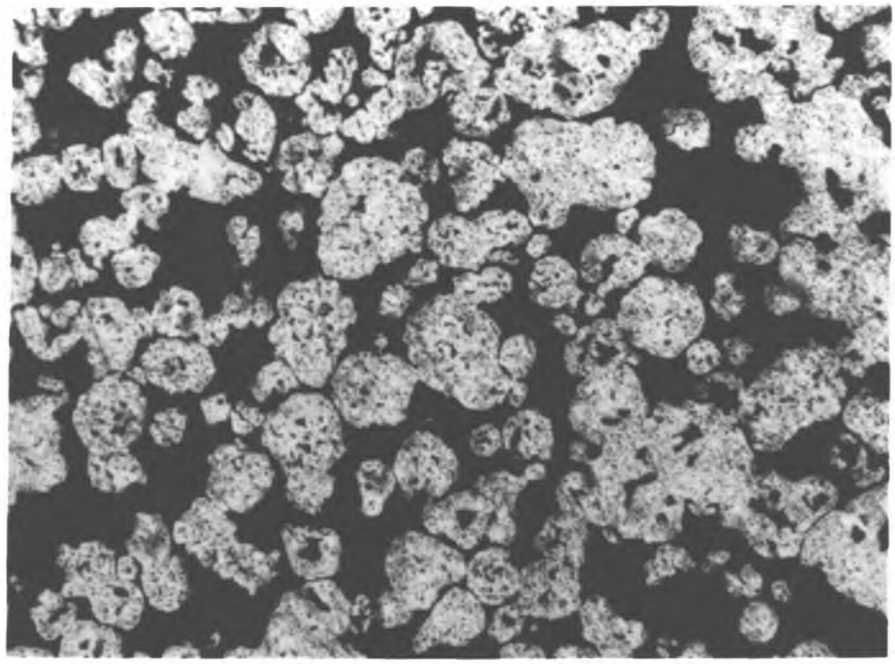
PLATE 5 (A) PHOTOMACROGRAPH OF SAMPLE NO. 113

(B) PHOTOMACROGRAPH OF SAMPLE NO. 112

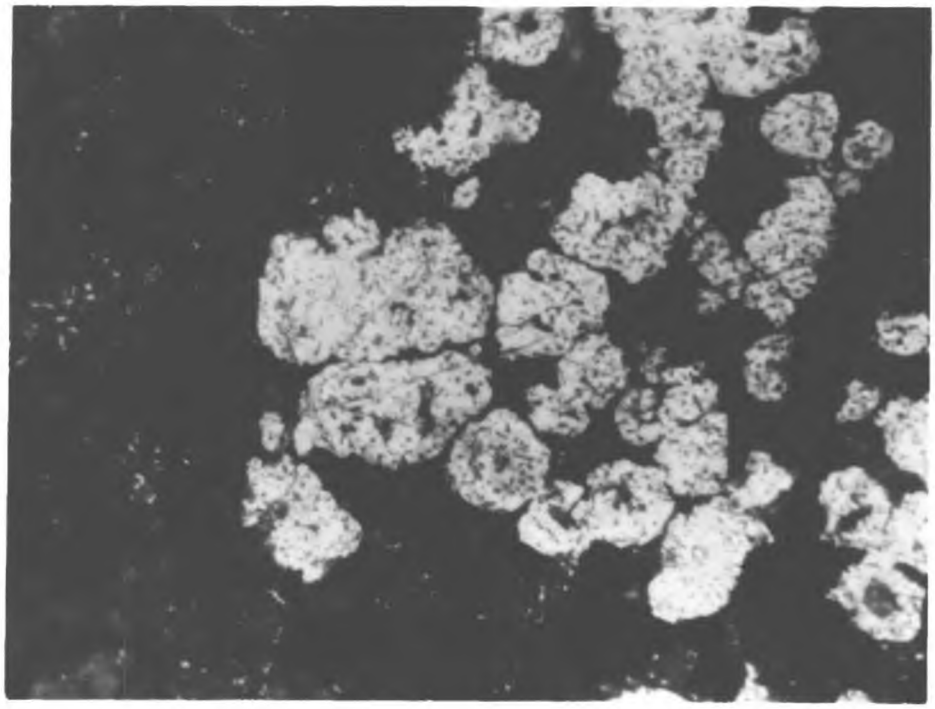


X 14·0

PLATE 6, PHOTOMACROGRAPH OF SAMPLE NO. 130



(A)
X 1250
(In Oil)



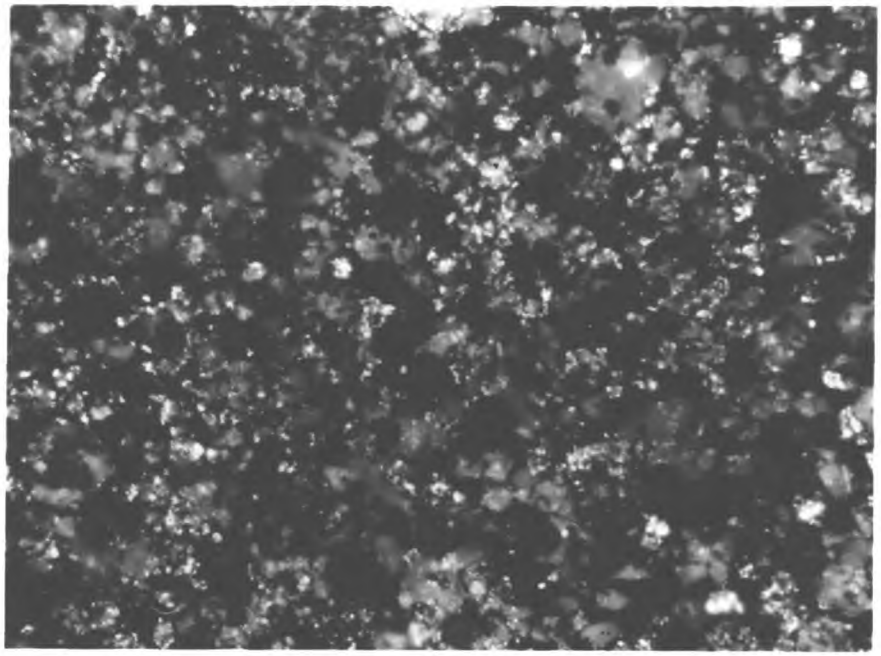
(B)
X 1400
(In Oil)

PLATE 7 (A) PHOTOMICROGAPH OF SAMPLE NO. 111

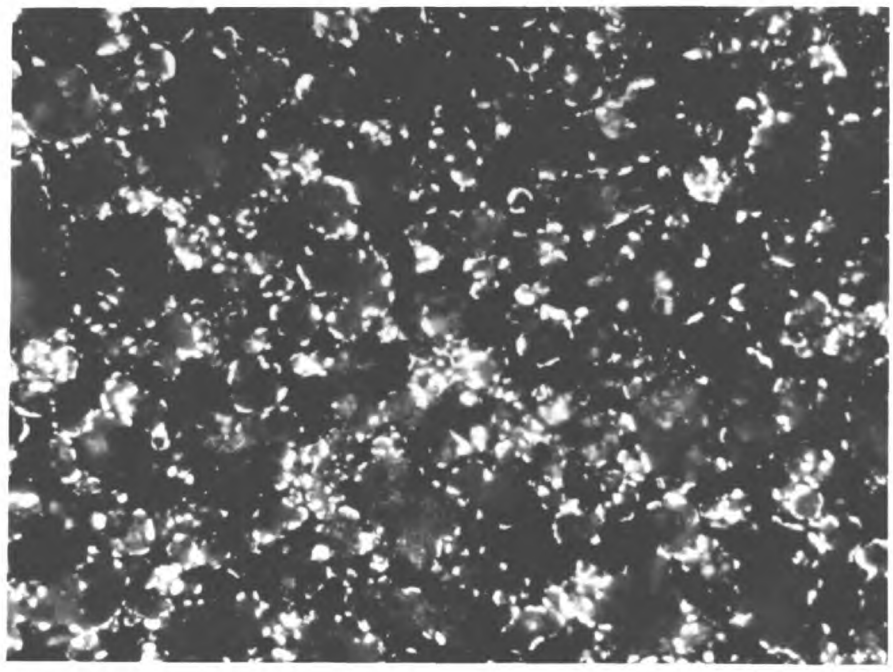
(B) PHOTOMICROGRAPH OF SAMPLE NO. 112

to reduce almost instantaneously once it has begun to react. This finding seems to indicate that solid state diffusion is unimportant and that a nucleation step may account for that part of the total resistance associated with chemical control. Moreover, it indicates that the model chosen by Szekely[95] to explain the non-topochemicality of similar reactions is not applicable to this reaction. Szekely assumes that a reaction zone exists because of the importance of solid state diffusion in the reduction of individual particles.

Plate 8 shows the appearance of areas close to the centre of the sample and remote from the reaction interface. At the lower reduction temperatures (Plate 8(A)) reduced at 574°C, there is hardly any reduced material. Indeed, the amount of reduced material which is shown was found to be present in the unreduced, untreated nickel oxide powder. In fact, as well as the small localized metallic areas shown in Plate 8(A), the original samples contained large (approximately 0.1 mm. diameter) areas of metallic nickel. The presence of these areas may explain some of the islands of reduced particles beyond the interface in the samples shown in Plates 4, 5 and 6. In any case, at the highest reduction temperature (Plate 8(B) - reduced at 826°C , the matrix shows marked attack by the reducing gas. Unfortunately, no plausible explanation has been found for this phenomenon.



(A)
X 1250
(In Oil)



(B)
X 1250
(In Oil)

PLATE 8, (A) PHOTOMICROGRAPH OF SAMPLE NO. 113

(B) PHOTOMICROGRAPH OF SAMPLE NO. 130

VI-J REDUCTION RESULTS

The results of the experimental study of the rate of reduction of nickel oxide spheres are summarized in Table V-9. As has been previously mentioned, all spheres had a green (NiO) porosity of approximately 40% after pretreatment.

The values for k_c are of particular interest in that they show the relative importance of the chemical step in determining the overall reaction rate. However, they must be viewed with caution. Figures V-2-3a, f, and g show that the shape and position of the predicted curve is substantially different from that of the experimental curve for these reduction conditions. In fact for temperatures of 750°C and above, (Figure V-2-3f and g), the curve predicted for high values of kc* (pure transport control) indicates that the model used to predict these curves is in error. This is to be expected, under these conditions, as the relative importance of Knudsen diffusion is large and thus the assumption of no pressure build-up at the interface would be invalid. The flux of water vapour through the reduced layer would be substantially larger under the combined pressure and composition gradients than under the composition gradient alone. The curve for the lowest temperature (Figure V-2-3a) cannot be satisfactorily predicted because of the lengthy incubation period and increasing rate period observed at this temperature.

The values of k_c listed in Table V-9, are plotted as an Arrhenius function in Figure VI-3. The large scatter is a consequence of the indirect method of determining this chemical

---

* FOOTNOTE:

The maximum value of k_c which the computer programme could easily handle was 10^6 and thus these curves are evaluated at this k_c.

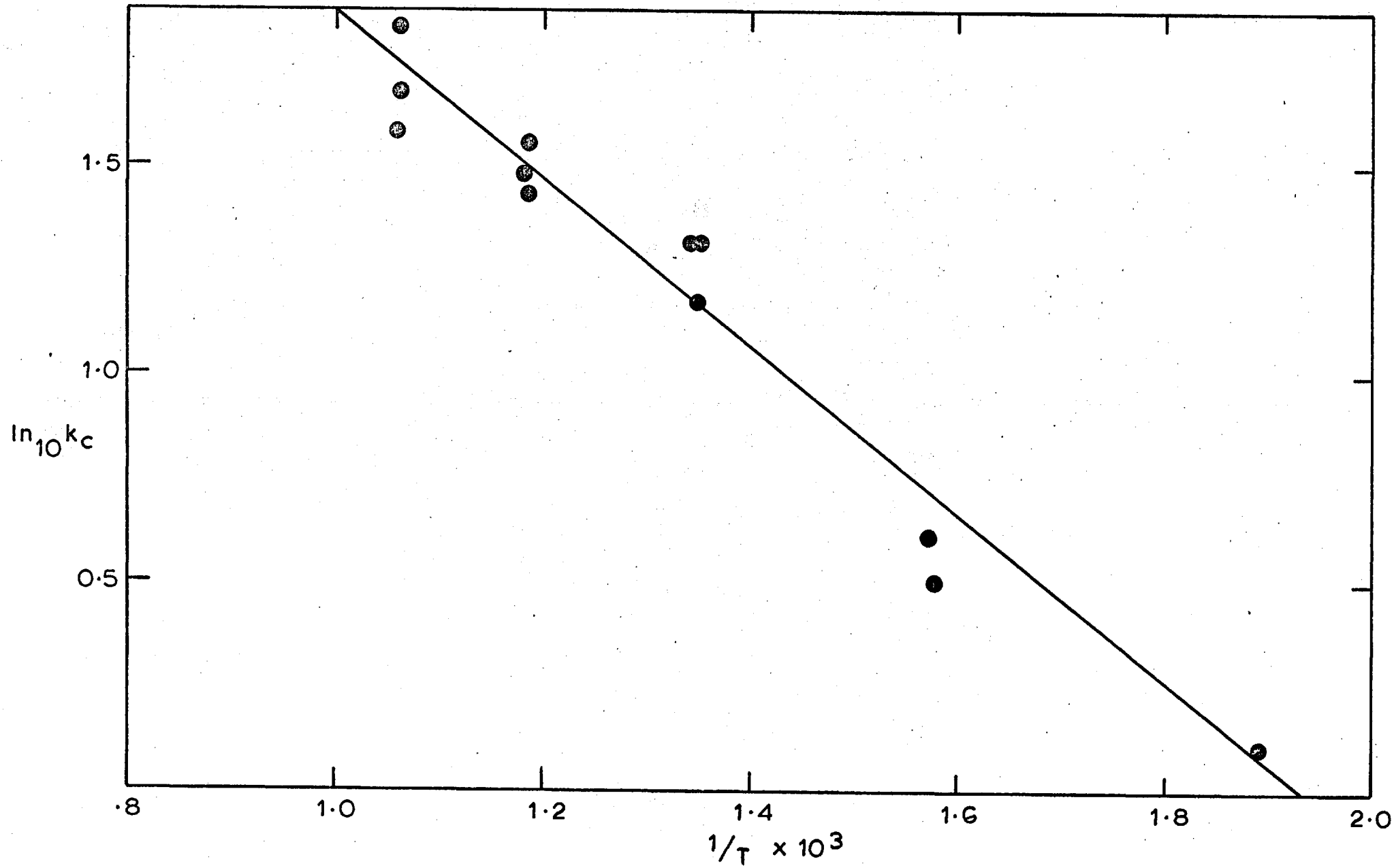


Fig. VI. 3. RELATIONSHIP BETWEEN CHEMICAL RATE CONSTANT AND REDUCTION TEMPERATURE.

rate constant. The slope of the best fit line gives an apparent activation energy of approximately 10.0 kcal/mole. The value of this activation energy is misleading, however. It refers only to the chemical reaction step, and thus one would expect it to be a larger value. The reason for the discrepancy can be readily appreciated with reference to Plates 4, 5 and 6. As the reduction temperature rises, the area over which the chemical reaction is taking place decreases. However, the area on the basis of which the chemical rate constant is determined, is that calculated for a sharp reaction interface. Consequently, the chemical rate constant values quoted for lower temperatures are seriously overestimated, yielding a lower slope for the activation energy plot.

The high k_c values determined for temperatures in excess of 500°C and the relatively sharp reaction front indicate that at these temperatures the reduction of nickel oxide by hydrogen is predominantly diffusion controlled. As the temperature decreases, the increasing role of the chemical step is reflected in a lower value of k_c and a much more diffuse reaction zone.

The relationships between the cube root of the unreacted mass and the reduction time (Figure V-2-4) show an almost linear correlation at all reduction temperatures except for the runs carried out below 300°C. This observation tends to validate the assumption of topochemicality in the model, since an average radius can be assigned to the reaction zone which decreases linearly with time.

An overall rate constant has been calculated from the slope of the $m^{*\frac{1}{3}}$ vs. t curves from the equation

$$k_r = \rho_i \, r_o \frac{dr^*}{dt} R\Theta$$

The values so obtained are shown as a function of temperature in Figure VI-4. It must be pointed out that, although this curve has been plotted as an Arrhenius function, the slope of the curve, yielding an activation energy of 3.1 kcal/mole, must not be used to attempt to elucidate any controlling mechanism. The results of the nickel oxide study show the reaction rate to be determined by both chemical and diffusional phenomena at low temperatures and solely by diffusion at higher temperatures. Normally, a change in slope in the Arrhenius plot is taken as an indication of this change in control. However, no such slope variation is observed in this work. Also, a very low activation energy is normally associated with a diffusion controlled reaction whereas this reaction appears to be of mixed control at lower temperatures. This curve and, in fact, the previous curve as well, point out the great danger in attempting to arrive at conclusions about the controlling mechanism for gas/solid reactions from the effect of temperature on the reaction rate.

In this case, the overall rate does not increase rapidly with reduction temperature mainly because the reduced layer is becoming more impervious to gaseous components as the temperature of reduction increases. A rate minimum would be encountered at somewhat higher temperatures than have been investigated in this work. These conclusions, while obvious from the measurement of diffusion coefficients in conjunction with reduction experiments, could not be arrived at solely from the observation of the effect of temperature on the rate of reaction.

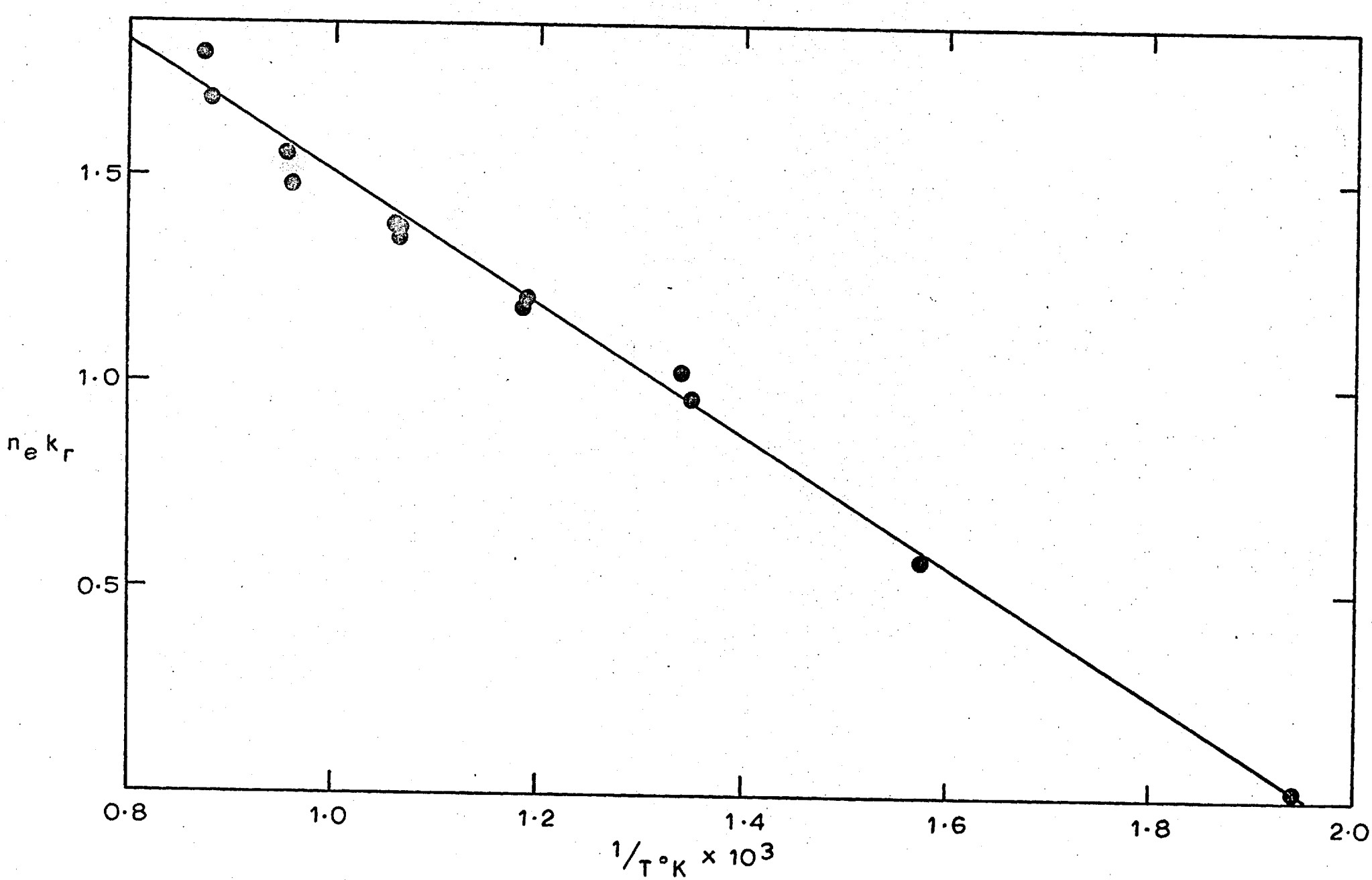


Fig. VI.4. EFFECT OF TEMPERATURE ON OVERALL RATE OF REDUCTION.

CHAPTER VII

CONCLUSIONS

The experimental technique developed to determine effective gas diffusion coefficients in porous solids was, for the most part, very satisfactory. It did fail when very large fluxes of diffusing species were encountered and when the boundary layer mass transfer resistances were relatively high. However, both of these shortcomings could be eliminated by increasing the length of the diffusion path. In any case, the interpretation of the experimental measurements using the 'dusty-gas model proved very successful, particularly in determining the relative importance of Knudsen and molecular diffusion and in extrapolating the measured results to different experimental conditions.

The heat and mass transfer model proposed by Hills for the thermal decomposition of calcium carbonate now seems to be entirely proved, as his conclusion that Knudsen diffusion is operating in the decomposed lime layer has been shown to be valid. Moreover, the transport coefficients which he determined from his decomposition experiments have been independently confirmed by direct measurement.

It would appear, by comparing the results of the diffusion coefficient measurements in porous iron with the results of Harwell on the reduction rate of ferrous chloride, that heat and mass transport are the controlling steps in this reaction.

The technique used to follow the course of the reduction of nickel oxide in hydrogen was entirely satisfactory. The short time interval between successive readings enabled the measurements to be accurately interpreted and any anomalies in the shape of experimental curves to be clearly shown.

Following the experimental strategy proposed by Hills, the reduction of the nickel oxide pellets investigated in this work has been shown to be a mixed control reaction up to approximately 700°C. The increasing role of Knudsen diffusion at reduction temperatures in excess of 700°C has precluded any conclusive elucidation of the controlling step, but it would seem most probable that at these temperatures, the reaction is almost entirely controlled by gaseous diffusion. Although microscopic examination has shown the reaction to take place over a reaction zone of finite width, its analysis assuming a sharp interface is not entirely invalid above reduction temperatures of 300°C. In particular, the linearity of the relationship between the cube root of the unreacted mass and time shows that this treatment is at least approximately correct.

Certainly, this work has not been exhaustive in its treatment of the reduction of nickel oxide. For instance, it would be of immense interest if the exact equations describing the flux of gases in porous media under combined composition and bulk pressure gradients were solved for reduction conditions, thus allowing for bulk pressure fluctuations in the reaction zone. Also, a more detailed treatment of the behaviour of the reaction zone at various temperatures and reduction times could lead to a model describing the progress of non-topochemical reactions. A workable model for non-topochemical reactions is notably absent from the literature at the present time.

APPENDIX A

CALCULATION OF EQUILIBRIUM COEFFICIENT FOR HYDROGEN REDUCTION OF NICKEL OXIDE

From tables of thermodynamic data, the following equations have been obtained for the relationship between the free energy change on reaction and the reaction temperature for the reduction of nickel oxide in hydrogen. Because of the three alotropic forms of nickel oxide and the two alotropic forms of nickel, any particular equation applies only up to the temperature of the next solid state transformation.

i) From $298^{\circ}K$ to $525^{\circ}K$ (αNiO and αNi)

$$\Delta G = -3440 - 9.72\ T\ \ln T + 14.38 \times 10^{-3} T^2 + 1.96 \times 10^{5}\ T^{-1} + 47.28T$$

ii) Between $525^{\circ}K$ and $565^{\circ}K$ (β NiO and αNi)

$$\Delta G = + 2030 + 9.15\ T\ \ln T - 4.41 \times 10^{-3}\ T^2 + 0.02 \times 10^{5}\ T^{-1} - 71.76T$$

iii) Between $565^{\circ}K$ and $633^{\circ}K$ (γ NiO and αNi)

$$\Delta G = + 868 + 6.45\ T\ \ln T - 2.12 \times 10^{-3}\ T^2 + 0.02 \times 10\text{-}5\ T\text{-}1 - 52.09\ T$$

iv) Between $633^{\circ}K$ and $1725^{\circ}K$ (γ NiO and β Ni)

$$\Delta G = + 660 + 4.51\ T\ \ln T - 0.78 \times 10^{-3}\ T^2 + 0.02 \times 10^{5}\ T^{-1} - 40.93T$$

The values of the equilibrium coefficient have been calculated at several temperatures using the values of ΔG above and the relation :-

$$\Delta G = - RT \ln K_{EQ}$$

TABLE A shows some of the values obtained over the temperature range of interest.

TABLE A - THERMODYNAMIC PROPERTIES OF THE REDUCTION OF NICKEL OXIDE BY HYDROGEN.

Temperature ^{o}K	Temperature ^{o}C	$\triangle G$	K_{EQ}
298	25	-3953	788
400	127	-5050	573
500	227	-6050	441
600	327	-6900	327
700	427	-7700	258
800	527	-8500	211
900	627	-9050	158
1000	727	-10,100	161
1100	827	-10,700	135
1200	927	-11,300	115

ACKNOWLEDGEMENTS

I should like to extend my most sincere thanks to all those who helped in the preparation of this work. I am indebted to my supervisor, Dr. A.W.D. Hills, for his continuous interest and assistance throughout the project. Also, to all members and staff of the John Percy Research Group who have contributed freely of their time and efforts on my behalf, a most heartfelt thankyou.

I should also like to thank my typist, Miss D. Blaseby, for her assistance.

I am most grateful to the Athlone Fellowships Scheme and the National Research Council of Canada for their generous financial support.

I should also like to thank my wife for her understanding, help and patience, during the long years of this study.

LIST OF SYMBOLS

Symbols previously defined in the text, for localized usage, are not redefined in this list.

ROMAN ALPHABET

A	Surface area
As	Diffusion shaft cross-sectional area
a'	Slope of K_{eq} vs. θ curve
Bo	Structural parameter of porous solid
b	Stoichiometric coefficient
bo	External boundary layer thickness
C	Concentration
D	Diffusion coefficient
F	Force on diffusion mixture
H	Heat of reaction
h	Heat transfer coefficient
K	Permeability of porous solid
K_{EQ}	Equilibrium coefficient
k	Boltzman's constant
k_p	Thermal conductivity of porous solid
k_c	Chemical rate constant
k_r	Overall rate constant
M	Molecular weight
$\dot{n}$	Rate of flow (flux)
$\dot{n}''$	Flux/unit area
p	Pressure
q	Tortuosity
R	Gas constant
R_o	Radius of particle in Stoke's Equation
R_1	External mass transfer resistance
R_2	Diffusion resistance
R_3	Internal mass transfer resistance
r	Radius
S	Shape factor
T	Temperature
t	Time
U_J	Jet velocity
V	Velocity
x,y,z	Co-ordinate directions

GREEK ALPHABET

α	Mass transfer coefficient
β	Flux ratio
γ	Stoichiometric coefficient
δ	Knudsen-molecular diffusion parameter
ϵ	Porosity
η	Viscosity
θ	Temperature
μ	Viscosity
ζ	Log-mean pressure term
ρ	Density
Ω	Effective resistance

DIMENSIONLESS QUANTITIES

p_i^*	Dimensionless partial pressure = $\frac{p_i}{p_T}$
r^*	Dimensionless radius = r_i/r_o
m^*	Dimensionless unreacted mass = $\frac{m_t - m_\infty}{m_o - m_\infty}$
C_i^*	Dimensionless concentration = C_i/C_T

SUBSCRIPTS

i	Internal, interface or species i
o	External
I	Species I
II	Species II
K	Knudsen diffusion
j	Species j
eff	Measured in porous solid (effective)
$\square_1$	First approximation
$\square_2$	Second approximation
1	Species 1
2	Species 2
d	Dust particles

b	Backward
f	Forward, or film conditions
c	Chemical step
S_{II}	Product solid
T	Total
R	At reaction front
G	In gas phase
EQ,eq	At equilibrium conditions
M	Mass transfer
H	Heat transfer
i,b	Inside bulk
i,s	Inside surface
o,s	Outside surface
o,b	Outside bulk.

LIST OF REFERENCES

1. Dye, R.F. and Dallavalle J.M..
'Diffusion of Gases in Porous Media', Ind.Eng.Chem. 50, 8, 1195 August 1958.

2. Scott, D.S. and Cox K.E.
'Real diffusivity of gases in porous solids', Can.Journ.Chem.Eng. 3, 201, 1960

3. Scott, D.S. and Dullien F.A.L.
'Diffusion of ideal gases in capillaries and porous solids', A.I.Ch.E.Jour., 8, 1, 113, March 1962.

4. Bokhoven C. and Hoogschagen J.
'Diffusion in porous catalysts', Journal Chem.Phys., 21, 1, 159 January 1953.

5. Hoogschagen J.
'Diffusion in porous catalysts and adsorbents', Ind.Eng.Chem. 47, 5, 906, 1955.

6. Olsson R.G. and McKewan W.M.
'Diffusion of H_2-H_2O through porous iron formed by the reduction of hematite', Trans.Met.Soc.AIME, 236, 1518, November 1966.

7. Wakao, N. and Smith J.M.
'Diffusion in catalyst pellets', Chem.Eng.Sc., 17, 825, 1962.

8. Currie,J.A.
'Gaseous diffusion in porous media', Brit.J.App.Physics, 11, 8, 314, August 1960.

9. Evans III, R.B., Watson G.M. and Truitt J.
'Interdiffusion of gases in a low permeability graphite at uniform pressure', J.Appl.Phys., 34, 2020, 1963.

10. Szekely J,
To be published (Abstract in Journal of Metals).

11. Knudsen M.
'The law of the molecular flow and viscosity of gases moving through tubes', Ann.Physik, 28, 75, 1909.

12. Pollard W.G. and Present R.D.
'Gaseous self-diffusion in long capillary tubes', Phys.Rev., 75, 762, 1948.

13. Weber S.
'Relation between self-diffusion coefficients and the laminar flow of pure gases through tubes', Konig.Danske.Vid.Sels., Mat.Fys.Med. 28, 2, 1954.

14. Barrer R.M.
'Diffusion in porous media', Applied Materials Research, 2, 3, 129, July 1963.

15. Bosanquet C.H.
British T.A. Report BR-507, 1944.

16. Wicke, E. and Kallenbach R.
'Surface diffusion of carbon dioxide in activated charcoals', Kolloid - Z. 97, 135, 1941.

17. Hoogschagen J.
'Equal pressure diffusion in porous substances', Journal of Chem. Phys., 21, 11, 2096, November 1963.

18. Weisz, P.B.
'Diffusivity of porous particles I measurements and significance', Z.Phys.Chem., 11, 1, 1957.

19. Mason E.A., Malinauskas, A.P., EvansIII, R.B.
'Flow and diffusion of gases in porous media', Journal of Chemical Physics, 46, 8, April 1967.

20. Evans III, R.B., Watson G.M. and Mason E.A.
'Gaseous diffusion in porous media at uniform pressure', Journal of Chemical Physics, 35, 6, December 1961.

21. Spiegler, K.S.
'Diffusion of gases across porous media', Ind.Eng.Chem.Fund. 5, 4, 529, 1966.

22. Evans III R.B., Watson G.M. and Mason E.A.
'Gaseous diffusion in porous media II effect of pressure gradients', Journal of Chem.Phys., 35, 7, April 1962.

23. Derjaguin B.F. and Bakanov, S.P.
'Theory of the flow of a gas in a porous medium in the near-Knudsen region', Sov.Phys.Doklady, 2, 326, 1957.

24. Zhadanov V., Kagan Y., and Sazykin A.
'Effect of viscous transfer of momentum on diffusion in a gas mixture', Sov.Phys.-Jetp., 15, 596, 1962.

25. Thiele, E.W.
'Relation b/w catalytic activity and size of particle', Ind.Eng. Chem., 31, 916, 1939

26. Wheeler, A.
'Reaction rates and selectivity in catalyst pores', Advances in Catalysis, 3, 249, 1951.

27. Weisz P.B. and Prater C.D.
'Measurements in experimental catalysis', Advances in Catalysis, 6, 167, 1954.

28. Walker P.L., Rusinko F. and Austin L.G.
'Gas reactions of carbon', Advances in Catalysis, 11, 133, 1959.

29. Aris, R.
'A normalization for the Thiele modulus', Ind. and Eng.Chem.Fund. 4, 1965 227 and 487.

30. Bischoff K.B.
'An extention of the general criterion for importance of pore diffusion with chemical reactions', Chem.Eng.Sci., 22, 525, 1967.

31. Petersen E.E.
'Chemical Reaction Analysis', Prentice Hall, New York, 1965.

32. Ishida M. and Wen C.Y.
'Comparison of kinetic and diffusional models for solid-gas reactions', AICHE.J.L., 14, 311, 1968.

33.. Calvelo A. and Cunningham R.E.
'Overall effectiveness factor for gas-solid reactions', Journal of Catalysis, 16, 3, 397, March 1970.

34. Spencer W.D. and Topley B.
'Chemical kinetics of the system $AgCO_3$ = AgO + CO_2', J.Chem.Soc., 1929, p. 2633.

35. Furnas C.C.
'Rate of calcination of limestone', Ind.Eng.Chem., 23, 534, 1931.

36. Zawadzki J. and Bretsznajder S.
'Mechanism of reactions of the type: solid = solid + gas', Trans.Farad.Soc, 34, 951, 1938.

37. Joseph T.L., Beatty H.M. and Bitsianes G.
'Calcination and sizing of blast furnace flux', Trans.AIME, 154, 148, 1943.

38. Ingraham T.R. and Marier P.
'Kinetic studies of the thermal decomposition of calcium carbonate', Can.J.Chem.Eng., 41, 170, 1963.

39. Hills A.W.D.
'Heat and mass transfer in the decomposition of single spheres and packed beds of calcium carbonate', Ph.D.Thesis, Univ.of London 1966.

40. Themelis N.J. and Gauvin W.H.
'A generalized rate equation for the reduction of iron oxides', Trans.Met.Soc.AIME, 227, 290, April 1963.

41. Warner N.A.
'Reduction kinetics of hematite and the influence of gaseous diffusion', Trans.Met.Soc.AIME, 230, 163, February 1964.

42. McKewan W.M.
'Kinetics of iron oxide reduction', Trans.Met.Soc.AIME, 218, 2, February 1960.

43. Kawasaki, E., Sanscrainte J. and Walsh T.J.
'Kinetics of reduction of iron oxide with carbon dioxide and hydrogen', A.I.Ch.E.Journal, 8, 1, 48, March 1962.

44. Ingraham T.R. and Marier P.
'Kinetics of the thermal decomposition of cupric sulphate and cupric oxysulphate', Trans.Met.Soc.AIME., 233, 363, 1965.

45. Peretti E.A.
'New method for studying the mechanism of roasting reactions', Discuss. Faraday Soc., 4, 174, 1948.

46. Von Destinon-Forstmann J.
'The hydrogen reduction kinetics of molybdenum oxides', Can.Metall.Quarterly, 4, 1, 1965.

47. Yamaguchi A. and Moriyama J.
'Kinetic study on the hydrogen reduction of some non-ferrous metal oxides', Memoirs Faculty of Eng.Kyoto Univ. 18, 389, 1966.

48. Bandrowski J., Bickling C.R., Yang K.H. and Hougan O.A.
'Kinetics of the reduction of nickel oxide by hydrogen', Chem.Eng. Sci., 17, 379, 1962.

49. Rigg T.
'Kinetics of the reduction of ferrous chloride with hydrogen', Can.J.Chem.Eng., 42, 247, 1964.

50. Yannopoulos Y.C. and Themelis N.J.
'A rate equation for the reduction of ferrous chloride by hydrogen', Can.J.Chem.Eng., 43, 173, 1965.

51. Seth B.B.L. and Ross, H.V.
'The mechanism of iron oxide reduction', Trans.AIME, 233, 180, January 1965.

52. Hills A.W.D.
'Role of heat and mass transfer in gas/solid reactions involving two solid phases within sintered pellets', Heat and Mass Transfer in Process Metallurgy, The Institution of Mining and Metallurgy, 1967.

53. Warner N.A.
'Kinetics of the gaseous reduction of hematite', Aust.I.M.M. Proceedings No. 210, 31, 1964.

54. Lu W.K. and Bitsianes G.
'Chemical kinetics of gaseous reduction of hematite', Canadian Met.Quarterly, 7, 1, 3, 1968.

55. Bowen J.H.
'Discontinuous and continuous models of direct reduction', Chemical Engineering in the Iron and Steel Industry, Institution of Chemical Engineers, London 1968.

56. Hartoutsios, S.J.
'Kinetics of reduction of iron oxide pellets', M.Phil.Thesis, Univ. of London, 1968.

57. McKewan W.M.
'Reduction kinetics of magnetite in H_2-H_2O-N_2 mixture', Trans.Met.AIME, 221, 149, February 1961.

58. McKewan W.M.
'Reduction kinetics of hematite in H_2-H_2O-N_2 mixture', Trans. Met.AIME, 224, 2, February 1962.

59. McKewan W.M.
'Reduction kinetics of magnetite in hydrogen at high pressures', Trans.Met.Soc.AIME, 224, 387, April 1962.

60. Lu W.K.
'The general rate equation for gas solid reactions in metallurgical processes', Trans.Met.Soc.AIME, 227, 204, February 1963.

61. Oates W.A. and Todd D.D.
'Kinetics of the reduction of oxides', J.Aust.Inst.Metals, 7, 2, 109, May 1962.

62. Hills A.W.D.
'The importance of macroscopic transport phenomena in gas/solid reactions', Heterogeneous Kinetics at Elevated Temperature, Plenum Press, 1970.

63. Stalhane B. and Malmberg T.
'Research on the rate of reduction of iron ores', Jernkontorets Annaler, 85, 1, 1930.

64. Quets J.M., Wadsworth M.E. and Lewis S.R.
'Kinetics of reduction of magnetite to iron and wustite in hydrogen-water vapour mixtures', Trans.Met.Soc.AIME, 221, 1186, December 1961.

65. Hyatt E.P., Cutler I.B. and Wadsworth M.E.
'Calcium carbonate decomposition in carbon dioxide atmosphere', J.Aer.Ceram.Soc., 41, 70, 1958.

66. Udy M.C. and Lorig C.H.
'The low temperature gaseous reduction of a magnetite', Trans.AIME, 154, 162, 1943.

67. Bogdandy L.V. and Janke W.
'Significance of diffusion in the reduction of iron ores', Z.Electrochem., 61, 1146, 1957.

68. Woods S.E.
'The reduction of oxides of iron as a diffusion controlled reaction', The Physical Chemistry of Process Metallurgy, 184, Faraday Soc., London, 1948.

69. Joseph T.L.
'Porosity, reducibility and size preparation of iron ores', Trans.Amer.Inst.MME, 120, 72, 1936.

70. Lewis T.R.
'Rate of reduction of Geneva iron ore', Trans.AIME, 172, 27, 1947.

71. Edstrom J.D. and Bitsianes G.
'Solid state diffusion in the reduction of magnetite', Journal of Metals, June 1955, p. 760.

72. Jorgensen P.J., Cutler I.B. and Wadsworth M.E.
'Oxidation of silicon carbide', J.Amer.Ceram.Soc., 42, 613, 1959.

73. Azbe V.J.
'Calcining behaviour tests of dolomite, magnesite and calcite', Rock Products, 47, 70, September 1944.

74. Satterfield C.N. and Feakes F.
'Kinetics of the thermal decomposition of calcium carbonate', A.I.Ch.E. Journal, 5, 115, 1959.

75. Campbell F.R., Hills A.W.D. and Paulin A.
'Transport properties of porous lime and their influence on the decomposition of porous compacts of calcium carbonate', Chem.Eng. Sci., 25, 929, 1970.

76. Themelis N.J. and Yannopoulos J.C.
'Mass and heat transfer phenomena in the reduction of cupric oxide by hydrogen', Trans.AIME, 236, 414, 1966.

77. Yagi T and Ono Y.
'A method of analysis for reduction of iron oxide in mixed-control kinetics', Trans.I.S.I.J., 8, 378, 1968.

78. St.Clair H.W.
'Rate of reduction of an oxide sphere in a stream of reducing gas', Trans.Met.Soc.AIME., 233, 1145, 1965.

79. Shen J. and Smith J.M.
'Diffusional effects in gas-solid reactions', Ind.Eng.Chem.Fund. 4, 3, 293, 1965.

80. Hawtin P. and Murdoch R.
'Role of in-pore mass transport resistance in the reactions of porous solids with gases', Chem.Eng.Sci., 19, 10, 819, 1964.

81. Benton A.F. and Emmett P.H.
'The reduction of nickelous and ferric oxides by hydrogen', J.Amer.Chem.Soc., 46, 2728, December 1924.

82. Taylor G.B. and Starckweather H.W.
'Reduction of metal oxides by hydrogen', J.Amer.Chem.Soc., 52, 2314, June 1930.

83. Sabatier P. and Espil L.
'On the reduction of nickelous oxide and on the existence of a sub-oxide', Comptes Rendus, 158, 668, 1914.

84. Berger E.
'Reduction of copper and nickelous oxides in the presence of a dehydratant', Comptes Rendus, 158, 1798, 1914.

85. Paravano G.
'The reduction of nickel oxide by hydrogen', J.Amer.Chem.Soc., 74, 1194, 1952.

86. Cech, R.E.
'The reduction of nickel oxide', Trans.Met.Soc.AIME, 215, 769, 1959.

87. Paulin A.
'Heat and mass transfer in the decomposition of calcium carbonate', Ph.D.Thesis, Univ. of London, 196

88. Vogel A.I.
A textbook of Quantitative Inorganic Analysis, 3rd Edition, Longmans, London, 1961.

89. Dawson, D.A. and Trass O.
'Mass transfer in a turbulent radial wall jet', Can.J.Chem.Eng., 44, 121, June 1966.

90. Perry J.H.
Chemical Engineers Handbook, 4th Edition, McGraw-Hill, New York, 1963.

91. Bradshaw A.V.
'Rate controlling factors in gas-solid reactions of metallurgical interest', Trans.Inst.Min.& Met., 79, C281, 1970.

92. Rowe P.N. and Claxton K.T.
'Heat and mass transfer from a single sphere to fluid moving through an array', Trans.Inst.Chem.Engrs. 43, 321, 1965.

93. Cornish A.,
Private communication.

94. Partridge B.,
Private communication.

95. Szekely J. and Evans J.W.,
'A structural model for gas-solid reactions with a moving boundary', Chem.Eng.Sci., 25, 6, 1091, June 1970.

Reprinted from

[redacted]

PERGAMON PRESS
OXFORD NEW YORK LONDON PARIS

Chemical Engineering Science, 1970, Vol. 25, pp. 929–942. Pergamon Press. Printed in Great Britain.

Transport properties of porous lime and their influence on the decomposition of porous compacts of calcium carbonate

F. R. CAMPBELL† and A. W. D. HILLS‡
Department of Metallurgy, Imperial College, London S.W. 7, England
and
A. PAULIN§
Department of Mining and Metallurgy, University of Ljubljana, Yugoslavia

(*First received* 28 *April* 1969; *in revised form* 16 *December* 1969)

Abstract—Special experimental techniques have been developed to measure the thermal conductivity of porous lime and the diffusion coefficient of carbon dioxide through it. Measurements have been made on lime whose porosity varied in the range $0{\cdot}45 < \epsilon < 0{\cdot}8$, and the results have shown that the diffusion process is Knudsen diffusion, a conclusion which is compatable with previous measurements of the specific surface of porous lime. The results have been used to confirm that the decomposition of calcium carbonate is controlled by heat and mass transfer. The decomposition rate can be predicted accurately using a heat and mass transfer model which assumes the reaction to occur on a receding interface and that chemical processes on this interface play no part in controlling the rate. These predictions are accurate even when the porosity of the original carbonate is as high as 0·66.

HILLS HAS recently shown[1] that the thermal decomposition of dense compacts of calcium carbonate is controlled by the rate at which heat is transferred to a receding reaction interface within the compact, and by the rate at which carbon dioxide is transferred away from this interface. He demonstrated the validity of this mechanism by calculating values of the relevant transport parameters from the measured reaction rate and showing that they agreed with values calculated from data presented in the literature. However, the most important transport parameter, the diffusion coefficient of carbon dioxide through the porous product lime, had not previously been measured directly. Thus the value calculated from the reaction rate was compared with a value calculated from the specific surface area of lime determined by Murray, Fischer and Sabean[2]. Some doubt could be attached to this calculation since a value had to be assumed for the tortuosity factor in porous lime, and it was therefore decided to measure the diffusion coefficient of carbon dioxide in porous lime directly, and use the result as further confirmation for the decomposition mechanism.

Experiments have been conducted in a separate investigation on the decomposition of packed beds of porous calcium carbonate spheres[3], and the results compared with theoretical predictions based on Hills' model. Before these predictions could be made, however, it was necessary to confirm that the model applied to porous spheres as well as it did to dense spheres, and to measure the thermal conductivity and the diffusion coefficient of carbon dioxide in the highly porous lime produced when the porous calcium carbonate spheres decompose.

In the work reported here, then, transport parameters of several different porous limes have been measured, the limes being produced by decomposing both dense and porous compacts of calcium carbonate. The results for lime porosities lower than 0·6 have been compared with the values determined by Hills, and those for higher porosities have been used to calculate the rate at which porous spherical compacts of calcium car-

†Athlone Scholar, John Percy Research Group in Process Metallurgy.
‡John Percy Research Fellow in Process Metallurgy.
§Assistant Professor.

bonate would decompose in air, the calculations being based on the heat and mass transfer mechanism. The validity of this mechanism for porous compacts has then been examined by comparing these calculated rates with the decomposition rates measured in an independent series of experiments.

DIFFUSION COEFFICIENT OF CARBON DIOXIDE THROUGH POROUS LIME

Experimental

The diffusion coefficient measurements were made using the hollow lime spheres shown in Fig. 1. The spheres were prepared from spherical compacts of calcium carbonate formed in Vinamould moulds using a conventional press. The technique was identical to that used by Hills [1] except that the spheres contained a smaller concentric sphere of Wood's metal, and their porosities were varied by varying the compaction pressure [3]. A small hole was drilled through each compacted carbonate sphere and the Wood's metal removed by gentle heating. The outer radius of the sphere was measured with a micrometer, several measurements being made in different directions, and the radius of the internal spherical cavity was measured by weighing the volume of mercury that just filled it. The sphere was then weighed and a twin bore alumina sheath, sometimes covered with a thin layer of glass, was inserted into the radial hole. The sphere was sintered in pure carbon dioxide at 845°C for 1½ hr, which caused the sphere to contract slightly, and to form a gas tight seal against the alumina sheath. The outer diameter of the sphere was again measured and it was placed in the centre of a horizontal tube furnace†, the alumina sheath protruding through a rubber seal in one end of the furnace. Two gas tight seals were prepared to connect each bore of the emergent alumina tube to a separate gas train. Thus a known flow rate of gas of known composition could be passed into the centre of the hollow sphere down one bore of the tube and the flow rate and composition of the gas emerging from the other bore could be measured. The gas compositions were determined by gas chromatography, samples being withdrawn in a hypodermic syringe through self sealing rubber plugs in the gas trains. Similar gas trains were connected to the two ends of the tube furnace.

Initial experiments were carried out on each sphere to determine the diffusion coefficient of carbon dioxide through the porous carbonate. Pure argon was passed down one bore of the alumina tube at a variety of different flow rates and pure carbon dioxide was passed through the furnace at a flow rate of 0·8 l/min. The compositions and flow rates of the emergent gases were measured as functions of the flow rate of argon

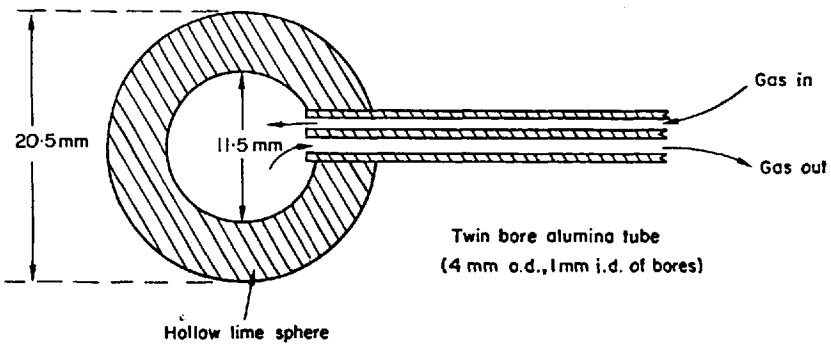


Fig. 1. Porous lime sphere used in the diffusion coefficient measurements. (Approximate measurements.)

†The internal diameter of the furnace tube was 26 mm.

into the sphere, and the results were analysed as described later. The experiment was then repeated except that carbon dioxide was passed into the centre of the sphere and argon was passed through the furnace.

The spheres were then decomposed by heating the furnace to 870° or to 950°C and passing air through it. The diffusion coefficient of carbon dioxide through the porous lime was determined in the manner described above, the furnace being held at 950°C. In some experiments, however, the furnace was held at 870°C and the pure carbon dioxide had to be replaced by 50:50 argon–carbon dioxide mixture in order to avoid any reaction between the lime and the carbon dioxide.

After the diffusion coefficient measurements had been made the furnace was allowed to cool and the lime sphere removed so that its outer diameter could be measured again.

Analysis of results

Three mass transfer steps were involved in the transfer of carbon dioxide between the bulk gas phase inside and outside the hollow spheres and in the counter mass transfer of argon. The experimental results were therefore analysed in terms of the equation:

$$\dot{n}_{CO_2} = \frac{[p_{CO_2}]_1 - [p_{CO_2}]_2}{R\theta\{\Omega_i + \Omega_s + \Omega_o\}} \qquad (1)$$

where Ω_i, Ω_s and Ω_o are, respectively, the mass transfer resistances inside, across and outside the spherical shell, and $[p_{CO_2}]_1$ and $[p_{CO_2}]_2$ are the bulk gas compositions in the two phases, the significance of suffices being changed so that $\dot{n}_{CO_2}$ was always positive.

Experimental values for the sum of the three resistances were determined from the molar transfer fluxes of CO_2 through the lime sphere and from the partial pressures of CO_2 in the bulk gas phases inside and outside the sphere, these variables being calculated from the measured gas compositions and flow rates. The calculations were simplified by the observation that the gas flow rates entering and leaving the hollow sphere were virtually equal. Thus, when pure CO_2 was blown into the hollow sphere, its molar transfer flux through the sphere was determined from the composition of the gases leaving the furnace, using the equation:

$$[\dot{n}_{CO_2}]_O = [\dot{N}_{Ar}]_F \times [C^*_{CO_2}]_F \qquad (2)$$

where $[\dot{N}_{Ar}]_F$ is the molar flow rate of argon passed into the furnace, and $[C^*_{CO_2}]_F$ is the mole fraction of CO_2 in the gas leaving the furnace.

Similarly, when pure CO_2 was passed through the furnace, its transfer flux through the sphere was determined from the composition of the gases leaving the sphere, using the equation:

$$[\dot{n}_{CO_2}]_I = [\dot{N}_{Ar}]_S \times [C^*_{CO_2}]_S. \qquad (3)$$

Where $[\dot{N}_{Ar}]_S$ is the molar flow rate of argon passed into the sphere, and $[C^*_{CO_2}]_S$ is the mole fraction of CO_2 in the gas leaving the sphere.

The total pressure in the furnace was one atmosphere, so that the partial pressure of carbon dioxide inside the furnace was either 1 atm, or zero. Gas enters the hollow sphere from one capillary bore of the alumina tube and leaves along the other. The transferred gas species must be transported by gaseous diffusion and bulk flow between the inner surface of spherical shell and the entrance to the exit bore of the alumina tube. Thus the effective pressure of the transferred gases in the inner gas space will be that at the entrance to the exit bore, and it can be calculated from the composition of the gas emerging from the exit bore.

$$[p_{CO_2}]_i = [p_T]_i \times [C^*_{CO_2}]_S. \qquad (4)$$

This equation was used when pure argon was passed into the sphere, so that, under these conditions, we have:

$$[p_{CO_2}]_1 - [p_{CO_2}]_2 = [p_{CO_2}]_o - [p_T]_i \times [C^*_{CO_2}]_S. \qquad (5)$$

The total pressure within the sphere, $[p_T]_i$, was greater than that within the furnace because of the pressure drop along the exit bore of the

alumina tube. It was determined from the pressures measured at the end of the exit bore and at the entrance to the inlet bore, assuming that the pressure drops along the two bores were equal. At the highest flow rates used in the experiments the value of $[p_T]_i$ could rise to 114 KN/m².

When carbon dioxide was passed into the sphere its concentration in the gas leaving the sphere was too high to be conveniently analysed by the gas chromatograph. It was therefore determined from the molar flow rate of carbon dioxide into the sphere, and from the molar transfer rates of argon and carbon dioxide through the sphere. Since the molar transfer rates of argon and carbon dioxide are equal, they are both given by Eq. (2), so that the partial pressure of argon within the sphere is given by:

$$[p_{Ar}]_i = \frac{[\dot{n}_{Ar}]_I}{[\dot{N}_{CO_2}]_S}[p_T]_i = \frac{[\dot{n}_{CO_2}]_O}{[\dot{N}_{CO_2}]_S}[p_T]_i$$
$$= [p_T]_i - [p_{CO_2}]_i. \qquad (6)$$

Where $[\dot{N}_{CO_2}]_S$ is the molar flow rate of carbon dioxide passed into the sphere. Since pure argon was passed through the furnace, the partial pressure of carbon dioxide in the boundary layer surrounding the sphere is zero so that, under these conditions, we can write:

$$[p_{CO_2}]_1 - [p_{CO2}]_2 = [p_T]_i \left\{1 - \frac{[\dot{n}_{CO_2}]_O}{[\dot{N}_{CO_2}]_S}\right\}. \qquad (7)$$

Figure 2 shows a typical set of results for an experiment involving a lime sphere. The concentration of carbon dioxide leaving the furnace measured when pure carbon dioxide was passed into the sphere, and the concentration of carbon dioxide leaving the sphere calculated from Eq. (6) when argon was passed into the sphere, are plotted as functions of the molar flow rate of gas into the hollow sphere. The calculated carbon dioxide flux through the sphere and the calculated partial pressure difference across it are also plotted on the diagram. It can be seen that these variables are all functions of the rate at which gas flows into the hollow sphere,

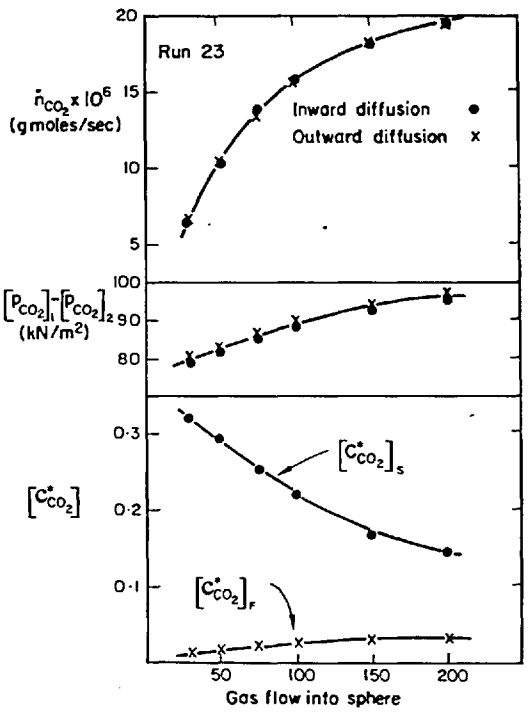


Fig. 2. The molar concentrations, partial pressure differences and molar transfer rates of carbon dioxide during a typical diffusion coefficient experiment, plotted against the volumetric gas flow rate into the hollow sphere (results taken from run 23).

although the last two variables are not affected by the direction in which diffusion takes place. This observation applied to most of the experimental results. The small discrepencies that were observed in some runs could be attributed to leakage across the seal.

The total resistance to the transfer of carbon dioxide between the bulk gas phases inside and outside the hollow sphere was then calculated from these results using Eq. (1). Values calculated from the data shown in Fig. 2 are plotted in Fig. 3 together with values calculated from a series of experiments on three other lime spheres in which measurements were made at higher gas flow rates. This figure shows that the total mass transfer resistance drops as the rate at which gas flows into the sphere is increased, until a flow rate of about 200 cm^3_{NTP}/min is reached. Further

increases in the flow rate into the sphere have no effect on the total resistance.

Since approximately equi-molar counter mass transfer is involved, the resistance due to mass transfer outside the sphere is given by the equation:

$$\Omega_o = \frac{1}{4\pi r_o^2 \alpha_o}. \quad (8)$$

Where α_o, the mass transfer coefficient to the outside of the sphere, can be calculated from the single sphere correlation proposed by Rowe, Claxton and Lewis[4]:

$$Sh = 2 + 0{\cdot}69(Re)^{1/2}(Sc)^{1/3}. \quad (9)$$

The resistance due to diffusion through the porous lime shell is given by the equation:

$$\Omega_s = \frac{1}{SD}. \quad (10)\dagger$$

Where D is the diffusion coefficient within the porous lime, and S is the shape factor. This shape factor is slightly less than that for a complete spherical shell owing to the space occupied by the alumina tube. It is given by the equation:

$$S = 3{\cdot}88\pi \frac{r_o r_i}{r_o - r_i}. \quad (11)$$

The mass transfer process between the inner surface of the hollow sphere and the entrance to the exit bore of the alumina tube is quite complicated, but can be represented by an equation similar to Eq. (8):

$$\Omega_i = \frac{1}{4\pi r_o^2 \alpha_i}. \quad (12)$$

Where α_i is the mass transfer coefficient between the inner surface and the entrance to the exit bore.

†The form of this equation assumes that concentration dependent processes such as surface diffusion play a negligible role in transporting gases through the porous lime. This is an entirely justifiable assumption, especially for the high temperature diffusion process[5].

The value of α_i would be expected to increase rapidly with the gas flow rate into the hollow sphere. Figure 1 shows that the gas inlet is very close to the gas outlet. When the internal gas flow is low, therefore, the gas will not penetrate very far into the internal gas space, and quiescent zones will exist. As the gas flow is increased, these zones will diminish until the entire gas space is turbulently mixed. At high gas flows, the internal mass transfer coefficient will be sufficiently large for Ω_i to make no sensible contribution to the total mass transfer resistance. Figure 3 shows that this would appear to occur

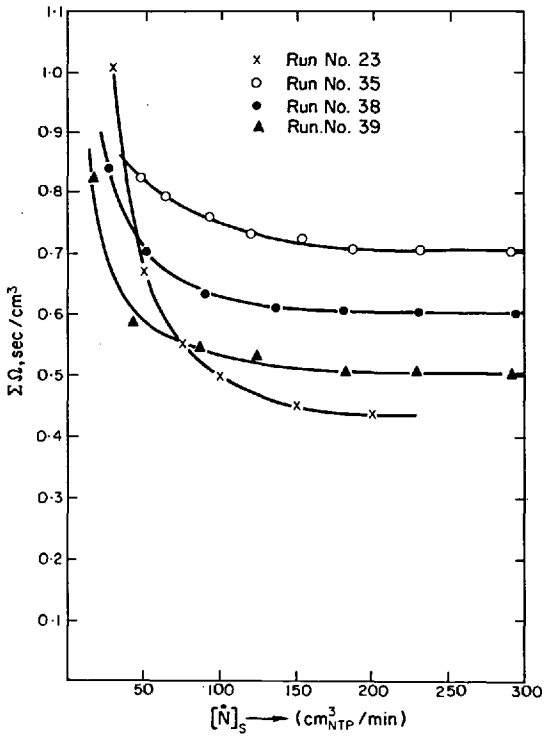


Fig. 3. The total mass transfer resistance for carbon dioxide during the diffusion coefficient measurements, plotted against the volumetric gas flow rate into the hollow sphere (results for run 23, 35, 38 and 39).

Run	ϵ_{CzO}	r_i(mm)	r_o(mm)	Temp. of measurement
23	0·596	5·76	10·43	870°C
35	0·473	5·68	9·93	950°C
38	0·528	5·59	9·96	950°C
39	0·535	5·70	10·27	950°C

when the internal gas flow is greater than 200 cm^3_{NTP}/min.

The total pressure within the hollow sphere also increases as the gas flow into the sphere is increased. Were the lime shell sufficiently permeable, Newtonian gas flow across it could contribute to the effective value of the diffusion coefficient which would therefore increase with the internal gas flow rate. However, the specific surface areas of lime measured by Murray, Fischer and Sabean[2] suggest that the Knudsen number in the lime is about 10, at which value Newtonian gas flow across the lime would be negligible. This conclusion will be discussed later, but it appears to be born out by the negligible variation in total mass transfer resistance that was found to occur at internal gas flow rates above 200 cm^3_{NTP}/min. It can therefore be concluded that the variation in the total resistance that occurs below 200 cm^3_{NTP}/min, is entirely due to the variation of α_i.

Thus the total mass transfer resistance at internal gas flows of 200 cm^3_{NTP}/min and above is only due to the diffusion resistance across the spherical lime shell and the mass transfer resistance outside it. Since the latter can be calculated from Eq. (9) and the molecular diffusion coefficient in CO_2–argon mixtures,† the diffusion resistance of the lime shell can be obtained by difference. Once this is done, the diffusion coefficient for carbon dioxide across the material of the hollow sphere can be calculated from Eq. (10) and (11).

The results obtained for the original calcium carbonate spheres and for the lime spheres produced by their decomposition are plotted in Figs. 4 and 5 against the relevant porosities. The latter have been calculated from the measured weight of the original carbonate sphere and from the internal and external radii of the lime and carbonate spheres. The external radii of the spheres were observed to decrease during sintering and during decomposition (about 5 per cent). The internal radii were assumed to suffer the same fractional contractions, and this was verified

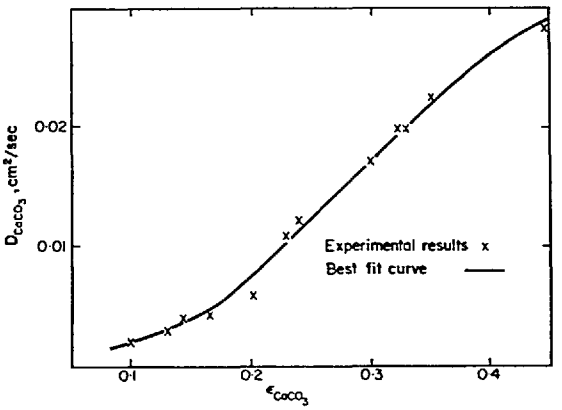


Fig. 4. Diffusion coefficient of CO_2 through porous calcium carbonate plotted against the porosity of the carbonate.

in certain experiments where sintered and decomposed spheres were sectioned and their internal radii measured. The results shown in Fig. 5 are discussed later.

THERMAL CONDUCTIVITY OF POROUS LIME

Experimental

Long thin hollow cylindrical samples of calcium carbonate were prepared by compaction and decomposed in air to form lime cylinders whose porosities varied from 20 to 80 per cent. An evenly wound coil of S.W.G. 30 Nichrome wire was inserted into the centre of each cylinder in turn, and a thin layer of alumina powder placed around it. Thermocouples were embedded in the inner and outer surfaces of the cylinder so that their beads lay in its mid-plane. A known current was passed through the coil at a known voltage and the temperatures indicated by the two thermocouples were recorded once they had achieved steady values. The current was then varied so that measurements could be repeated with the lime at different average temperatures. After these measurements had been made, the lime cylinders were weighed, and their internal and external diameters were measured.

Analysis of results

The cylinders were long enough for axial conduction to be ignored in the centre region. Here, the conduction of heat across the cylindrical

†The value obtained at 950°C is 0·015 sec/cm³.

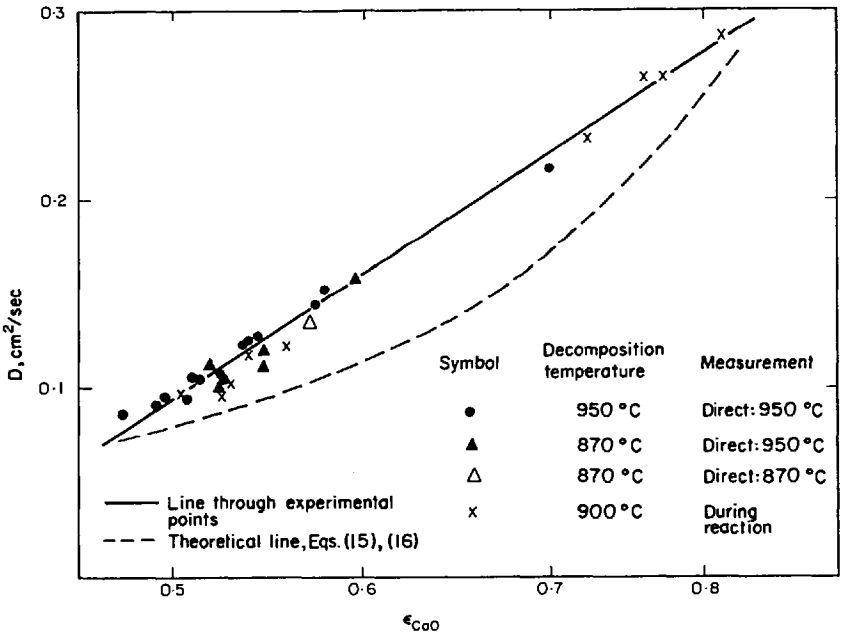


Fig. 5. Diffusion coefficient of CO_2 through porous lime plotted against the porosity of the lime.

shell obeyed the conventional heat conduction equation:

$$\dot{q}'' = \frac{2\pi k(\theta_i - \theta_o)}{\text{Ln}\,\{d_o/d_i\}}. \qquad (13)$$

This equation was used to calculate the thermal conductivity of the porous lime from the power dissapated in the nichrome coil, and the measured temperatures. The results were observed to vary slightly with the average lime temperature, decreasing with temperature when the porosity was high, and increasing with temperature when it was low. The total variation was never more than 10 per cent in the temperature range 200°–900°C. The results were used to determine the conductivity of lime at 800°C, and these values are plotted against porosity in Fig. 6.

DECOMPOSITION EXPERIMENTS ON SINGLE SPHERES

Spherical compacts of calcium carbonate of varying porosity, prepared by compaction, by balling[3] and by pelletising[3], were supported from a thermo-balance and hung in a furnace heated to 900°C, air being passed through the furnace at 1 l. per min. The experimental technique used was the same as that used by Hills. Typical results are shown in Fig. 7, in which the fractional unreacted mass of three spheres is plotted against the reaction time. The figure also shows curves predicted from Hills' theoretical model, and from the transport properties measured as described in the previous sections.

In certain of the decomposition experiments Hills' method was used to determine the diffusion coefficient of carbon dioxide through the porous lime from the measured decomposition rates. Values determined in this way are plotted on Fig. 5 together with the values measured directly. These values are discussed later.

DISCUSSION

Transport properties of porous lime

(a) Diffusion coefficient of carbon dioxide. The measured values of the diffusion coefficient

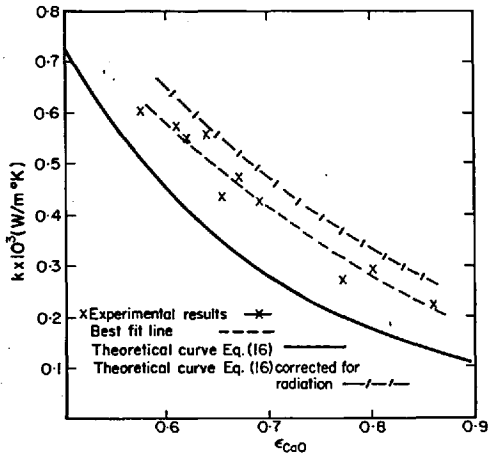


Fig. 6. Thermal conductivity of lime at 800°C plotted against porosity.

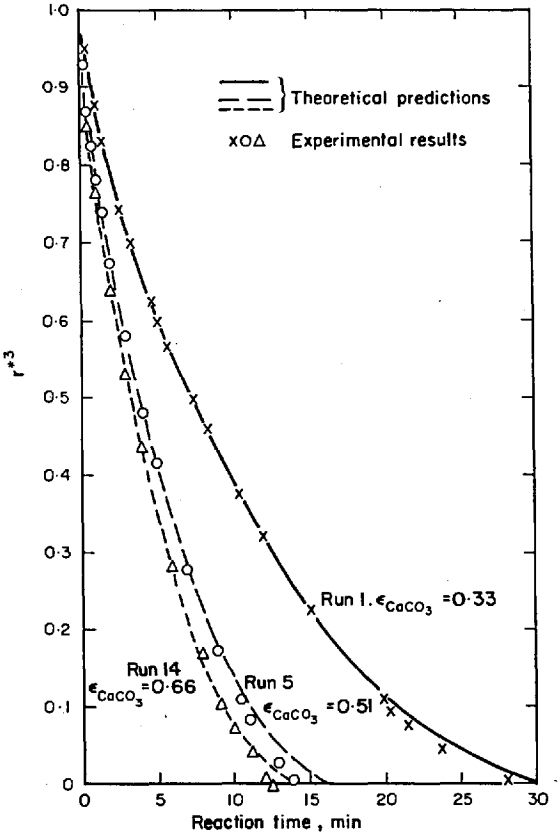


Fig. 7. Decomposition rates of calcium carbonate of varying porosity—fractional unreacted mass plotted against the reaction time.

of carbon dioxide in porous lime are shown in Fig. 5. The values marked with dots and triangles have been measured directly using the technique described here. The values plotted as crosses have been determined during the decomposition of calcium carbonate using the technique described by Hills[1], the values at porosities below 0·6 having been measured previously[1] and the values at porosities above 0·6 measured in the decomposition experiments described here. All the results lie close together, although values for any one porosity tend to increase both with the temperature of measurement and with the temperature at which the lime was formed†. With this tendency in mind, the values measured during the previous decomposition experiments for $\epsilon_{CaO} < 0{\cdot}6$ can be seen to agree with the direct measurements made here, especially since the mean lime temperature during the decomposition experiments was about 870°C.

The diffusion coefficient values are far too low to be explained in terms of molecular diffusion. The molecular diffusion coefficient in a porous solid, $D_{p,AlB}$ is related to the free gas diffusion coefficient, D_{AlB}, by the equation:

$$D_{p,AlB} = \frac{\epsilon}{\tau} D_{AlB} \qquad (14)$$

where ϵ is the porosity, and τ is an empirical tortuosity factor.

The free gas diffusion coefficient for argon/carbon dioxide mixtures may be determined using the correlation of Wilke and Lee[7] to an accuracy of about 5 per cent, the value obtained at 950°C being 1·75 cm²/sec. The mean of the values measured here for lime whose porosity is 0·5 is 0·094 cm²/sec, and would correspond to a tortuosity factor of 9·3 were carbon dioxide to diffuse through lime by molecular diffusion. In their review of diffusion data in porous solids, Satterfield and Sherwood[5] show that measured

†This latter tendency agrees with the observations of Azbe[6]. He used the electron microscope to show that the size of individual lime crystals increased with the temperature at which they were formed. At any given porosity, then, the size of channels in porous lime will also increase with the temperature at which it was formed.

diffusion data in unconsolidated solids correspond to tortuosity factors for molecular diffusion that fall in the range $1{\cdot}4 < \tau < 1{\cdot}8$, when $\epsilon = 0{\cdot}5$.

Thus it appears that molecular diffusion will not contribute very much to the diffusion of carbon dioxide through porous lime. Indeed, the behaviour of the experimental system strongly suggests that the diffusion process is entirely governed by Knudsen diffusion. The total gas pressure within the hollow sphere is greater than the pressure outside it due to the pressure drop along the exit bore of the alumina tube, and, moreover, this difference in pressure increases as the internal gas flow rate is increased. Figure 3 shows that the total resistance to the transfer of carbon dioxide across the hollow lime sphere is not affected by the internal gas flow rate as long as this is greater than 200 cm^3_{NTP}/min. Furthermore it has been observed in most of the experiments that the resistance to the transfer of carbon dioxide inwards across the lime sphere equals the resistance to its transfer outwards†. These transfer resistances have been determined by dividing the flux of carbon dioxide into the difference between the partial pressures of carbon dioxide in the internal cavity and in the furnace. The observations described above show that this resistance is independent of the total pressure gradient. If the pore structure of the lime were such that molecular diffusion could contribute to the diffusion mechanism, it would also allow Newtonian bulk gas flow to occur under the action of this total pressure gradient. This bulk flow would contribute to the transport process within the lime, so that the measured mass transfer resistance would continue to decrease as the internal gas flow was increased. If, however, the pore structure were such that Knudsen diffusion was the dominant diffusion mechanism, the flow process through the lime would be slip flow, and no distinction can be made between flow and diffusion. Under these conditions each gas would flow through the lime independently, and the mass transfer resistance calculated as described above could be regarded as a resistance either to the flow of carbon dioxide through the lime, or to its diffusion. This resistance would obviously be independent of the total pressure gradient as has been observed experimentally. Thus it can be concluded that the Knudsen diffusion process dominates the diffusion of carbon dioxide through porous lime, molecular diffusion making a negligible contribution.

This conclusion is born out by the magnitude of the experimental results. The Knudsen diffusion coefficient through porous lime can be calculated from the specific surface area measurements made by Murray, Fischer and Sabean[2], using the equation presented by Satterfield and Sherwood[5].

$$D_{K,A} = 19{,}400 \frac{\epsilon^2}{\tau s \rho_p} \sqrt{\frac{\theta}{M_A}} \qquad (15)$$

where $D_{K,A}$ is measured in $cm^2\,sec^{-1}$, ρ_p is the apparent density of the porous solid in $g\,cm^{-3}$, θ is the absolute centigrade temperature and M_A is the molecular weight.

The specific surface data of Murray *et al.* are rather scattered, but approximately follow the dimensional equation:

$$\frac{s}{10^4} = 35{\cdot}5\epsilon - 4{\cdot}6. \qquad (16)$$

where s is measured in cm^2/g.

The dashed line shown in Fig. 5 has been calculated by substituting this equation into Equ. (15) using an assumed value for the tortuosity factor: $\tau = 1{\cdot}5$. The agreement between this line and the experimental results is quite good. It shows that if the diffusion process is Knudsen diffusion, the tortuosity factor in porous lime will be about 1·5, but will probably vary with porosity. However, the agreement can only be taken as further evidence for Knudsen diffusion once some justification has been advanced for the assumed value of the tortuosity factor. Lime melts at about 2850°K and it would not be ex-

†In the few experiments where this was not true, the difference was small and was due to leakage across the seal.

pected to sinter at all below its Tammann temperature (1425–1766°K). The lime studied here has been formed by decomposing calcium carbonate at temperatures below 950°C, and this temperature was not exceeded at any time during the experiments. Thus the lime would not sinter and would be, in fact, an unconsolidated porous solid. As stated previously, measured diffusion data for unconsolidated porous solids fall in the range $1{\cdot}4 < \tau < 1{\cdot}8$, so that the chosen value is perfectly reasonable.

Thus both the values of the diffusion coefficient measured here and the behaviour of the experimental system show that carbon dioxide diffuses through lime by Knudsen diffusion and not by molecular diffusion. In the decomposition of calcium carbonate, then, the diffusion of carbon dioxide through porous lime is independent of the presence of an inert gas species, as was demonstrated by Hills[1] from the results of decomposition experiments. The diffusion coefficient values measured here have been used to predict the rate at which calcium carbonate will decompose in air, and these predictions are discussed later.

(b) Thermal conductivity of porous lime. The measured values of the thermal conductivity of porous lime at 800°C are plotted in Fig. 6 against the porosity of the lime. Several different methods have been derived to predict the thermal conductivity of porous solids, of which the simplest is that proposed by Woodside and Messmer[8]. They give the following equation for the effective conductivity of a porous material:

$$k = k_d \left\{\frac{k_c}{k_d}\right\}^{1-w} \qquad (17)$$

where k_c and k_d are, respectively, the thermal conductivities of the continuous and discontinuous phases, and w is the volume fraction of the discontinuous phase.

Kingery[9] has measured the thermal conductivity of a single lime crystal and found it to be 8·0 W/m°K, and Eckert and Drake[10] give the thermal conductivity of air as 0·067 W/m°K at 800°C. This data can be substituted into Eq. (17) to determine a theoretical value for the thermal conductivity of porous lime, and the full line in Fig. 6 has been determined in this way.

The theoretical line falls below the experimental results, no doubt due to the effect of radiative heat transfer across the pores in the lime, since this is ignored in Eq. (17). Yagi and Kunii[11] have developed equations which allow the influence of radiation on the effective thermal conductivity to be assessed. A correction factor has been determined from their equations and has been applied to the values predicted from Eq. (17), giving the dash-dotted line in Fig. 6. This line falls above the experimental results, although it is much nearer to them, and it can be concluded that radiation plays an important role in the transfer of heat through the porous lime at 800°C.

The importance of the transport properties in determining the decomposition rates of calcium carbonate

Figure 5 shows that the diffusion coefficient values measured directly in this work agree within the limits of experimental error with the values calculated by Hills from the decomposition rates of dense compacts of calcium carbonate[1]. This work, therefore, confirms the suggestion that heat and mass transfer control the decomposition of dense pellets of calcium carbonate. However, this conclusion does not necessarily apply to the decomposition of porous pellets, since the higher diffusion rates involved could increase the relative importance of the chemical processes that occur in the reaction zone. If this occurred, the rate of the reaction would be slower than predicted by the heat and mass transfer model, and, moreover, the reaction zone could no longer be considered of negligible thickness.

In his work on dense pellets, Hills sectioned partially decomposed pellets and painted them with an alcohol solution of thymolphthalein. This turned dark bue in contact with the lime but was unaffected by the carbonate, and it showed that the reaction zone was of negligible thickness and could be considered to be an inter-

face as far as the heat and mass transfer equations were concerned. Unfortunately, this experimental technique could not be used for the porous pellets considered here since they soaked up the indicator too readily. It was therefore decided to investigate whether or not the heat and mass transfer model applied to porous pellets by making a direct comparison between the decomposition rates predicted by the model and the rates measured experimentally.

The model assumes that the reaction occurs at a shrinking interface within the pellet and that the chemical step on this interface does not affect the reaction rate. The partial pressure of carbon dioxide in the gas pores at the interface is thus equal to the equilibrium decomposition pressure of carbon dioxide at the temperature of the interface. The rate of the reaction is determined by the relationship between these two quantities and by the equations for heat and mass transfer between the interface and the atmosphere surrounding the reacting particle. The temperature of the particle varies during the reaction, so that the heat transfer process occurs under unsteady conditions, but little error is introduced if the thermal mass of the particle is assumed to act at the reaction interface[1]. For a spherical particle decomposing in air then, the fractional radius and temperature of the reaction front, are to be determined by solving the following two ordinary, non-linear, differential equations.

$$\frac{dr^*}{dt} = -\frac{Dp_o \exp\left\{\frac{\Delta S}{R} - \frac{\Delta H}{R\theta_R}\right\}}{\rho r_o^3 R\theta_G\{r^* - (1 - Bi_M)r^{*2}\}} \quad (18)\dagger$$

$$\frac{d\theta_R}{dt} = \frac{k\left\{\frac{\theta_G - \theta_R}{(1/r^*) - 1 - Bi_H}\right\} - \frac{DHp_o}{r_o\theta_G}\left\{\frac{\exp[(\Delta S/R) - (\Delta H/R\theta_R)]}{(1/r^*) - 1 - Bi_M}\right\}}{r_o^2 \rho c_{CaO}\left\{1 + r^{*3}\left(\frac{c_{CaCO_3}}{c_{CaO}}\right) - 1\right\}} \quad (19)\dagger$$

m^*, the fractional mass of the particles can then be determined from the identity:

$$m^* = (r^*)^3 \quad (20)$$

Figure 7 shows how the fractional mass computed from Eqs. (18–20) using a Runge–Kutta method on the Imperial College IBM 7094, varies with time for conditions that correspond to three of the decomposition experiments described earlier. The values used for the diffusion coefficient of carbon dioxide in porous lime and for the conductivity of lime were taken from the curves drawn through the experimental points in Figs. 5 and 6. The mass transfer coefficient and the convective heat transfer coefficient were determined from Eq. 9 using tabulated property values[10]. The radiation heat transfer coefficient was calculated as outlined by Hills [1] using measured values of the emissivity of lime[12]. The values taken for enthalpy and entropy changes for the reaction were those measured by Hills[13].

Figure 7 also shows the experimental values of m^* determined at different times during the decomposition experiments. It can be seen that the predicted curves agree remarkably well with the experimental points during the first 93 per cent of the reaction, after which the experimentally determined decomposition rates are slightly faster than the predicted rates. The difference is very small and cannot be due to an extension of the reaction zone, or to any chemical step in that zone, since their effects would be to slow down the rate of the reaction. Thus it can be concluded that the assumptions made in Hills' model are valid during the decomposition of highly porous calcium carbonate pellets, even when the porosity of the lime produced is as high as 80 per cent. In fact, the agreement shown in Fig. 7 is very good, since the data on which the theoretical predictions are based, have been measured in experiments that are completely

†These equations are rearranged forms of Eqs. (35) and (33) in [1].

independent of the decomposition experiments.

Some of the spherical carbonate compacts used in the decomposition experiments contained a thermocouple placed so that its bead lay at the centre of the compact. Typical temperatures recorded by these thermocouples are shown in Fig. 8 together with the reaction interface temperatures predicted theoretically and it can be seen that the experimental points lie above the theoretical curves. This would be expected during the initial stages of the reaction since some of the heat absorbed at the reaction interface would be provided by cooling the sphere and the reaction interface would thus be colder than the centre of the sphere. Neither is the lack of close agreement during the later stages altogether unexpected. Some small degree of error would be involved in the temperature measurement since the conduction of heat down the thermocouple leads could maintain the bead at a temperature slightly above its surroundings. The discrepancy is, however, mainly due to the theoretical approximations made in treating the unsteady heat transfer process. Figure 8 shows that these approximations do not produce too great an error in the predicted pellet temperature, and Fig. 7 shows that they have a negligible effect on the predicted reaction rates.

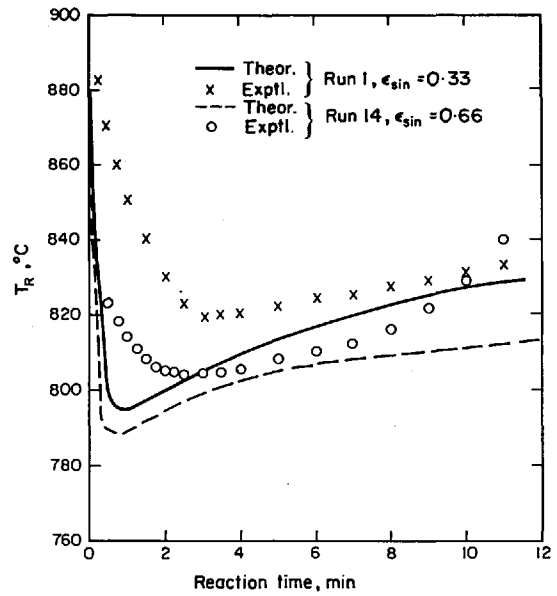


Fig. 8. Sample temperatures during the decomposition of calcium carbonate.

CONCLUSIONS

This work has shown that the decomposition rates of porous calcium carbonate pellets can be predicted once values of the relevant transport properties of porous lime have been determined in an independent series of experiments. The predictions have been based on a reaction model which assumes that the decomposition takes place at a precisely defined interface, and that the chemical step at this interface plays no part in controlling the reaction rate. The close agreement that exists between the measured reaction rates and the predictions of the theory shows that these assumptions are valid, even when the porosity of the original carbonate compact is as high as 66 per cent.

Acknowledgments—The authors wish to thank the British Scholarship Fund for Yugoslavs for supporting A. Paulin during the period of this research and the Athlone Fellowships Management Committee for supporting F. R. Campbell. They also wish to thank Professors Richardson and Bradshaw of the Metallurgy Department at Imperial College for the support that they have given this work, and for the interest they have shown in it.

NOTATION

Bi_H "Biot modulus" for heat transfer ($= k/hr_o$)
Bi_M "Biot modulus" for mass transfer ($= D/\alpha r_o$)
C molar specific heat
C^* mole fraction
d diameter of cylindrical sample
D diffusion coefficient of CO_2 in porous lime
h heat transfer coefficient
H heat of decomposition of calcium carbonate
k thermal conductivity
m mass of a reacting compact
m^* fractional mass of reacting compact ($= (m - m_\infty)/(m_b - m_\infty)$)
M molecular weight
$\dot{n}$ molar transfer rate through the lime sphere

$\dot{N}$ molar flow rate
p partial pressure of a gas species
p_T total gas pressure
p_o pressure of a standard atmosphere (= 101·3 kN/m²)
$\dot{q}'$ heat flow rate per unit length
r radius of a spherical compact, or reaction front
R gas constant (= 8·32 kJ/kg-mole °K)
r^* fractional radius of the reaction front ($= r/r_o$)
Re Reynold's number
S shape factor for diffusion or conduction
ΔS entropy change for decomposition of calcium carbonate
s specific surface of a powder
Sh Sherwood number
Sc Schmidt number
t reaction time

Greek symbols

α mass transfer coefficient
τ tortuosity factor for diffusion in porous solid
ϵ porosity
ρ molar density of a compact
ρ_p apparent density of a porous solid
θ temperature
Ω mass transfer resistance
ω volume fraction of discontinuous phase in a porous solid

Suffices

1,2 values at ends of mass transfer path
b value at beginning of reaction experiment
c value for continuous phase
d value for discontinuous phase
F value in gas phase entering or leaving furnace
G value in gas phase surrounding decomposing compact
I transferred inwards through hollow sphere
i value within hollow sphere
O transferred outwards through hollow sphere
o value outside hollow sphere
R value at reaction interface
S value in gas phase entering or leaving hollow sphere
s value across hollow sphere
A/B value for a binary gas mixture
$p,A/B$ value for a binary gas mixture within porous solid
K,A value for Knudsen diffusion of gas "A" in a porous solid

REFERENCES

[1] HILLS A. W. D., *Chem. Engng. Sci.* 1968 **23** 297.
[2] MURRAY J. A., FISCHER H. C. and SABEAN D. W., *Proc. Am. Soc. test. Mater.* 1950 **50** 1263.
[3] PAULIN A. Ph.D. Thesis, London University 1968.
[4] ROWE P. N., CLAXTON K. T. and LEWIS J. B., *Trans. Instn chem. Engrs* 1965 **43** T14.
[5] SATTERFIELD C. N. and SHERWOOD T. K., *The Role of Diffusion in Catalysis*, p. 17. Addison-Wesley 1963.
[6] AZBE V. J., *Rock. Prod. Stone Edn., 1944*, Vol. 47, 1968.
[7] WILKE C. R. and LEE C. Y., *Ind. Engng Chem.* 1955 **47** 1253.
[8] WOODSIDE W. and MESSMER J. H., *J. appl. Phys.* 1961 **32** 1688.
[9] KINGERY W. D., *Progress in Ceramic Science, Vol.* 2. Pergamon Press 1962.
[10] ECKERT E. R. C. and DRAKE R. M., *Heat and Mass Transfer*, p. 304. McGraw-Hill 1959.
[11] YAGI S. and KUNII D., *A. I. Ch. E. Jl* 1957 **3** 273.
[12] HILD K., *Mitt. K.-Wilhelm-Inst. Eisenforsch. Dusseld.* 1932 **14** 59.
[13] HILLS A. W. D., *Trans. Inst. Min. Metall. Series C* 1967 **76** C241.

Résumé– Des techniques expérimentales spéciales ont été mises au point pour mesurer la conductivité thermique de la chaux poreuse et le coefficient de diffusion de l'acide carbonique à travers la chaux. Des mesures ont été effectuées sur la chaux dont la porosité variait dans la gamme de 0,45 $< \epsilon <$ 0,8, et les résultats ont montré que le processus de diffusion est la diffusion de Knudsen, conclusion qui est compatible avec les mesures antérieures de la surface spécifique de la chaux poreuse. Les résultats ont été utilisés pour confirmer que la décomposition du carbonate de calcium est contrôlée par le transfert de chaleur et de masse. On peut prévoir le taux de décomposition en employant un modèle de transfert de chaleur et de masse qui suppose que la réaction se produit sur une interface

en retrait et que les processus chimiques sur cette interface ne jouent aucun rôle dans le contrôle de ce taux. Ces prévisions sont exactes même lorsque la porosité du carbonate original est aussi élevée que 0,66.

Zusammenfassung—Es sind Versuchsmethoden entwickelt worden um die Wärmeleitfähigkeit von porösem Kalk und den Diffusionskoeffizienten von Kohlendioxyd durch denselben zu messen. Es wurden Messungen an Kalk durchgeführt dessen Porosität innerhalb des Bereiches $0{,}45 < \epsilon < 0{,}8$ schwankte, und die Ergebnisse deuten darauf hin, dass es sich um Knudsensche Diffusion handelt, wobei diese Folgerung mit früheren Messungen der spezifischen Oberfläche von porösem Kalk im Einklang steht. Die Ergebnisse wurden dazu verwendet um zu bestätigen, dass die Zersetzung von Calciumkarbonat durch Wärmeund Stoffübertragung gesteuert wird. Die Zersetzungsgeschwindigkeit kann eindeutig durch Verwendung eines Wärme- und Stoffübertragungmodells vorausgesagt werden, das auf der Annahme beruht, dass die Reaktion auf einer zurückweichenden Grenzschicht stattfindet, und dass die chemischen Vorgänge auf dieser Grenzschicht nicht an der Steuerung der Geschwindigkeit beteiligt sind. Die Vorhersagen sind zutreffend, auch wenn die Porosität des ursprünglichen Karbonates eine Höhe bis zu 0,66 hat.